PTYCHOGRAPHIC IMAGING

OF

MIXED STATES

Darren Batey

A thesis submitted for the degree of

Doctor of Philosophy

Department of Electronic and Electrical Engineering

University of Sheffield

England

September 2014

Contents

Abstract

Ptychography is a lens-less imaging technique which, by replacing the function of a lens with a computer algorithm, allows for aberration free, complex imaging, of all manner of specimens in a variety of situations. Compared to alternative methods, the technique has relatively loose requirements on the physical setup and has been demonstrated to operate across the visible light, x-ray, and electron regimes.

This thesis reviews progress in the field followed by four chapters of original work. The unique imaging process of ptychography is initially examined in theoretical terms and the conclusions that are drawn are subsequently applied in all three of the main imaging domains; visible light, x-ray, and electron. The development of several new algorithms is discussed, which alleviate many of the current experimental constraints. These include the processing of diffraction patterns that are sampled grossly below the conventional Nyquist limit, the automatic correction of detector imperfections, the imaging of mixed states through multiple wavelength illumination, and the reconstruction of partially coherent data in the STEM configuration through the deconvolution of an extended source.

Declaration

The work presented in this thesis is my own, based on research carried out in the Department of Electronic and Electrical Engineering, University of Sheffield, England. No part of this thesis has been submitted elsewhere for any other degree or qualification and unless explicitly referenced to the contrary is solely my own work.

Darren Batey

29th of September 2014

Acknowledgements

Throughout my PhD studies, I have been very lucky to work alongside some fantastic people, whose assistance, advice, and perpetual discussion has played no small part in the work outlined in this thesis. In particular I would like to thank Tega Edo for his boundless enthusiasm and wide ranging exchanges, Francis Sweeney for his assistance with the electron microscope and useful discussions, Andrew Maiden for kind access to his up-to-date code on day one, Daniel Claus for his expertise with the optical bench work, and Peng Li for the numerous helpful conversations.

Special thanks also go to my supervisor, John Rodenburg, whose extensive knowledge, insight, and advice have not only guided me expertly through my PhD but left me with a solid understanding of how to conduct meaningful scientific research.

The work presented here would also not be possible without the appropriate funding and so I would like to acknowledge the financial support from the EPSRC Basic Technology Grant (EP/E034055) and Doctoral Training Partnership (DTP) along with Phase Focus Ltd. who funded a sponsorship towards the end of my studies.

Most importantly of all, I thank my family for their unwavering support.

Publications

Batey, D. J., Edo, T. B., Rau, C., Wagner, U., Pešić, Z. D., Waigh, T. A. & Rodenburg, J. M. 2014b. Reciprocal-space up-sampling from real-space oversampling in x-ray ptychography. *Physical Review A,* 89, 043812.

Batey, D. J., Claus, D. & Rodenburg, J. M. 2014a. Information multiplexing in ptychography. *Ultramicroscopy,* 138**,** 13-21.

Edo, T. B., Batey, D. J., Maiden, A. M., Rau, C., Wagner, U., Pešić, Z. D., Waigh, T. A. & Rodenburg, J. M. 2013. Sampling in x-ray ptychography. *Physical Review A,* 87, 053850.

Wang, P., Batey, D. J., Rodenburg, J. M., Sawada, H. & Kirkland, A. I. 2013. Towards Sub-Angström Ptychographic Diffractive Imaging. *Microscopy and Microanalysis,* 19**,** 706-707.

List of Symbols

S: A function representing the distribution of flux across the mutually incoherent elements of a source of radiation.

P: A complex function representing the patch of illumination at the specimen (referred to as the probe).

O: A complex function representing the refractive index of the specimen (referred to as the object).

ψ: A complex function representing the illumination after interaction with the specimen (referred to as the exit-wave) in real-space.

Ψ: A complex function representing the illumination after interaction with the specimen (referred to as the exit-wave) in reciprocal-space.

$\mathbb{U}_o$: The real-space update function for the object.

$\mathbb{U}_p$: The real-space update function for the probe.

$\mathcal{P}_r$: A real-space projection of an estimate onto a set of constraints.

$\mathcal{P}_u$: A reciprocal-space projection of an estimate onto a set of constraints.

α: The global update step of an array.

β: The local (element-wise) update step of an array.

D_p: The physical width of the probe at the object plane.

D_s: The synthetic (reconstructed) width of the probe at the object plane.

θ_p: The physical angular range of the detector as subtended at the object plane.

θ_s: The synthetic (reconstructed) angular range of the detector as subtended at the object plane.

$\Delta\theta_p$: The physical angular range of the detector pixel-pitch as subtended at the object plane.

$\Delta\theta_s$: The synthetic (reconstructed) angular range of the detector pixel-pitch as subtended at the object plane.

U_p: The physical width of the detector in reciprocal units.

U_s: The synthetic (reconstructed) width of the detector in reciprocal units.

ΔU_p: The physical pixel-pitch of the detector in reciprocal units.

ΔU_s: The synthetic (reconstructed) pixel-pitch of the detector in reciprocal units.

X_p: The width of the real-space Fourier-repeat unit cell associated with the reciprocal-space separation between physical detector pixels.

X_s: The width of the real-space Fourier-repeat unit cell associated with the reciprocal-space separation between synthetic (reconstructed) detector pixels.

ΔX_p: The real-space pixel-pitch associated with the reciprocal-space width of the physical detector.

ΔX_s: The real-space pixel-pitch associated with the reciprocal-space width of the synthetic (reconstructed) detector.

R: The real-space scan coordinate.

ΔR: The real-space scan step size.

r: The real-space spatial coordinate.

u: The reciprocal-space spatial coordinate.

η: The non-spatial coordinate for mutually incoherent modes.

ξ: The non-spatial coordinate for forward estimates.

$\widehat{\boldsymbol{S}}$: The ptychographic sampling factor for intensity measurements.

Algorithms

This thesis describes several new reconstruction algorithms, each of which makes relatively subtle but powerful amendments to an existing algorithm, ePIE. For clarity, these are described separately below. Although described and demonstrated individually, these algorithms are not mutually exclusive. They may form one single algorithm, where varying combinations may be executed simultaneously. Also, although for the purposes of this work the new methods are described in terms of the ePIE algorithm, the principles are general and should be easily applicable to other ptychographic reconstruction algorithms.

1. Low Dose

Ptychography relies on the processing of subsets of data, which are related through mutual areas of the specimen. As a result the total dosage through the specimen is necessarily distributed across many diffraction patterns and so preserving a low level of specimen irradiance produces individual measurements that are heavily affected by noise. ePIE currently updates the probe and object functions in an identical manner, however, the probability of arrival of a photon at an object element relates to the square of the modulus of the wave-field at that point whereas the probability of transmission through that object element relates only to the modulus of its transmission function. Altering the probe update to account for this asymmetry prevents the algorithm from diverging as the total dose in each diffraction pattern is lowered. A second issue with the current algorithm with relation to low dose data is in the update of the exit-waves at the detector plane. For diffraction patterns with good counting statistics, each forward estimate may be updated fully by the measured intensities at that scan position because each measurement may be assumed to be correct. However, as the dose per diffraction pattern is lowered each individual measurement has lower counting statistics. As the forward estimate is generated from a region at the object plane which consists of overlapping exposures, each such forward estimate has a greater statistical relevance

than the intensity measurements made at that single scan position. The new algorithm addresses this issue by introducing a weighting function within the detector plane update step. To begin with, the object estimate contains no information (it is entirely an unknown) and so each forward estimate must be updated fully by the measured diffraction patterns. However, as the reconstruction proceeds, the weighting function is adjusted so that the forward estimates are altered by ever decreasing amounts. In so doing, a consistent solution is continually reinforced as the inconstancies decay away. These two alterations to the current algorithm allow for the reconstruction of data which has the total dosage distributed across a very large number of measurements, even when that results in extremely low counting statistics per measurement. As the information content per count is optimised under such conditions, these alterations are an important step for low dose ptychography of beam sensitive specimens.

2. Up-sampling (sPIE)

The sPIE algorithm is designed to process diffraction patterns which have been sampled well below the Nyquist limit and so do not satisfy the conventional single-shot CDI sampling condition. By exploiting the four-dimensional ptychographic sampling condition, sPIE is able to utilise a reduction in the real-space step size to allow for an increase in not only the pixel-pitch but, importantly, the pixel-size of the detector. sPIE allows the whole reconstruction process to run on an array which does meet the Nyquist sampling condition, therefore creating a conflict between the sampling pitch of the forward exit-wave estimates and the physical pixel-size. In order to overcome this, the detector plane update step is altered so that groups of estimated pixels which exist within a region covered by a single larger physical pixel may be constrained by that value without affecting their relative internal distributions. This is achieved by comparing the measured intensity from the large pixel with that of the sum of intensities within the corresponding group of estimates in order to create an update ratio. Multiplying each forward intensity estimate within the sub-group by this ratio, it is possible to ensure only the information that has been recorded (the total intensity within

that area) is able to constrain the forward estimates whilst all other information (the internal distribution and relative phases of that region) is preserved. The new algorithm liberates ptychography from the conventional wisdom that each diffrcation pattern must itself be sampled within the Nyquist limit, significantly relaxing some of the major limitations of the experimental setup (probe size, specimen-detector distance, and pixel-size).

3. Mixed States (MS-PIE)

sPIE demonstrates an ability to update a set of estimated, complex-valued, exit-wave elements using knowledge only of their sum of intensities in the detector plane. The MS-PIE algorithm employs the same reciprocal-space update step as sPIE but introduces a multi-dimensional real-space update procedure whereby separate states of emission may exist in the source and each subsequent element in the system (the optics and the specimen) may respond to each of those states separately. Processing of such data using MS-PIE allows for the imaging of dynamic events within a specimen, spectroscopy of a specimen using multiple wavelength radiation, or indeed the decomposition of mutually incoherent modes of any kind given sufficiently sampled data.

4. Detector Response (DR-PIE)

Current algorithms rely heavily on data being recorded on a detector with an ideal, linear, response. DR-PIE exploits the fact that each physical pixel in a ptychographic setup is recording different levels of intensities as the illumination is scanned across the specimen, creating a spread of measured values per pixel. As the reconstruction algorithm runs through an iteration (converging towards a solution which is globally consistent), there is also a spread of estimated values created per pixel. By plotting the measured values against the estimated values for each pixel and fitting a polynomial, it possible to extract estimates of the offsets and gains for each pixel. The measured data may then be adjusted using the estimated values of offset and gains. Following iteration(s) then update the exit-waves with the adjusted intensity values. Repeating this process throughout the reconstruction

allows the algorithm to extract a single consistent solution from the corrupted data, producing a series of masks which characterise the response of the detector pixels in the process. Reducing the sensitivity of diffractive imaging to the quality of the detector used (and the quality of the reference images conventionally used for post-processing) is an important step as the quality of the detector within diffractive imaging currently defines the transfer function of the imaging system.

5. Partial Spatial Coherence (PC-PIE)

Although the MS-PIE algorithm is fully able to handle all types of partial coherence through the alteration of the number of probe and object states per source element; unless the form of incoherence is known, the end result is often ambiguous. PC-PIE adds extra constraints to the MS-PIE algorithm in order to deconvolve a source function in a particular plane. For the case of an extended source, PC-PIE extracts a single impulse response from the optics and a single image of the source. Reducing the number of reconstruction elements required (fewer probe states for example) reduces the ambiguities within the reconstruction, improves the underlying sampling condition (there are less unknowns), and in-so-doing improves the reconstruction quality. As the source of incoherence is deconvolved from the impulse response of the system, the method may also be used for equipment characterisation, measuring effects of optical instabilities and source configurations.

1 Introduction

Many scientific discoveries and engineering advancements have been made possible through advancements in the field of microscopy, providing us with the ability to see directly the structure and processes of nature in a multitude of different ways and at smaller and smaller length scales. The human desire to explore and understand the unknown, coupled with the tools afforded by the advancements in machinery, have allowed us to observe a whole world of intricate processes; from the behaviour of cells and mapping of activity within the brain; the structure of materials in the manufacturing of cars, aircraft, and a space station; to the semiconductor world of transistors and mobile communication.

Expanding the horizons of microscopy in all directions, from the observation of specimens at smaller length scales, under new conditions, and on smaller time scales, is a vital part of human progress.

The work outlined in this thesis explores some of the possibilities afforded to us when the physical manufacturing of optical elements is replaced by carefully constructed computer algorithms, which remove many of the previous barriers and unlock exciting new possibilities.

Diffractive imaging is a lens-less imaging technique which, by replacing the function of a lens with an array of intensity measurements and a computer algorithm, is able to produce an image of the specimen which is free from the imperfections of an imaging lens. A particular diffractive imaging method, named ptychography, introduces a scanning element to the data acquisition process and in so doing produces a dataset that is very rich in information content.

The original aim of ptychography was to overcome the issues presented with the electron lens, where until the development of sophisticated (and expensive) lens correction procedures were the limiting factor in the attainment of higher resolution images. It transpired that the electron microscope introduced many extra problems when collecting data. The electron microscope is a purpose built machine that is extremely good at running as intended, ptychography removes the need for many of the elements that have been finely tuned but instead requires a few of the other elements to remain stable.

Nevertheless, in recent years there has been substantial development of the reconstruction methods used with ptychographic imaging within the realm of visible light and x-ray energy photons. Although some attempts have been made within electron ptychography, and some initial results published in the literature, the method is very much lagging behind that of its equivalent in the photon regime. This thesis describes developments that I have made in the theory of ptychographic imaging and demonstrates practical results in both visible light and hard x-ray regimes. Those principles are then focussed on some of the issues more specific to the electron microscope and through simulations and experiment show that ptychography still offers exciting possibilities within the electron world.

Beginning with an overview of the required background theory, chapter 2 covers some of the essential principles of imaging. The field of diffractive imaging is then introduced in the context of recovering a complex image of the specimen after recording only a single diffraction pattern on a detector some distance away. An issue, known historically as the phase problem, is described along with a review of the strategies and methods that were developed to overcome it. Ptychography is one such method and is the focus of the work presented in later chapters.

The process of imaging via the ptychographic method is then examined in more detail in chapter 3. A new sampling condition, more suitable to ptychography (with multiple diffraction patterns) than the conventional single-shot condition (with only one diffraction pattern), is introduced. The single-shot condition is currently perceived to be a fundamental requirement of ptychography. However, demonstrations of simulated reconstructions with as few as four pixels in the diffraction pattern overturn this principle and show that the physical experimental constraints may be significantly relaxed. An intrinsic part of the new sampling condition is that many diffraction patterns must be recorded, leading to the issue of dose fractionation: Can the total dose through an object element remain constant even when that dose is shared across several diffraction patterns and where each diffraction pattern contains many fewer pixels than is required for the reconstruction from a single exposure?

Chapter 4 presents work carried out in the hard x-ray regime. As a co-investigator on the first ever experiment at the I-13 coherence branch at the Diamond Light Source I have helped to develop a functioning ptychographic x-ray microscope. Some of the issues associated with being a first user on a beam line passing through the final stages of commissioning is presented along with subsequent runs with improved experimental conditions and as a consequence, better results. The ability to process data that has previously been considered grossly under sampled is demonstrated, putting the theory of chapter 3 into the realm of practical science.

The handling of under sampled diffraction patterns when recorded on a detector which integrates over large pixels involves the interpolation of those pixels during the reconstruction process. As the large pixels record intensity, the separation of them into a set of smaller complex-valued pixels can be considered a form of modal decomposition. Chapter 5 extends the algorithm developed in chapter 4 into one which may handle completely parallel source modes (in this case emitting at multiple energies) that are recorded on an unfiltered greyscale detector. The new reconstruction algorithm is able to decompose each of the emission energies into separate reconstructions post-acquisition. Surprisingly, this is true even when those source modes interact differently with the optics of the instrument and with the specimen. Using multiple wavelength illumination in the visible light regime an RGB image of a biological specimen is generated purely from the information encoded in the ptychographic dataset.

Chapter 6 investigates electron ptychography. Initial results from a high resolution TEM are shown, with a description of the required pre-reconstruction processing and the methods used to improve the reconstruction. Building on the general algorithm developed in chapter 5, new algorithms are created which, by applying extra constraints to the reconstruction process, exploit the rich dataset produced in a ptychographic scan. The first algorithm provides the ability to solve for detector imperfections such as false offsets and gains that can occur. A second algorithm is developed which, by applying certain extra constraints, is able to separate out the effects of partial spatial coherence. Not only are the negative effects from such low levels of coherence removed, but an image of the extended source distribution is also extracted from a single ptychographic dataset.

Chapter 7 concludes the thesis with an overview of the developments made within this work. Some applications of the work presented are outlined alongside the direction of future work.

2 Background

All of the work presented in this thesis is based around the field of computational optics, essentially replacing the operation of a lens with a computational algorithm. This background chapter covers some of the general principles and foundation theory which permeates throughout the chapters that follow. The propagation of a wave-field; the conventional, lens-based, imaging system; the diffractive, lens-less, imaging system; and the extension to ptychographic imaging is all discussed in an historical context.

2.1 The Computational Propagation of Radiation

The ability to model and manipulate an optical wave-field computationally as it propagates through space is crucial and the most basic form, the diffraction of a photon through an aperture, is shown in Figure 2.1.

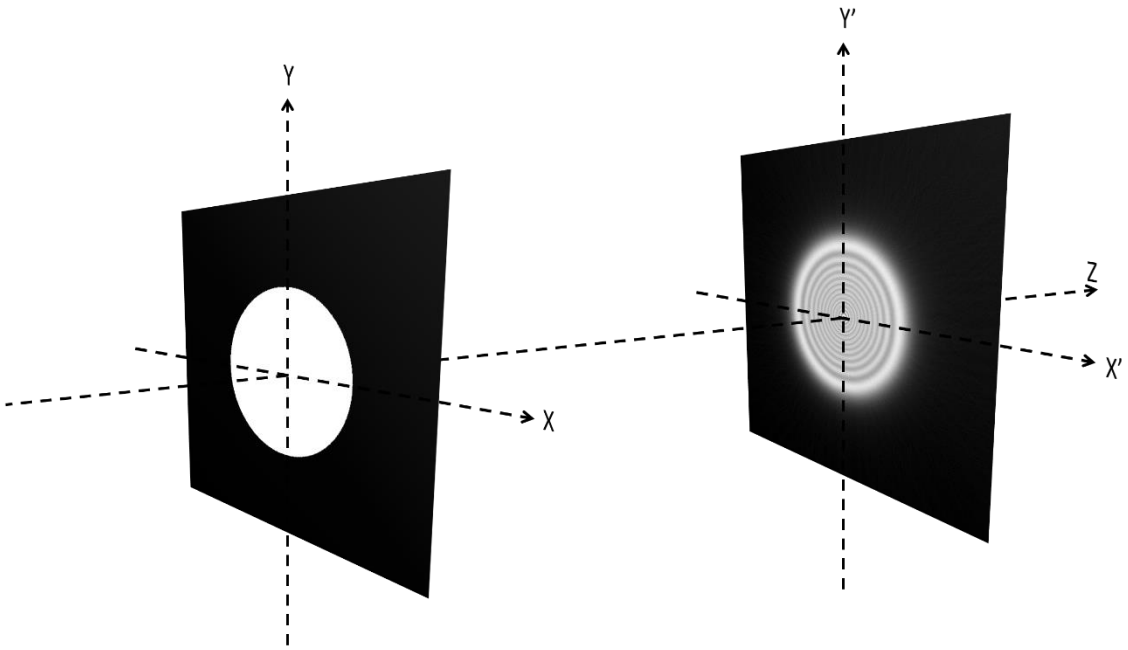

Figure 2.1: A visualisation of the computational propagation of a wave-field between two parallel planes using the angular spectrum method. A plane wave at an aperture in the XY plane is propagated along Z to the X'Y' plane. (Not to scale: the propagation distance along Z is 20 times the diameter of the aperture.)

If a detector was positioned in the plane X'Y' then a photon passing through the aperture in plane XY would be detected within a single pixel of that detector, where the intensity (modulus squared) of the wave-field describes the probability of arrival at any given point. The business of computational optics and modelling is concerned with the underlying complex wave-field and only when linked to experimental measurement is the issue of detecting a beam of individual photons (or electrons) addressed.

2.1.1 Scalar Representation of Light

The computational propagation of an optical wave-field as performed within this body of work relies upon a scalar description of the wave-field. Light may initially be described as electromagnetic waves which satisfy Maxwell's equations in the absence of free charge (shown here in their differential form),

$$\nabla \times \boldsymbol{\mathcal{E}} = -\mu \frac{\partial \boldsymbol{\mathcal{H}}}{\partial t}, \qquad 2.1a$$

$$\nabla \times \boldsymbol{\mathcal{H}} = \epsilon \frac{\partial \boldsymbol{\mathcal{E}}}{\partial t}, \tag{2.1b}$$

$$\nabla \cdot \epsilon \boldsymbol{\mathcal{E}} = 0, \tag{2.1c}$$

$$\nabla \cdot \mu \boldsymbol{\mathcal{H}} = 0, \tag{2.1d}$$

where $\boldsymbol{\mathcal{E}}$ represents the electric field, $\boldsymbol{\mathcal{H}}$ represents the magnetic field, μ and ϵ are the permeability and permittivity of the medium, respectively, and time is represented by t (Goodman, 2005).

When the medium in which the electromagnetic wave-field is propagating can be considered linear, isotropic, homogenous, and non-dispersive the four equations above may be combined into two wave equations for the electric and magnetic waves,

$$\nabla^2 \boldsymbol{\mathcal{E}} - \mu\epsilon \frac{\partial^2 \boldsymbol{\mathcal{E}}}{\partial t^2} = 0, \tag{2.2a}$$

$$\nabla^2 \boldsymbol{\mathcal{H}} - \mu\epsilon \frac{\partial^2 \boldsymbol{\mathcal{H}}}{\partial t^2} = 0. \tag{2.2b}$$

The orthogonal scalar components of the vectors in equations 2.2 ($\mathcal{E}_x$, $\mathcal{E}_y$, $\mathcal{E}_z$, $\mathcal{H}_x$, $\mathcal{H}_y$, and $\mathcal{H}_z$) each satisfy those equation separately and so they may be decomposed into a scalar form. The scalar wave-field, φ, may then be represented as,

$$\nabla^2 \varphi(P,t) - \frac{n^2}{c^2} \frac{\partial^2 \varphi(P,t)}{\partial t^2} = 0, \tag{2.3}$$

where P represents the position of the wave-field in space, n is the refractive index of the medium,

$$n = \sqrt{\frac{\mu\epsilon}{\mu_0 \epsilon_0}}, \tag{2.4}$$

c is the propagation velocity in free space,

$$c = \frac{1}{\sqrt{\mu_0 \epsilon_0}}, \tag{2.5}$$

and μ_0 and ϵ_0 are the permeability and permittivity of free space, respectively.

As all the work presented here is built on the recording of a wave-field at an instant in time (or at least integrated over a finite period of time) it is sufficient to employ a time-independent form of the wave equation. A monochromatic scalar wave-field is described by,

$$\varphi(\boldsymbol{r},t) = Re\{A(\boldsymbol{r})e^{i(\phi(\boldsymbol{r})-\omega t)}\}, \tag{2.6}$$

which can be expressed as,

$$\varphi(\boldsymbol{r},t) = Re\{\psi(\boldsymbol{r})e^{-i\omega t}\}, \tag{2.7}$$

where,

$$\psi(\boldsymbol{r}) = A(\boldsymbol{r})e^{i\phi(\boldsymbol{r})}, \tag{2.8}$$

Substitution of equation 2.6 into equation 2.3 produces the time-independent Helmholtz equation,

$$(\nabla^2 + k^2)\psi = 0, \tag{2.9}$$

where k is the wave number,

$$k = |\boldsymbol{k}| = \sqrt{\boldsymbol{k}_x^2 + \boldsymbol{k}_y^2 + \boldsymbol{k}_z^2} = \frac{2\pi}{\lambda}, \tag{2.10}$$

and λ represents the wavelength.

2.1.2 Time Independent Schrödinger Equation

This thesis contains work carried out within the electron microscope, where electrons replace photons as the source of radiation. In much the same way as a photons may be described by the wave equation that is shown in equation 2.3, a time dependent description of an electron is given by Schrödinger's equation,

$$i\hbar\frac{\partial\varphi}{\partial t} = V\varphi - \frac{\hbar^2}{2m}\nabla^2\varphi, \tag{2.11}$$

where V is the potential through which the electron is moving, $\hbar$ is a scaled version of Planck's constant, h,

$$\hbar = \frac{h}{2\pi}, \tag{2.12}$$

and m is the electron mass.

The equivalent time-independent form of equation 2.11, which satisfies equation 2.6 for the electron is given by,

$$\left(\frac{\hbar^2}{2m}\nabla^2 + V\right)\psi = 0\,. \tag{2.13}$$

2.1.3 Wave Forms

Whether describing a photon or an electron, a wave-field, ψ, may be decomposed into a linear sum of constituent components in the form of either spherical or plane waves. It takes an infinite number of plane waves to construct a perfect spherical wave and an infinite number of spherical waves to construct a perfect plane wave.

A spherical wave is the isotropic form that radiation takes when emitting from an ideal point source: the phase of the wave-field changes only as a function of distance from the point source. A time-independent spherical wave takes the form,

$$\psi(r) = \frac{Ae^{ikr}}{r}, \tag{2.14}$$

where r is the distance from the source such that $r = \sqrt{\boldsymbol{r}_x^2 + \boldsymbol{r}_y^2 + \boldsymbol{r}_z^2}$ and A is the amplitude of the wave at the source.

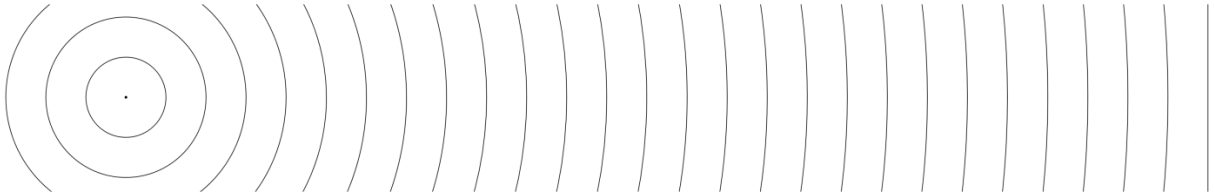

Figure 2.2: A source point radiating isotropically creating a spherical wave (left) and a plane wave (right)

A plane wave is the form that radiation takes when propagated away from an ideal point source into the far-field. Figure 2.2 shows the evolution of a spherical wave into a plane wave as it propagates away from a point source. A time-independent plane wave takes the form,

$$\psi(\boldsymbol{r}) = Ae^{i\boldsymbol{k}\cdot\boldsymbol{r}}\,, \tag{2.15}$$

where $\boldsymbol{k}$ is the wave vector,

$$|\boldsymbol{k}| = \frac{2\pi}{\lambda}\,, \tag{2.16}$$

and $\boldsymbol{k}\cdot\boldsymbol{r}$ is such that the wave-field varies only along the direction normal to, and is uniform perpendicular to, the wave vector.

2.1.4 Rayleigh-Sommerfield Diffraction Integral

The Huygens-Fresnel principle decomposes the wave-field emanating from a source into a set of secondary point sources. For example, an observer viewing a source through an aperture may treat the aperture as a set of secondary source points. Each secondary point source has an associated magnitude and phase, which emits as a spherical wave (see equation 2.14). Each point of the wave-field now propagates as an independent point source and so the whole wave-field can be computationally propagated by first propagating each point individually and forming their superposition. The operation can be described as a convolution integral,

$$\psi_2(x', y') = \iint_{-\infty}^{\infty} \psi_1(x, y)\, h(x' - x, y' - y)dxdy, \tag{2.17}$$

where the impulse response, h, is a spherical wave,

$$h(x', y') = \frac{e^{(ikr)}}{r}. \tag{2.18}$$

In practice there are two extra terms required. Firstly, the secondary waves are de-phased by a quarter of a period and are scaled relative to their wavelength. Secondly, as the secondary sources emit isotropically an obliquity factor must be added. Taking the first Rayleigh-Sommerfield solution for the case that the propagation distance, z, is much greater than the wavelength of radiation, the impulse response becomes,

$$h(x', y') = \frac{z}{i\lambda}\frac{e^{(ikr)}}{r^2}. \tag{2.19}$$

The Rayleigh-Sommerfield diffraction integral is then given as,

$$\psi_z(x', y') = \frac{z}{i\lambda}\iint_{-\infty}^{\infty} \psi_0(x, y)\frac{e^{ikr}}{r^2}dxdy, \tag{2.20}$$

where,

$$r = \sqrt{(x' - x)^2 + (y' - y)^2 + z^2}\,. \tag{2.21}$$

2.1.5 Fresnel Approximation

Rearranging equation 2.21 and employing the paraxial Fresnel approximation through the omission of terms above the first two in the binomial expansion of r**,**

$$r = z\sqrt{1 + \left(\frac{x' - x}{z}\right)^2 + \left(\frac{y' - y}{z}\right)^2}\,, \tag{2.22a}$$

$$\sqrt{1 + b} = 1 + \frac{b}{2} - \frac{b^2}{8} + \cdots, \tag{2.22b}$$

$$r \approx z\left[1 + \frac{1}{2}\left(\frac{x' - x}{z}\right)^2 + \frac{1}{2}\left(\frac{y' - y}{z}\right)^2\right], \tag{2.22c}$$

the Rayleigh-Sommerfield impulse response may be approximated by the Fresnel impulse response,

$$h(x',y') = \frac{e^{ikz}}{i\lambda z} e^{\frac{ik}{2z}(x'^2+y'^2)} . \quad 2.23$$

The Fresnel diffraction integral is formed by applying the impulse response of equation 2.23 with the convolution integral of equation 2.17,

$$\psi_z(x',y') = \frac{e^{ikz}}{i\lambda z} \iint_{-\infty}^{\infty} \psi_0(x,y) e^{\frac{ik}{2z}[(x'-x)^2+(y'-y)^2]} dxdy . \quad 2.24$$

When the exponential term on the right hand side of equation 2.23 is factored outside of the integral in equation 2.24 (there is no dependence on x or y) then the diffraction integral becomes,

$$\psi_z(x',y') = \frac{e^{ikz}}{i\lambda z} e^{\frac{ik}{2z}(x'^2+y'^2)} \iint_{-\infty}^{\infty} \psi_0(x,y) e^{\frac{ik}{2z}[x'^2+y'^2]} e^{-\frac{i2\pi}{\lambda z}[xx'+yy']} dxdy , \quad 2.25$$

which contains a phase pre-factor, a Fourier transform, and a phase post-factor. A major benefit of the Fresnel propagator is that only a single Fourier transform is required, an important consideration when performing a large number of them throughout an algorithm. It should be noted however, that this method is only valid within the Fresnel regime, which may be defined by the following criterion,

$$z^3 \gg \frac{\pi}{4\lambda}[(x-x')^2+(y-y')^2]^2_{max} , \quad 2.26$$

where λ is the wavelength of radiation and the other variables are as shown in Figure 2.1 (Goodman, 2005). Below this condition a separate method, the angular spectrum, should be used, which is described in section 2.1.7.

2.1.6 The Fourier Transform

There is a special case of the Fresnel regime - the Fraunhofer regime - where beyond certain propagation distances the propagated wave-field can be approximated by a Fourier transform (FT). The Fourier Transform is powerful and is used extensively in computational optics (it is based on the

bilateral Laplace transform with a purely imaginary term in the exponential) and allows fast decomposition from a point source distribution to its plane wave counterpart and *vice versa*. The forward Fourier transform and its inverse are defined as,

$$\Psi(\boldsymbol{u}) = \mathcal{F}\{\psi(\boldsymbol{r})\} = \int_{-\infty}^{\infty} \psi(\boldsymbol{r}) \cdot e^{-i2\pi(\boldsymbol{u}\cdot\boldsymbol{r})} d\boldsymbol{r}\,, \tag{2.27a}$$

$$\psi(\boldsymbol{r}) = \mathcal{F}^{-1}\{\Psi(\boldsymbol{u})\} = \int_{-\infty}^{\infty} \Psi(\boldsymbol{u}) \cdot e^{i2\pi(\boldsymbol{u}\cdot\boldsymbol{r})} d\boldsymbol{u}\,, \tag{2.27b}$$

where u is an angular coordinate that is related to the propagation angle, θ,

$$u = \frac{\sin\theta}{\lambda}\,. \tag{2.28}$$

The Fourier transform is valid within the Fraunhofer regime, which exists when,

$$z \gg \frac{k\left(x'^2 + y'^2\right)_{max}}{2}\,. \tag{2.29}$$

2.1.7 The Angular Spectrum

An alternative method of propagation is the angular spectrum method. The principle is that a wave-field may be decomposed into an angular distribution of plane-waves, instead of the decomposition into spherical waves required for the Fresnel approach. The decomposition is described by the angular spectrum of a point,

$$\Psi\left(\frac{\alpha}{\lambda}, \frac{\beta}{\lambda}, 0\right) = \iint_{-\infty}^{\infty} \psi(x_0, y_0, 0) e^{-i2\pi\left(\frac{\alpha}{\lambda}\cdot x + \frac{\beta}{\lambda}\cdot y\right)} dx_0 dy_0\,. \tag{2.30}$$

A propagation is achieved by imparting a phase change to each plane wave, adjusting for the difference in path length with the optic axis such that,

$$\Psi\left(\frac{\alpha}{\lambda}, \frac{\beta}{\lambda}, z\right) = \Psi\left(\frac{\alpha}{\lambda}, \frac{\beta}{\lambda}, 0\right) e^{\frac{i2\pi z}{\lambda}\left(\sqrt{1-\alpha^2-\beta^2}\right)}\,. \tag{2.31}$$

The addition of this term along with a limiting function, which removes evanescent waves, gives the angular spectrum propagation equation,

$$\psi(x,y,z) = \iint_{-\infty}^{\infty} \Psi\left(\frac{\alpha}{\lambda},\frac{\beta}{\lambda},0\right) e^{\frac{i2\pi z}{\lambda}\left(\sqrt{1-\alpha^2-\beta^2}\right)} circ\left(\sqrt{\alpha^2+\beta^2}\right) e^{i2\pi\left(\frac{\alpha}{\lambda}.x+\frac{\beta}{\lambda}.y\right)} d\frac{\alpha}{\lambda} d\frac{\beta}{\lambda}, \qquad 2.32$$

where $circ$ describes a circular mask with transmission only within the given radius.

Unlike Fresnel propagation, the angular spectrum method is valid for any propagation distance; the only constraint being the available computing power. This is because the sampling at the pre and post propagation planes is equal. Under this regime the non-zero portion of the wave-field soon extends out further than the original array, which results in aliasing. The method is therefore mainly used for small propagation distances. When Fresnel condition is met (equation 2.26) then it is often best to employ the Fresnel propagation method.

2.1.8 Computational Considerations

Described above is the necessary mathematics for computational propagation of a wave field in the field of optics. In practise such propagations and Fourier transforms are performed on a discrete form of the signal as the detector groups the data into discrete points (pixels). When operating on a discrete array the continuous transforms above may be expressed as discrete Fourier transforms (DFT) where,

$$\Psi[\boldsymbol{u}] = \mathcal{F}\{\psi[\boldsymbol{r}]\} = \sum_{\boldsymbol{r}=-N/2}^{(N/2)-1} \psi[\boldsymbol{r}] \cdot e^{\frac{-i2\pi[\boldsymbol{u}\cdot\boldsymbol{r}]}{N}} \qquad 2.33a$$

$$\psi[\boldsymbol{r}] = \mathcal{F}^{-1}\{\Psi[\boldsymbol{u}]\} = \frac{1}{N}\sum_{\boldsymbol{u}=-N/2}^{(N/2)-1} \Psi[\boldsymbol{u}] \cdot e^{\frac{i2\pi[\boldsymbol{u}\cdot\boldsymbol{r}]}{N}} \qquad 2.33b$$

Another important factor to consider when computationally manipulating wave fields is the conservation of flux through the free-space propagation. This is described by Parseval's theorem in the spatial domain,

$$\sum_{\boldsymbol{r}=-N/2}^{(N/2)-1} |\psi[\boldsymbol{r}]|^2 = \frac{1}{N} \sum_{\boldsymbol{u}=-N/2}^{(N/2)-1} |\Psi[\boldsymbol{u}]|^2 \,. \tag{2.34}$$

A consequence of recording the data on a detector with a finite number of discrete pixels in the far-field is that there is an associated width at the specimen plane within which the whole of the beam must exist. When the width of the beam at the specimen plane becomes too large, the interference fringes formed from the extremal edges of that beam in the detector plane are no longer resolvable by the pixels and aliasing occurs. Truncation of the measured data due the finite width of the detector may also cause a violation of Parseval's theorem as not all of the flux through the specimen is recorded.

2.2 Direct Imaging

As the work in this thesis is based upon the principle that imaging can be enriched with the replacement of the lens with computational algorithms, it is worthwhile reviewing the process of conventional lens based image formation. Within the conventional imaging system, a lens (an optical element with the ability to alter the phase distribution of the wave-field) is used to bring the radiation emanating from a specimen, after some form of illumination either through or reflected back from the specimen, to a focus in a secondary (image) plane. The image plane contains the wave-field in the same state (although usually magnified) as when the wave-field was interacting with the specimen.

2.2.1 The Imaging Lens

The function of a lens is to receive a diverging wave-front and to invert the phase distribution such that it becomes a converging wave-front. It is then possible to place a detector at the focus of the

converging wave-front and capture an image of an object that is in front of the lens, in an image plane at some position behind the lens.

Figure 2.3 shows the principle action of a lens through a ray diagram, where the rays are representative of the path of least time as described by Fermat's principle (Hecht, 2002). The wave-front emanating from the specimen (in the object plane) passes through the lens to the back focal plane. The back focal plane of the lens is the plane at which a parallel wave-front (plane wave) incident upon the front of the lens is focussed into a single point. The distance between the lens and the focal plane, *f*, is known as the focal length of the lens.

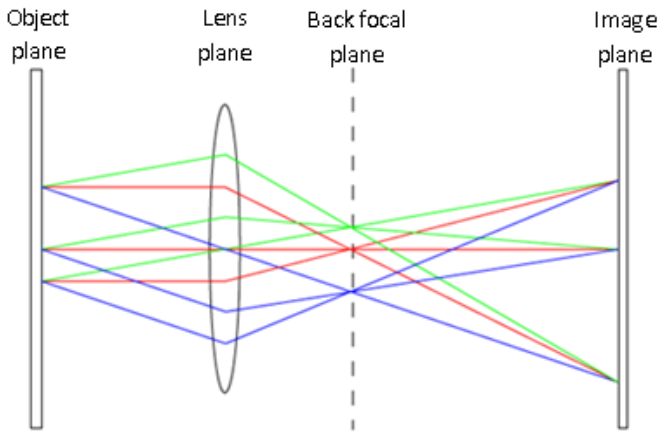

Figure 2.3: A ray diagram displaying the action of a lens, showing how components that are scattered a common angle are brought to focus at the same point in the back focal plane. The rays continue until it is scatter from common object positions that are brought to focus at the same points in the image plane.

Abbé suggested that the action of a lens could be broken down into Fourier transforms, where the transforming lens brings all parallel components in the exit wave to focussed point in the back focal plane (Abbe, 1873). The first Fourier transform propagates the object plane to the back focal plane of the lens and the second propagates the back focal plane to the image plane. This results in a conjugate representation of the object in the image plane. A representation of the Abbé imaging principle is shown in Figure 2.4.

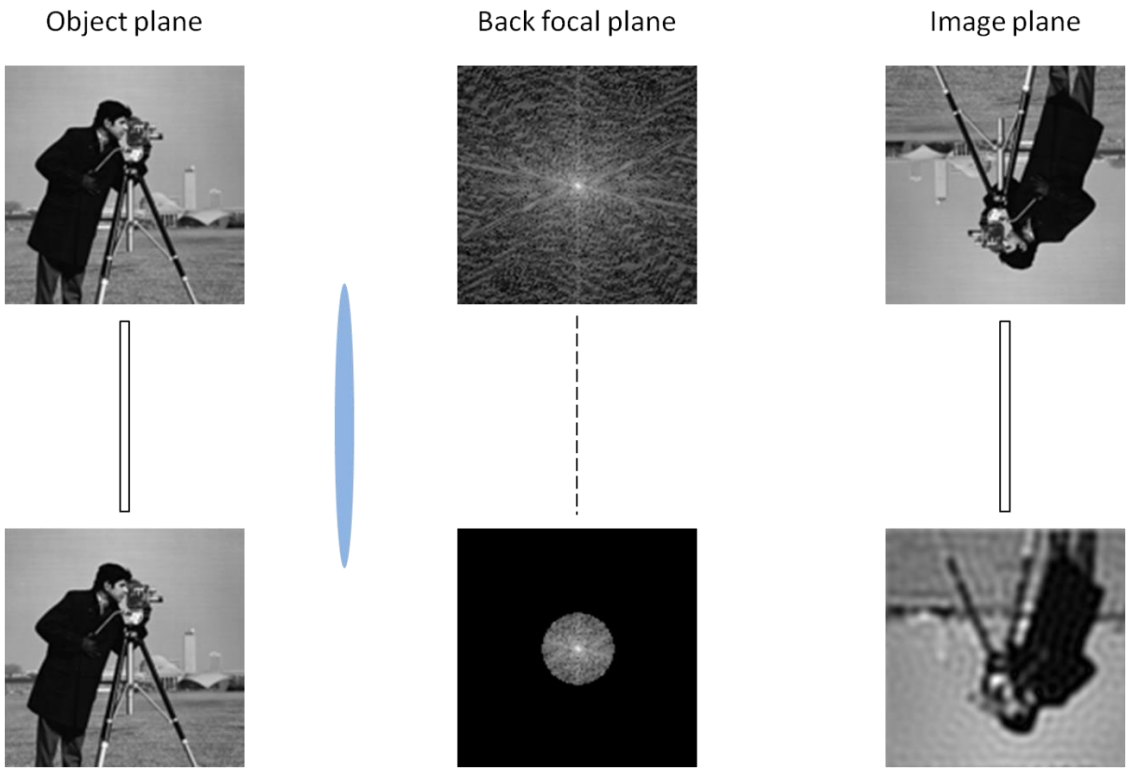

Figure 2.4: The Abbé imaging process through two imaging systems - the illumination passes from left to right. The top row represents an ideal lens of infinite physical extent, the middle row represents the physical setup with a lens in between the object and back focal planes, and the bottom row represents an aberration free lens of finite physical extent.

The maximum amount of information transmitted through the lens and into the image plane is determined by the wavelength of the illumination and the numerical aperture (NA) of the lens used to refocus the exit wave, where the NA of the lens is given by $n \sin \alpha$. This results in a minimum equivalent pixel size in the image plane, after which smaller pixel sizes will yield no extra information about the object plane. This principle is expressed in Abbé's equation,

$$d = \frac{\lambda}{2n \sin \alpha}, \tag{2.35}$$

where n is the refractive index of the surrounding medium, α is the maximum angle captured and refocused by the lens, and d is the resolving power of the lens.

The resolving power alone does not describe fully the resolution of the image produced by the lens, contrast between two points is required so that they may be distinguished. The Rayleigh criterion, which gives a minimum distinguishable separation in the image plane for any predefined lens NA and wavelength, is given as,

$$\ell_{min} = \frac{0.61\,\lambda}{NA} = 1.22d, \qquad 2.36$$

where ℓ_{min} is the minimum distance between any two points in the object that can be resolved in the image (Goodman, 2005).

2.2.2 Aberrations

An ideal image may be described as a scaled version of a wave exiting an object at a different location in space, one where a detector may be placed. In practice though, the lens used to create the image is never ideal. Firstly, as the lens is only physically able to process a finite region of any wave-front, the extent of that wave-field is limited perpendicular to the optical axis and, due to the uncertainty principle of quantum mechanics, the momentum of the wave-field perpendicular to the optical axis post lens can only be known to within a finite degree of accuracy. This is known as the diffraction limit and is a fundamental property of all imaging systems that process the scattered radiation in the far-field.

The problem with lens imaging is the manufacture of high NA lenses with no aberrations. These aberrations can be described and quantified in terms of a phase alteration in the back focal plane of the lens (Williams, 2009). These aberrations increase the minimum resolvable separation distance even further. The most common aberration is defocus, where the additional phase term in the back focal plane is,

$$\Delta P_f(u,v) = e^{i\frac{\pi}{\lambda}W_f\left(u^2+v^2\right)}, \qquad 2.37$$

where W_f describes the distance between the image plane and the focal plane of the lens. As this distance reduces, the image comes into focus. Spherical aberration results in a spread of focal points along the optic axis, each focal point relates to the angle subtended at the lens by that ray. The additional phase term due to spherical aberration is,

$$\Delta P_s(u,v) = e^{i\frac{\pi}{2\lambda}W_s\left(u^2+v^2\right)^2}, \quad 2.38$$

where W_s describes the difference in focal lengths of paraxial rays and those rays that pass through the extremal edges of the lens.

Astigmatism occurs when there is a non-uniform lens, whose focal length varies as a function of angle about the optic axis. This causes focal points from rays along one direction to differ from those rays along another. The above examples are only two of the most common forms of aberration. In fact there exists a whole Taylor series of aberration terms, where a different coefficient is attributed to each order. For small angles of scatter (low resolution) it is the lower order terms that have the largest effect. However, as the angular range is increased, the higher order terms become large and so their coefficients must also be reduced to produce a clear image.

2.2.3 The Detector

The detector is a critical element of the imaging process, with several important factors; pixel pitch, pixel size, number of pixels, bit depth, and bandwidth. Unfortunately, at the wavelengths required for optical imaging, no detector currently exists with sufficient bandwidth so that the underlying complex wave function can be measured completely. Instead, only the flux of quanta arriving at any given point may be measured. The number of quanta arriving within a discrete time provides us with the intensity of the underlying wave function (its probability density function), which relates to the modulus of the wave function raised by the power of two. We are therefore able to measure the modulus of the wave function directly but, critically, lose all phase information.

$$I = \psi \cdot \psi^*, \quad 2.39$$

where ψ^* represents the complex conjugate of ψ,

$$\psi = a + ib \text{ and } \psi^* = a - ib \quad 2.40$$

For this reason, a conventional image is the intensity of light being emitted, reflected, or transmitted through or from the specimen of interest.

2.2.4 Microscope Setups

The work described in later chapters covers three main imaging domains, photons in the visible light regime, photons in the hard x-ray regime, and electrons. The manufacturing process of lenses in the visible light regime is very good and these systems are now limited not by aberrations but the fundamental elements of equation 2.35. Modern optical systems are able to increase the numerical aperture of the current lenses through oil immersion, so altering the refractive index, n.

Focussing x-rays, particularly high energy x-rays, is not as simple as for lower energy visible light photons. Creating a single refractive lens with a sufficient refractive index is impractical, although it has been shown that compound lenses may be fabricated which are suitably efficient for the focussing of high energy x-rays (Snigirev et al., 1996). The highest resolution optics available are in the form of Fresnel zone plates (a form of diffractive optic) where a focal point is created by diffraction of the diverging wave-front with the use of concentric rings of either absorption or phase change. These are however strongly dependent on photon energy (the focal length is a function of wavelength) and only the one of the diffraction orders is selected, an aperture is used to remove the flux from other orders. A third type of x-ray focussing exists in the form of reflective optics, where curved glancing mirrors such as the Kirkpatrick-Baez (K-B) mirrors are able to focus x-rays (Kirkpatrick and Baez, 1948). Such optics offer greater efficiency as they are achromatic and have a high numerical aperture. The downside though is that the quality of the focus is limited due to aberrations and surface imperfections, resulting in significant side flares.

The transmission electron microscope employs electromagnetic lenses in order to focus a beam of electrons throughout the microscope. The machine is most commonly operated in one of two distinct ways, diagrams of which are shown in Figure 2.5. The first uses a condenser lens system in order to collimate the beam into a uniform, flat-field illumination on the specimen. The objective

lens focuses the resultant scatter into an image, where a TEM detector is positioned to record the results. The TEM detector is a two-dimensional array of pixels, which read-out in parallel to produce an image (see Figure 2.6a).

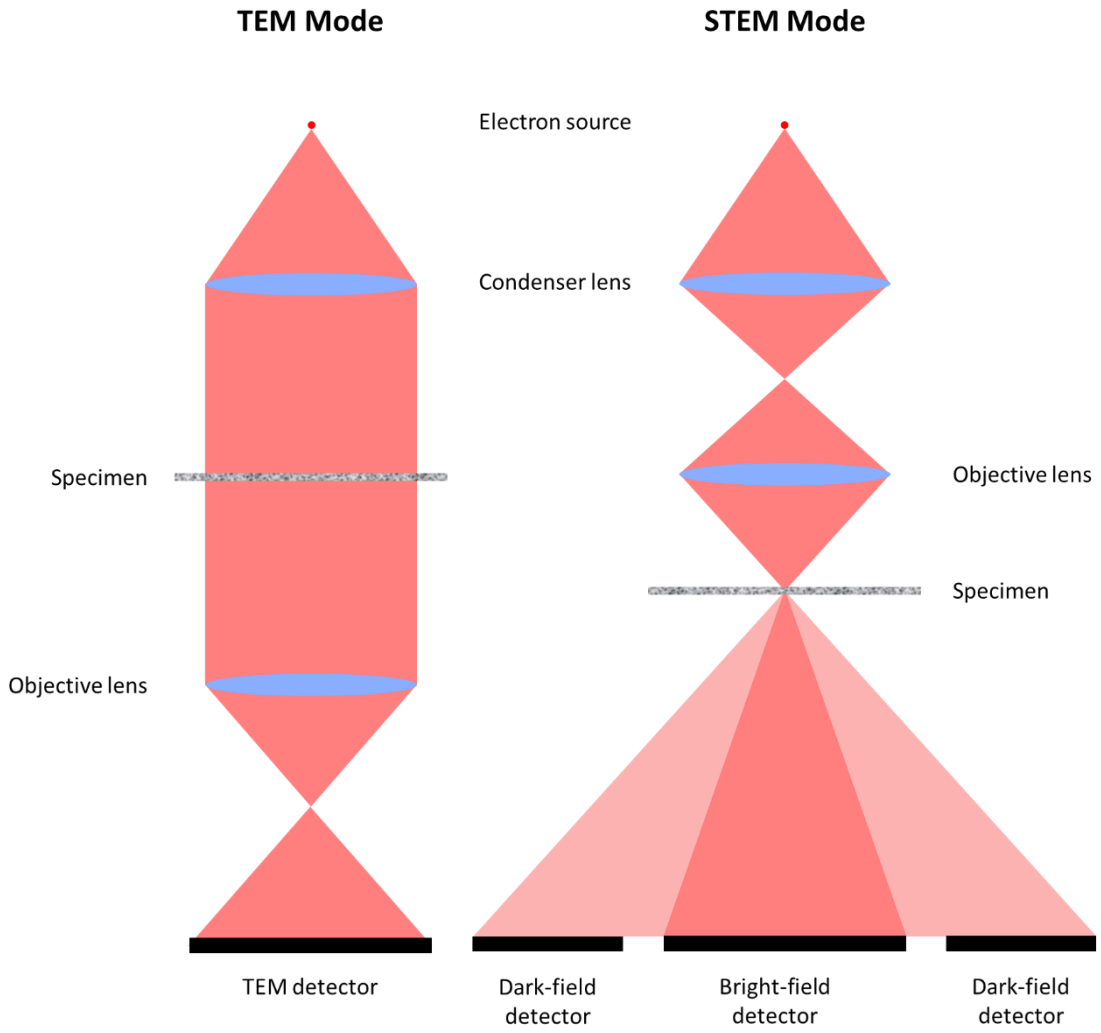

Figure 2.5: Simplified diagrams of the two main transmission microscope configurations, TEM mode (left) and STEM mode (right). The detectors are shown from above in Figure 2.6. Note that although the specimen scattering is shown for the STEM setup, such scattering is not shown in the TEM setup for simplicity.

The second setup exploits the principle of reciprocity (Cowley, 1969), effectively switching the positions of the source and detector. The condenser system is now used in conjunction with the objective lens before the specimen in order to bring a focussed point of electrons incident on the specimen. The result of this in the detector plane is shown in Figure 2.7e. The principle of STEM imaging is that the object must be scanned through the focussed beam (in the electron microscope the beam is actually shifted by scanning coils) while the resulting scattered radiation is captured by

an integrating, single-pixel, detector. There are two main types of STEM detector, the bright-field and the annular dark-field, as shown in Figure 2.6b. Whichever is employed, the aim is to record the change in scattering strength from each element of the specimen, which is isolated from the rest of the specimen by the focussed beam. When using the bright-field detector, the signal is high when scattering is low (in free space for example) and the signal is low when scattering is high (on an atomic column for example). Essentially, as the beam (or probe) is scanned across the specimen a portion of the electron beam is displaced from the bright-field to the dark-field area of the detector. Careful alignment of these detectors (only one is required to form either a bright or dark-field image) allows for contrast to be represented in the image by integrating the total scatter on either detector (or indeed by reading out both simultaneously) as the beam is scanned.

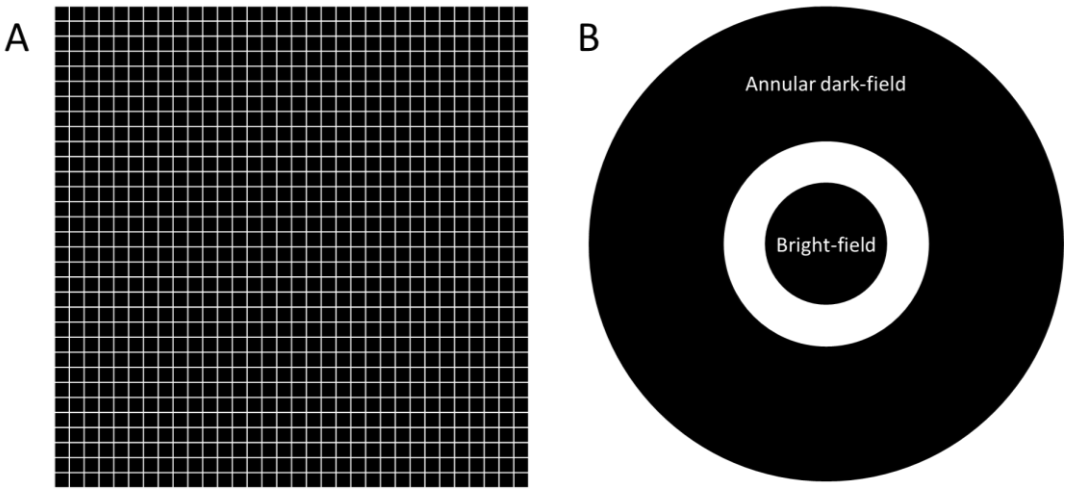

Figure 2.6: Detectors for (a) TEM mode and (b) STEM mode

Electron microscopes offer an increase in resolution by reducing the wavelength of the radiation. Unfortunately, the lenses used to focus the beam of electrons are far from ideal and have kept the resolution well away from the diffraction limit. In 1936 it was shown that electron lenses without aberrations could never be produced (Scherzer, 1936). This is due to the limited magnetic-field configurations that can exist within a rotationally symmetric round electron lens and was a big problem in the field of electron microscopy as it showed that the resolution limit would be many times lower than the diffraction limit expected from the reduction in wavelength. Scherzer later

showed that non-round lenses could be manufactured and that these lenses could be used in series with the original lens in order to compensate for these aberrations (Scherzer, 1949).

The first electron microscopes that utilised non-round lenses along with auto tuning software in order to successfully correct for aberrations in the objective lens were demonstrated in the mid-1990s (Krivanek et al., 1997) (Haider et al., 1998). Advances have since been made in aberration correction within electron microscopes and a modern machine can resolve on the sub-Ångström scale (Hawkes, 2001), a resolution that is still a factor of about 25 times lower than that promised by the wavelength of the high energy electrons used.

The formation of the Ronchigram, the diffraction pattern created when a focussed and convergent beam is incident on a specimen and recorded at a large distance, is shown in Figure 2.7. An object is multiplied (the kinematic approximation is followed here) with the electron beam to create the resultant wave-field which continues to propagate into the detector plane. Figure 2.7e shows what is recorded when a TEM detector is inserted under a STEM configured TEM (actually the square root of the intensity is displayed). The sharpness of the bright-field disc here is due to an aperture, which is positioned in the back focal plane of the condenser optics, helping to form a well localised illumination spot onto the object. The electron ptychography work carried out in chapter 6 employs this setup.

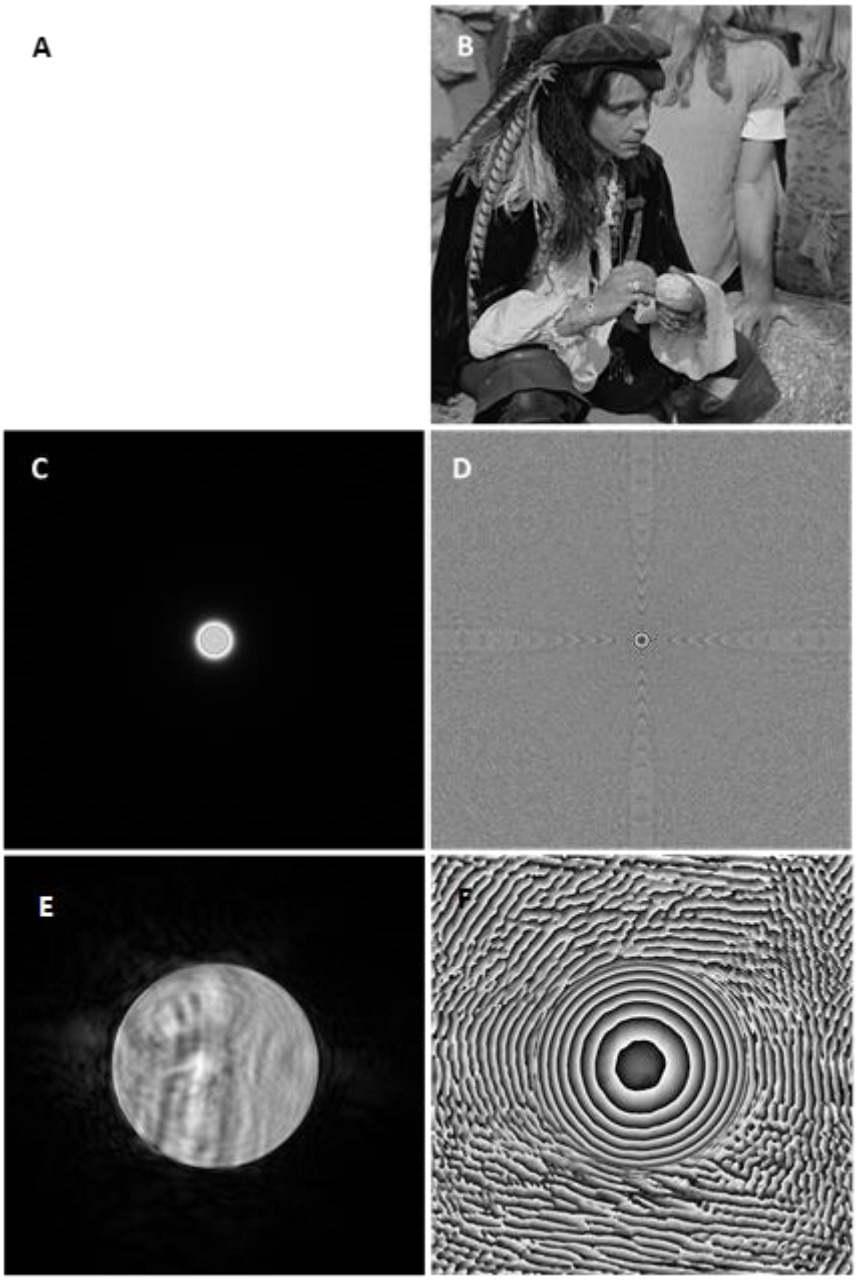

Figure 2.7: The generation of the Ronchigram. (a) and (b) are the specimen in modulus and phase, respectively. (c) and (d) are the probe function in modulus and phase, respectively. (e) and (f) are the exit-wave (formed as a product of the probe with the specimen) after propagation to the far-field in modulus and phase, respectively.

2.2.5 Direct Imaging as a Transmission System

The process of image formation may be expressed in terms of the transmission of information from an unknown object to an image via a beam of illuminating radiation. A schematic showing the flow of information through the various elements within a direct (lens-based) imaging system is shown in Figure 2.8. The transmission of information relies upon several factors, namely the wavelength and coherence level of the radiation, the stability of lens, and the properties of the detector (pixel-pitch, pixel-size, number of pixels, and bandwidth).

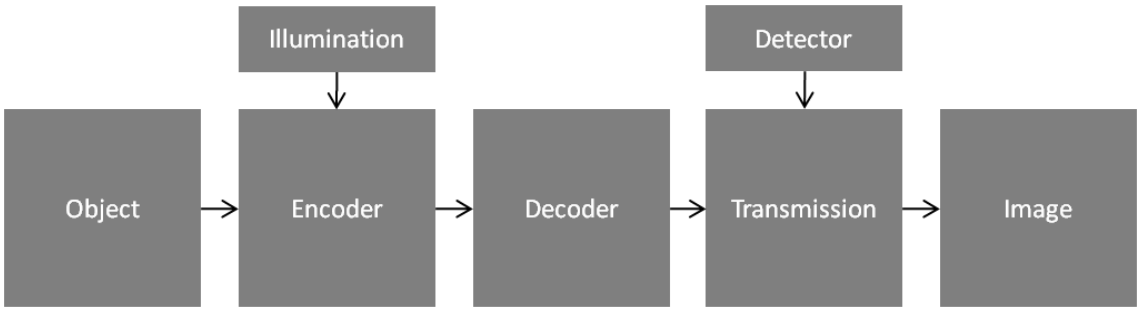

Figure 2.8: The direct imaging system as a transmission channel, where the object information is encoded by a flat field illumination profile before a lens is employed to decode the object information (replicating the wave-field from the object plane at a focus plane) where it is processed (transmitted) through a detector (where the phase information is lost) and an image of the intensity profile of the object is produced.

In this case, the object's information content is encoded by a flat-field illuminating beam of radiation, which is processed in real-time by the lens where the state of the wave-field at the object plane is replicated (with a magnification term) in an image plane. The information is then transmitted into the final recorded image through (via) the detector, which is unable to transmit the phase portion of the wave. Each element has a function and a limitation; the illumination is required so that the information may be transmitted away from the object, magnified, and ultimately recorded onto a detector; the lens is required in order to reproduce the state of the illuminating beam at the exit plane of the specimen onto the detector plane; and the detector is required to record that image. This system has two main limitations; the lens, which cannot transmit all of the spatial frequencies present within the object; and the detector, which can only measure the intensity of the wave-field.

2.3 Diffractive Imaging

An alternative way of creating an image of an object is to record its diffraction pattern directly onto a detector and computationally invert that from the far-field domain (reciprocal-space) into the image domain (real-space). Such a method removes the requirement for an imaging lens and hence the associated aberrations of that lens. If the detector is able to record both the phase and modulus of the radiation incident upon its pixels then there is enough information recorded such that the content of the object is recoverable by a single inverse discrete Fourier transform (see equation 2.33b). The image produced from such a method is a fully complex (the response of the specimen is measured in both transmission and relative phase), diffraction limited (aberration free) image.

2.3.1 The Phase Problem

Unfortunately, a detector does not currently exist that is able to measure the phase of a wave-field for the frequencies involved in optical (and shorter wavelength) imagery. In practice only the intensity of the radiation at the detector is recorded. The lack of available phase information when attempting to invert diffraction data has historically been referred to as “the phase problem”. Figure 2.9 shows a test object represented in real-space before and after the wave-field is collapsed into an intensity distribution in reciprocal-space.

Losing the phase distribution in reciprocal-space gravely affects the modulus information in real-space. There is a common demonstration of this where two real images are Fourier transformed, the modulus of the diffraction patterns are then switched before the inverse Fourier transforms are taken. The resultant images are only slightly degraded and important features are preserved: it is the phase portion of the wave-field in reciprocal-space which is heavily coupled with the modulus in real-space. For this reason the diffractive imaging techniques described later are able to produce very good phase reconstructions in real-space and this is invariably of a higher quality than its modulus counterpart.

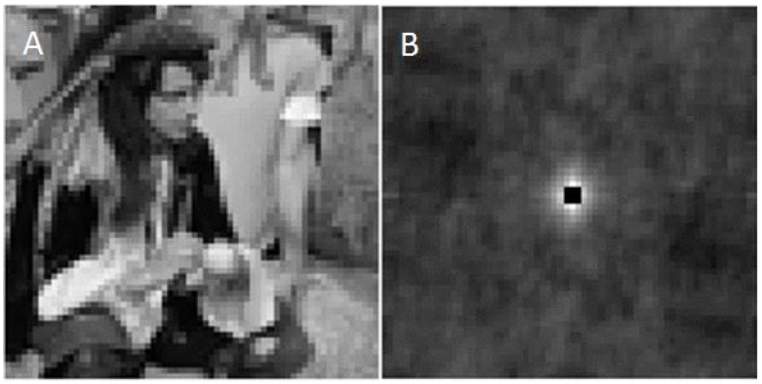

Figure 2.9: Demonstration of the phase problem for a two-dimensional object. a) A sample object. b) The real-space autocorrelation of the object (formed from the inverse Fourier transform of the intensity of the object in reciprocal-space), which represents in real-space what is recorded on a detector in reciprocal-space. The central peak from (b) is set to zero for display purposes.

2.3.2 Ptychography

In a series of papers at the end of the 1960's, Walter Hoppe outlined and developed a method for phasing the Bragg peaks within the diffraction pattern of a crystalline specimen in the STEM that does not contain a complex conjugate ambiguity (Hoppe, 1969a, Hoppe and Strube, 1969, Hoppe, 1969b, Hegerl and Hoppe, 1970). The technique involves stepping a patch of illumination (the probe), functionally similar to the real-space support constraint in the single-shot CDI situation discussed later, across a specimen laterally in an overlapping fashion. The result of which is a dataset that comprises several diffraction patterns. Such a dataset is a convolved mixture of the specimen with itself and an illumination function. The convolution operation is a kind of folding of data and so the technique was named ptychography, with ‘ptych’ being Greek for ‘fold’. Although the single-shot case, discussed later, also relies on a convolution term, this is only in reciprocal-space. Ptychography is uniquely differentiated as there is also a convolution operation occurring across real-space through overlapping scan positions.

The shifting of the illumination that occurs in real-space has an equivalent phase ramp in reciprocal-space (due to the Fourier shift theorem) that alters the measurements such that the phase relationship between neighbouring diffraction spots may be uniquely determined. The unlocking of the complex conjugate ambiguity from the knowledge of real-space shifts of the illumination is shown in terms of interfering diffraction peaks in Figure 2.11.

Figure 2.10a shows an example diffraction pattern containing two spots, the square roots of which represent the modulus of the underlying complex value of the wave-field at those points, $|Z_1|$ and $|Z_2|$. As the convergent beam is introduced those two points spread out into discs such that they now share a mutual region with a modulus value of $|Z_0|$, as shown in Figure 2.10b.

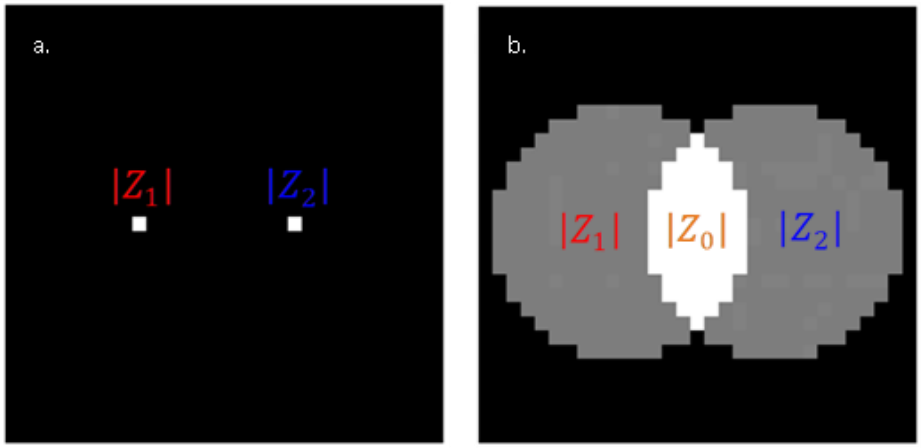

Figure 2.10: The convolution of two diffraction spots with a convergent probe in reciprocal-space. a) Two diffraction spots under plane wave illumination with modulus values of $|Z_1|$ and $|Z_2|$, b) Introducing a convergent beam creates overlapping discs with a mutual region of modulus $|Z_0|$.

The mutual region, $|Z_0|$, must equal the sum of the contributing points such that,

$$|Z_0| = |Z_1 + Z_2| . \qquad 2.41$$

Figure 2.11a illustrates the two possible solutions to equation 2.41 as vectors on a phasor diagram. Figure 2.11b then shows that shifting Z1 in phase relative to Z2 (via the application of a phase ramp) forces each potential solution to now reveal different values for $|Z_0|$, $|\tilde{Z}_{0,a}|$ and $|\tilde{Z}_{0,b}|$. Re-measuring the physical value of $|Z_0|$indicates which phase term is correct and reduces the problem down to a single solution.

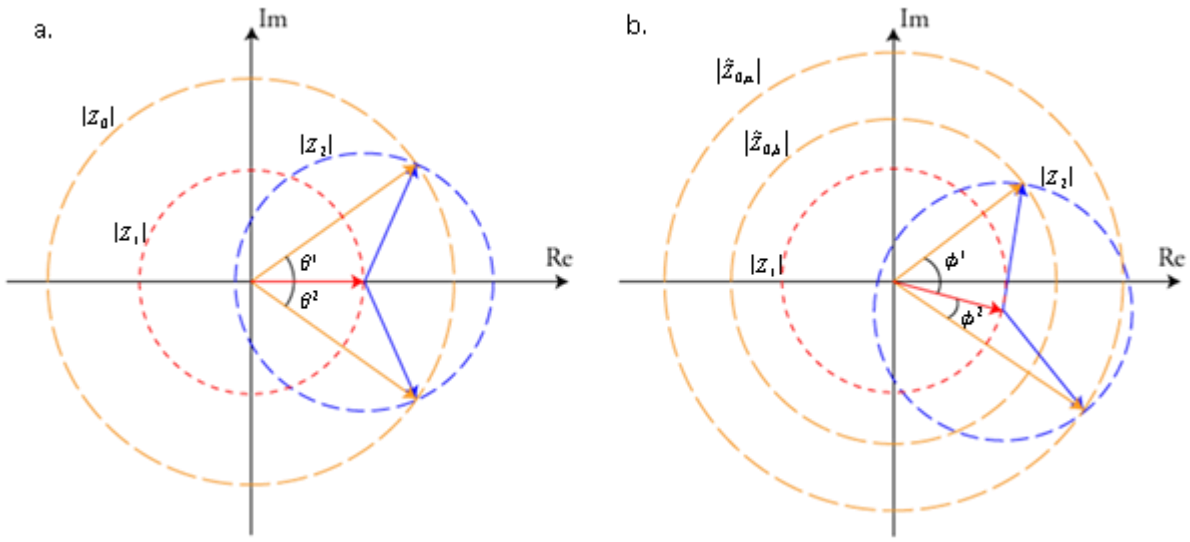

Figure 2.11: A vector representation of two interfering diffraction discs in reciprocal-space. a) Two diffraction discs $|Z_1|$ and $|Z_2|$ with a mutual region $|Z_0|$. b) The same two interfering diffraction discs after the introduction of a phase ramp produces two possible solutions for $|Z_0|$, of which only one is physically true.

In 1992 an analytical solution to the deconvolution of a microdiffraction dataset from a STEM using the Wigner-distribution deconvolution was described, where the resolution obtainable was limited by the wavelength of the electrons and not by the probe forming lens or the partial coherence within the beam (Rodenburg and Bates, 1992). The method was then demonstrated in the visible light regime under a STEM configuration in at first one, then two dimensions in order to exceed the point resolution limit of the lens (Friedman and Rodenburg, 1992, McCallum and Rodenburg, 1992).

It was shown using experimental data in the electron regime that a double-resolution image could be produced over that afforded by the same microscope under conventional imaging methods (Rodenburg et al., 1993). Although this work did not break the resolution record of the time (superior microscopes were available), it did show that ptychography was able to extend the resolution of an electron microscope beyond the previous limitations of the electron lens. A year on and the same principle was extended further; the processing of 'stepping out' in reciprocal-space was shown to produce a virtual objective aperture (a form of aperture synthesis) which is insensitive to chromatic aberrations and lens instabilities. The resolution was now not only extended beyond the point resolution of the electron microscope but could also be extended beyond the conventional

information limit (Nellist and Rodenburg, 1994, Nellist et al., 1995). The same methods were applied to a scanning transmission x-ray microscope (STXM) for the first time soon after (Chapman, 1996). For a comprehensive and insightful review of the development of ptychography see the review by Rodenburg (Rodenburg, 2008).

2.3.3 Single-Shot Coherent Diffractive Imaging

Meanwhile, a separate solution to the phase problem which did not rely on successive shifts between the beam and the specimen had been proposed in 1972 in the form of an iterative algorithm (Gerchberg and Saxton, 1972). The Gerchberg-Saxton algorithm requires that the intensity distribution of the wave-field is recorded in the object plane (real-space) and diffraction plane (reciprocal-space). The method iteratively steps between the two planes, constraining the estimated modulus to be the square root of the recorded intensity in each plane.

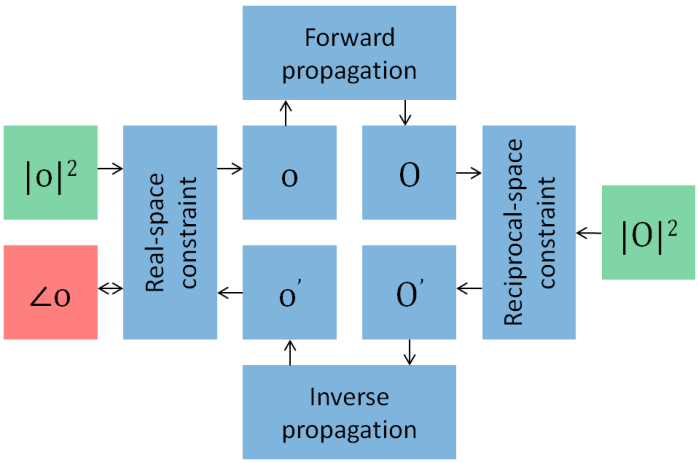

Figure 2.12: Flow diagram of the Gerchberg-Saxton phasing algorithm. The object's intensity profile is known in both real and reciprocal-space.

The Gerchberg-Saxton algorithm employs an identical update (an estimate is said to be updated after it has been constrained by the known values) in real-space to that used in reciprocal-space. The constraints in both planes can be described as a projection of estimated values within a complex array, O, onto a set of known intensities, $|O^m|^2$, where m denotes the measured values. (Here a projection is when a phasor representing a complex estimate is projected onto a radius of known modulus in a direct line with the origin without altering the phase.) Those projections, indicated by

$\mathcal{P}_r$ and $\mathcal{P}_u$ for the object and diffraction space updates respectively, are described by the following equations,

$$\mathcal{P}_r\{O(\boldsymbol{r})\} = O(\boldsymbol{r})\frac{\sqrt{|O^m(\boldsymbol{r})|^2}}{|O(\boldsymbol{r})|}, \tag{2.42a}$$

$$\mathcal{P}_u\{O(\boldsymbol{u})\} = O(\boldsymbol{u})\frac{\sqrt{|O^m(\boldsymbol{u})|^2}}{|O(\boldsymbol{u})|}, \tag{2.42b}$$

where $O(\boldsymbol{u})$ is the Fourier transform of $O(\boldsymbol{r})$,

$$O(\boldsymbol{u}) = \mathcal{F}\{O(\boldsymbol{r})\}, \tag{2.43}$$

and O^m is the measured state of the object. Each iteration of the Gerchberg-Saxton algorithm can then be described as a double projection,

$$O_{n+1} = \mathcal{P}_r\{\mathcal{P}_u\{O_n\}\}. \tag{2.44}$$

Fienup later modified the Gerchberg-Saxton algorithm by altering the object space constraint from a modulus update over the whole object to a more general support constraint. Rather than updating the modulus of every pixel in the object, a set of known values are updated completely with the other unknown values left unconstrained (Fienup, 1978). A typical support constraint is shown in Figure 2.13a (the boundary of zeros) alongside the real-space autocorrelation function.

Figure 2.9 shows the effect of object isolation on the sampling condition when recording diffraction patterns on a real detector. Processing the object without isolation results in severe aliasing and so the information is corrupted beyond recovery. After isolation in real-space the aliasing is removed from the data (see Figure 2.13b). Although not the original object, this data contains some of the information from the object and so given the correct reconstruction strategy, an image of the object should be recoverable.

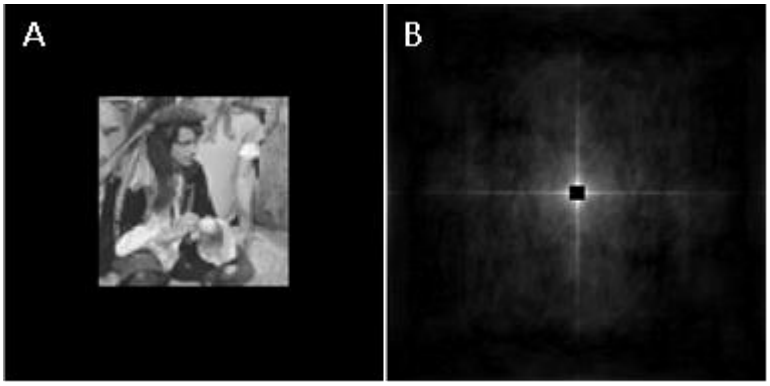

Figure 2.13: Demonstration of the phase problem for a two-dimensional object within a support boundary. a) A sample object within a support boundary. b) The real-space autocorrelation of the object and support (formed form the inverse Fourier transform of the intensity of the object in reciprocal-space), which represents in real-space what is recorded on a detector in reciprocal-space. The central peak from (b) is set to zero for display purposes.

The Fienup reconstruction method requires a real, nonnegative, object but removes the need for a real-space image to be recorded alongside the reciprocal-space diffraction pattern. The diffraction update is computed in the same way as the Gerchberg-Saxton method, except the wave-field now represents the object and a support, not just the object and a plane wave. The modulus of the estimated exit-wave is directly replaced with the square root of the corresponding measured intensity distribution and the phase portion is preserved, such that,

$$\Psi'(\boldsymbol{u}) = \Psi(\boldsymbol{u})\frac{\sqrt{I(\boldsymbol{u})}}{|\Psi(\boldsymbol{u})|}, \tag{2.45}$$

where Ψ' is the updated version of the exit-wave in reciprocal-space, Ψ. The difference is in the object update, where any points outside of the support area, S, are set to zero,

$$\mathcal{P}_r\{O(\boldsymbol{r})\} = \begin{cases} O(\boldsymbol{r}) \\ 0 \end{cases} \begin{matrix} \boldsymbol{r} \in S \\ \boldsymbol{r} \notin S \end{matrix}, \tag{2.46}$$

The alteration to the real-space element of the algorithm can be seen in Figure 2.14. There is now a fully unknown object, O, and a fully known support region, D. The unknown values within the object are left fully unconstrained. The unconstrained values in real-space are in fact updated in the reciprocal-space constraint and so the algorithm converges to a consistent solution.

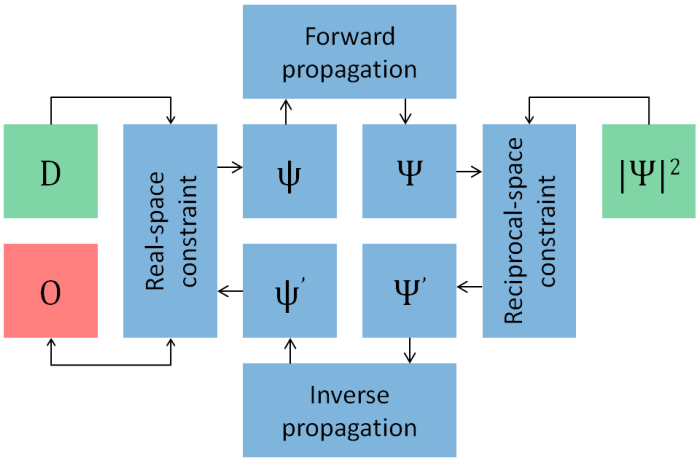

Figure 2.14: Flow diagram of the general iterative reconstruction process. D is the known support constraint, O is the unknown object, and $|\Psi(\boldsymbol{u})|^2$ is the recorded intensity pattern.

The convergence of the iterative phase retrieval algorithm was later shown to be improved with the implementation of an input-output approach (Fienup, 1982). In the new real-space update it is the previous input that is modified, using information from the corrected output, in order to create the next input rather than directly modifying the previous output. This creates a negative feedback loop into the system, speeding up convergence in comparison to the error reduction algorithm. The object space update for the input-output algorithm is now given as,

$$O_{n+1}(\boldsymbol{r}) = \begin{cases} O_n(\boldsymbol{r}) - \beta \mathcal{P}_u\{O_n(\boldsymbol{r})\} \\ \mathcal{P}_u\{O_n(\boldsymbol{r})\} \end{cases} \begin{matrix} \boldsymbol{r} \in S \\ \boldsymbol{r} \notin S \end{matrix}. \qquad 2.47$$

The method was shown to work for complex-valued objects so long as a sufficiently strong support constraint is in place. In this case Fienup demonstrated that certain support shapes could provide such a constraint (Fienup, 1987).

Forming an isolation support constraint is practically achieved through one of two methods. Firstly, the object can be known *a priori* to be localised (i.e. a single nano-particle) such that over half of the reconstructed object elements are known to be transparent and contain no scattering mechanism. Secondly, the illumination can be designed to be localised at the plane of the object (i.e. with an aperture) such that over half of the reconstructed object elements are known to be zero. Example diagrams of each experimental setup are shown in Figure 2.15.

The width of the support constraint is ultimately limited by the Nyquist sampling condition of the recorded intensities. As shown in Figure 2.13, meeting this condition requires isolating an object region such that its autocorrelation is not aliased. The sampling pitch of the diffraction pattern must therefore be sufficiently fine to resolve interference fringes from the extremal outer edges of the support, had they existed. The largest possible support size is given as half that of a complex valued measurement,

$$D = \frac{\lambda}{2\Delta\theta}, \tag{2.48}$$

where D is the support width, λ is the wavelength of radiation, and $\Delta\theta$ is the angle subtended between neighbouring detector pixels at the specimen plane. The essence of the phase problem is that a loss of half of the information in reciprocal-space requires that half of the information in real-space (i.e. the zero elements of the aperture function) must be known *a priori* in order to facilitate a reconstruction. It is worth noting that the requirements of sampling and coherence are identical for each setup (Spence et al., 2004).

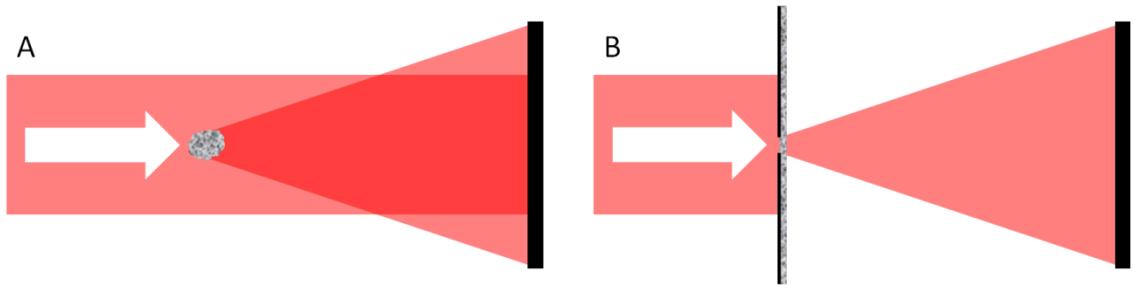

Figure 2.15: Schematic diagrams of two forms of support constraint. a) Isolated object within an extended beam. b) Localised illumination incident upon an extended object.

In 1999 the method was applied to soft X-rays (with a wavelength of 1.7nm) where an image of an isolated object with a resolution of 75nm was produced: consistent with the diffraction limit set by wavelength of the x-rays and the angular range of the detector (Miao et al., 1999). The result is shown in Figure 2.16. The technique was also applied to the electron microscope, when in 2003 a reconstruction of a carbon nanotube was successfully reconstructed with features resolvable down to 1Å. The nominal point resolution of the microscope used was 2.2Å (Zuo et al., 2003).

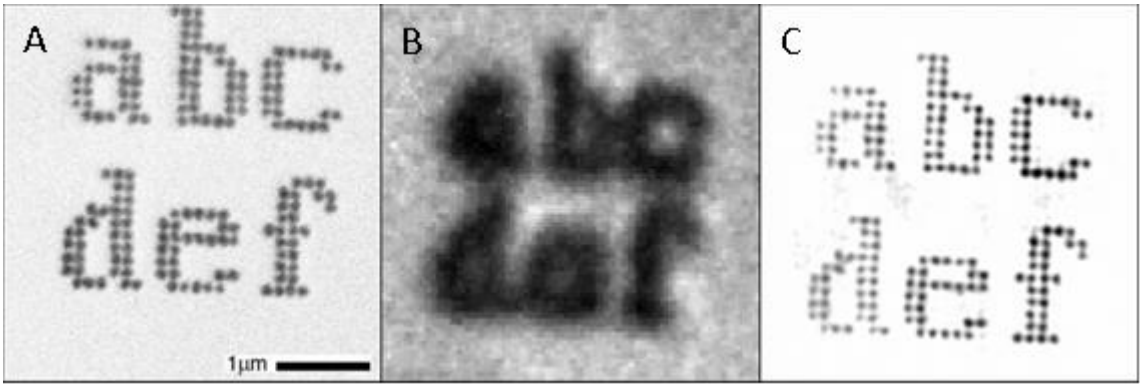

Figure 2.16: A fabricated specimen of gold dots, which are 100nm in diameter and 80nm thick, deposited on a silicon nitride membrane. The specimen is shown in a scanning electron microscope image (a), an optical microscope image (b), and a corresponding CDI reconstruction. Reproduced from (Miao et al., 1999).

2.3.4 Coherent Diffractive Imaging as a Transmission System

The direct imaging method has been described above in terms of a transmission system. In order to more easily see the difference between the conventional, lens-based, imaging system and that of diffractive imaging, the same elements are used in Figure 2.17 to describe the diffractive imaging system. The principle difference is in the switching of the processing stage from a lens to a computer algorithm and that the detector is now positioned in the lens plane, where it captures the raw scattered radiation after interaction with the object.

The object is once again encoded by the illumination, which is then propagated into a far-field pattern where it is transmitted through (via) the detector into the reconstruction algorithm. The reconstruction algorithm then uses the *a priori* illumination information to decode the object from the illumination and an image is produced.

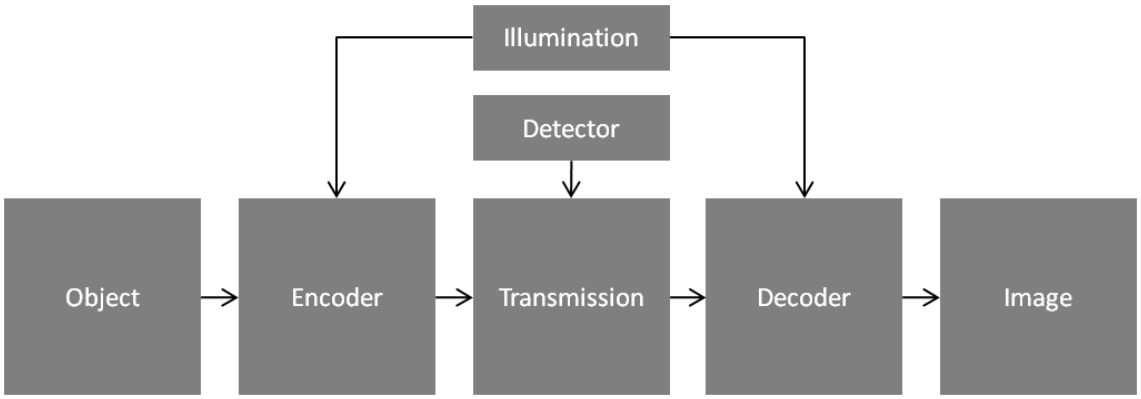

Figure 2.17: The diffractive imaging system as a transmission channel, where the object information is encoded by the localised illumination profile before transmission through a detector (where the phase information is lost) before an algorithm uses the illumination information to decode the object information to produce an image.

Unlike the direct method, where the processing is done before detection (and crucially the phase distribution is preserved), here the detection process occurs pre-processing. The important point being that the phase information is lost before the processing stage. Recovering any real-space image from such a position necessarily requires the recovery of the accompanying phase distribution. The reconstruction algorithm is able to do this so long as it has the 'key' to the decoder, which is the complex illumination function.

2.4 Iterative Ptychographic Reconstruction Methods

In 2004, the principles of ptychography were combined with the iterative methods of Fienup in order to produce an iterative ptychographic reconstruction method. Doing so made ptychographic imaging a more practical proposition. The new technique exploited the best elements from both previous methods: the ptychographic scan provided an information rich dataset whose solution was well constrained and free from the complex conjugate ambiguity and the iterative search algorithm could efficiently converge towards that solution without requiring very many diffraction patterns.

2.4.1 Ptychographic Iterative Engine (PIE)

The first algorithm was named PIE (ptychographic iterative engine) and simulations using a hard (binary) aperture as the illumination function were reconstructed in order to show that an iterative ptychographic solution could produce a complex image of object over an extended field of view (Faulkner and Rodenburg, 2004) . The difference to Fienup's approach comes primarily in the

accommodation of several diffraction patterns - each contributing to a different region of the final image. The improvement gained from the overlapping real-space scan is shown in Figure 2.18.

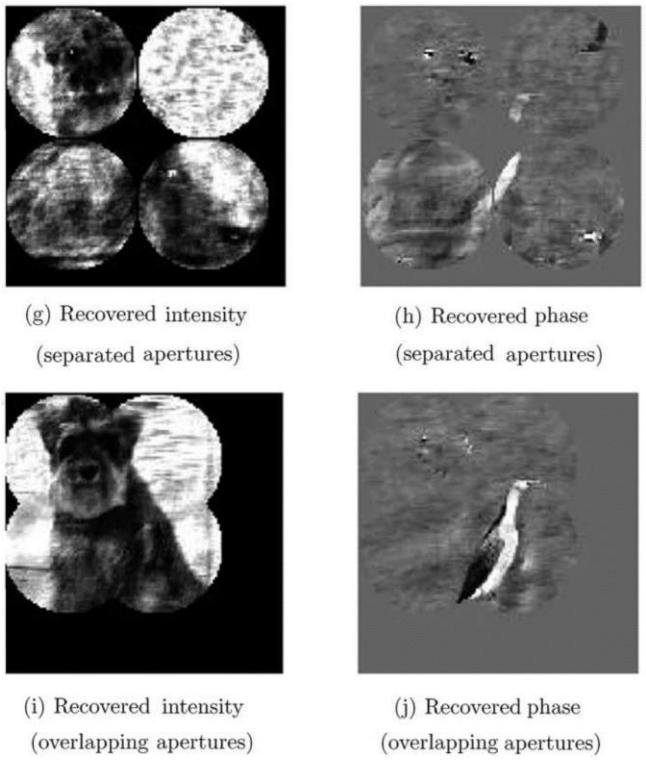

Figure 2.18: First results from the PIE algorithm showing the improvement in reconstruction quality from separate single-shot reconstructions (g-h) to an overlapping PIE equivalent. Reproduced from(Faulkner and Rodenburg, 2004).

The issue with this method is the requirement for a hard aperture at the plane of the object, which is very impractical in many experimental setups; especially true in the electron microscope where a defocused STEM probe contains many circular fringes. Such illumination profiles are said to be 'soft' as they do not have a sharp cut off and they may contain zeroes (see Figure 2.19d). The PIE algorithm was later improved to accommodate a soft illumination function, provided such an illumination remained sufficiently localised (Rodenburg and Faulkner, 2004). This was a subtle yet critical improvement and one that brought iterative ptychography to many new experimental setups. No longer was it a case of replacing regions within the support region in a binary fashion, the update strength of each object element is now scaled to accommodate fluctuations in the irradiance at that object element during that exposure. Figure 2.19 shows a reconstruction of the improved PIE algorithm when applied to simulated STEM data.

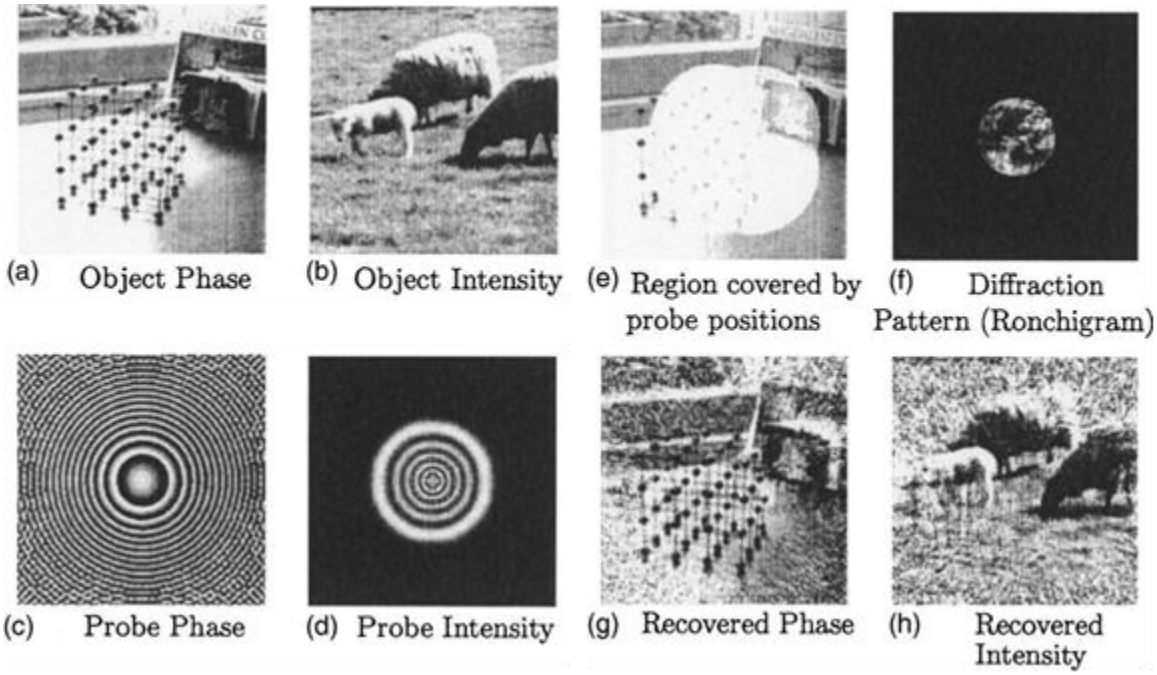

Figure 2.19: PIE reconstruction after the alteration to handle soft illumination function. Reproduced from (Rodenburg and Faulkner, 2004).

The principle of the PIE algorithm is to use the difference between the exit-wave for a single position before and after the reciprocal-space constraint such that,

$$O'(\boldsymbol{r}) = O(\boldsymbol{r}) + \Delta O(\boldsymbol{r})\,, \tag{2.49}$$

where,

$$\Delta O(\boldsymbol{r}) = \frac{\psi'(\boldsymbol{r})}{P(\boldsymbol{r})} - \frac{\psi(\boldsymbol{r})}{P(\boldsymbol{r})}\,, \tag{2.50}$$

and where $P(\boldsymbol{r})$ is a complex function describing the illumination wave-field at the plane of the specimen.

The combination of equation 2.49 with 2.50 produces an update equation for each object region,

$$O'(\boldsymbol{r}) = O(\boldsymbol{r}) + \frac{1}{P(\boldsymbol{r})}\big(\psi'(\boldsymbol{r}) - \psi(\boldsymbol{r})\big). \tag{2.51}$$

The key to processing a soft illumination function is the introduction of a weighting function such that,

$$O'(\boldsymbol{r}) = O(\boldsymbol{r}) + \frac{1}{P(\boldsymbol{r})}\frac{|P(\boldsymbol{r})|^2}{|P(\boldsymbol{r})|^2_{max}}\left(\psi'(\boldsymbol{r}) - \psi(\boldsymbol{r})\right). \quad 2.52$$

As the probe function must be allowed to contain zeroes, the division by P is altered so that,

$$\frac{1}{P(\boldsymbol{r})} = \frac{P^*(\boldsymbol{r})}{(|P(\boldsymbol{r})|^2 + \delta)}, \quad 2.53$$

where the δ prevents any division by zero. The final update equation becomes,

$$O_{n+1}(\boldsymbol{r}) = O_n(\boldsymbol{r}) + \mathbb{U}_o(\boldsymbol{r})\left(\psi_n'(\boldsymbol{r}, \boldsymbol{R}) - \psi_n(\boldsymbol{r}, \boldsymbol{R})\right), \quad 2.54$$

where $\boldsymbol{R}$ is the real-space scan coordinate and $\mathbb{U}_o$ is an update function to perform a weighted division of the difference in the estimated and updated exit waves by the probe function, where,

$$\mathbb{U}_o(\boldsymbol{r}) = \frac{|P(\boldsymbol{r})|^2}{|P(\boldsymbol{r})|^2_{max}}\frac{P^*(\boldsymbol{r})}{(|P(\boldsymbol{r})|^2 + \delta)}. \quad 2.55$$

The PIE algorithm can be described by the flow diagram shown in Figure 2.20.

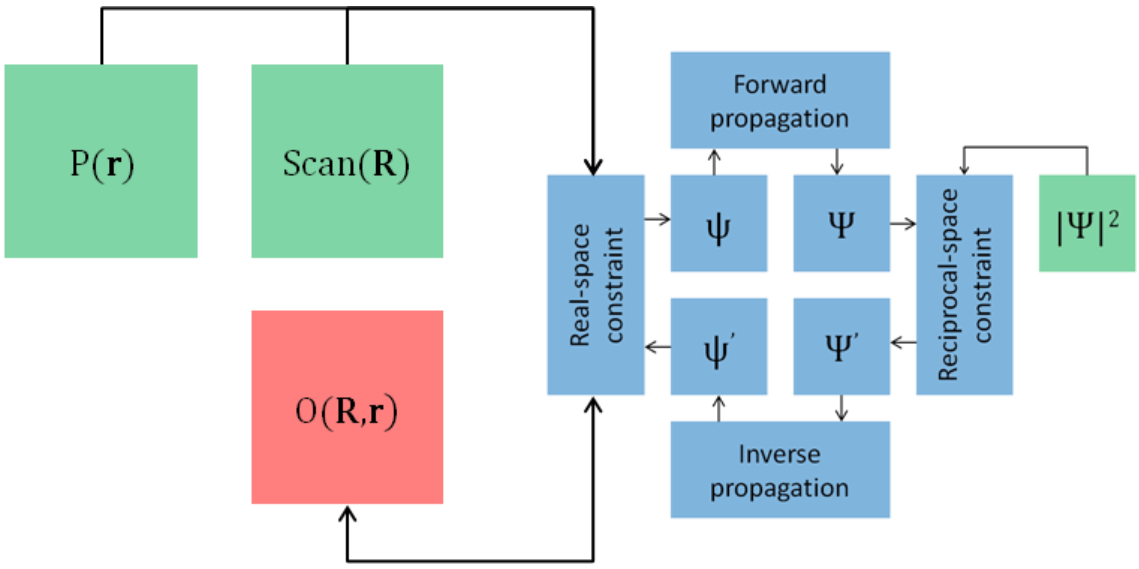

*Figure 2.20: A flow diagram of the PIE reconstruction algorithm for a single iteration at scan position **R**, where **r** represents the real-space coordinates. The kernel of the algorithm (shown in blue) feeds from the known values (shown in green) in order to solve for the unknown object (shown in red).*

2.4.2 Experimental Demonstrations of PIE

The first experimental demonstration of ptychography using iterative methods was produced in the visible light regime in Sheffield in 2007, which showed that the technique could produce good quality images in both modulus and phase over an extended object and without lenses (Rodenburg et al., 2007b). The resolution achieved here was 17μm. In order to form a localised illumination spot, an aperture was positioned upstream of the object, the effective gain in resolution over a scanning image with the same aperture was 47.

The technique was then implemented for hard x-rays, demonstrating a lens-less x-ray microscope with an extendable field of view at the Swiss Light Source (Rodenburg et al., 2007a). This was a big improvement to other x-ray CDI techniques, which require a finite sized object. The object used was a zone plate (a diffractive optic composed of several concentric rings of radially reducing widths), the wavelength was 0.155nm and a resolution of 50nm was achieved. The phase image was also consistent with theoretical predictions, showing that this technique could be used for quantitative phase analysis in this regime.

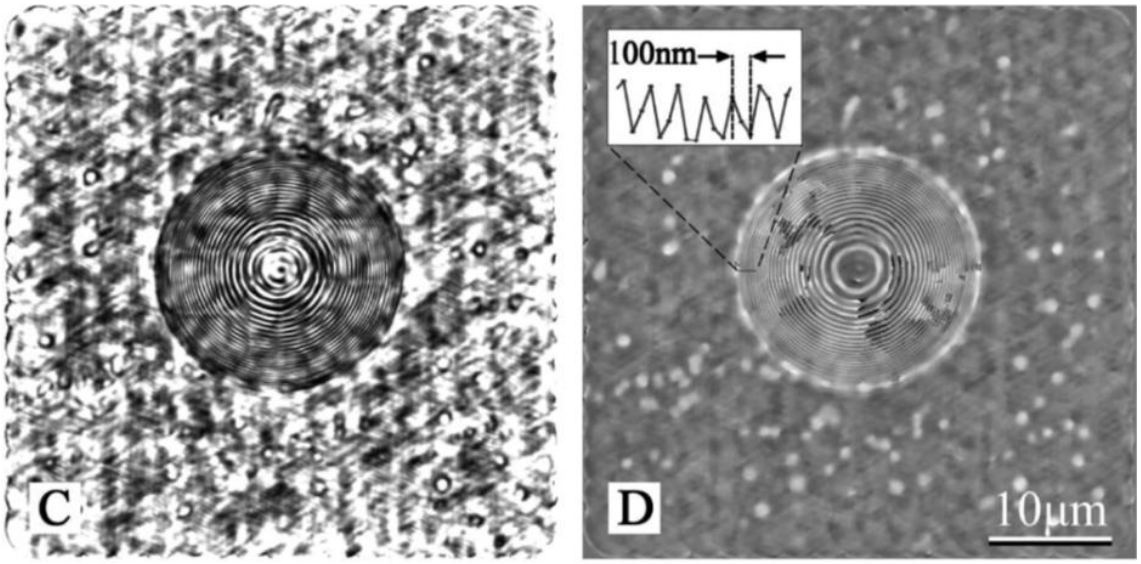

Figure 2.21: First hard x-ray ptychographic reconstruction of a zone plate showing both the modulus (c) and the phase (d) performed at the Swiss Light Source. Reproduced from (Rodenburg et al., 2007a).

2.4.3 The Difference Map

Knowing the form of the illumination profile at the specimen plane is often difficult and is a limiting factor of the above mentioned reconstruction algorithms. Some work was carried out into probe recovery methods that operate before the object reconstruction is performed (Atkinson et al., 2010). Improvements were later made to the ptychographic reconstruction algorithms though that allow for the refinement of the complex illumination function along with the usual complex object function within the reconstruction process.

The principle of simultaneous probe refinement was demonstrated in 2008, where a new reconstruction algorithm was suggested (Thibault et al., 2008, Thibault et al., 2009). A method known as the difference map, a general search algorithm that may be used to solve many problems where there exists a set of constraints, was used in order to find a solution to the ptychographic dataset. Rather than stepping through each position within an unknown object, updating separately at each such position, the difference map approach computes all of the exit-waves associated with each scan position in a parallel process. In this way it is a set of exit-waves that are updated in one operation (a projection onto the recorded data) before a separate real-space step deconvolves the probe and the object from the set of updated exit-waves. The averaging effect of the parallel update process seems to offer clean results in the presence of noise. A reconstruction showing the specimen (an insect's wing) along with the refined probe function taken from the publication is shown in Figure 2.22. Propagation back to the aperture plane shows a very clean disc which, along with the structure in the specimen plane and the quality of the reconstructed object, demonstrates both the high information density within a ptychographic dataset and the robustness of the reconstruction strategy.

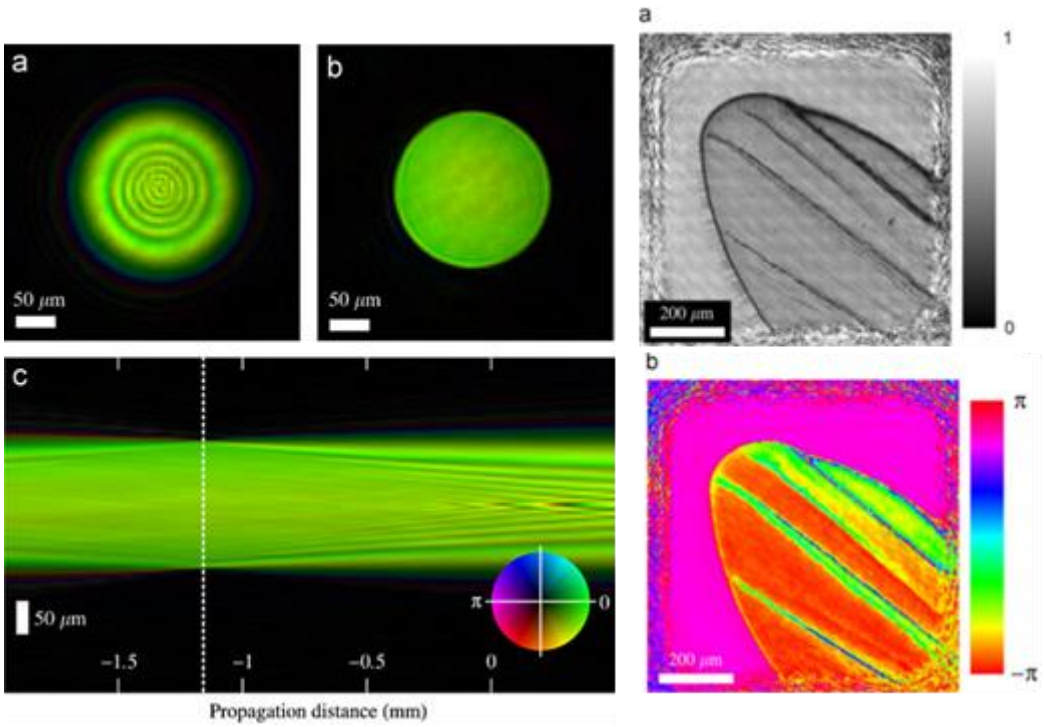

Figure 2.22: Reconstruction of an insect wing using the difference map reconstruction algorithm with probe update. The probe reconstruction is on the left with the probe modulus at the object plane (a), at the aperture plane (b), and a y-z slice through focus (c). Object reconstruction on the right in modulus (a) and phase (b). Reproduced from (Thibault et al., 2009).

2.4.4 Extended Ptychographic Iterative Engine (ePIE)

A similar alteration was made to the serial PIE algorithm outlined above (Maiden and Rodenburg, 2009), which is known as ePIE (extended PIE). It is the ePIE algorithm that forms the basis of all the reconstruction algorithms within this thesis and so a more detailed description of the algorithm and its development follows. ePIE contains a second real-space update step, which updates the illumination estimate alongside the specimen in a parallel calculation (the previous probe estimate is used to update the object and the previous object estimate is used to update the probe). The object is updated in a similar fashion to the original PIE,

$$O_{n+1}(\boldsymbol{r}) = O_n(\boldsymbol{r}) + \mathbb{U}_O(\boldsymbol{r})\left(\psi_n^{'}(\boldsymbol{r},\boldsymbol{R}) - \psi_n(\boldsymbol{r},\boldsymbol{R})\right), \tag{2.56a}$$

and the process is mirrored for the probe, p, update,

$$P_{n+1}(\boldsymbol{r}) = P_n(\boldsymbol{r}) + \mathbb{U}_P(\boldsymbol{r})\left(\psi_n^{'}(\boldsymbol{r},\boldsymbol{R}) - \psi_n(\boldsymbol{r},\boldsymbol{R})\right). \tag{2.56b}$$

The flow diagram in Figure 2.23 shows that the illumination function is no longer a known but, as a reasonable initial estimate is likely to be available in most circumstances (through model calculations) and so is partially known, is now updated during the reconstruction process alongside the object.

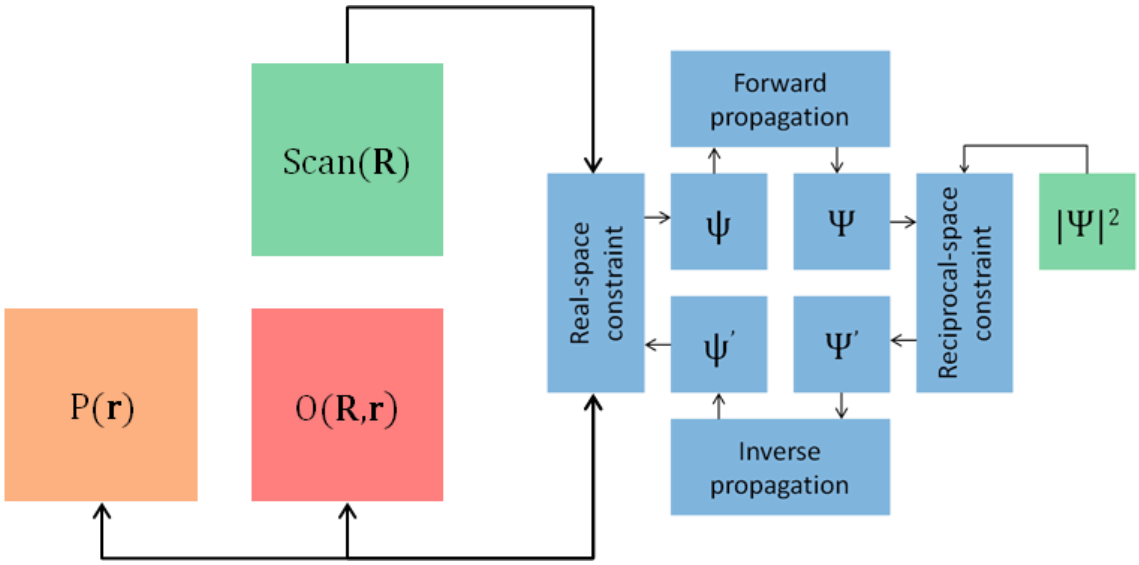

*Figure 2.23: A flow diagram of the ePIE reconstruction algorithm for a single iteration at scan position **R**, where **r** represents the real-space coordinates. The kernel of the algorithm (shown in blue) feeds from the known values (shown in green) in order to solve for the unknown object (shown in red) and partially known probe (shown in orange).*

Note that equation 2.55 has a delta term in the denominator. This prevents zeroes in the probe function from destabilizing the algorithm. In the extended PIE algorithm the update function is altered such that the 'divide by probe' term is,

$$\frac{1}{P(\boldsymbol{r})} = \frac{P^*(\boldsymbol{r})}{|P(\boldsymbol{r})|^2}, \tag{2.57}$$

and the object's scaling function is,

$$\beta_O = \left(\frac{|P(\boldsymbol{r})|}{|P(\boldsymbol{r})|_{max}}\right)^{\gamma}, \tag{2.58}$$

where γ can be any positive number. For most values of γ, the issue of dividing by a zero in the probe function remains. However, when γ is set to two the product of equations 2.57 and 2.58 produces the update function for the object,

$$\mathbb{U}_O(\boldsymbol{r}) = \alpha_O \frac{1}{P(\boldsymbol{r})}\beta_O = \alpha_O \frac{P(\boldsymbol{r})^*}{|P(\boldsymbol{r})|^2_{max}}, \quad 2.59$$

and the probe,

$$\mathbb{U}_P(\boldsymbol{r}) = \alpha_p \frac{1}{O(\boldsymbol{r})}\beta_p = \alpha_P \frac{O(\boldsymbol{r})^*}{|O(\boldsymbol{r})|^2_{max}}, \quad 2.60$$

where α scales the size of the step through the solution space at each position (typically set to one). Note that there is no longer an additional delta in the denominator of the update function. It is quite elegant that the new update no longer has the potential to divide by a zero.

2.4.5 The Error Metric

The ptychographic dataset contains a certain number of pixels, T, where T is the product of the number of pixels per diffraction pattern, N_u, and the number of scan positions, N_R. When fitting a set of unknown values to this set of known values through an iterative process, each possible solution configuration has an associated error when propagated to and compared with the recorded data. In that manner, a multi-dimensional error space may be used to describe the landscape across which the algorithm must seek a global minimum. In practical situations the error space often contains many local minima and this is something that all ptychographic reconstruction algorithms must overcome. (For an analysis of the various reconstruction methods as they search an error space see (Marchesini, 2007).) In order to follow the progress of the reconstruction, and to define a condition at which a solution is deemed to have been found, it is useful to generate an error metric based on a root mean square of the error space. The RMSE error metric is defined as,

$$RMSE = \sqrt{\frac{\sum_{\boldsymbol{R}}\sum_{\boldsymbol{u}}\left[\left|\Psi'_{\boldsymbol{R},\boldsymbol{r}}\right| - \left|\Psi_{\boldsymbol{R},\boldsymbol{u}}\right|\right]^2}{N_R N_u}}. \quad 2.61$$

An alternative reconstruction strategy based on nonlinear optimization, which minimizes a normalized invariant field RMSE in order to find a consistent solution within the recorded ptychographic dataset, has also been demonstrated (Guizar-Sicairos and Fienup, 2008b). This

technique tends to require good initial estimates of all the elements and is more often used to 'polish' reconstructions after initial processing from one of the above techniques. In fact, it is possible to construct a reconstruction 'recipe' where several algorithms are used for varying amounts of time in varying order - a method used widely in the single-shot case.

2.4.6 Experimental Demonstrations of ePIE

Visible light ptychography was later improved upon in 2010, where a U.S. Air Force 1951 resolution test target was used to show the technique could resolve down to 1μm (Maiden et al., 2010). Applying ePIE (without the probe update) to an electron ptychography dataset recorded on a TEM at short wavelengths (200keV) was first demonstrated to produce quantitative phase images at the nanometre scale in 2010 (Hüe et al., 2010). The results suggested that ptychography was as an alternative to electron holography and through focal series methods.

The imaging of biological cells in the x-ray regime has been demonstrated, showing the phase sensitivity afforded through ptychography (Giewekemeyer et al., 2010). Other biological imaging has been shown in the visible light regime, with observations of cancerous cells (Claus et al., 2012), and cell division (Marrison et al., 2013). Ptychography has also been successfully applied to optical metrology, where the high quality phase signal achieved through ptychographic reconstructions in conjunction with the dual wavelength method produces a topographic map of high fidelity (Claus et al., 2013). The improvements over more traditional white light methods are particularly apparent across sharp features.

It has been recently demonstrated that the resolution of a 30keV scanning electron microscope (SEM), where the setup is significantly simpler with no post specimen lenses, may be increased significantly so that 0.24nm atomic fringes within gold particles become visible (Humphry et al., 2012). The experiment was the first to exploit the dark field information in electron ptychography, which allowed for the resolution to be increased beyond that set by the objective lens. The data for this result is used in a later chapter to demonstrate a technique development, the original result is

shown in Figure 6.18. More recent STEM ptychography experiments have also shown promise for atomic resolution reconstructions through electron ptychography (Putkunz et al., 2012, D'Alfonso et al., 2014).

2.4.7 Scan Position Correction

Although ptychography relies heavily on the *a priori* knowledge of the scan coordinates, the scanning stages used to record practical ptychographic datasets often suffer from hysteresis, backlash, and other imperfections. These lead to errors in the scan coordinates and can corrupt the reconstruction process. This was pointed out as one of the restricting factors in the progress of electron ptychography (Hue et al., 2011). Initial attempts to overcome this issue in the electron microscope based on sum-squared error (SSE) minimization alongside cross correlation analysis of the recorded Ronchigrams (formed from a convergent electron beam incident upon a specimen as recorded in reciprocal-space) implied that the issue of inaccurate scan positions may be surmountable (Hurst et al., 2010). Later work based on evolutionary search methods showed that simulations with artificially added errors to the scan positions on the order of a few pixels could be recovered (Shenfield and Rodenburg, 2011). At the time this method was mainly limited by the computational effort required and the associated time cost.

More recently an algorithm has been constructed based on the method of annealing (Maiden et al., 2012b). Simulated annealing is a more general method used for global optimization across a wide range of disciplines. It is based on the concept of annealing in metallurgy, where a material is heated to a certain temperature before being cooled in a controlled manner, altering the properties of the material. When a material is heated its constituent atoms have a large amount of thermal energy and 'jiggle' around, as the temperature is decreased they may gradually settle into a certain low energy configuration. The computational version, exploited in this position correction technique treats each position like an atom in a material, to begin with the estimated positions are shifted to a selection of other trial positions at large distances from the original. As the iterations pass, the

distance between the current estimate positions and their trials is reduced – the search radius contracts.

The execution of the scan correction is built into the ePIE algorithm, a set of trial exit-waves (each having a slightly different scan position) are generated at each scan position. All of the estimates are then propagated to the detector plane where, by comparing the error metric associated with each estimate, a single estimate position is selected. The other estimates are disposed of and the algorithm continues as normal.

A position correction algorithm based on cross correlations has also been demonstrated (Zhang et al., 2013). Here it is the algorithm's attempts to shift the illumination relative to the object during the reconstruction that is monitored and used to drive a position correction feedback loop. Due to the simplistic nature, hence reduced computational effort, and the ease at which it may be integrated into existing computer code, the annealing method is used when necessary in the work shown throughout this thesis. An updated flow diagram of the reconstruction algorithm is shown in Figure 2.24 which represents the ability to refine the probe's relative shifts as well as its physical form.

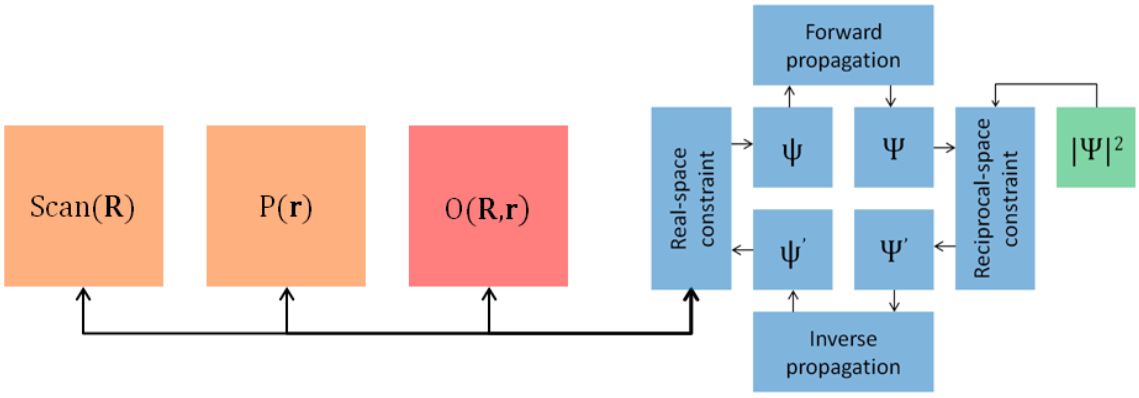

*Figure 2.24: The flow diagram of the reconstruction algorithm for a single iteration at scan position **R**, where **r** represents the real-space coordinates. The kernel of the algorithm (shown in blue) feeds from the known values, $|\Psi|^2$, (shown in green) in order to solve for the unknown object(s) (shown in red), and the partially known probe(s), P, scan, and source, S, (shown in orange).*

2.4.8 Bragg Ptychography

There has also been much activity in the area of Bragg ptychography, where the detector is placed in line with a Bragg reflection angle instead of the usual position in line with the optic axis. The recorded signal is highly sensitive to strain deviation within the specimen as a shift in the Bragg peak relates directly to strain within the specimen and is represented in the reconstruction as a quantitative phase distribution.

The processing of a collection of single-shot CDI reconstructions from a single ZnO nanorod has been shown to offer a three dimensional strain map (Newton et al., 2010) and model calculations have shown that the same geometry could be applied to ptychography (Godard et al., 2011). The technique has also been shown to provide quantitative imaging of lattice distortions in semiconductors (Hruszkewycz et al., 2012, Holt et al., 2014) and strain fields due to dislocations in a silicon crystal (Takahashi et al., 2013).

2.4.9 Fourier Ptychography

Just as conventional ptychography synthesises an aperture function in real-space by scanning a physical illumination in real-space whilst recording intensity patterns in reciprocal-space, the inverse of this has also been demonstrated. Fourier ptychographic microscopy (FPM) instead records intensity patterns in real-space (conventional images) with an aperture positioned in reciprocal-space (the back focal plane of the image forming lens) (Zheng et al., 2013). The aperture is effectively scanned through reciprocal-space although a similar effect be achieved by illuminating the specimen from different angles (where conventional ptychography illuminates at different lateral positions). The properties of conventional ptychography are turned on their head with this method as the reconstructed field of view (FoV) is now determined by the size of the detector and the resolution relies upon the scanning, and subsequent synthesis, of an aperture function. The method is similar to that used in the electron microscope for aperture synthesis (Kirkland et al., 1995, Kirkland et al., 1997, Haigh et al., 2009)

2.4.10 Structured Illumination and Detector Extrapolation

ePIE has the ability to separate out the illumination function from the object function (in an operation equivalent to the deconvolution of the two contributions in reciprocal-space) and so there is no longer a reliance on the ability to accurately model the illumination function (or otherwise determine its structure through direct imaging methods). The technique therefore has the ability to a use convergent or otherwise structured illumination profile, which opens up the possibility of using a variety of different illumination functions with different structures. It has been shown that employing a diffuse illumination profile improves the signal-to-noise ratio (SNR) of the detected intensity pattern (Guizar-Sicairos et al., 2012).

In fact, the use of a convergent beam allows higher angle scatter to be recorded for any given detector size (Edo et al., 2010). It is worth noting that in this setup the image resolution no longer directly correlates with the final range of scattering angle. A demonstration of double resolution imaging in the STEM using a different theoretical approach, but which exploits this characteristic of the four-dimensional dataset, was carried out in the early 1990's (Rodenburg et al., 1993, Plamann and Rodenburg, 1994).

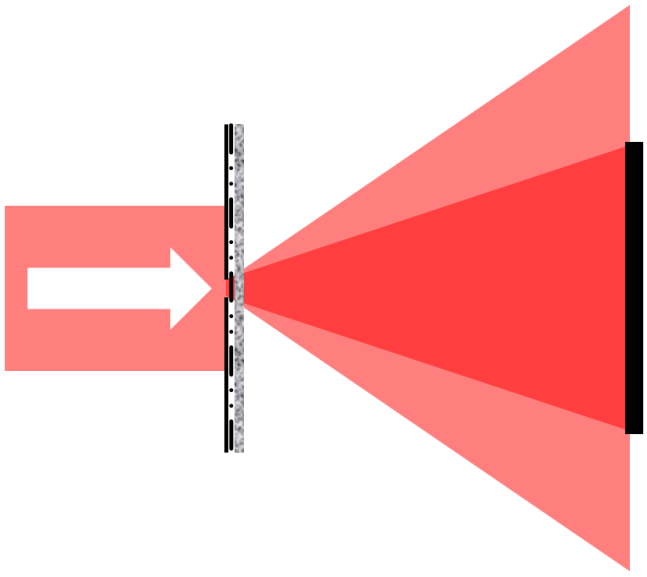

Figure 2.25: A parallel incident beam is localised by an aperture in the plane of a diffuse membrane that introduces a wide range of k-vector, some of which are not recorded by the detector.

A further extension to the ePIE algorithm was made in early 2011 that provided the technique with the ability to computationally extend the detector size post acquisition, given certain illumination conditions (Maiden et al., 2011). The result is reconstructed images with a resolution greater than that expected from the intrinsic angular range of any one of the diffraction patterns alone.

As the structured beam is scanned across the specimen, each object element will be expressed onto different regions in reciprocal-space (due to the change in incident k-vectors). This allows the possibility that high angle scatter from a point in object space can be incident on the detector at one position and yet not at the next position even though that point is being illuminated in both cases. It is this principle that is exploited in order to improve the resolution of the reconstructions further, beyond the limit imposed by the angular range of the detection area(Maiden et al., 2011). The method, named super-resolution, runs the reconstruction as though the detector had been physically larger than in reality. It is then at the reciprocal-space intensity update step that the ePIE algorithm is modified. As only a section of the estimated values have a corresponding intensity measurement, not all values can be updated. A support constraint, similar to that used in real-space for the Fienup algorithms, is employed in reciprocal-space. The reciprocal-space intensity update step under these conditions becomes,

$$\psi(\boldsymbol{u})' = \begin{cases} \psi(\boldsymbol{u})\dfrac{\sqrt{I(\boldsymbol{u})}}{|\psi(\boldsymbol{u})|} \\ \psi(\boldsymbol{u}) \end{cases} \begin{matrix} \boldsymbol{u} \in S \\ \boldsymbol{u} \notin S \end{matrix}, \qquad 2.62$$

where S is the set of pixels that contain a valid intensity measurement. Pixels outside of *S* are said to be 'floating' pixels. The addition of 'virtual' pixels to the dataset allows the reconstruction process to be executed on an extended synthetic detector. While these pixels are not able to constrain their respective regions within the dataset, they do remove false constraints on the solution. For example, dead pixels will contain values which do not have any connection with the rest of the dataset and instead of guiding the algorithm towards the correct solution will instead cause an inconsistency in the solution space. An example of the algorithm's performance is shown in Figure 2.26, where a

conventional dataset is cropped down, removing a significant region of the scattered intensity, before the reconstruction algorithm fills in the missing values.

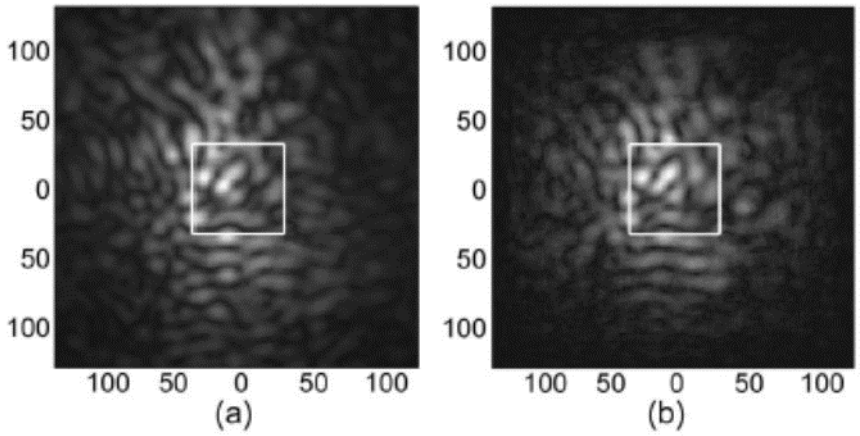

Figure 2.26: Typical diffraction pattern from a conventional dataset (a) is cropped down to the area within the white box. The super-resolution algorithm is used to recover the whole diffraction pattern (b). Reproduced from (Maiden et al., 2011).

Recovering the 'lost' values that were scattered past the detectors edges using the super resolution algorithm is actually removing a false constraint that existed previously, a constraint that the regions beyond the detector contained no radiation. A globally consistent solution to the phase problem for the ptychographic set of intensities only exists when some radiation is allowed to exist beyond the extent of the physical detector.

Although ptychography is traditionally executed with the detector in the far-field position, it has been demonstrated that under the correct conditions and with a diffuse illumination function (required), ptychography may yield results with a detector placed in the near-field (Stockmar et al., 2013).

2.4.11 3D Ptychography

The high resolution images produced from ptychographic reconstructions have been successfully combined with the three dimensional reconstruction techniques of x-ray tomography. X-ray tomography takes a set of 2D projections through a specimen recorded at many overlapping rotation angles and reconstructs a high quality three dimensional image of a specimen. The combined technique, ptycho-tomography, was first demonstrated to produce quantitative phase

reconstructions in three dimensions on a bone specimen, with features on the order of 100nm resolved, in 2010 (Dierolf et al., 2010). Similar techniques have been used since to examine the structure of corrosion-resistant barrier coatings used in the marine industry, for an example see (Chen et al., 2013). Recent results have demonstrated a three dimensional resolution of 16nm in each direction with an x-ray wavelength of 0.2nm (Holler et al., 2014).

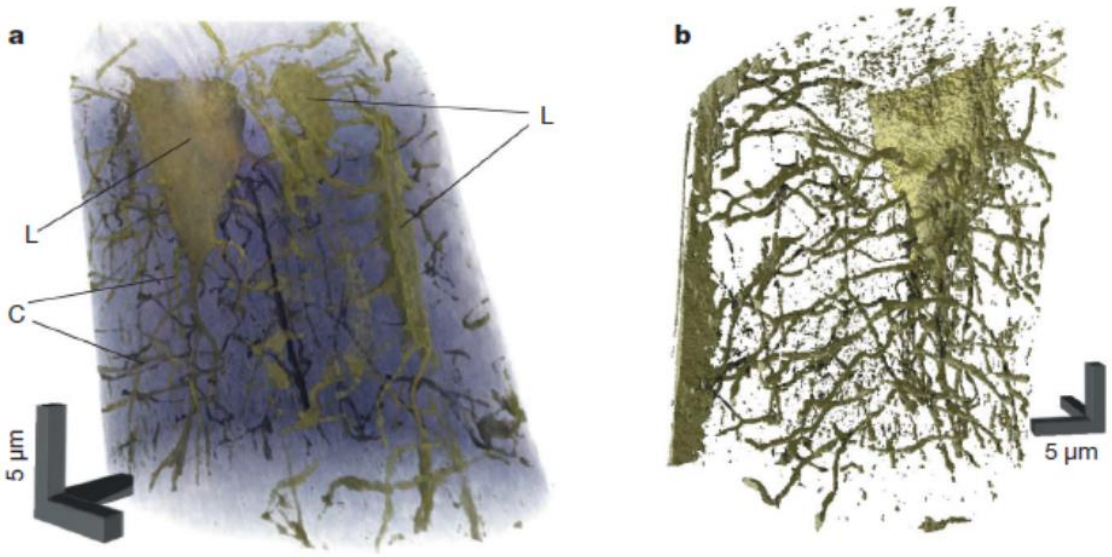

Figure 2.27: 3D rendering of the ptycho-tomographic reconstruction. a) Volume rendering with the bone matrix in translucent colours to show osteocyte lacunae (L) and the connecting canaliculi (C). b) Isosurface rendering of the lacuna-canalicular network. Reproduced from (Dierolf et al., 2010).

The ptycho-tomographic reconstruction relies on the projection approximation holding for each separate 2D reconstruction. It has been shown recently that an alternative method of extracting three dimensional information exists, one which relies on an illumination function containing a wide range of k-vectors coupled with the usual real-space scanning element within ptychography. The algorithm is then able to separate out layers within a three dimensional specimen (Maiden et al., 2012a). The method, named 3PIE, is based on the multislice approach developed for the study of electrons as they scatter through a crystal (Cowley and Moodie, 1957, Cowley and Moodie, 1959a, Cowley and Moodie, 1959b). The probe function is passed through an estimate of an object (layer 1), rather than propagating the exit-wave to the detector, the exit-wave is propagated to a second object estimate (layer 2). The process continues through the remaining layered estimates of the object until finally, after the exit-wave is passed through the last object (layer n), the resultant exit-

wave is propagated to the detector plane. The reciprocal update step is executed as normal (equation 2.45) before the updated wave-field is propagated back to layer n. The usual ePIE update (as described in equations 2.56a and 2.56b) is applied to the layer n, leaving an updated object estimate and a new exit-wave. The exit-wave is then propagated back to layer n-1 and so on until after an update of layer 1 results in a new estimate of the probe function at the entrance plane of the specimen.

Recent work has shown that the technique (using a diffuse illumination in conjunction with a lens assisted ptychographic setup) is able to section a specimen that is up to 150µm thick with a depth resolution below 5µm (Godden et al., 2014). The result moves the technique away from an optical sectioning method (where only distinctly separate slices may be imaged) towards a more comprehensive three dimensional imaging technique (where the depth resolution is increased).

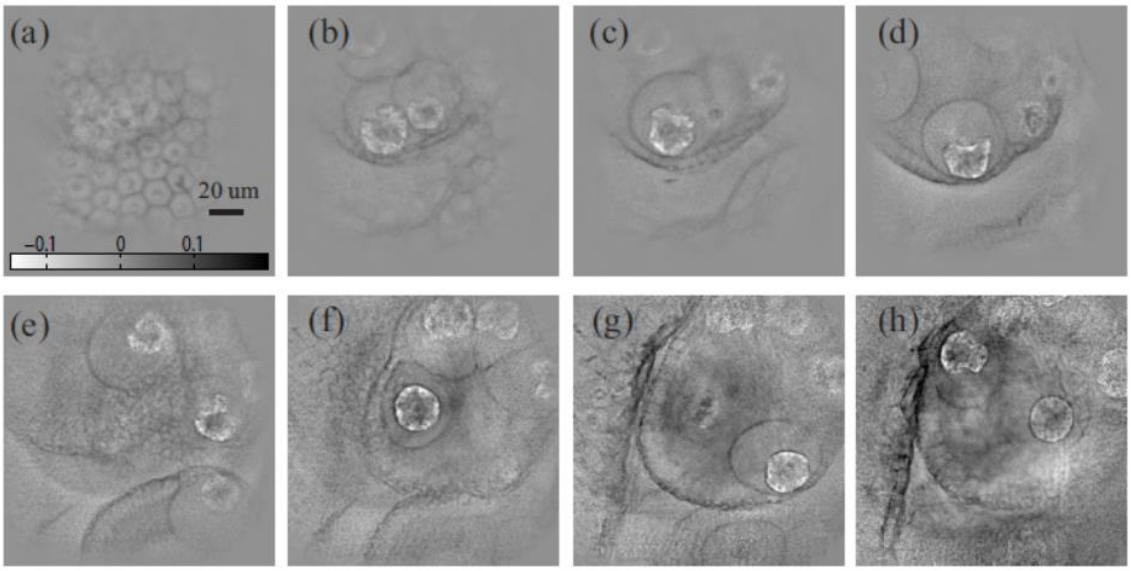

Figure 2.28: Selected slices from a reconstruction of the phase of the complex transfer function of a Volvox algae specimen with total thickness 150 µm. The slices (a)–(h) correspond to planes 1, 3, 5, 11, 17, 21, 24 and 28 out of a total of 33. The separation between adjacent planes is 4.7 µm. The colour bar in (a) indicates the phase shift in radians. Reproduced from (Godden et al., 2014).

The 3PIE method has also recently been applied in the x-ray regime, where two distinct layers with a separation distance of 105µm were reconstructed at a lateral resolution of approximately 50nm (Suzuki et al., 2014).

2.4.12 Ptychography as a Transmission System

As with both direct and diffractive imaging systems, ptychography is now described in terms of a transmission system. The evolution of Figure 2.29 from Figure 2.17 comes in the form of an added scan parameter in the 'key' to the encoder/decoder.

The object is again encoded within the illumination, although this now occurs at each scan position and from each sub-set of the object. It is the full four-dimensional wave-function that is propagated into the far-field and transmitted through the detector into the reconstruction algorithm. The reconstruction algorithm now requires the *a priori* illumination and scan information in order to decode the object from the array of diffraction patterns in order to create a complex real-space image. Due to the introduction of the scan to the encoding process, the information density of the wave-field that is transmitted through to the dataset may be greatly increased. It is this that provides ptychography with the ability to recover not only the aberration free complex object in real-space but also all of the extra information, such as illumination and scan refinements, missing pixels through super-resolution, and three dimensional structure. It is the power of this configuration and its ability to encode a large amount of information into a single scan that is explored throughout this thesis.

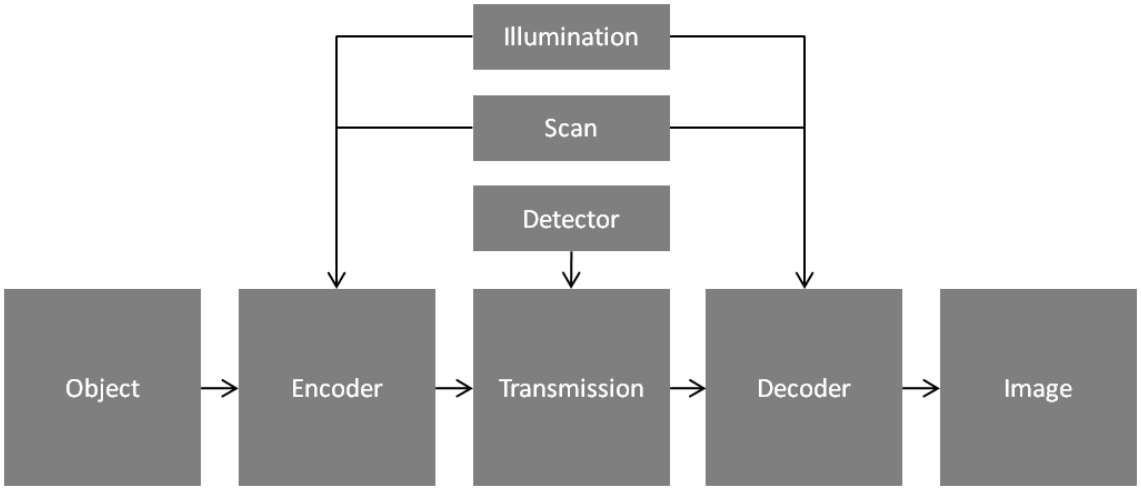

Figure 2.29: The ptychographic imaging system as a transmission channel, where the object information is encoded by the localised illumination profile along with a scan of that illumination before processing (transmission) through a detector (where the phase information is lost) where an algorithm uses the illumination and scan information to decode the object information to produce an image.

2.5 Summary

The field of computational optics and lens-less imaging is extensive. Many methods exist which aim to remove the reliance on high quality optical elements in order to build aberration free, phase sensitive microscopes. Other methods, such as holography, have not been included here as the whole of this work is focussed on developments within iterative ptychography.

First described in 1969 as a method of phasing the diffraction peaks of a crystal, the ptychographic principle did not prove to be very practical for general imaging for many years. In the 1990's it was demonstrated that the Wigner-distribution deconvolution could provide a solution to a ptychographic dataset and demonstrations were produced in the visible light, x-ray, and electron regimes. Although shown to offer a method of extending the resolution of a microscope beyond the information limit, the use of ptychography remained limited as microdiffraction patterns were required from each position as a beam was scanned across each object element.

Meanwhile, in 1972, Gerchberg and Saxton demonstrated an iterative solution to the phase problem which could be applied by iterating between an image of a specimen and its diffraction pattern, applying constraints until the phase distribution of each was self-consistent. Fienup later altered the Gerchberg-Saxton method so that only a single exposure of the diffraction pattern was required so long as the beam was suitably localised. In 2004, Faulkner and Rodenburg successfully combined the methods of ptychography with those of Fienup's iterative algorithm to produce a new, iterative, ptychographic imaging algorithm (PIE).

Since the more practical demonstration of ptychography, where the PIE algorithm significantly relaxed the number of scan positions required, the technique has seen an explosion of research activity. Early developments included the ability to recover an image without knowing the structure of the beam which illuminated it, since then there have been too many to list. The aim of the above review however is to provide an overview of this rapid development, much of which has occurred in tandem with my own work, and the main highlights were selected for discussion.

3 The Ptychographic Imaging Framework

Ptychography has been seen throughout its more recent development as an extension to the single-shot CDI imaging method. The single-shot CDI method can be generally described as one that samples the intensity of a diffraction pattern at its Nyquist limit (or finer) and, by obtaining *a priori* knowledge about the specimen (or the illuminating beam of radiation), is able to iteratively search for a consistent solution to the phase problem. The ptychographic imaging method is built upon similar principles, however each detector pixel now records several separate measurements relating to each object element. This is a more general sampling framework which, by introducing a scanning pitch in real-space, R, allows for a dataset that may be much richer in information content per object element than any single diffraction pattern alone.

Reducing the ptychographic method down to the fundamental elements, it is possible to describe how the real-space scan produces a much richer, four-dimensional, sampling condition. One which is able to capture more information than is required to solve the phase problem for an unknown specimen within a known illumination patch. It is this extra information, often referred to as 'redundancy' in the literature, that allows ptychographic reconstruction algorithms to also refine the probe function (Thibault et al., 2009, Maiden and Rodenburg, 2009), scan positions (Maiden et al., 2012b, Zhang et al., 2013), and resolve three-dimensional structure (Maiden et al., 2012a).

This chapter provides a more general sampling condition which predicts that the probe size is no longer constrained by the pixel-pitch in the detector plane, overturning the cornerstone of diffractive imaging. A model calculation is performed which demonstrates that a full reconstruction is possible when the pixel-pitch in reciprocal-space produces a real-space window that is exactly the same size as the illuminating beam. In other words there is no longer any reciprocal-space convolution, which overturns the conventional view of ptychography (Rodenburg, 2008). In this case, the phase problem is unlocked purely from the real-space sampling offered by the ptychographic method. The principle is pushed to its limit, where pixels are removed from the diffraction pattern to leave a super-sparse dataset. The real-space window is now very much smaller than the illuminating beam, but a reconstruction is still possible.

Finally, the act of trading sampling pitch between real and reciprocal-space will only offer any practical gains if the principle of dose fractionation holds. A model calculation is performed whereby the total number of photons through the specimen remains constant but the number of real-space positions is increased. Alterations to the algorithm in both real and reciprocal-space are made which show that, regardless of dose fractionation (having very few counts in each diffraction pattern), reducing the real-space step produces a superior image. The result suggests that the information content per dose is increased - a vital discovery in the development of low dose imaging for beam sensitive specimens.

3.1 The Synthetic Illumination

In order to satisfy the Nyquist sampling condition of the intensity measurements made on a detector with a finite pixel-pitch positioned in the far field (reciprocal-space), single-shot CDI irradiates a patch of specimen with a suitably localised illumination function. The lateral extent of the specimen which may have all elements phased relative to every other is limited, not only by the pixel-pitch of the detector in reciprocal-space (due to the Nyquist sampling criterion) but also on the coherence properties of the illuminating beam (Spence et al., 2004).

The unique property of ptychographic imaging is in the stepping of a localised patch of coherent radiation across a specimen. When this step is sufficiently precise and stable over the acquisition time of the diffraction pattern then, using the algorithms discussed in section 2.4.1, it is possible to build a synthetic illumination function with an indefinitely extended spatial coherence envelope at the specimen plane that is no longer constrained by the spatial extent of the beam. More formally, the two dimensional local (physical) illumination function is coupled with a two dimensional scanning stage such that the specimen may now be sampled in four dimensions - the specimen is probed by a four-dimensional, global, illumination function. The real-space view of the global illumination function (referred to as the synthetic illumination) from the convolution of the physical beam and the scan coordinates is shown in Figure 3.1c. For the initial sampling theory discussed here, the illumination is assumed to be ideally coherent, and indeed the whole experiment to be stable. The more practical issue of experimental instabilities and partial coherence is discussed later.

Viewing the process in reverse (in theoretical terms) it is possible to see ptychography as a decomposition of the single-shot CDI technique. Supposing that the synthetic illumination shown in Figure 3.1c was a single patch of illumination then, with a sufficiently sampled diffraction pattern, a reconstruction could be performed. By employing a smaller patch of illumination in conjunction with a scanning stage, ptychography effectively partitions the single diffraction pattern recorded from the specimen by the hypothetical illumination function into several diffraction patterns recorded from

several exposures of the specimen by the physical beam at overlapping positions. A reconstruction of the specimen across the whole region of irradiance relies upon the synthesis of such a set of diffraction patterns (measured in intensity only) into a single synthetic diffraction pattern composed of complex valued pixels.

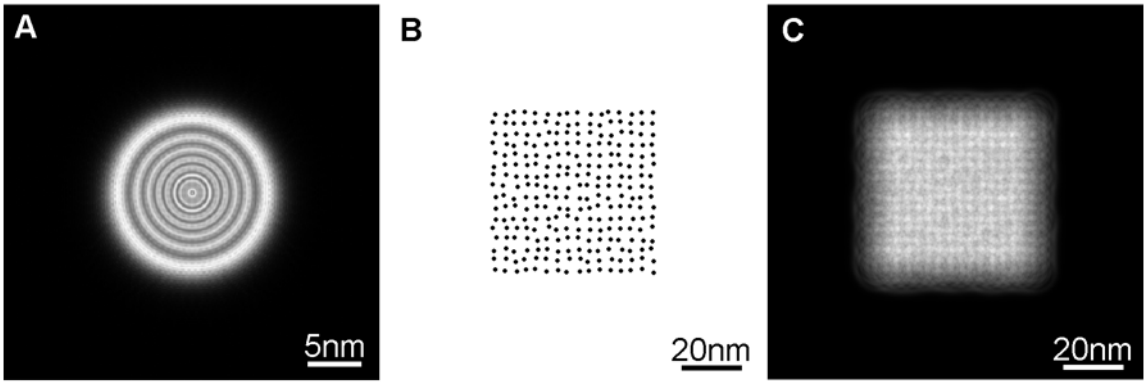

Figure 3.1: The synthetic illumination function. a) The local (physical) illumination function. b) The scan coordinates. c) The local illumination function is convolved with a distribution of delta functions, one at each scan position, to produce the synthetic illumination function. Note the difference in scale bars, (b) and (c) cover a larger than (a).

3.1.1 The Real-Space Scan

The scan element allows the object to be shifted laterally (perpendicular to the detector) with steps less than the spatial extent of the illumination. It has been discovered that under certain circumstances a uniformly spaced rectilinear scan can lead to periodic artefacts appearing in the reconstructed image (Thibault et al., 2009, Huang et al., 2014). It is now common throughout the community to use a scan with random offsets applied to each position, such as that shown in Figure 3.2b. Note that these random offsets are known and so do not introduce any more uncertainty into the data. In order to preserve a symmetry between the uniform distribution of pixels in reciprocal-space with the scan steps in real-space, the ptychographic sampling condition is derived with a scan as in Figure 3.2a.

When the points along R are within ΔR, all points are independent measurements within the interval ΔR. If the points spread outside of these intervals then the effective ΔR may increase and the separation of measurements across R-space decrease. The closer two points become in adjacent cells, the further away they must be from their other neighbours. If the scan is cyclic (a scan may be

considered cyclic when it exists across a specimen of tiled identical unit cells) then the mean is forced to be ΔR. When the scan is not cyclic, the edges may all double their distance from all other points and so the mean is potentially reduced in this case. The edge positions should consequently be positioned at the centre of their cells.

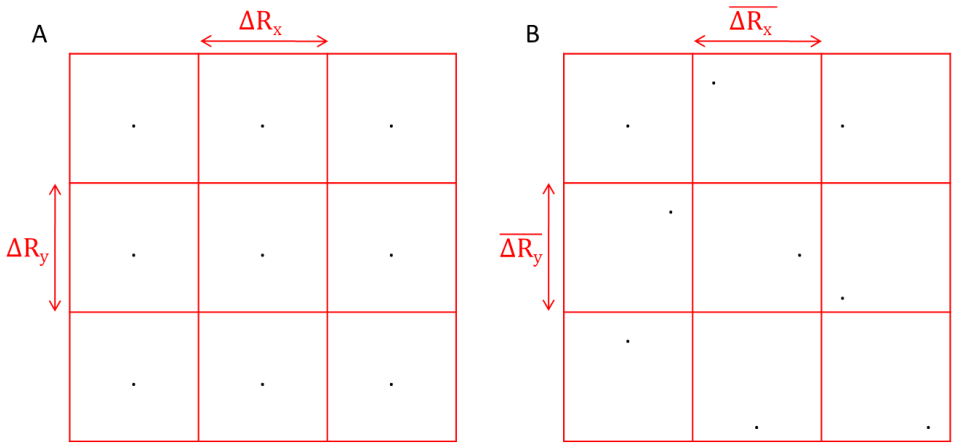

Figure 3.2: Scan positions within a rectilinear grid of mean separation $\overline{\Delta \boldsymbol{R}}$, without (a) and with (b) random offsets.

3.1.2 The Four-Dimensional Dataset

The dataset produced from a typical ptychographic scan is four dimensional, with two dimensions expressed across the detector plane (u_x, u_y) and two across the scan coordinates (R_x, R_y). The recorded dataset relates to real-space by a two dimensional Fourier transform acting on the detector coordinates (see Figure 3.3).

Ptychography extends the sampling condition further by stepping the object relative to the illumination perpendicularly to the optic axis. By arranging the scan coordinates to be less than half of the width of the illumination in each direction, it is possible to sample every object element at least twice. This double measurement essentially facilitates the recovery of the lost half of the information in reciprocal-space (the lost phase).

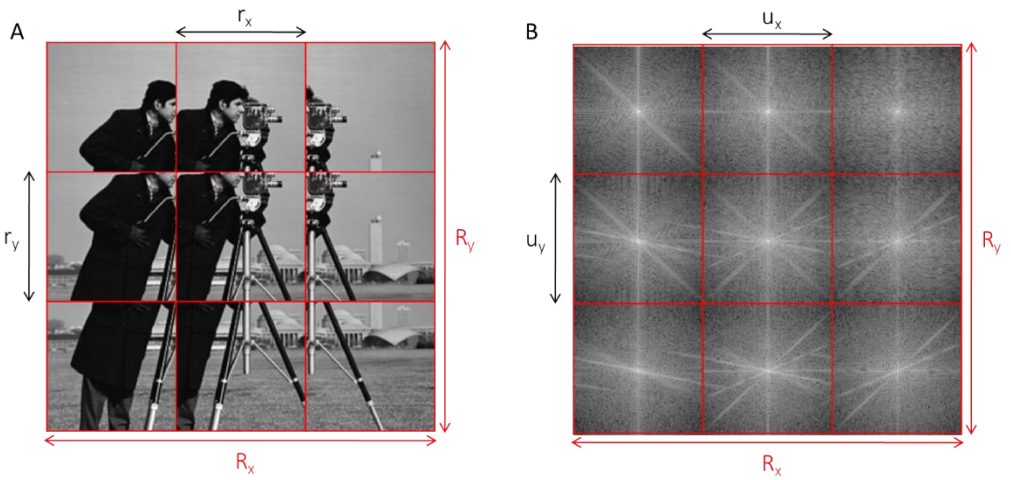

Figure 3.3: An example ptychographic dataset with the information represented in real-space (a) and reciprocal-space (b). The coordinates r_x and r_y represent the real-space coordinates of each exposure, u_x and u_y represent the reciprocal-space coordinates of each exposure, and R_x and R_y represent the scan coordinates. For display purposes (b) is displayed on a log scale.

3.2 The Ptychographic Sampling Condition

Building on the concept of a decomposed synthetic illumination function it is possible to generalise the sampling criterion required for a single-shot CDI diffraction pattern into that for a ptychographic dataset. Just as the single-shot case relies on an overlap of the illumination with the specimen in reciprocal-space, in a ptychographic dataset each diffraction pattern is also coupled with several others within the dataset through an overlap in real-space. This section brings both aspects of overlapping measurements into a single new sampling condition which is much more suitable to the realm of ptychographic imaging.

Starting from the Nyquist sampling limit of any complex wave-field with respect to its discrete Fourier transform, the real-space field of view, X_p, is defined by the inverse relationship with the detector pixel-pitch in reciprocal units, ΔU_p, such that,

$$X_p \Delta U_p = 1 \,, \tag{3.1a}$$

$$\Delta U_p = \frac{\sin \Delta\theta_p}{\lambda} \,, \tag{3.1b}$$

where $\Delta\theta_p$ represents the angle subtended by the detector's pixel-pitch at the specimen plane and λ is the wavelength of the illuminating radiation.

As the intensity of an object's Fourier transform is the Fourier transform of that object's autocorrelation, which is twice the spatial extent of the original object, the sampling pitch in reciprocal-space when recording intensities must be half of that required to satisfactorily sample the amplitudes (which contain both the phase and the modulus of the wave). For the two dimensional case such a sampling condition is sufficient to reduce the number of phase solutions down to two (Bruck and Sodin, 1979). This is the single-shot CDI condition as shown in Figure 3.4b (and c) and is expressed more formally as,

$$D_p \Delta U_p = \frac{1}{2}, \tag{3.2}$$

where D_p is the spatial extent of the local illumination function in real-space. It has been suggested that only the ratio between the total number of measurements and the number of unknowns is important (Miao et al., 1998), here the condition is limited to the number of measurements within a certain pitch in each orthogonal direction such that there is no issue from significantly irregular forms of illumination or indeed detectors.

In order to physically meet the sampling condition of equation 3.2, a set of real-space elements, which cover half of the field of view in each X-Y direction, must be known *a priori*. This is generally achieved either with knowledge that the specimen within the beam is itself localised (Figure 3.4b) or with an aperture placed directly in (or imaged onto) the specimen plane (Figure 3.4c).

Ptychographic datasets are often referred to as being highly redundant, allowing the technique, given suitable reconstruction algorithms, to yield high quality images under harsh experimental situations. Figure 3.5 shows two examples of ptychographic datasets (represented in both real and reciprocal-space) taken under the support constraints shown in Figure 3.4a and Figure 3.4c. Note that some regions of the object are repeated; this is where the so called redundancy originates. The following section explores what the redundancy is, where it comes from, and how much of it is actually required.

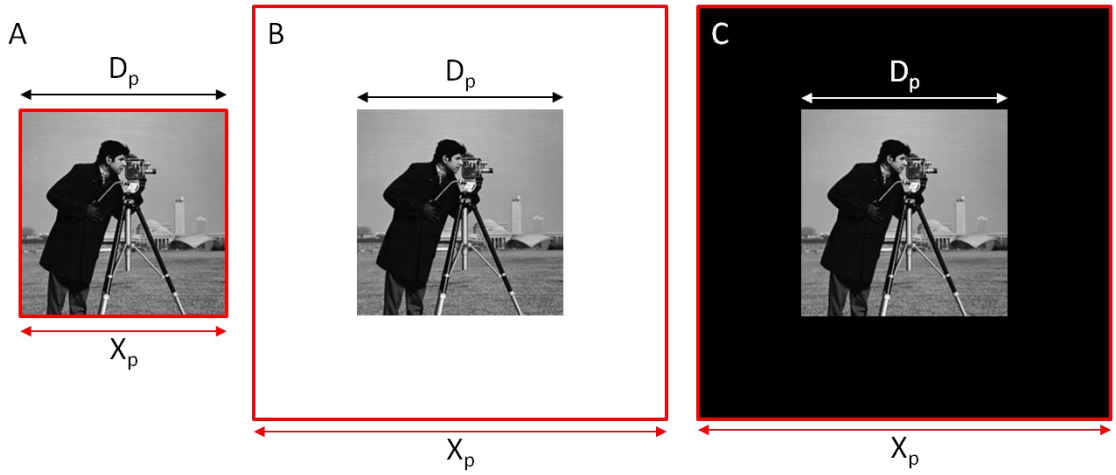

Figure 3.4: A specimen embedded within a Fourier repeat unit cell. a) The beam width matches the Nyquist limit of the complex values in reciprocal-space. b) The beam width matches the Nyquist limit of the intensity values in reciprocal-space but the object is isolated to half of that. c) The beam is half of the width of that required to match the Nyquist limit of the intensity values in reciprocal-space.

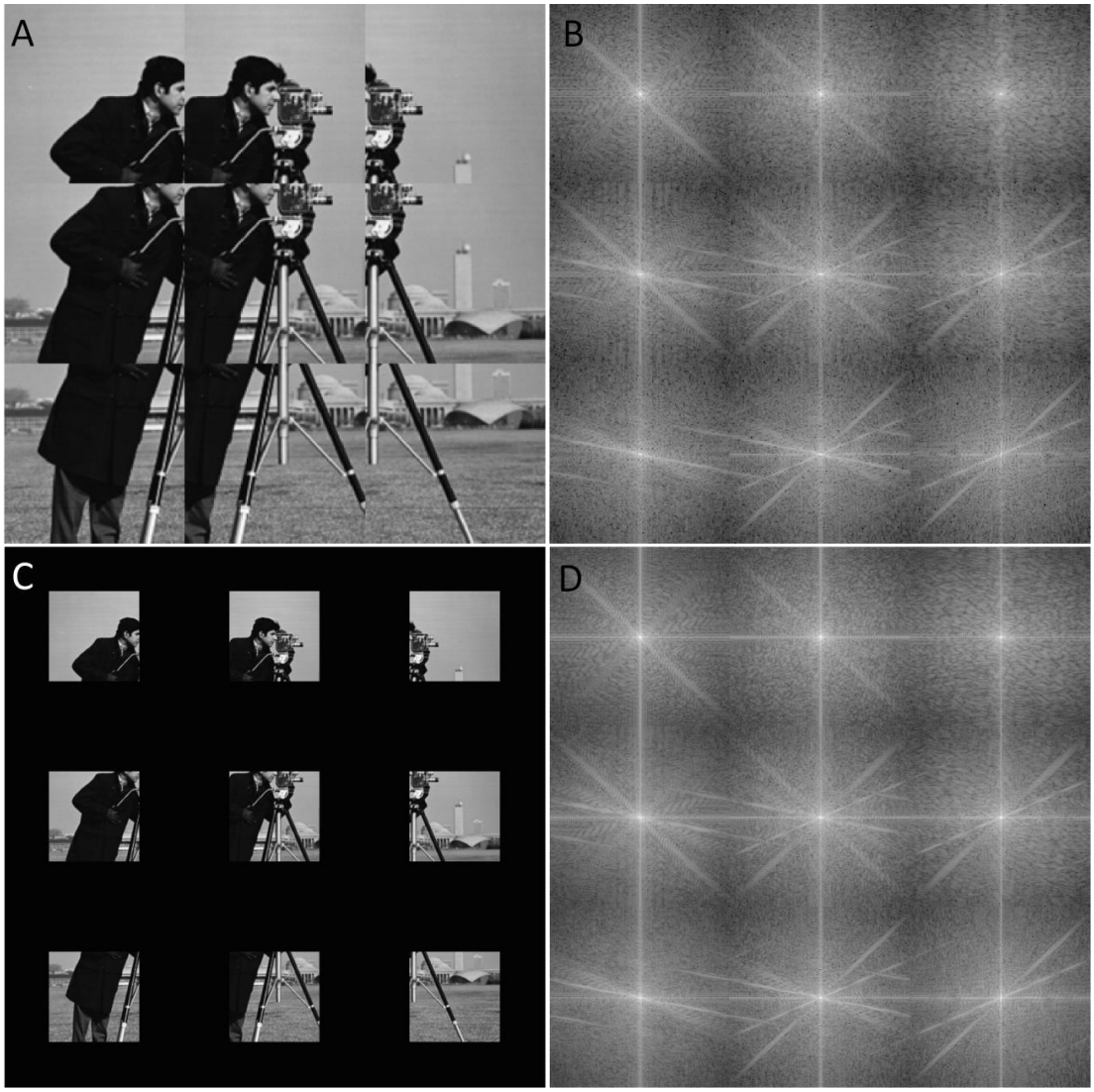

Figure 3.5: a,b) Example ptychographic datasets in both real and reciprocal-space, respectively, under the conditions of Figure 3.4a (a,b). c,d) Example ptychographic datasets in both real and reciprocal-space, respectively, under the conditions of Figure 3.4c (c,d). The coordinates and sampling pitches within the four dimensional dataset are shown in Figure 3.6.

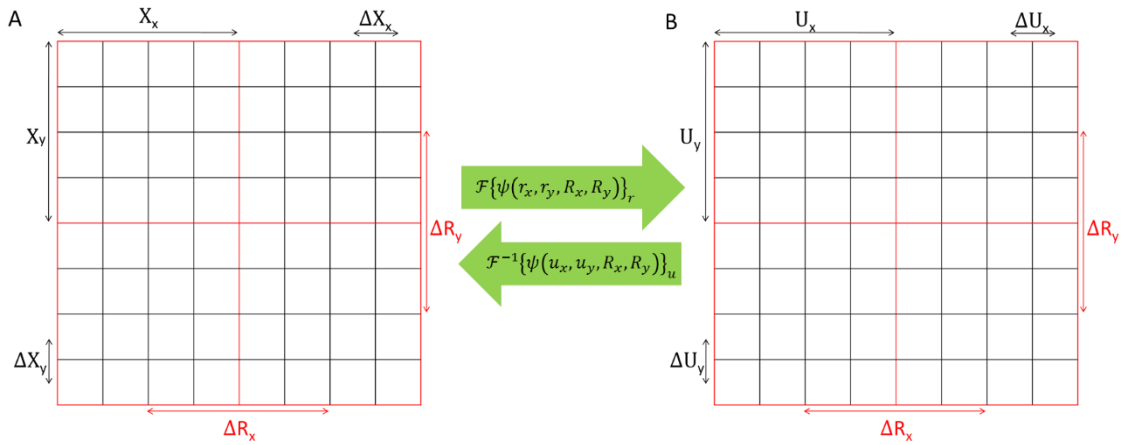

Figure 3.6: The sampling relationship between the real and reciprocal-space domains of a ptychographic dataset. a) Real-space. b) Reciprocal-space. Note that the scan dimensions, R, are unaffected as the Fourier transform is applied along only the spatial dimensions.

It is much easier to follow the ptychographic sampling from the overlap in real-space than in reciprocal-space. As each exposure in Figure 3.5d meets the single-shot condition, each separate object segment (shown in Figure 3.5c) may be considered as a reconstructed single-shot exposure. The nine single exposures in Figure 3.7a (sampled at the single-shot limit), when combined with the knowledge of their relative shifts (Figure 3.7b), create a final reconstruction (Figure 3.7c). The final field of view has been extended above that of the local illumination function, but not by the maximum amount of nine times the area of D_p (the beam has been scanned across nine positions). Some of the information was instead overlapped across real-space. This redundancy can be represented in real-space as the amount of zeroes outside of the conventional sampling condition, shown as a green border in Figure 3.7d. The green area represents the amount of information within the dataset that is recorded over that required to solve for the complex object function. It is this region that recent algorithms have begun to exploit, solving for experimental uncertainties that arise from the physical setup.

Figure 3.8 shows a representation of the total amount of measurement points from the dataset in real-space, T, with the local illumination function, D_p, nested in the centre. The sampling pitch of the physical detector is represented in real-space, X_p, and surrounds the local illumination function. The ratio between X_p and D_p gives the sampling factor for each single exposure. The synthetic

illumination function, D_s, is also shown and is surrounded by the real-space representation of the synthetic detector pixel-pitch, X_s. The ratio between X_s and D_s then gives the sampling factor of the full ptychographic dataset.

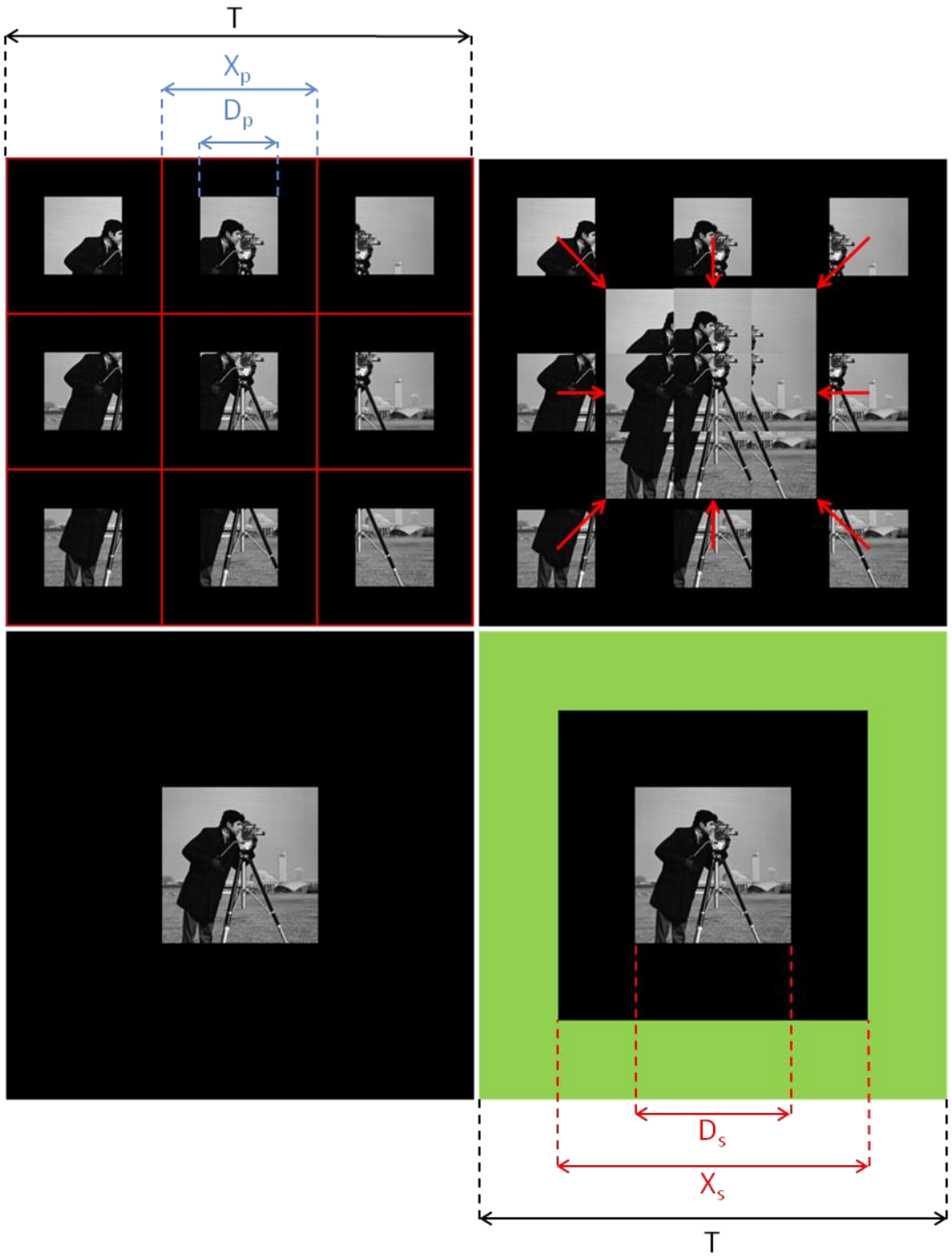

Figure 3.7: Ptychographic oversampling represented in real-space. The physical illumination function (D_p) and the physical detector's real-space Fourier repeat cell (X_p), the synthetic illumination function (D_s) and the synthetic detector's real-space Fourier repeat cell (X_s), the total number of measurements represented in real-space (T).

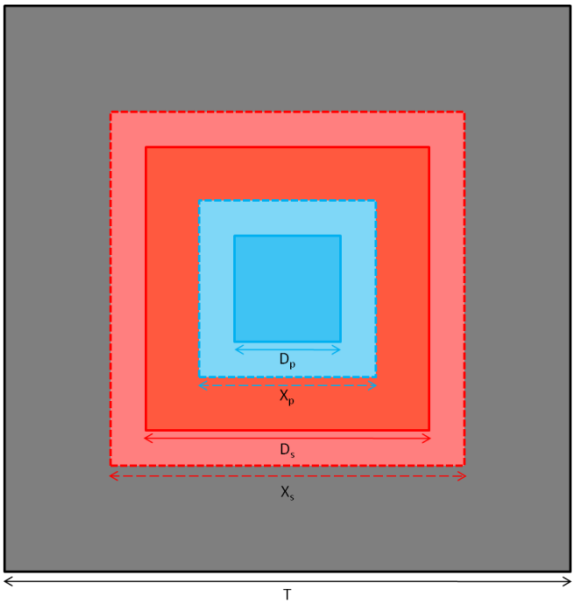

Figure 3.8: The elements of Figure 3.7 expressed are within each other so that their relationship is more obvious. The physical illumination function (D_p) and the physical detector's real-space Fourier repeat cell (X_p), the synthetic illumination function (D_s) and the synthetic detector's real-space Fourier repeat cell (X_s), the total number of measurements represented in real-space (T).

D_s represents the number of complex elements which are recovered in real-space, while T is the number of reciprocal-space intensity measurements represented in real-space. For the single-shot case, T is equal to X_p. As with single-shot CDI, the area within D_s may only be solved for by isolating it from the rest of T.

The size of the synthetic illumination function is given by,

$$D_{s(x|y)} = D_{p(x|y)} + \Delta R_{(x|y)}\left(N_{(x|y)} - 1\right), \tag{3.3}$$

while the size of the real-space unit cell produced by the synthetic detector is given by,

$$X_{s(x|y)} = X_{p(x|y)} + \Delta R_{(x|y)}\left(N_{(x|y)} - 1\right). \tag{3.4}$$

The total number of measurements (knowns) within a dataset is given by T,

$$T_{(x|y)} = N_{(x|y)} X_{p(x|y)}. \tag{3.5}$$

The total number of illuminated points in the object (unknowns) is given by the size of the synthetic illumination from equation 3.3. A sampling factor can be created from the ratio between the known measurements and unknown object elements,

$$\hat{S}_{(x|y)} = \frac{N_{(x|y)} X_{p(x|y)}}{2\, D_{s(x|y)}}, \tag{3.6}$$

where the factor of two in the denominator is due to the object elements being complex while the measured detector elements are real (intensities).

Substituting equations 3.1a and 3.3 into equation 3.6 produces a more practical ptychographic sampling condition,

$$\hat{S}_{(x|y)} = \frac{1}{2\,\Delta U_{\mathrm{p}(x|y)}\left[D_{p(x|y)}\mathrm{N}_{(x|y)}^{-1} + \Delta R_{(x|y)}\left(1 - \mathrm{N}_{(x|y)}^{-1}\right)\right]}. \tag{3.7}$$

This sampling condition has two terms in the denominator, one represents the conventional sampling and the other represents ptychographic sampling. Depending on the size of N, or whether the specimen is periodic and the scan may be considered cyclic, the complete sampling condition reaches two limits. When only one real-space scan position is used (single-shot) then,

$$N_{(x|y)} = 1\text{:}\quad \hat{S}_{(x|y)} = \frac{1}{2\, D_{p(x|y)} \Delta U_{\mathrm{p}(x|y)}}. \tag{3.8}$$

When the scan tends towards infinity, or the scan may be considered cyclic, then,

$$N_{(x|y)} \to \infty\text{:}\quad \hat{S}_{(x|y)} = \frac{1}{2\,\Delta R_{(x|y)} \Delta U_{\mathrm{p}(x|y)}}, \tag{3.9}$$

where $(x|y)$ denotes that the condition applies separately to orthogonal spatial dimensions.

Note that as the number of exposures moves from the single-shot ($N = 1$) regime to the highly ptychographic regime ($N \to \infty$), the real-space term moves from D_p to ΔR. Single shot CDI is based on a convolution in reciprocal-space and ptychography adds a real-space convolution. The phrase

'highly ptychographic' describes a setup where there are very many exposures from different regions of the specimen as in such a case much of the information comes from the real-space convolution. As the number of scan positions approaches infinity, the isolating probe function from the single-shot case is effectively shifted to the size of the scan step, ΔR. In such a situation the size of the illuminating beam is no longer important.

3.3 The Four-Dimensional Interference Kernel

In a ptychographic dataset, the measured modulus must be phased with respect to every other measured modulus, which is also the case with single-shot CDI. In ptychography, however, there is a four-dimensional measurement space (as opposed to two dimensional in single-shot CDI) and the measurement points may be phased across either reciprocal-space, U, real-space, R, or indeed both. This allows for there to be a pixel-pitch in reciprocal-space (at the detector plane) that is larger than the width of the illumination in that plane (if the diffraction peaks in Figure 2.10a represent pixels then the discs in Figure 2.10b would no longer overlap). The recorded intensities may still be phased so long as the global illumination overlaps suitably in real-space (at the specimen plane). Under such a configuration the measured intensities are coupled to others through their mutual object elements in real-space.

Ptychography has to date been viewed as an extension to the single-shot CDI method, offering redundancy and robustness into the recorded data. Ptychography is however more than simply an extension to the single-shot case. Single-shot CDI is a special case of the more general ptychographic imaging framework, where N is equal to one and the interference kernel (represented by the global illumination function and the convolution operator) acts solely in reciprocal-space. Pushing ptychography to the limit in the opposite direction, where the only convolution operation occurs in real-space (by the stepping of the illumination across the specimen in an overlapping fashion), reveals the truly four dimensional nature of the ptychographic imaging technique.

3.3.1 The Real-Space Convolution

In order to demonstrate the real-space aspect of the ptychographic imaging system, that is a dataset with no convolution between the object's Fourier components in reciprocal-space, a simulated dataset is generated with no localisation of the illumination function (further than the computational constraints of the array size). This is similar in form to that shown in Figure 3.5 (a and b). The dataset was generated with a sampling factor, $\hat{S}$, of 2.8 and the subsequent ePIE reconstruction is shown in Figure 3.9.

Figure 3.9: ePIE reconstructions of a dataset with no reciprocal-space interference. a) The modulus of the illumination. b) The phase of the object. c) The modulus of a typical diffraction pattern estimate (log scale).

Diffractive imaging is built upon the basis that the phase problem is unlocked by the interference of object elements in reciprocal-space (as in Figure 2.10). The above result demonstrates that ptychography does not simply rely on the same principles as single-shot CDI, with the real-space scan producing an over-redundant dataset, but instead introduces a completely independent sampling mechanism - the real-space interference kernel.

3.3.2 Sparse Detector Pixel Simulations

The sampling condition defined in equation 3.7 suggests that the reciprocal-space sampling pitch may be relaxed with respect to the width of the probe function in reciprocal-space so long as the ptychographic sampling factor, $\hat{S}$, remains greater than 1. That situation is now explored for the case of a sparse detector - one with a large pixel-pitch but small pixel-size.

A simulated dataset with a sampling factor, $\hat{S}$, of 1 is now processed based on the principle that when as few as four detector pixels in reciprocal-space (two in each orthogonal direction) are sampled on a sufficiently fine grid in real-space, the resulting dataset may still be adequate for a ptychographic reconstruction. The limit of four pixels relies on information being encoded on a sub-pixel level in real-space and while the reconstruction is able to show details much finer than the width of the illumination, any imperfections within the reconstruction algorithm are amplified in this reconstruction.

In order to process such data computationally, the pixels must be embedded into a virtual detector of many fine pixels. The pixel-pitch of the virtual detector is such that the illumination function in real-space is not aliased. The reconstruction algorithm is then altered so that only the measured pixels are used to constrain the estimated exit-wave at the detector plane during the reciprocal-space constraint step, the estimates corresponding to the virtual pixels maintain the same values and the result is projected back to real-space. Other than this alteration to the reciprocal-space update step, the algorithm functions as normal.

The four pixel dataset has produced a reconstruction with a resolution many times greater than the diameter of the probe function. Although the quality is degraded in comparison to more conventional setups it is still an amazing result given that only four pixels are required. In order to further examine the reconstruction process around the sampling limit, a similar dataset is simulated with sixteen pixels (4x4). The pixel-pitch in reciprocal-space, ΔU_{p}, is halved and as all other aspects remain unchanged, the sampling factor is doubled to two. The result of the reconstruction from this dataset is shown in Figure 3.11.

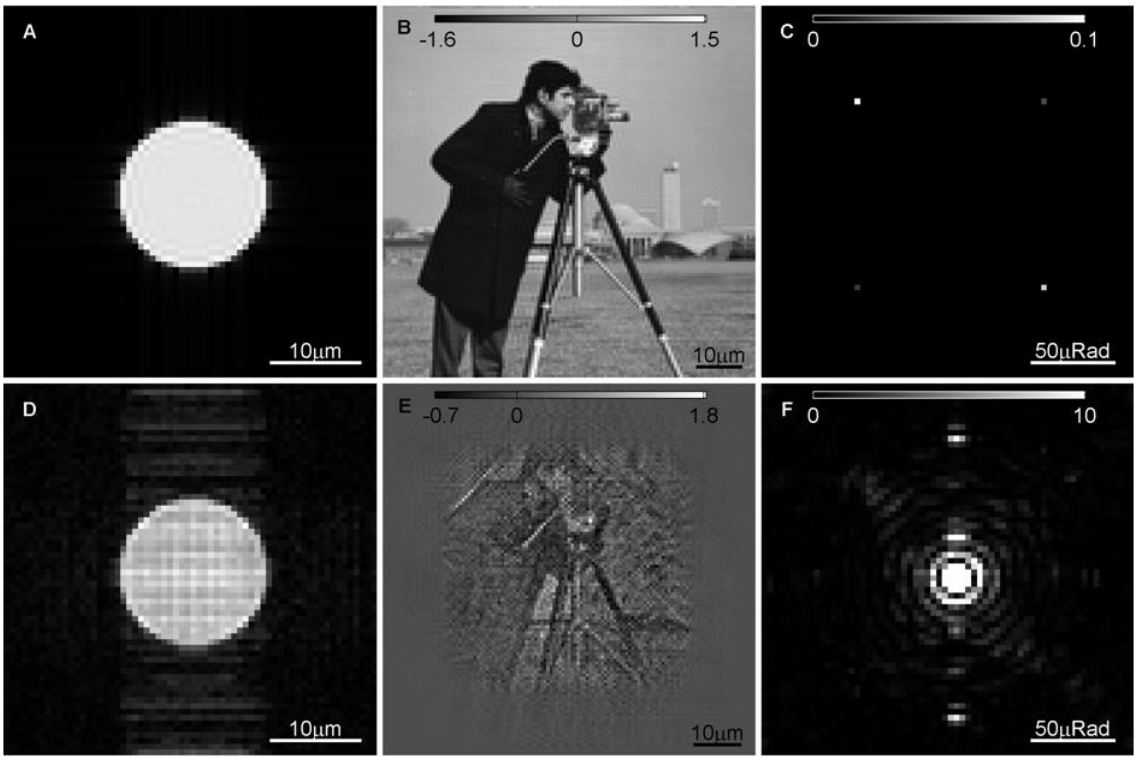

Figure 3.10: fPIE reconstruction of sparsely sampled data with $\hat{S}$=1. a) Original probe modulus. b) Original phase image. c) Input diffraction pattern with 4 sparse pixels. d) Reconstructed probe modulus. e) Reconstructed phase image. f) Reconstructed diffraction pattern with 1024 reconstructed pixels.

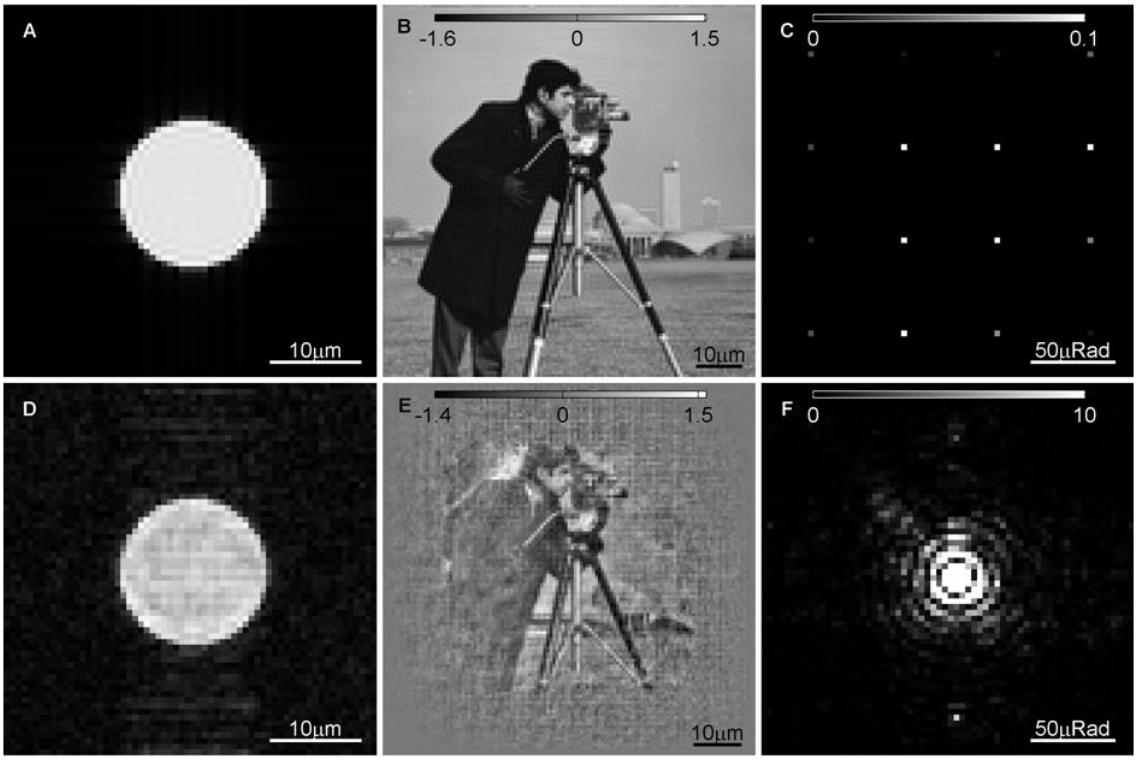

Figure 3.11: fPIE reconstruction of sparsely sampled data with $\hat{S}$=2. a) Original probe modulus b) Original phase image with 16 sparse pixels. c) Input diffraction pattern. d) Reconstructed probe modulus e) Reconstructed phase image. f) Reconstructed diffraction pattern with 1024 reconstructed pixels.

Although improved, the artefacts that exist within the reconstruction suggest that the current algorithm is still not sufficient to extract all of the information contained within the dataset. Reconstructing diffraction limited, fully complex, images of extended specimens from sets of diffraction patterns which contain only 4 and 16 physical pixels is still a breakthrough in diffractive imaging. Such a result would have previously been seen as impossible.

3.4 Dose Fractionation

Both the generation of a synthetic illumination function and the sampling factor are intrinsically linked with the issue of dose fractionation. The question here is how splitting a large synthetic illumination function (with total flux N) into many (M) physical illumination functions (with flux per exposure of N/M) affects the dataset and hence the reconstruction.

The principle of dose fractionation would suggest that so long as the total irradiance per object element and exposure time is maintained then there should be no information loss from partitioning the flux across several exposures as the object is scanned. Although this is sound in principle, in practice the algorithm will not automatically handle the low counting statistics of each diffraction pattern favourably. The current algorithm is built from single-shot principles and, although generally acts as a good noise filter in the diffraction plane, the manner in which the noisy diffraction patterns are processed in both real and reciprocal-space are sub optimal. Problems with the current PIE algorithm do occur when the total radiation through the specimen is fractionated such that each individual diffraction pattern becomes heavily affected by Poisson statistics.

3.4.1 Illumination Function Update

When the PIE algorithm was extended to also update the illumination function alongside the object (ePIE), the update function for the object was replicated (with the object and specimen functions switched) to create the update function for the illumination (Maiden and Rodenburg, 2009). For reasonably high levels of radiation per diffraction pattern this works well. However, as the levels of dose fractionation are increased, the current algorithm begins to break down. There has been much

discussion about what the optimal update function should be but for the purposes of this work a simple modification has been made that overcomes the issue. The new $\mathbb{U}_P$ for the update equation shown in equation 2.56b is,

$$\mathbb{U}_P = \alpha_p \frac{O_L^*}{|O_L|_{max}}, \tag{3.10}$$

where O_L is the local object from the current scan position and O_L^* is the complex conjugate. Notice that the denominator is now to the power of one where previously this has been to the power of two. It is possible that the required change is linked to the fact that the probability of transmission through an object is given by that objects modulus where the probability of arrival of a photon at a position of the object is given by the modulus of the wave-field squared. As mentioned above, this requires a more extensive study.

3.4.2 Reciprocal-Space Update

As well as improving the real-space update step, in order that the algorithm may come to a globally consistent result whilst constantly relying on individually noisy diffraction patterns, the reciprocal-space update step must also be modified. Again, the current update step is sufficient when the counting statistics are good, but when they are not, no single diffraction pattern should be fully constraining the estimate at a position. Remember that each such estimate has come from a region in real-space that has more flux through it than the individual diffraction pattern. By reducing the weighting factor in the reciprocal-space update step, which will be referred to as the alpha parameter, to less than one, it is possible to allow the noisy information from overlapping diffraction patterns to blend together. This process effectively prevents any single diffraction pattern from altering the global solution too far towards an incorrect result and can be treated as a negative feedback factor.

The update step from equation 2.45 may be rewritten in a form similar to the real-space update equations such that,

$$\Psi'(\boldsymbol{u},\boldsymbol{R}) = \Psi(\boldsymbol{u},\boldsymbol{R}) + \alpha_\Psi \beta_\Psi \big([\gamma(\boldsymbol{u},\boldsymbol{R}) \cdot \Psi(\boldsymbol{u},\boldsymbol{R})] - \Psi(\boldsymbol{u},\boldsymbol{R}) \big) , \tag{3.11a}$$

$$\gamma(\boldsymbol{u},\boldsymbol{R}) = \sqrt{\frac{I(\boldsymbol{u},\boldsymbol{R})^m}{|\Psi(\boldsymbol{u},\boldsymbol{R})|^2}} , \tag{3.11b}$$

where α_Ψ and β_Ψ represent the update steps across all pixels equally and on a pixel by pixel basis, respectively.

When the diffraction patterns are noisy the initial updates should be strong, with alpha set to one, as the information is combined by the real-space update it becomes favourable to reduce the value of alpha. As the desirable level of difference between the estimated and measured diffraction patterns at the end of the reconstruction is zero, it fits that the alpha should take a trajectory from one to zero throughout the reconstruction process. In so doing, the consistent information is able to build up as inconsitancies decay away. A similar Fourier weighting strategy has been employed in the single-shot CDI case in order to suppress unwanted sidelobes caused by the truncation of the diffraction pattern in the recording process (Guizar-Sicairos and Fienup, 2008a).

The processing of low dose datasets has been discussed in terms of a new update function based on Poisson statistics within a parallel algorithm (Godard et al., 2012). Although a comparison has not yet been made, this should be the subject of future work.

3.4.3 Real-Space Error Metrics

In order to understand more completely how the algorithm is behaving during the reconstruction process it is useful to formulate a form of error metric in real-space as well as in reciprocal-space (see equation 2.53). As no absolute real-space measurements are available in a reconstruction of experimental ptychographic data, the next-best error metric that can be formed is of the differential of each reconstruction element across iterations. Equations 3.12(a-c) show how three such error metrics are formed for the object, probe, and exit-wave at each iteration.

$$O_{error} = \sqrt{\frac{\sum_{\boldsymbol{r}} \sum_{\boldsymbol{R}} [|O'(\boldsymbol{r},\boldsymbol{R})| - |O(\boldsymbol{r},\boldsymbol{R})|]^2}{N_R N_r}} \quad 3.12a$$

$$P_{error} = \sqrt{\frac{\sum_{\boldsymbol{r}} \sum_{\boldsymbol{R}} [|P'(\boldsymbol{r},\boldsymbol{R})| - |P(\boldsymbol{r},\boldsymbol{R})|]^2}{N_R N_r}} \quad 3.12b$$

$$\psi_{error} = \sqrt{\frac{\sum_{\boldsymbol{r}} \sum_{\boldsymbol{R}} [|\psi'(\boldsymbol{r},\boldsymbol{R})| - |\psi(\boldsymbol{r},\boldsymbol{R})|]^2}{N_R N_r}} \quad 3.12c$$

3.4.4 Low Dose Simulations

The principles set out above are now tested through simulated diffraction patterns. The behaviour of the current and new algorithm(s) is examined with error metrics in the form of equations 3.12 as well as the usual reciprocal-space error of equation 2.53. All of the datasets have a nominal total of 10^6 counts and Figure 3.12 shows the effects of such a level of radiation dosage to an otherwise ideal single exposure diffractive imaging setup. A pure phase object is used here in order to ensure that the total flux is preserved across the different setups to be explored. The low dose version of the object under otherwise ideal conditions (no phase problem) gives a good representation of the original object. This may be used as a guide to the quality of reconstructions under varying levels of dose fractionation.

The first two datasets shown are simulated with a slightly propagated aperture scanned to 4x4 and 16x16 real-space positions, producing sampling factors of 1.3 and 4.6, respectively. Both sets of diffraction patterns are recorded on an array of 256x256 pixels with a total flux throughout the whole dataset of 10^6 counts. The result is two datasets containing an average of 62500 and 3907 counts per diffraction pattern respectively. Both datasets contain the same number of counts through the same real-space field of view but those counts are fractionated differently in each, increasing the sampling factor whilst preserving total irradiance reduces the counts per diffraction

pattern. The illumination function and a typical diffraction pattern from each dataset is shown in Figure 3.13.

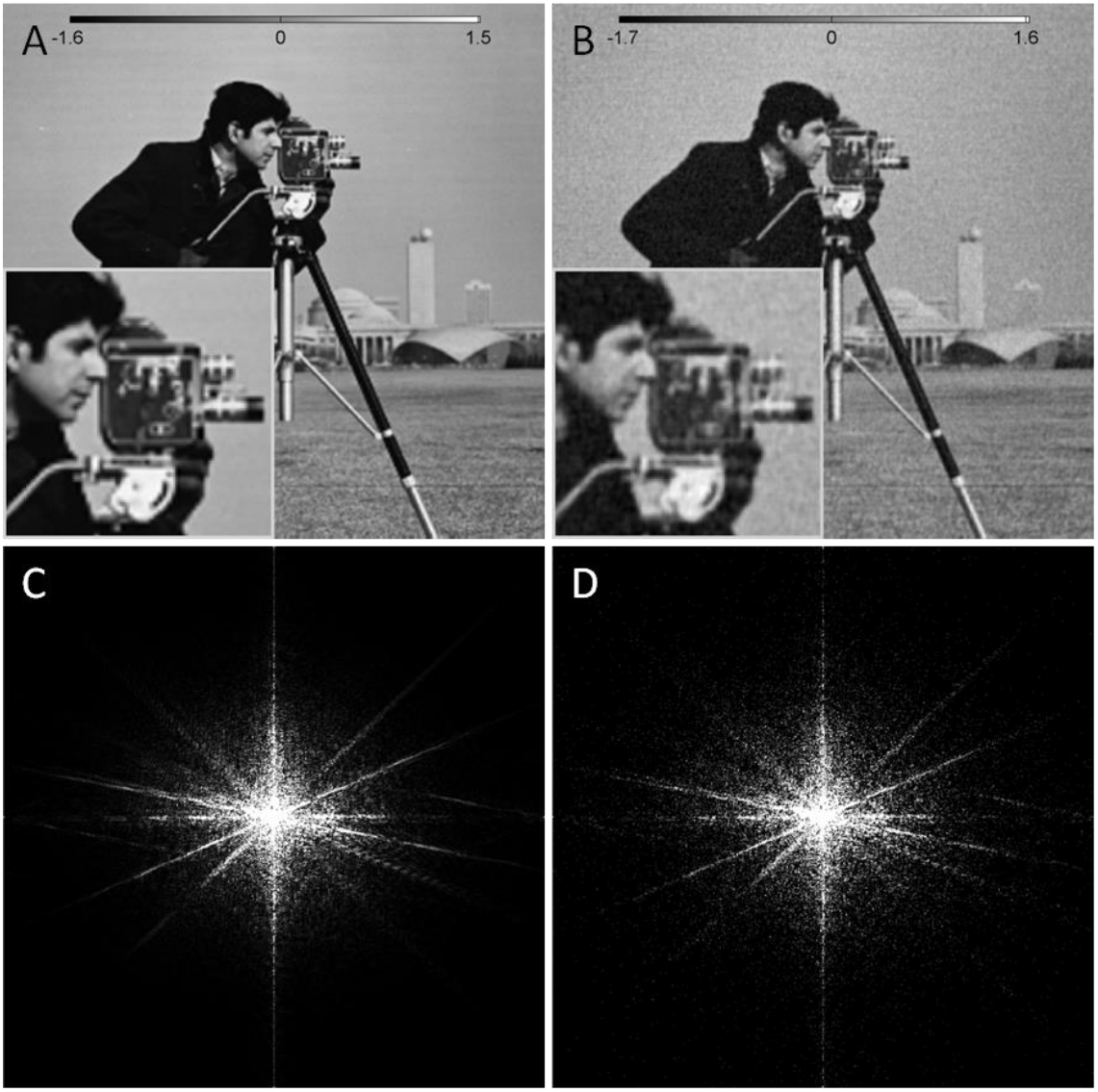

Figure 3.12: a,c) A phase object with a modulus of unity and its diffraction pattern, respectively, without Poisson noise present. d) The same diffraction from (c) is set to 10^6 counts and Poisson noise is added to produce. b) The inverse Fourier transform of (d) is taken to produce a reconstruction that is ideal other than the effects of counting statistics (b).

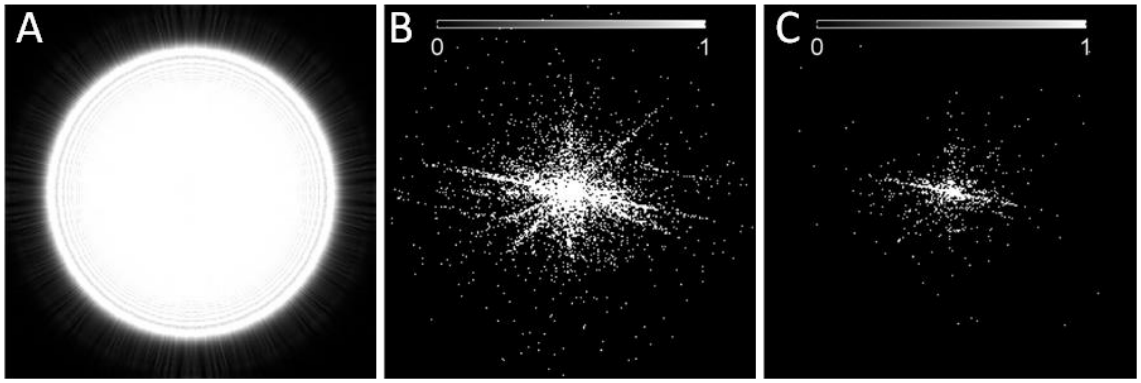

Figure 3.13: Inputs for the aperture datasets. a) Modulus of the illumination function. B) Typical diffraction pattern from the dataset with $\hat{S}$= 1.3. c) Typical diffraction pattern from the dataset with $\hat{S}$= 4.6.

Each dataset is processed through four different reconstruction algorithms in order to demonstrate the properties and effectiveness of each. The first algorithm is the conventional ePIE and the second is ePIE with the new probe projection shown in equation 3.10. The third and fourth reconstructions are a repeat of the first and second with the addition of the reciprocal-space alpha decay procedure as in equation 3.11.

Figure 3.14 shows the outputs from the dataset with a sampling factor of 1.3 and a propagated aperture illumination without diffuser (a typical diffraction pattern for which is shown in Figure 3.13b) for the four reconstruction algorithms. There appears to be little difference between the four algorithms in the reconstructed object for the first dataset. The new probe update function does seem to remove a vertical artefact from the illumination (compare columns 1 and 3 with 2 and 4) and the reciprocal-space decay has produced a lower level of noise in the estimated diffraction patterns (compare columns 1 and 2 with 3 and 4).

In order to more completely understand the inner workings of the algorithm, error plots have been created to show the relative progression of the probe, object, and exit-wave in real-space (in accordance with equations 3.12) along with the absolute error in reciprocal-space (in accordance with equation 2.53). Figure 3.15 shows each of these error metrics for each reconstruction algorithm for the first dataset as a function of iteration number.

It can be seen from Figure 3.15 that for ePIE (line plots A) the diffraction pattern error begins to increase throughout the reconstruction and it can also be seen that this effect correlates strongly with the increase in the error of the probe function. When the new probe update function is employed (line plots B) it can be seen that the diffraction pattern is much more stable and does not diverge. In this case the probe error remains flat and is also stable. Line plots C and D represent the same real-space updates as A and B with the addition of the reciprocal-space decay. Both of these seem to perform well and it can be seen from the probe error that the introduction of the reciprocal-space decay to the original ePIE algorithm prevents the probe from diverging at about 50 iterations.

Figure 3.16 shows the reconstructions from the same algorithms, executed under the same conditions, for the second dataset. The dataset is the same as that in Figure 3.14 except with an increased sampling condition of 4.6 (a typical diffraction pattern is shown in Figure 3.13c). The conventional ePIE algorithm clearly breaks down, although the reconstruction is saved somewhat from collapsing with the introduction of the reciprocal-space alpha decay. As the initial estimate of the illumination is correct and the object estimate is reasonable (free space) the reconstruction after a single iteration does show a rough image, it is the instability of the algorithm which then causes the reconstruction to drastically diverge (see Figure 3.16a).

Although the outputs remain severely affected by the reduction of counts per diffraction pattern, the new probe update function is at least able to reconstruct the data in a stable manner. Any issues arising from the low dose measurements are subsequently relieved entirely with the introduction of the reciprocal-space alpha decay (see Figure 3.16d). Not only does the new algorithm not collapse under such conditions, the reconstruction is actually improved in every area over and above that shown in Figure 3.14. It is therefore advantageous, given the correct reconstruction strategy, to partition the total flux through a specimen into many diffraction patterns, reducing the counting statistics required of any single measurement. Showing that increasing the sampling condition yields

higher quality reconstructions for the same total irradiance, is an important result and further experimental tests may lead to improvements in low dose imaging. Figure 3.17 shows the error metrics associated with the reconstructions shown in Figure 3.16.

The impact that low dose diffraction patterns have on the current ePIE algorithm is very clear in the above error metrics. It is evident that the exit-wave and diffraction pattern errors are following the divergence of the probe for the line plots A. Again the introduction of the reciprocal-space alpha decay prevents the algorithm from completely collapsing at about 75 iterations, although the final reconstruction remains meaningless. The new algorithms both have a striking effect on the error metrics, both remain extremely stable and never show signs of divergence. The D plots in particular show how the information is able to come to a more globally consistent solution as all error plots decay towards the end of the reconstruction.

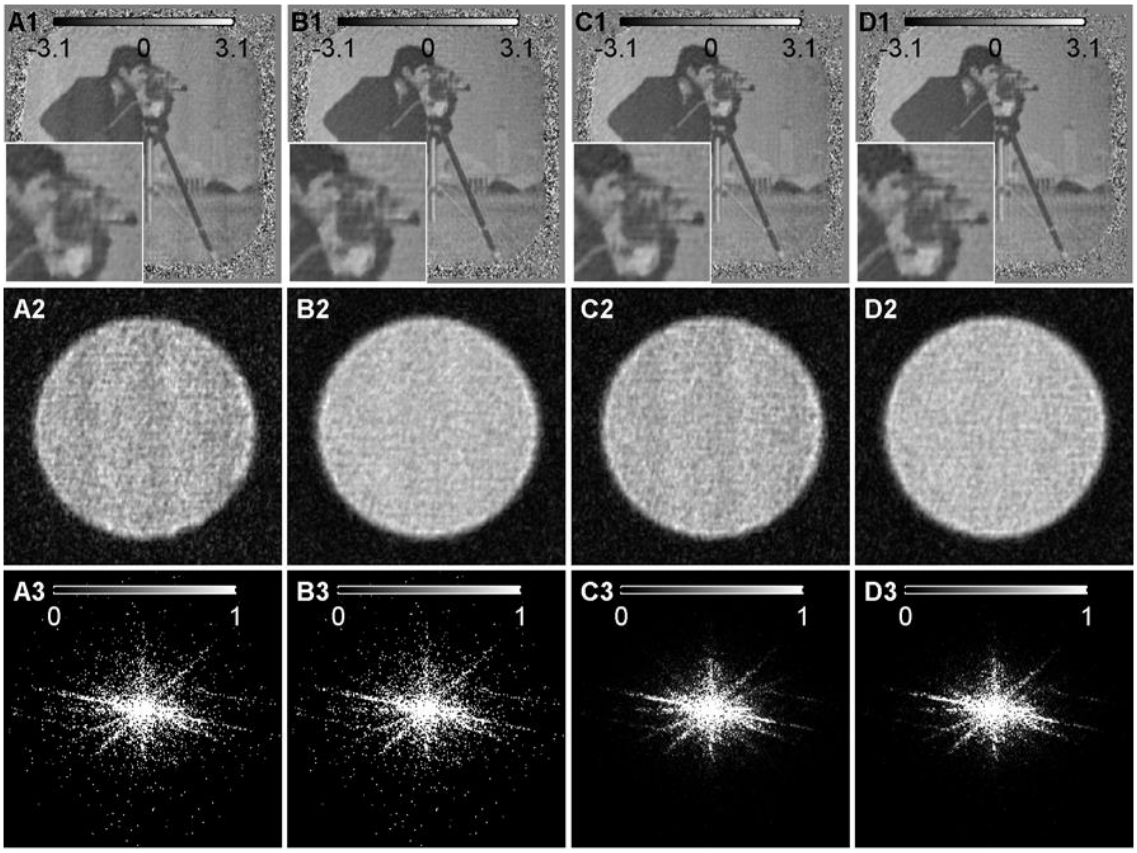

Figure 3.14: Reconstruction outputs from the aperture dataset with a sampling factor of 1.3: original ePIE and the new probe update with alpha constantly 1 (columns 1 and 2 respectively) and the original ePIE and the new probe update with alpha decaying from 1 to 0 (columns 3 and 4 respectively). The top row shows the phase image, the middle row shows the illumination modulus, and the bottom row shows the diffraction patterns intensity.

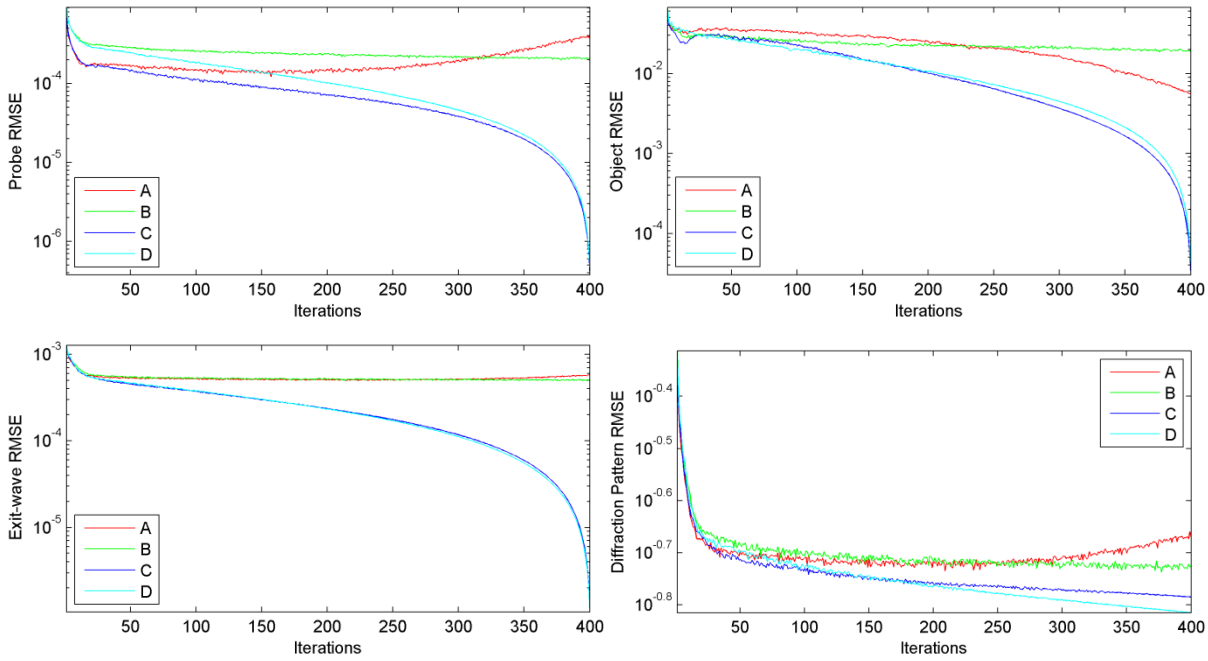

Figure 3.15: RMSE plots (log of RMSE) plots with iteration number. Lines A-D correspond to columns 1-4 in Figure 3.14.

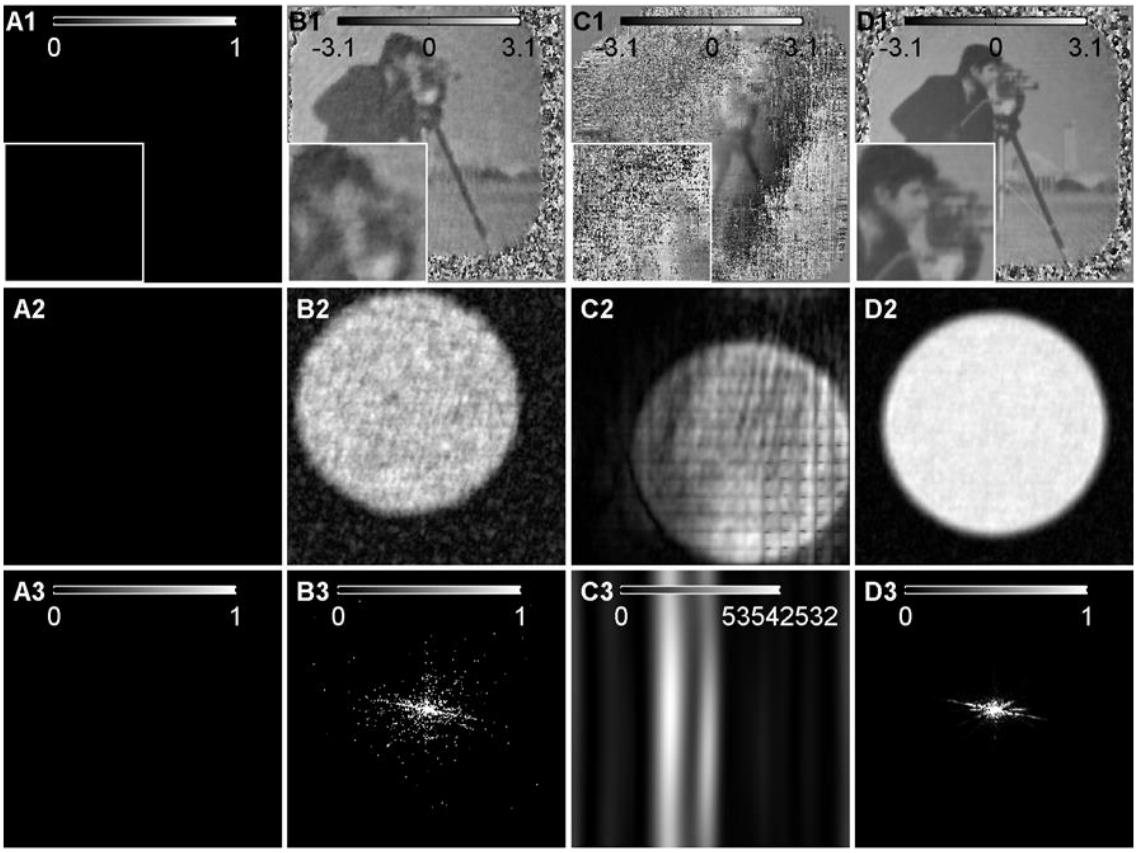

Figure 3.16: Reconstruction outputs from the aperture dataset with a sampling factor of 4.6: original ePIE and the new probe update with alpha constantly 1 (columns 1 and 2 respectively) and the original ePIE and the new probe update with alpha decaying from 1 to 0 (columns 3 and 4 respectively). The top row shows the phase image, the middle row shows the illumination modulus, and the bottom row shows the diffraction patterns intensity.

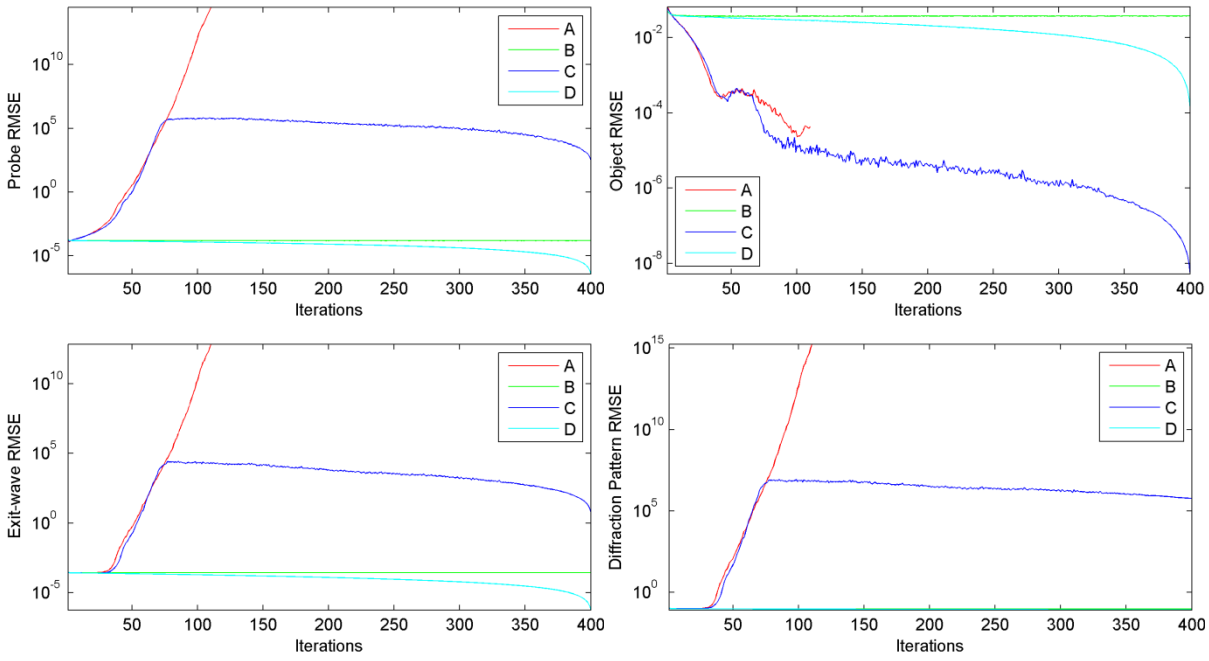

Figure 3.17: RMSE plots (log of RMSE) with iteration number. Lines A-D correspond to columns 1-4 in Figure 3.16.

The second two datasets are a repeat of the first two with a change of illumination function. A spatial 'diffuser' is now introduced into the aperture plane, which is then slightly propagated as previously. The diffuser shifts the effects of Poisson noise in each diffraction pattern from high resolution information to a more equal effect across all spatial frequencies. The inputs for the reconstructions that follow are shown in Figure 3.18.

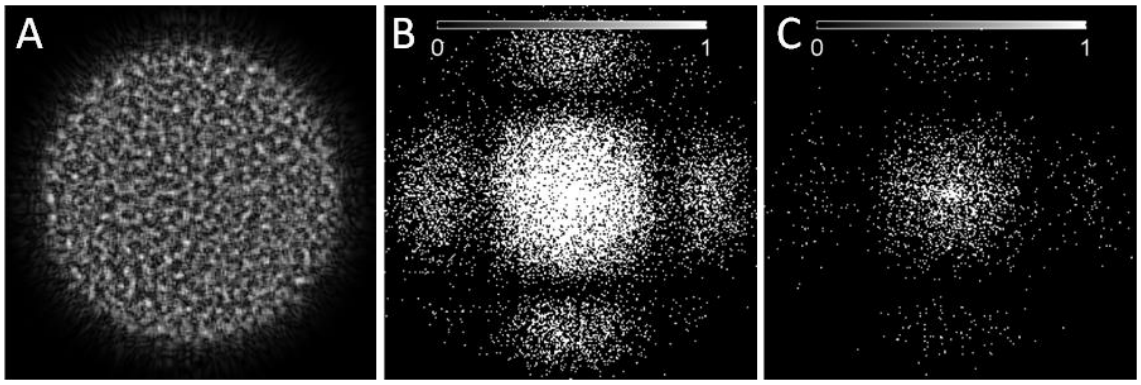

Figure 3.18: The diffuser datasets. a) Modulus of the illumination function. B) Typical diffraction pattern from the dataset with $\hat{S}$= 1.3. c) Typical diffraction pattern from the dataset with $\hat{S}$= 4.6. The structure of the diffraction pattern (side lobes) is formed due to the nature of the simulated diffuser, an array of square regions with random phase fluctuations.

The addition of a diffuser at the aperture plane has added some structure to the illumination function in real-space but the main effect can be seen in the diffraction patterns, which are in reciprocal-space. The detector is now illuminated much more evenly and how this affects the final dataset and in particular the reconstruction process is largely unknown. Some work has suggested that spreading the illumination function in reciprocal-space improves the signal-to-noise ratio (Guizar-Sicairos et al., 2012), a principle which is tested here with very low exposure diffraction patterns; any improvements should become evident.

Figure 3.19 shows the reconstruction outputs, as for the previous reconstructions for the diffuser dataset, with a sampling factor of 1.3 (a typical diffraction pattern for which is shown in Figure 3.18b). As with the previous dataset with a sampling factor of 1.3 (see Figure 3.14), there is little difference between the outputs of the reconstruction algorithms. The addition of the reciprocal-space alpha decay has reduced the noise level in the estimated diffraction patterns (compare columns 1 and 2 to 3 and 4). The structured illumination does not now show any variation, whether

this is simply hidden from view or a genuine alleviation of an issue is debatable. As with previous reconstructions, the corresponding error plots are shown in Figure 3.20. Unlike the error plots from the first dataset (shown in Figure 3.15), the equivalent plots with the diffuser present do not show any sign of probe divergence. This is good evidence that the diffuser may intrinsically improve the quality of the recorded dataset or at least facilitate a robust reconstruction.

The results with the diffuser show the same basic trend as for the same dataset without the diffuser (see Figure 3.16). The current ePIE algorithm has failed completely and while the introduction of a decaying reciprocal-space alpha prevents total failure it remains unable to produce a reconstruction with any meaning. The A plots (corresponding to Figure 3.21a) end prematurely, this is the point at which the algorithm has completely collapsed. Both of the reconstructions with the new probe update function were able to reconstruct satisfactory object and illumination functions (see columns 2 and 4). As previously, the combination of new probe update and reciprocal-space alpha decay has produced the cleanest results, even when compared with the equivalent from the more conventional dataset shown in Figure 3.19. The B plots follow the same path until the reciprocal-space alpha decay begins to take effect.

The reconstructed object from the diffuser dataset (see Figure 3.21 column 4) seems to contain higher resolution structure than its counterpart recorded without a diffuser (see Figure 3.16 column 4). Although it is not clear that the information content is higher (the diffuser spreads the noise across many spatial frequencies) this does suggest that that information per dose may actually be increased in the finely scanned, low dosage, diffuser setup.

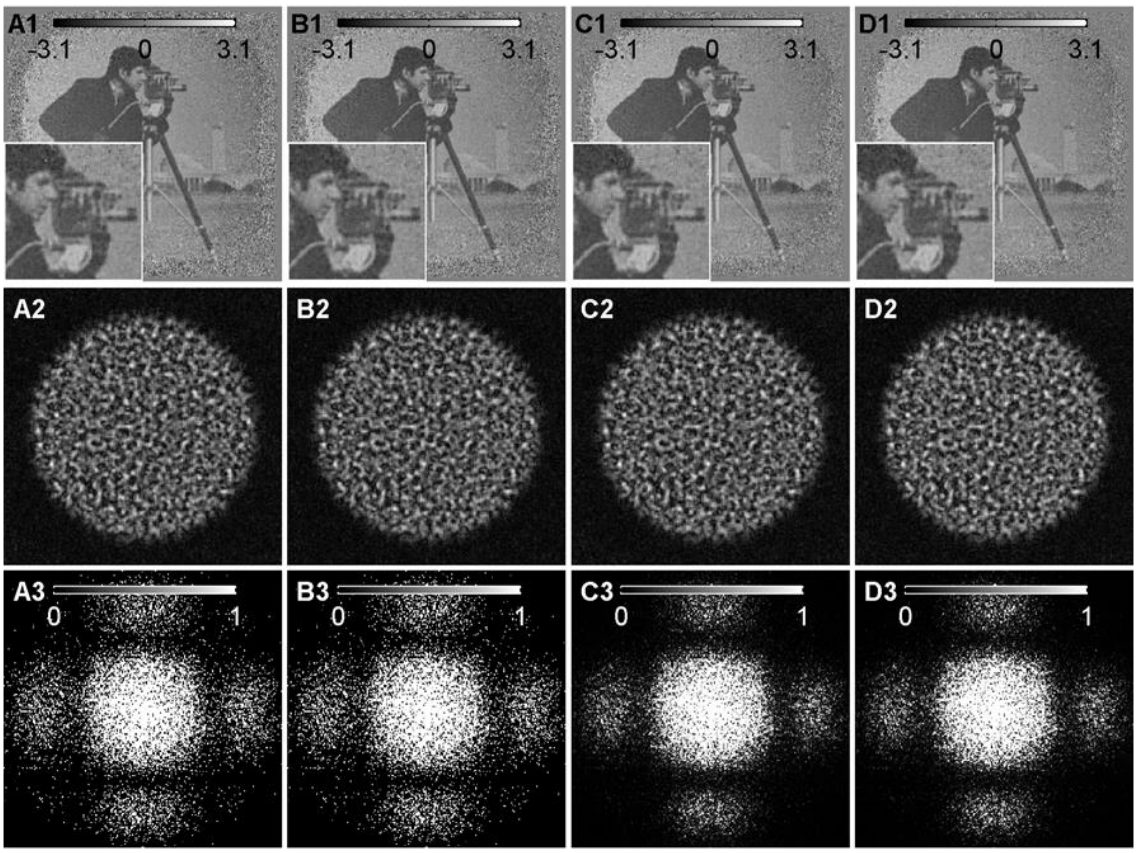

Figure 3.19: Reconstruction outputs from the diffuser dataset with a sampling factor of 1.3: original ePIE and the new probe update with alpha constantly 1 (columns 1 and 2 respectively) and the original ePIE and the new probe update with alpha decaying from 1 to 0 (columns 3 and 4 respectively). The top row shows the phase image, the middle row shows the illumination modulus, and the bottom row shows the diffraction patterns intensity.

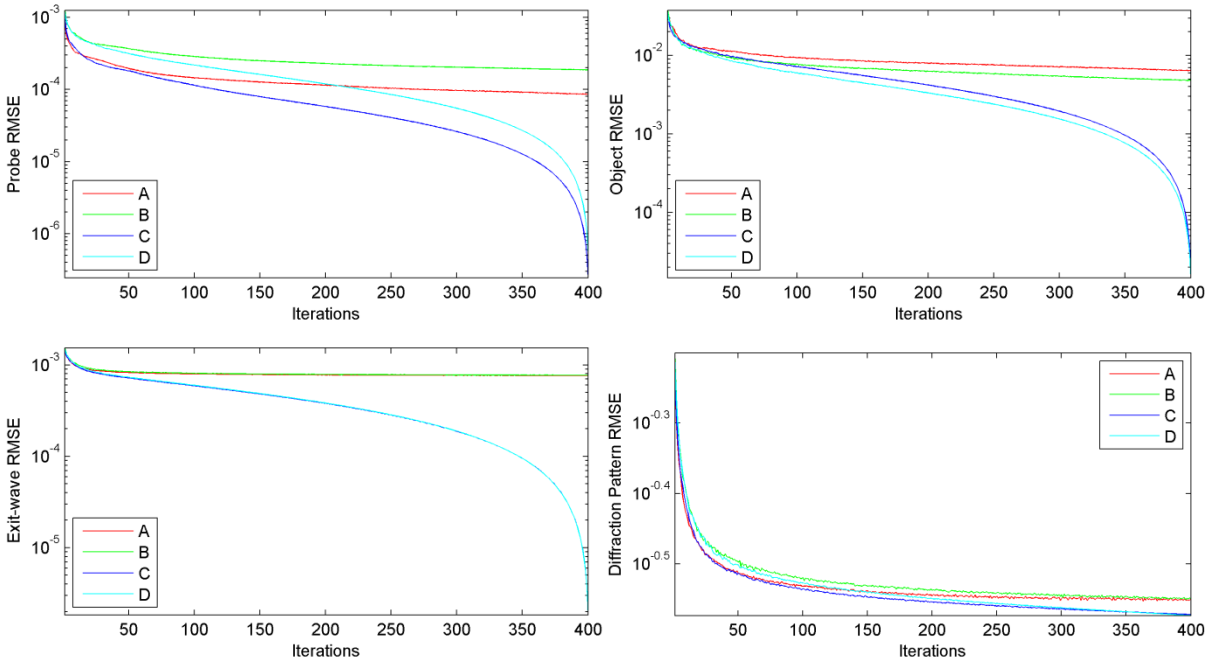

Figure 3.20: RMSE plots (log of RMSE) plots with iteration number. Lines A-D correspond to columns 1-4 in Figure 3.19.

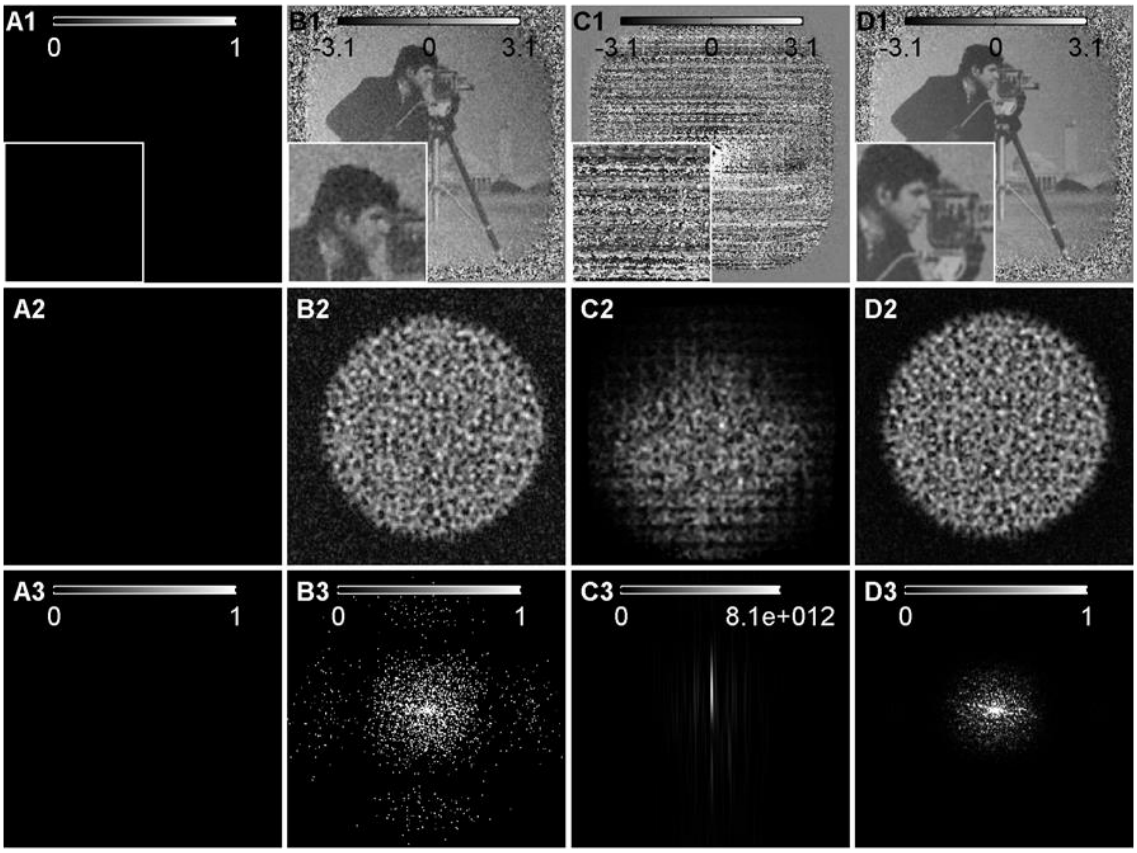

Figure 3.21: Reconstruction outputs from the diffuser dataset with a sampling factor of 4.6: original ePIE and the new probe update with alpha constantly 1 (columns 1 and 2 respectively) and the original ePIE and the new probe update with alpha decaying from 1 to 0 (columns 3 and 4 respectively). The top row shows the phase image, the middle row shows the illumination modulus, and the bottom row shows the diffraction patterns intensity.

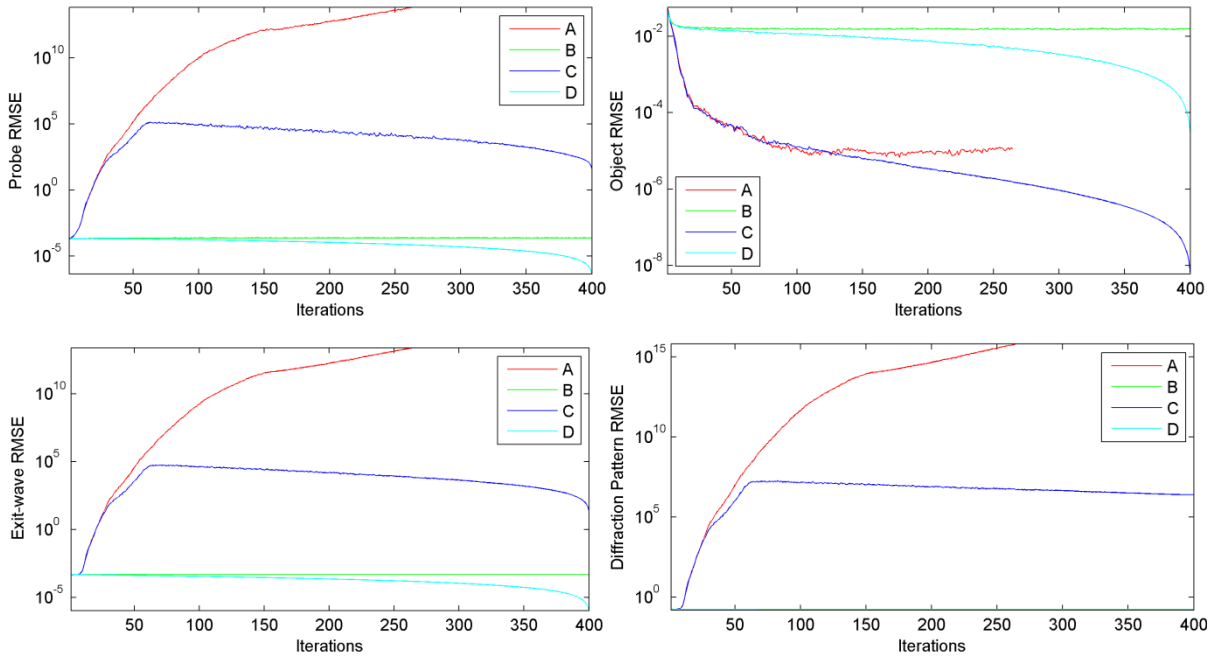

Figure 3.22: RMSE plots (log of RMSE) plots with iteration number. Lines A-D correspond to columns 1-4 in Figure 3.21.

In order that the final reconstructions may be more easily and quantitatively compared, a table of final error metrics is shown (see Table 3.1). The new probe update function coupled with the reciprocal-space alpha decay results in a lower diffraction pattern error metric for all of the datasets when compared with the other three algorithms. These results not only show that the sampling condition is not affected by dose fractionation but also that the new algorithm is the best for all datasets. Further to this, the reconstructed object in Figure 3.21d (finely sampled with both algorithmic improvements) actually appears to be a higher quality than all others. Although it may be that the information content is preserved and so no fundamental gain is being made, this does suggest that partitioning the available dose across both the diffraction patterns and the pixels within those diffraction patterns allows for a more uniform reconstruction, with all regions and all frequencies represented to a similar level. The results presented here will be used in the future development of low dose ptychography with beam sensitive specimens.

Table 3.1: Final RMSE error metrics for all reconstructions from the simulated datasets. The real-space error is the addition of the object, probe, and exit-wave errors. The four different algorithms are separated by the coloured horizontal bands (in accordance with the error plots above) and DP is the column for errors in the plane of the diffraction pattern.

Reconstruction				RMSE error metric				
#	Dataset	Counts per DP	Algorithm	Object	Probe	Exit-wave	Real-space	DP
1	Aperture; S=1.3	62500	ePIE	5.55E-03	4.05E-04	5.69E-04	6.52E-03	2.13E-01
2	Aperture; S=1.3	62500	ePIE + α decay	3.05E-05	3.80E-07	1.15E-06	3.20E-05	1.64E-01
3	Aperture; S=1.3	62500	new probe update	1.92E-02	2.12E-04	5.07E-04	1.99E-02	1.89E-01
4	Aperture; S=1.3	62500	new probe update + α decay	3.94E-05	4.20E-07	1.06E-06	4.08E-05	1.53E-01
5	Aperture; S=4.6	3907	ePIE	NaN	NaN	NaN	0.00E+00	NaN
6	Aperture; S=4.6	3907	ePIE + alpha decay	5.28E-09	3.11E+02	5.90E+00	3.17E+02	6.04E+05
7	Aperture; S=4.6	3907	new probe update	3.73E-02	1.54E-04	2.72E-04	3.77E-02	9.90E-02
8	Aperture; S=4.6	3907	new probe update + α decay	1.37E-04	3.83E-07	5.80E-07	1.38E-04	8.39E-02
9	Diffuser; S=1.3	62500	ePIE	6.45E-03	8.56E-05	7.68E-04	7.31E-03	2.82E-01
10	Diffuser; S=1.3	62500	ePIE + α decay	1.85E-05	2.45E-07	1.85E-06	2.06E-05	2.68E-01
11	Diffuser; S=1.3	62500	new probe update	4.83E-03	1.87E-04	7.72E-04	5.79E-03	2.82E-01
12	Diffuser; S=1.3	62500	new probe update + α decay	1.46E-05	5.20E-07	1.84E-06	1.70E-05	2.67E-01
13	Diffuser; S=4.6	3907	ePIE	NaN	NaN	NaN	0.00E+00	NaN
14	Diffuser; S=4.6	3907	ePIE + α decay	6.06E-09	4.06E+01	2.47E+01	6.54E+01	2.53E+06
15	Diffuser; S=4.6	3907	new probe update	1.56E-02	2.30E-04	4.97E-04	1.64E-02	1.73E-01
16	Diffuser; S=4.6	3907	new probe update + α decay	2.85E-05	4.50E-07	1.11E-06	3.00E-05	1.61E-01

3.5 Summary

This chapter has developed a new sampling condition, built on the principles of conventional diffractive imaging, which allows an experimenter to design a ptychographic microscope with much greater freedom than has previously been possible. The ability to process diffraction patterns that fall well below the Nyquist sampling condition on their own relaxes the condition on beam size, reducing further the requirements on the quality of the optics. An additional benefit of the theory is that the specimen-detector may be reduced which has particular importance in the x-ray regime where hutch size is generally very restricting, especially when operating at a Bragg angle.

The practicality of the sampling condition only holds though if the total dose per unit area of the specimen must not be increased. Simulations have been used to demonstrate that the sampling condition does, given the correct reconstruction strategy, hold when the dose fractionation level is increased, even when that means only 3907 counts per recorded pattern.

4 X-Ray Ptychography

Since the first hard x-ray ptychographic image using iterative reconstruction methods was recorded (Rodenburg et al., 2007a), ptychography has become a widely implemented technique at x-ray sources across the world (see chapter 2 for a review). The I-13 beam line at the Diamond Light Source (the UK's third generation synchrotron located on the Harwell site in Oxfordshire) is a newly commissioned beam line (Pešić et al., 2013, Rau et al., 2010) built with a dedicated coherence branch for diffractive imaging. All of the experimental x-ray data shown in this thesis has been collected from the I13 coherence branch.

The synchrotron produces x-rays by accelerating electrons, which circle the storage ring, by two mechanisms. The first is via a bending magnet, which 'steers' the electrons at the beginning of each end station such that they may complete the roughly circular journey. In so doing, the electrons

eject energy in the form of high energy photons. It is these photons which are channelled along to an experimental hutch where they may be used to illuminate a specimen. While the bending magnet itself produces a broad spread of photons (spatial coherence in the horizontal direction is particularly poor), an undulator is inserted (on insertion beam lines such as I-13) to oscillate the electrons in a controlled manner such that they produce a specific energy of photon.

Diffractive imaging techniques, including ptychography, require a coherent beam of illumination to interact with the specimen before creating a coherent diffraction pattern in the far-field. I-13 was commissioned with spatial coherence at its heart and is constructed in a unique way. The beam line protrudes out of the synchrotron building along to a separate external end station. An aerial view of the synchrotron is displayed in Figure 4.1, showing the I-13 beam line extending out from the main ring building out to an external building. This external building houses both the optics and the experimental hutches. As a result, there is a distance between the x-ray producing undulator and the experimental hutch of some 250m (see Figure 4.1). The van Cittert-Zernike theorem relates an extended source distribution to a coherence width, W, in the far-field as a function of wavelength and angle, θ_{source}, where the angle is as subtended at the specimen plane by the source ($W = \lambda/\theta_{source}$). Therefore, as the source is moved further away from the experimental hutch, the coherence width within the hutch increases. At I-13 the coherence envelope is approximately 100x800um (Rau et al., 2011) and the range of x-ray energies available is between 6 and 20keV (Pešić et al., 2013).

The work in this chapter begins with the first ever experimental run carried out on the I-13 coherence branch. As the x-rays had only just been successfully steered into the hutch, the experimental setup was un-commissioned. Conducting an experiment under such conditions involved overcoming many issues and some of those are initially discussed. Although access to a beam line is rather rare (experimental proposals must be submitted to a reviewing panel and the lead time is more than six months) because the work here was essentially carried out in a

commissioning phase (we were installing the ptychographic imaging method) time was granted for two further experiments, where the experimental conditions began to improve and some positive results were obtained.

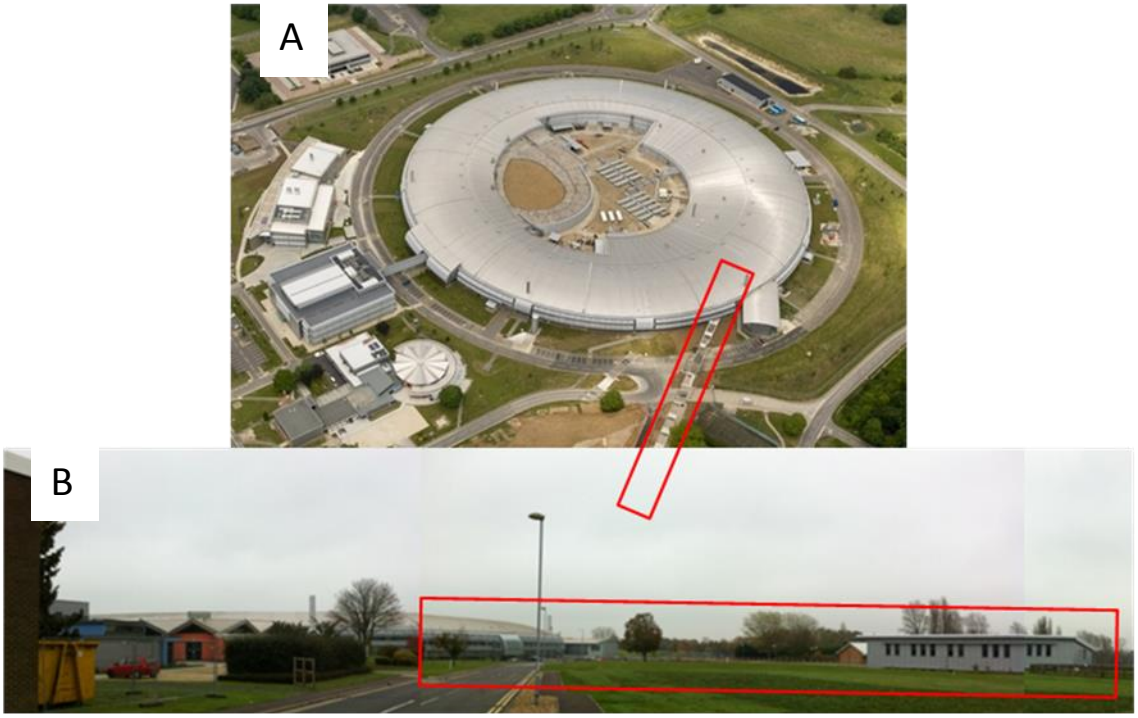

Figure 4.1: Images of the I-13 beam line at the Diamond Light Source in Oxfordshire, UK. a) An aerial photograph of the synchrotron building with I-13 extended out as indicated by the red box. b) A ground view of the I-13 building showing the distance between the experiment and the synchrotron source.

Figure 4.2 shows the entire layout of the apparatus within the experimental hutch, from the condensing optics, to the specimen stage, and finally the detector. The gap between the specimen and the detector is bridged by a vacuum tube in order to reduce x-ray attenuation.

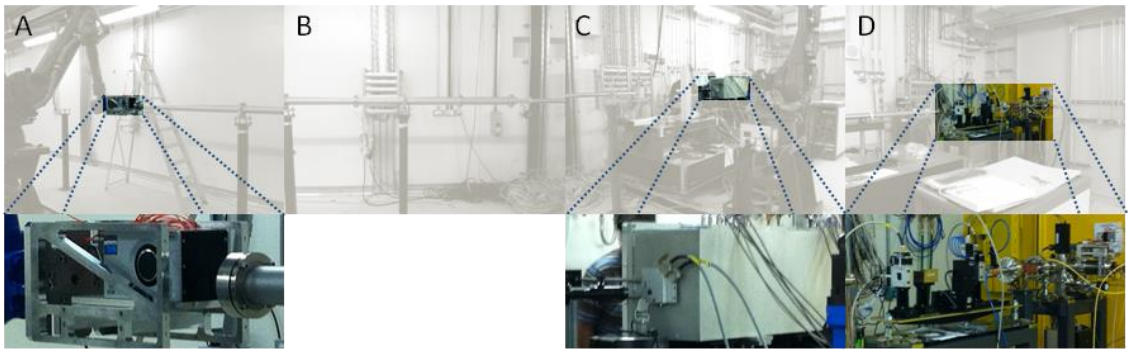

Figure 4.2: The setup within the experimental hutch at the I-13 coherence branch with the beam entering on the right hand side and progressing through to the left. a) The detector mounted on robot arm. b) The vacuum tube used to reduce scattering of the x-rays with air. c) The specimen stage and K-B mirror system. d) The entrance of the beam from the optics hutch.

A clearer view of the specimen stage is shown in Figure 4.3. The rotation base stage is positioned immediately after the condensing optics. The lateral scanning stage, on which the specimen is mounted, is attached to the rotation base stage and positioned as close to the focal plane of the of the condensing optics as possible.

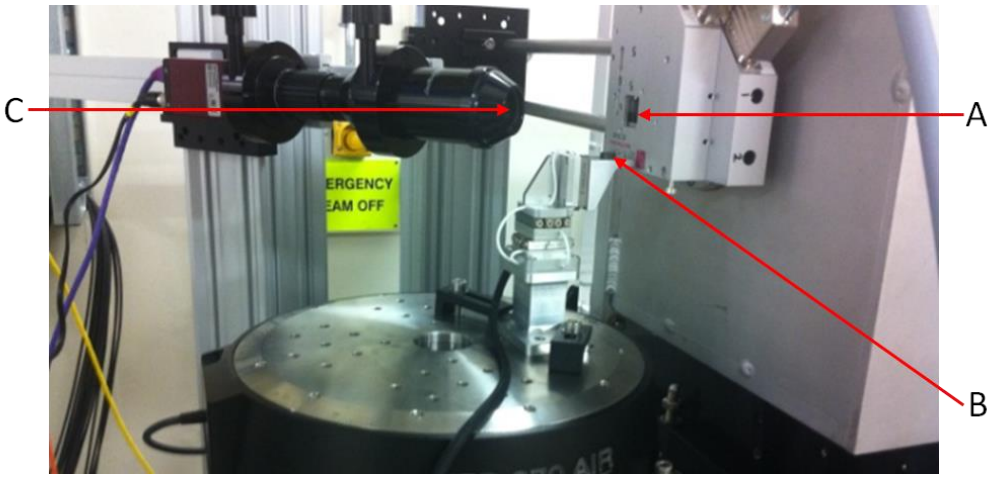

Figure 4.3: Experimental setup after K-B focussing mirror. a) The exit aperture of the K-B mirrors. (b) The specimen stage with magnetic mounting stub. c) An optical microscope used for specimen alignment. Note that the specimen stage is shifted as close as possible to the exit slits, the ideal plane (where the beam is smallest) was obscured by the slits and their housing.

The detector used for this experiment was the Maxipix TAA22PC (Ponchut et al., 2011). The detector is able to directly resolve, and therefore count, the arrival of every single incident x-ray photon. Figure 4.4 shows the data sheet of the Maxipix detector, this model is manufactured with a combination of four chips (in a 2x2 grid) each of which contains 256x256 pixels of 55umx55um pixel pitch, with a small gap between each chip. Such a photon counting detector offers many advantages to the ptychographic imaging technique, where the quality of the whole process is limited by the properties of the detector.

The advantages of the direct photon counting capabilities do however come at some cost. One of the limitations of the detector is the dynamic range (11180 counts). For a typical specimen with a modest amount of scattering power, limiting the central peak in such a way will reduce the higher resolution components to extremely low counts and so either multiple exposures will be required or the illumination must be spread out at the detector plane. The illumination may be spread at the detector plane with either a convergent beam or a strongly scattering spatial diffuser near the

specimen plane. Actually there are many good reasons for employing a spatial diffuser but as these were preliminary experiments no such element is employed here. The addition of a diffuser in the x-ray regime is to be explored in the future and will serve to improve the data acquisition time.

Imaging	
Sensor	Silicon 500 µm thick
Readout chip	Timepix *
Pixel pitch	55 x 55 µm2
Image dimensions	516 x 516
Detection area (mm2)	28.4 x 28.4
Maximum count rate	200 000 cps/pixel
Pixel counter depth	11180 counts
Absorption efficiencies	100% (8keV), 68% (15 keV), 37% (20 keV)
Dark noise	~1 count/pixel/day (cosmic background)
Minimum adjustable threshold	3.5 keV typ. (noise floor)
Exposure time range	1 µs - 1023 s
Readout dead time (@100MHz clock)	0.29 ms
Max. frame rate	350 Hz
Data output time	2.8 ms
Image file format	edf (ESRF data format)

Figure 4.4: Data sheet for the Maxipix TAA22PCtaken from the manual

4.1 Initial Experiment

4.1.1 Pink Beam

As discussed above, I-13 is able to produce a large spatial coherence width in the experimental hutch. Unfortunately though, although the requirements on temporal coherence are not so tight, some form of energy filtering is required in order to record the coherent diffraction patterns required. For the duration of this initial beam time the monochromator was not operational. The lack of a monochromator leaves an ill conditioned beam which has two detrimental characteristics. Firstly, each harmonic present in the beam as produced directly from the undulator remains in the beam and is not filtered out. Secondly, the temporal coherence length of the beam is reduced and so each of these spectral peaks have a large full width half maximum (FWHM). Such temporal spread in the illuminating beam is referred to as 'pink beam'.

Using upstream filters designed for use in beam diagnostics, some of the peaks were successfully suppressed (see Figure 4.5). The Maxipix detector also has an energy threshold (see Figure 4.4) such

that the lower energy peak could be removed. Employing both of these methods together produced a beam with a single energy peak of 10keV with a spectral spread ($d\lambda/\lambda$) of 10^{-2}.

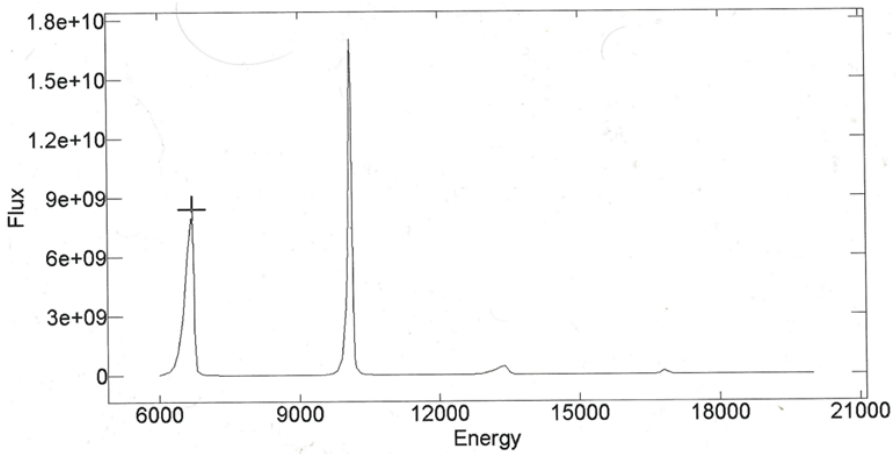

Figure 4.5: Energy spectrum of I13 beam without monochromator, after filtration through diagnostic absorbers.

In order to see the effect that the spectral spread has on the remaining energy peak and then how that in turn affects the data recorded, the shape of the energy spectrum both with and without a monochromator has been modelled (as Gaussian distributions about a mean photon energy of 10keV). Each of the two beam profiles is applied to a simple model calculation in order to understand the effect that a difference in energy spread has on a dataset (in this case a single diffraction pattern of periodic object). Figure 4.6 shows how the energy spread effects the diffraction pattern, the higher scattering angles are stretched out radially, proportionally to their distance from the optic axis, and so the lower scattering angles are much less affected. This suggests that with a simple optical setup (a plane-wave incident upon an aperture) it is the predominantly the resolution of the reconstruction that is impaired.

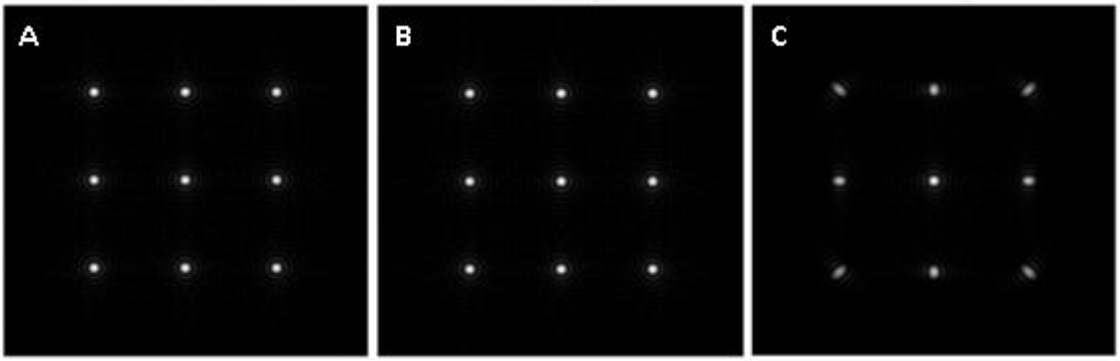

Figure 4.6: Effect on the far-field pattern of a periodic structure illuminated under different amounts of temporal coherence. a) $d\lambda/\lambda$=0. b) $d\lambda/\lambda$= 1e-4. c) $d\lambda/\lambda$=1e-2.

4.1.2 Kirkpatrick-Baez Mirrors

In order to make use of all the available coherent flux that I-13 offers and at the same time satisfy the conventional CDI sampling condition, some condensing x-ray optics were employed. The aim of such an optical element is to bring all of the available coherent flux into a suitably localised spot in the specimen plane. This improves the levels of flux and so reduces the required exposure time. The optical element available at the time was a pair of Kirkpatrick-Baez (K-B) mirrors. Such reflecting optics are in principle well suited to condensing the x-ray beam as they are highly efficient (they do not lose flux in diffraction peaks as with Fresnel zone plates) and may achieve high values of numerical aperture (NA).

The K-B mirror system comprises two reflecting surfaces orientated in each vertical and horizontal plane. The beam is therefore focussed in two separate planes as shown in Figure 4.7, where the nominal focus was just within the exit slits of the K-B system. The specimen-to-focus distance was therefore limited by the experimental constraints shown in Figure 4.3. As depicted in Figure 4.7, the specimen was eventually positioned 15mm away from the nominal focal plane.

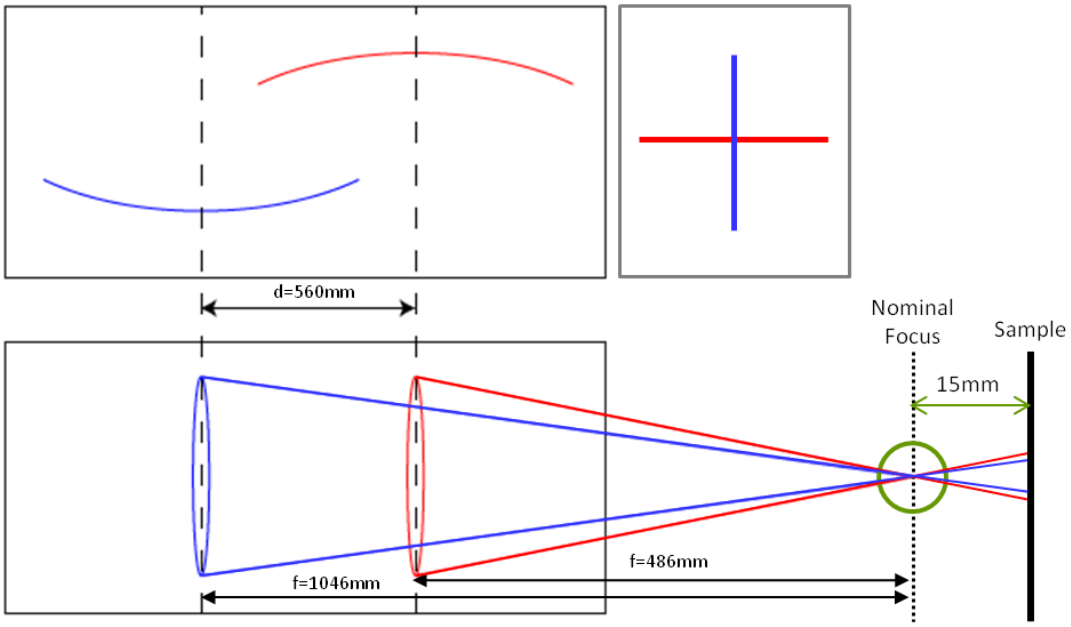

Figure 4.7: Schematic of the Kirkpatrick-Baez focussing mirror system, where the red mirror lies in the horizontal plane and the blue mirror lies in the vertical plane. Adjusting the focal length of each mirror separately allows for a nominal focal point to be formed. The beam is travelling from left to right.

Due to the physical distance between the two mirrors, the resultant beam exhibits two-fold astigmatism, because the beam is formed with a different focal point in the two orthogonal (horizontal and vertical) directions. Figure 4.8 shows a more detailed view of these focal points and how they generate only two planes where the illumination function is square.

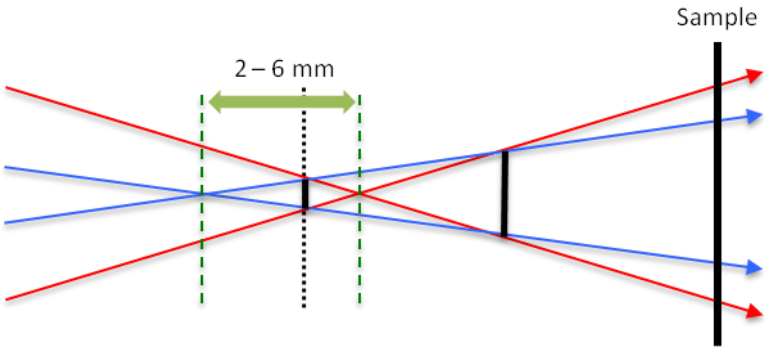

Figure 4.8: Detailed ray diagram of the beam around the nominal focal point of the K-B mirrors. The two black vertical lines in the centre show the two planes where the illumination is square. The specimen was positioned upstream from the ideal plane (the left most black line) due to experimental limits (see above).

The experimental work described in this chapter was carried out at a time when the full ptychographic sampling condition was not understood and so the datasets were recorded according to the single-shot CDI sampling condition (equation 3.2). Although it was known that the strict limitation of equation 3.2 could be relaxed so that the illumination could be slightly larger, the

wisdom was that the beam still had to be localised within the $1/\Delta U$ real-space window, which for the given object-detector distance and pixel-pitch is 14.3x14.3µm. With the setup described above, the best probe obtainable was about 20x20µm. Due to the structure of the experimental setup, the positioning of the specimen in the desired plane proved to be a difficult and imprecise task. Figure 4.8 shows where the specimen was assumed to be.

The probe formed from the K-B mirrors contains substantial power in the side flares and so even at the ideal focal point, the localisation of the beam is an issue. In order to remove these flares, slits where closed down upstream of the specimen. The reconstructions later suggested that the horizontal component of the beam was near focus at the specimen plane while the vertical component was largely defocused, producing an oblong illumination function. This suggests that the slits were positioned near to the vertical focal point (of the horizontal mirror) and so the beam expands quickly in the vertical direction while the angular range of the horizontal component has been suppressed.

4.1.3 Specimen

Initially, a simple test specimen is used that comprises a dispersion of superparamagnetic dynabeads, which are 2.8um diameter spheres composed of Fe2O3(14%) and C8H8(86%) onto a carbon support film attached to a 3mm TEM slot grid. Conventional white light transmission images of the specimen at different magnifiactions are shown in Figure 4.9. These show how the dynabeads have been dispersed onto a carbon film, which is suspended across a 3mm TEM slot grid and mounted onto a pin mount. Although not visible in the image, the pin is attached to a magnetic stub that is used to secure the pin to the scanning stage.

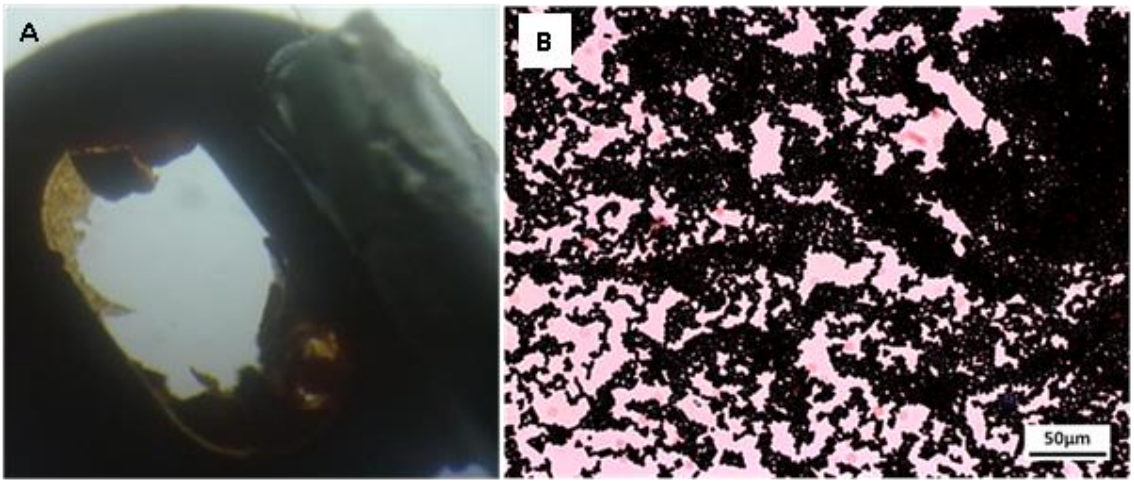

Figure 4.9: Conventional white light images of the test specimen. a) The support film suspended across a TEM slot grid (reflection). b) A magnified region of the dynabeads dispersed across the support film (transmission).

Figure 4.10 shows a scanning electron microscope (SEM) image of the dynabeads on the surface of a copper grid. It can be seen from this image that the spheres pack together in predominantly flat clusters with some spheres overlapping. The sizes of the spheres appear to be non-uniform with some variation in size visible.

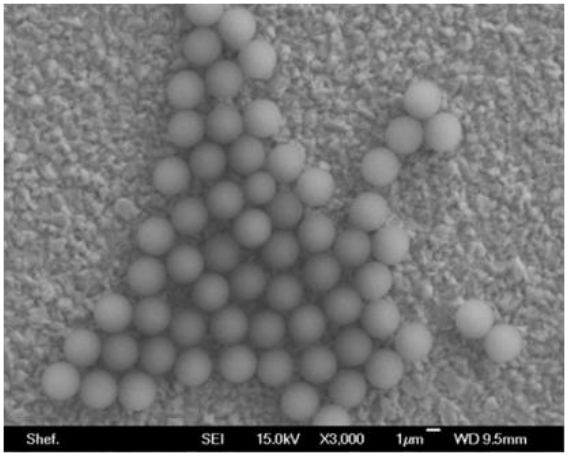

Figure 4.10: An SEM image of dynabeads on a copper TEM grid.

In order to record the ptychographic dataset shown below, the specimen was scanned through the beam across a grid of 28x20 positions with a nominal step size of 0.5µm in each x-y direction. A diffraction pattern was collected at each position on the detector, which was placed 6.4m downstream of the specimen in the usual ptychographic manner. A typical diffraction pattern from the recorded dataset is shown in Figure 4.11a. Only one of the four available chips was used here as to avoid the missing cross that exists across the full detection area due to the gap between chips.

Such a missing cross is recoverable when the illumination has a spread of k-vectors that bridge across the gaps, however the simple setup here would leave missing frequencies within the reconstruction and result in artefacts in the resultant images.

Due to the low level of temporal coherence within the x-ray beam, processing of the original data was unsuccessful. In order to reduce the effect that the temporal coherence level has on the reconstruction the diffraction patterns have been cropped down to varying levels. This is in line with the findings of Figure 4.6.

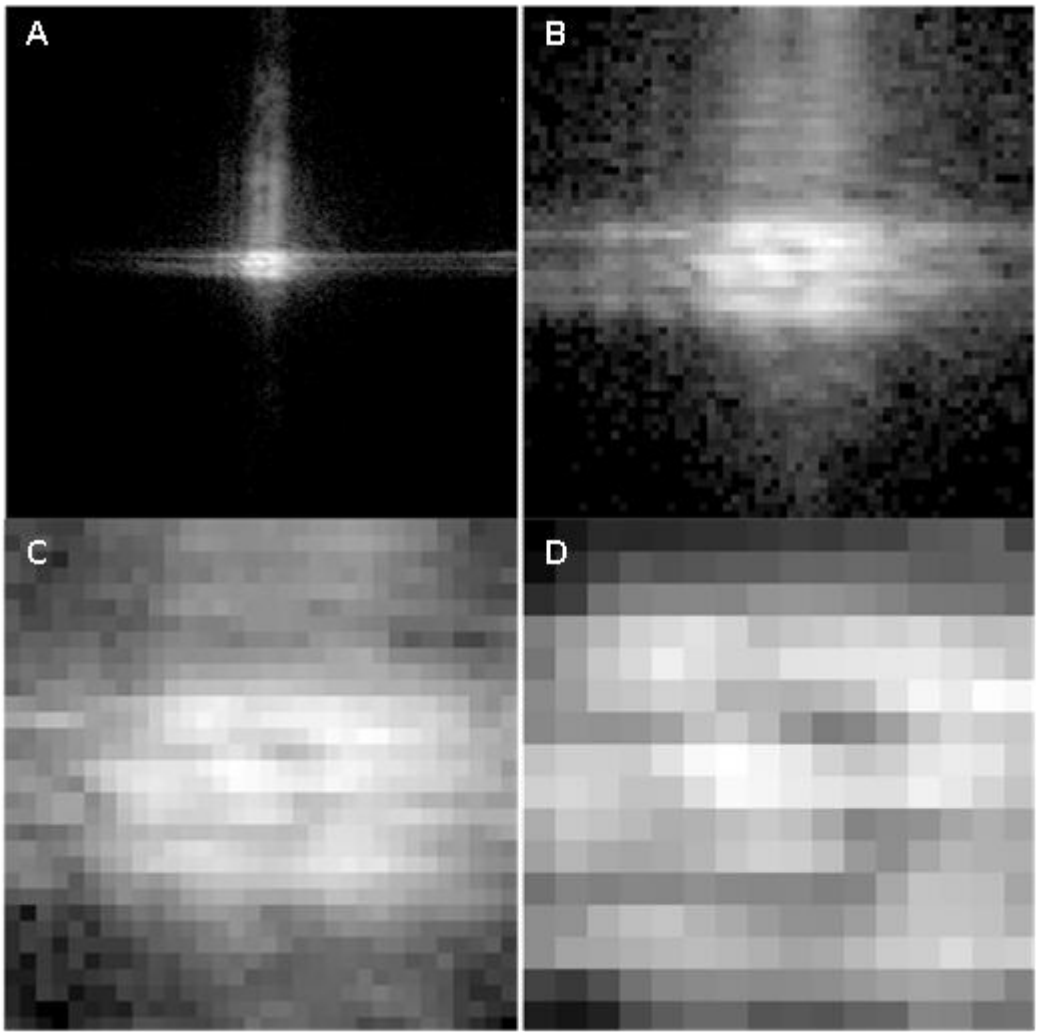

Figure 4.11: A typical diffraction pattern from the recorded dataset. a) The original 256x256 pixel pattern captured on a single detector quadrant. b) The diffraction pattern from (a) cropped down to the central 64x64 pixels. c) The diffraction pattern from (a) cropped down to the central 32x32 pixels. d) The diffraction pattern from (a) cropped down to the central 16x16 pixels.

4.1.4 Reconstruction

Running the cropped datasets through the ePIE algorithm produced the reconstruction as shown in Figure 4.12. There appears to be a trade-off between removing the incoherent area of the data and preserving the specimen information that is encoded around the central peak. Figure 4.12-A2 seems to produce the best reconstruction (the field of view is slightly improved). However, while there is definitely some structure within the reconstructed object on the scale of the dynabeads and some form of localised beam within the illumination function, the result does not offer any significant information about the specimen and is unconvincing.

It can be seen in Figure 4.12 that the probe function contains artefacts at its corners. From work carried out later relating to the effects of incoherent data it seems that a likely cause of this artefact is low levels of temporal coherence. When the dataset is cropped strongly the artefacts in the corner vanish and instead the illumination function appears to be elongated in the vertical direction and potentially under-sampled in the vertical direction. As mentioned earlier, this would be explained by the specimen being positioned at the focal point of the vertical mirror (which focuses the beam in the horizontal plane).

Although some progress has been made during this experiment, the end result is not of any particular scientific use. With regards to ptychography the main issues were those of the sampling requirements and the temporal coherence. As I-13 was a newly commissioned beam line and I was a member of a small user group that was implementing ptychography at Diamond for the first time, more beam time was made available the following year. Access to such large amounts of time at a beam line is rare and reflects the 'user-assisted commissioning' mode in which the work here was carried out. The following work describes a second and third experimental run, carried out in March 2012 and October 2012 respectively, in which the experimental conditions were gradually improved.

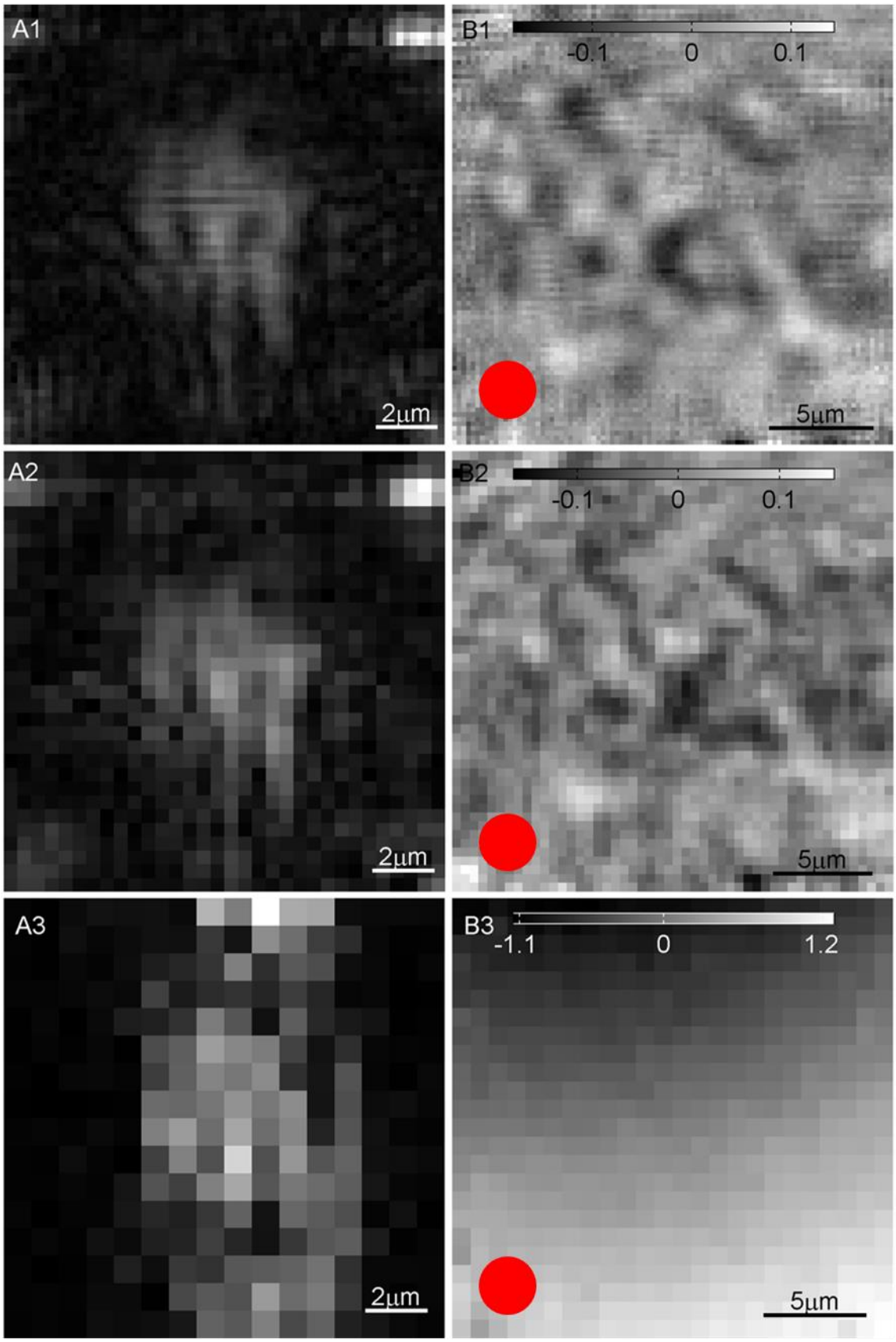

Figure 4.12: Outputs from the ePIE algorithm. a) Modulus of the reconstructed probe functions. b) The phase of the reconstructed objects. 1) 64x64 detector pixels. 2) 32x32 detector pixels. 3) 16x16 detector pixels. The red disc in the bottom left of the phase images represent the scale of single dynabead as quoted by the manufacturer.

4.2 Secondary Experiments

4.2.1 Experimental Setup

The lack of temporal coherence in the initial experiment is a prime candidate for the poor quality of the reconstructions. A second experiment was carried out were the undulator gap was set to maximize the photon flux at 8.7keV (λ = 0.14 nm) and now selected by a pseudochannel cut Si (111) crystal monochromator. The introduction of the monochromator produces a single energy peak with the spectral spread (dλ/λ) reduced from 10^{-2} to 10^{-4}. The effect of this reduction in spectral spread on the recorded diffraction pattern is modelled in Figure 4.6 and the full diffraction pattern may now be used without degradation of the quality of the whole dataset. The experimental setup employed when recording the datasets in this experiment is as shown in Figure 4.13 and is essentially as simple as the requirements of ptychography will allow, with only two sets of slits in order to suitably localise the beam.

While I-13 produces x-rays with a large spatial coherence envelope, the requirements set at the time by the conventional CDI sampling condition limited the size of the illumination at the specimen. In order to avoid experimental uncertainties, no focussing optics were employed. The two sets of slits (horizontal and vertical) were placed in the beam upstream of the specimen with gaps of 20µm and 16µm, respectively. The resulting x-ray beam incident on the specimen was a localised spot of 37µm^2. Importantly, this is only a fraction of the available coherence width at I-13 (approximately 100x800µm) and so it is clear that this will not ultimately be the optimal setup. In order to process all of the available flux, either condensing optics are required, or the sampling condition must be improved (either a smaller pixel-pitch or a longer hutch). (The alleviation of the current constraints by exploiting the new ptychographic sampling condition is discussed later.)

Due to the installation of an extended vacuum tube, the distance between the detector (a Maxipix TAA22PC (Ponchut et al., 2011)) and the specimen was able to be significantly extended, satisfying the single-shot CDI sampling condition. The detector was now 14.62m downstream of the specimen

at the very end of the experimental hutch; a diagram showing this along with the other elements of the setup is shown in Figure 4.13.

In order to collect the ptychographic dataset, the specimen was scanned laterally with respect to the incident x-ray beam, covering an approximately square grid over 1024 positions with a nominal step size of 6µm. The scan positions had random offsets of ±5% to avoid the periodic artefacts that can otherwise occur during the reconstruction process. The detector was set to capture diffraction data over an 18 second exposure period per scan position. In order to remain within the count depth of the detector, 9 separate exposures of 2 seconds were recorded and integrated together computationally post acquisition. The resultant ptychographic dataset has an instrinsic sampling factor (in accordance with equation 3.7) of 2.94.

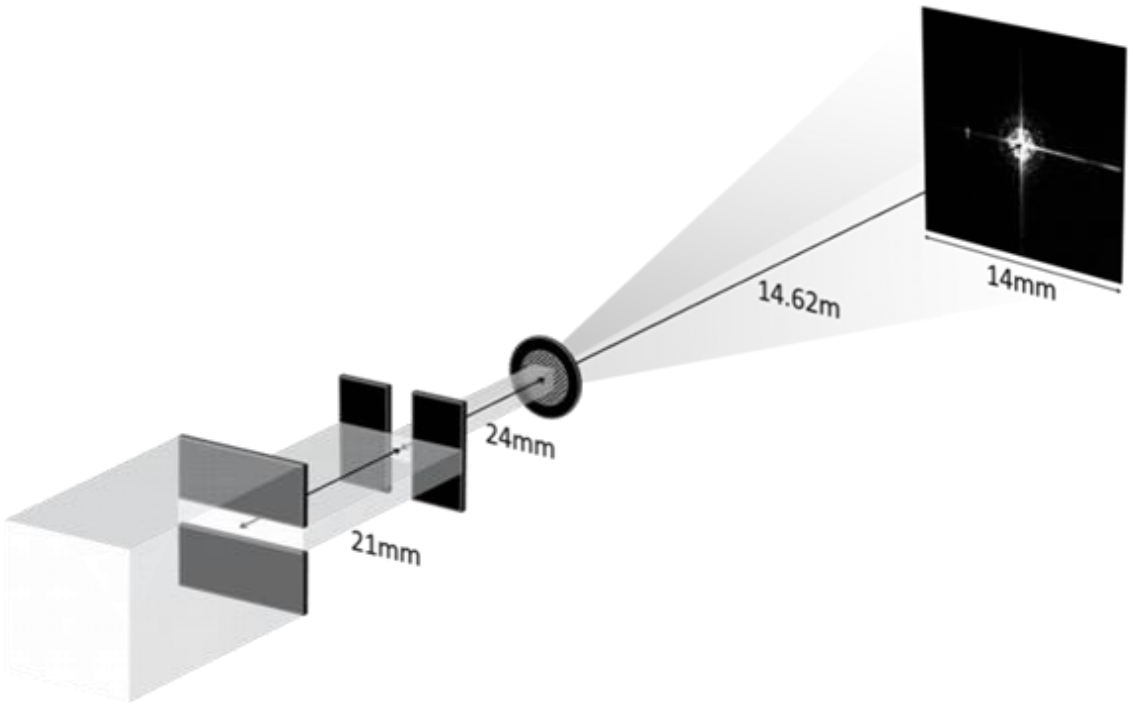

Figure 4.13: Schematic diagram of the experimental setup with beam direction from left to right.

4.2.2 Reconstruction

The dataset is processed through the ePIE algorithm, where the initial estimate of the illumination function is a simple computational model of a plane wave passing through two sets of slits with the propagation distance as described above. The reconstruction produced a clean phase image of the

specimen at a resolution on the order of hundreds of nanometres across a field of view on the order of hundreds of micrometres, see Figure 4.14. Considering that the physical beam was 20µm at the specimen, both of these figures are a substantial result for the quality of optics required (just slits in this case). The background is uniform (with a slight ramp from top left to bottom right which may arise from sub-pixel misalignment of the optic axis) and the spheres compare well with the SEM image shown above in Figure 4.10.

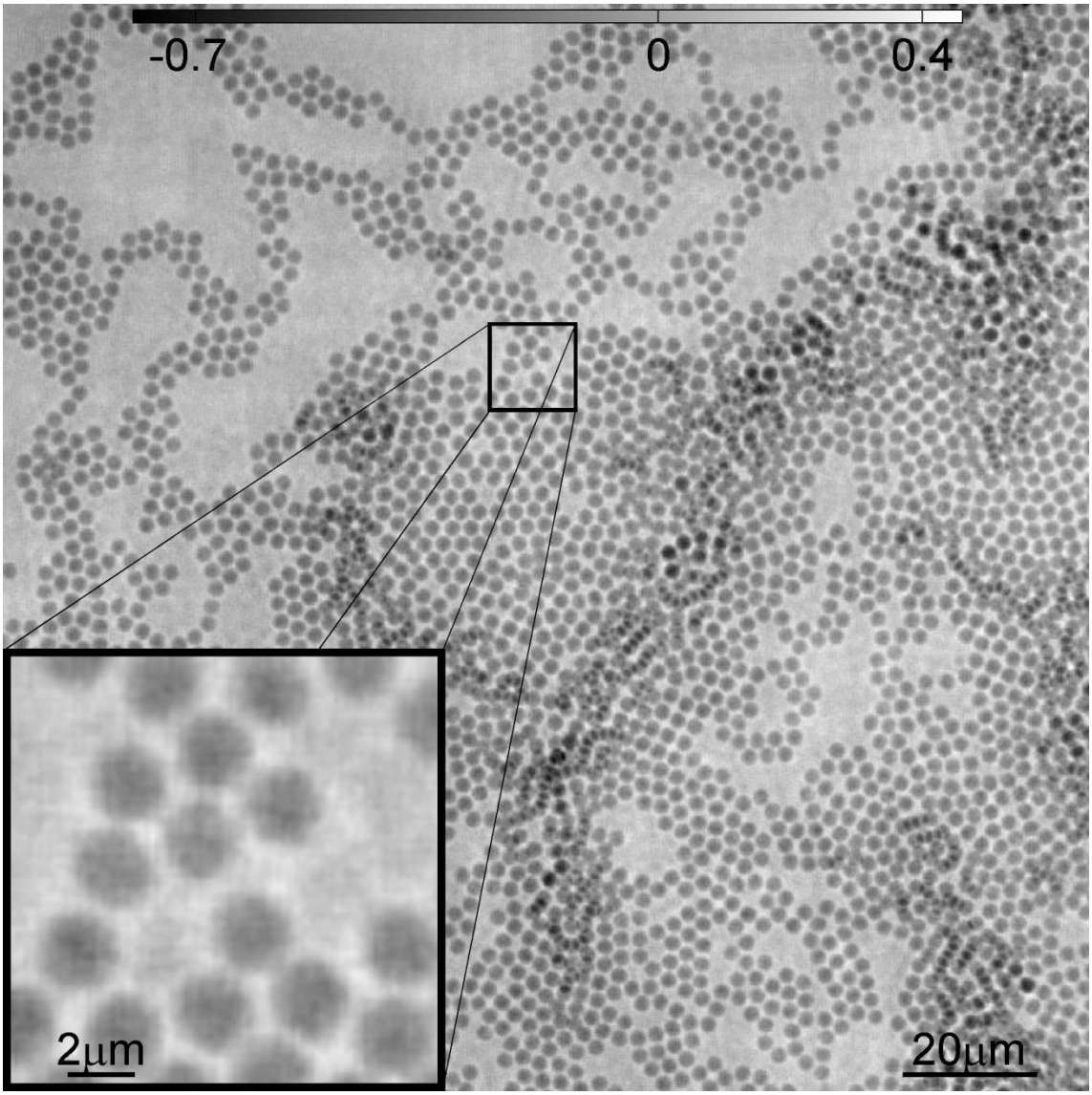

Figure 4.14: ePIE reconstruction: phase image of the dynabeads with a magnified inlay.

4.2.3 Analysis of the Reconstruction Quality

The ability for ptychography to synthesize an extended coherent illumination function and thus quantitatively phase features over an extended field of view is now examined.The accuracy and sensitivity of the phase measurements are tested. Line plots are taken through the reconstructed phase image and used to obtain an average phase change through each sphere. The reconstructed phase profile is compared to theoretical values.

Figure 4.15 shows a surface plot that represents the phase image shown in Figure 4.14. The surface plot improves the dynamic range of the image (the pixel-depth is translated into Z height) and allows for the shape of the dynabead to be examined more easily. The phase signal has been halved such that the single dynabeads may be seen topographically, although this does break down where the dynabeads overlap.

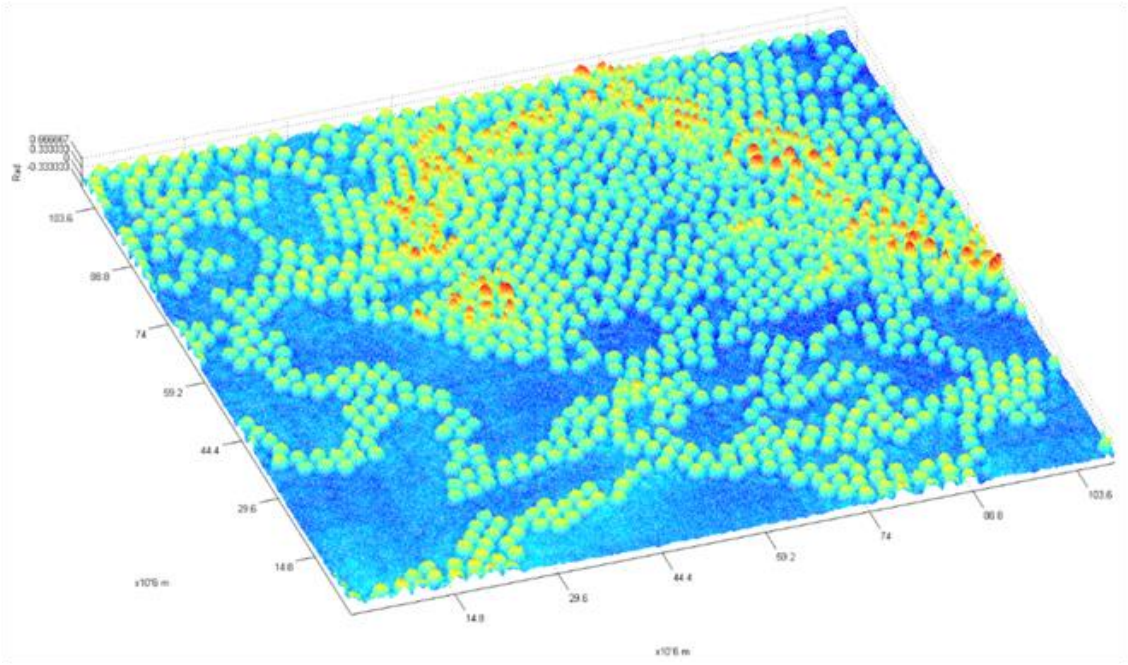

Figure 4.15: Surface plot of the phase image shown in Figure 4.14. The values have been halved to represent the surface structure from the projection through the whole volume.

In order to more clearly and precisely examine the quality of the phase image produced, line plots have been taken through three different regions of the reconstruction. Figure 4.16 shows where these line plots have been taken from and Figure 4.17 shows the corresponding plots along with

average maxima and minima values of the single dynabeads. These average values are used to show that the phase images produced across an extended field of view are indeed of a sufficient accuracy to be considered quantitative.

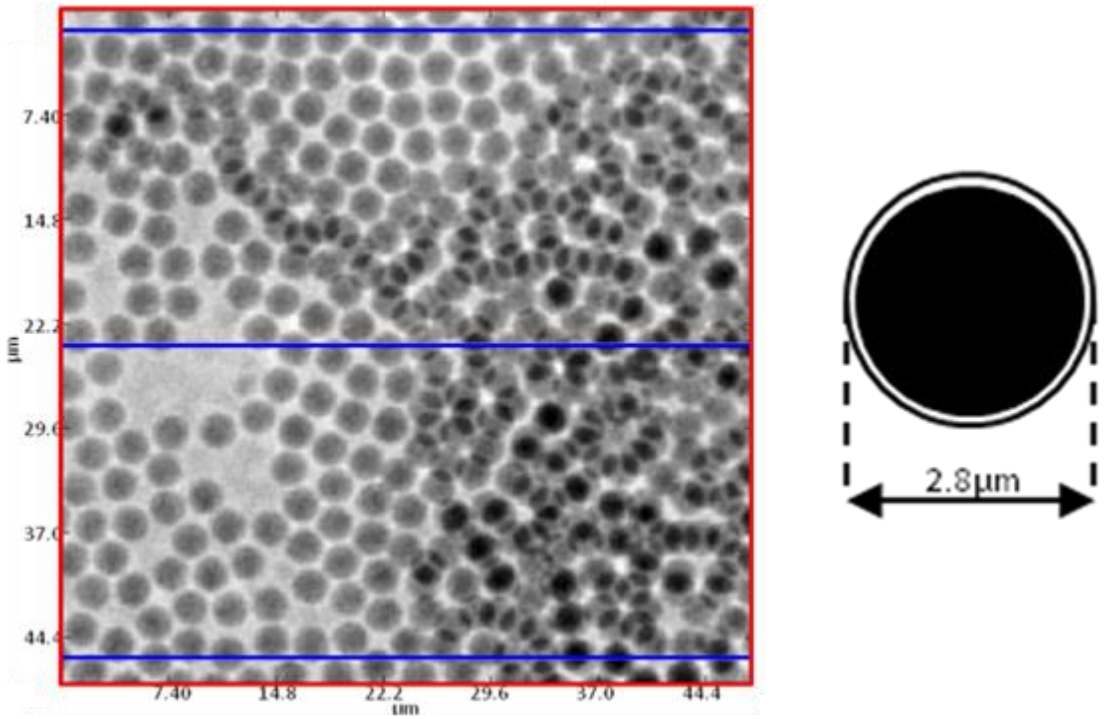

Figure 4.16: (a) Magnified region of Figure 4.14 with blue lines depicting the lineplots shown in Figure 4.17. (b) A schematic of a single dynabead.

For x-rays, the refractive index of a specimen may be given by,

$$\tilde{n} = 1 - \delta + i\beta \,, \tag{4.1}$$

where β is the absorption term and δ is related to the phase change seen by a photon such that,

$$\Delta\phi = \frac{-2\pi}{\lambda} . \delta . \Delta s \,, \tag{4.2}$$

where λ is the wavelength associated with the photons energy and Δs represents the thickness of the material.

Table 2 shows the delta component of the materials that make up the spheres. Combining them in the appropriate proportions along with the expected diameters (in line with the manufacturer's

datasheet) gives the combined phase change through the centre of the spheres for the photon energy used in this experiment.

Table 2: Physical parameters of the dynabeads and subsequent theoretical phase change.

$\delta(Fe_2O_3)$	$3.35x10^{-6}$
$\delta(C_8H_8)$	$3.84x10^{-6}$
Δs	$2.80x10^{-6}$ m
λ	$1.40x10^{-10}$ m
$\Delta\phi(Fe_2O_3)$	-0.42 rad
$\Delta\phi(C_8H_8)$	-0.48 rad
$\Delta\phi(Fe_2O_3(14\%) + C_8H_8(86\%))$	- 0.47 rad

The dynabeads are spheres composed of polystyrene (C_8H_8) and iron oxide (Fe_2O_3) coated in a glycidyl ether. The beads have a diameter of 2.8µm, a density of 1.6g/cm^3 and an iron content of 14%. The theoretical phase retardation of the x-rays at 8.7keV at the centre of the spheres - neglecting the glycidyl ether - is 0.47 radians. The theoretical values were taken from the online database available from the Center for X-ray Optics, see (CXRO) in the references. Analysing the three line plots shown in Figure 4.17 at different regions of the specimen (the three lines in Figure 4.16), shows the nominal phase change across the centre of a single bead to be 0.495±0.025 radians, which compares to the theoretical value of 0.47rad.

One of the great advantages that ptychography has over other diffractive imaging techniques is the ability to recover the illuminating wave-field along with the object. Figure 4.18 shows how, using the angular spectrum propagation technique outlined in section 2.1.7, the reconstructed illumination function may be viewed in the plane of the probe forming optics (Schropp et al., 2010, Schropp et al., 2012) and in this case the probe forming slits. The ability to not only recover the gap between the horizontal and vertical slits (approximately 1cm) but also the gaps between the blades in each

case (approximately 0.2cm) provides a high level of confidence that the illumination function is an accurate representation of the physical free-space wave-field. It can be seen that the slits have some feature which is transferred into the illumination function. The back propagation technique is able to resolve which slits this feature occurs at and allows the correct piece of apparatus to be cleaned.

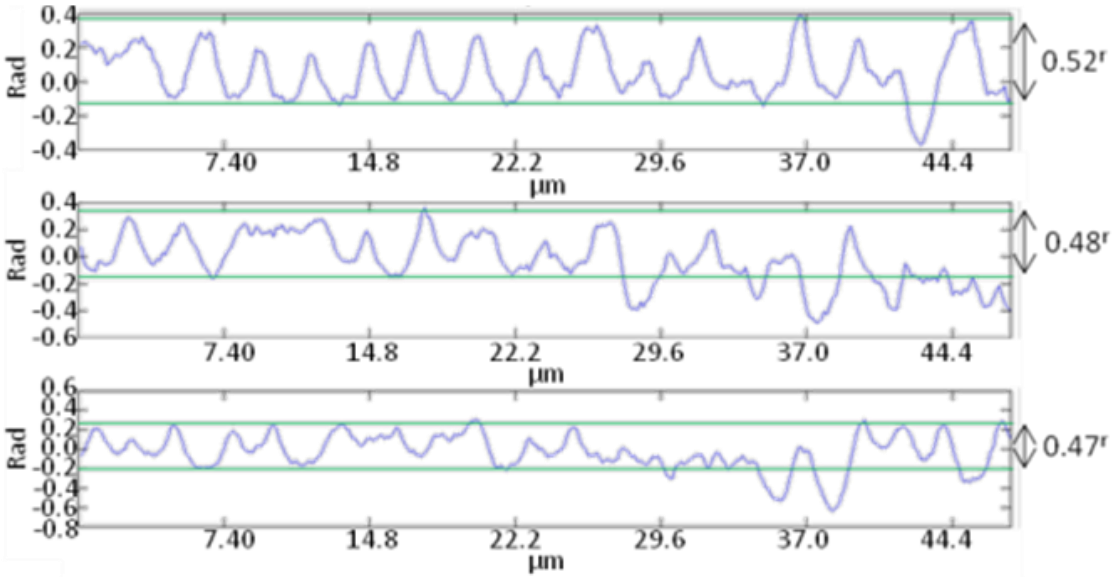

Figure 4.17: Line plots of the phase image with average values for the phase change across a single sphere.

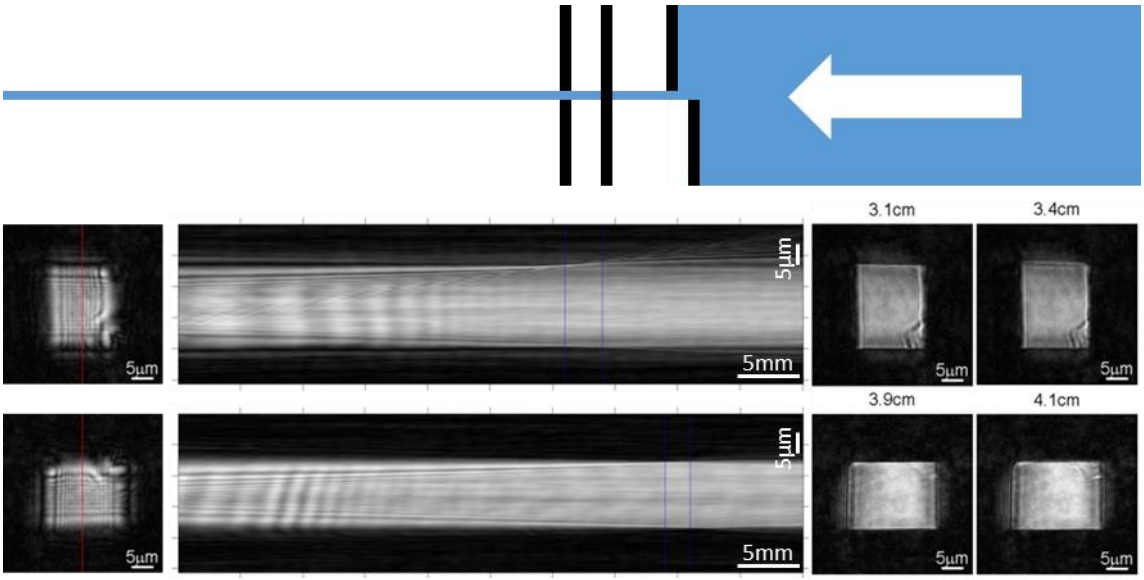

Figure 4.18: Computational propagation (via the angular spectrum method) of the recovered illumination function from the specimen plane (left) to the probe forming slits (blue lines).The propagation is shown in both the horizontal plane (top) and vertical plane (bottom). The two images to the right of each propagation is the probe profile at each edge of the slits.

Analysis of the reconstructed object has shown a strong correlation beween the physical measurements and theoretical calculations. Analysis of the reconstructed illumination function has shown that the reconstructed wave function is consistent with the upstream slits and is actually able to resolve defects within the probe forming element. This experiment has therefore shown that ptychography is able to quantitatively image the complex transmission function of a specimen over an indefinitely large field of view within the hard x-ray regime. Employing only the simplest setup, with sub-optimal sampling conditions, a field of view of 162µm x 162µm at a resolution of approximately 300nm has been achieved.

In order to test the technique across a different type of specimen, a Nickel tip with a periodic nano-structure was also imaged. The reconstruction shown in Figure 4.19 shows small scale structure even though the specimen is a very steep wedge shape, which is represented in the reconstruction as a large amount of phase wraps towards the bottom of the image.

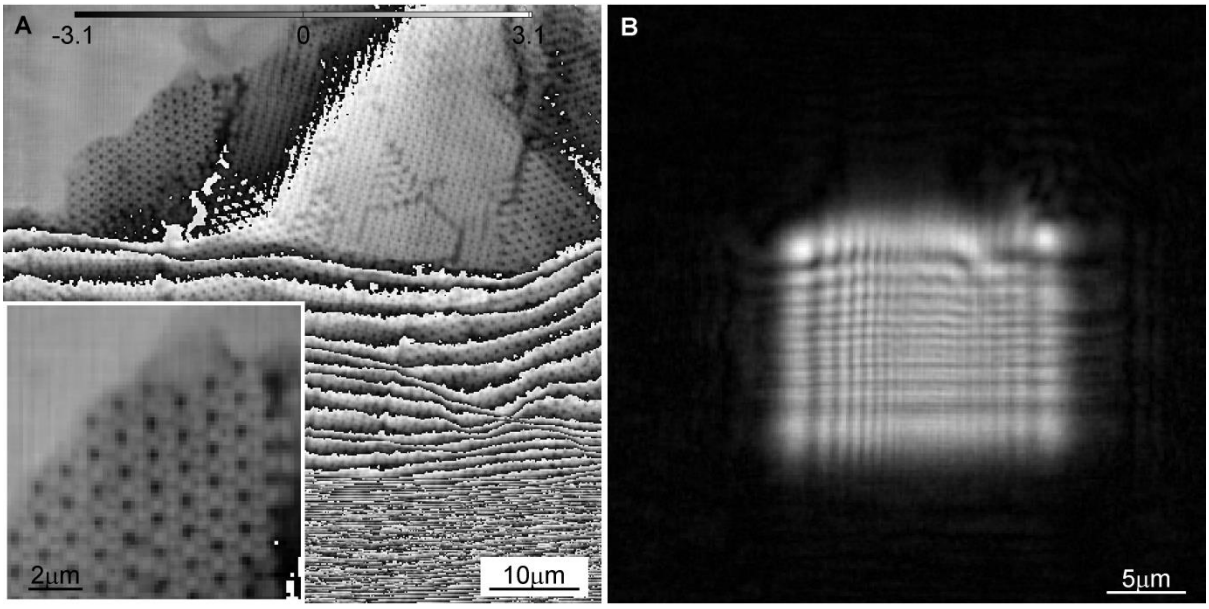

Figure 4.19: A reconstruction from the tip of a Nickel specimen with a periodic nano-structure. a) The phase of the object with magnified inlay (Note the steep wedge shape which has produced many phase wraps). b) The modulus of the probe function.

4.2.4 Convergent Beam Experiment

The downside to the aperture only setup used in the above experiment is that only a small fraction of the available flux at the Diamond Light Source is used and large amounts of coherent flux are

wasted. A third experimental run was granted in which the K-B mirrors were reinserted into the beam. By capturing and condensing the more of the beam, the total flux density at the specimen was greatly increased. The K-B mirrors were highly aberrated and the perturbations on the surface of the mirrors resulted in a poor quality illumination spot. To improve this, a 10µm aperture was inserted upstream of the specimen (see Figure 4.20) and the resultant beam profile in the specimen plane can be seen in Figure 4.21b, Figure 4.22b, and Figure 4.23b. A step size of 2µm was used and the detector was positioned at a distance of 14m from the specimen. As the illumination was convergent the full detector could be used; similar principles to the detector extrapolation from section 2.4.1 are used to solve for the missing data.

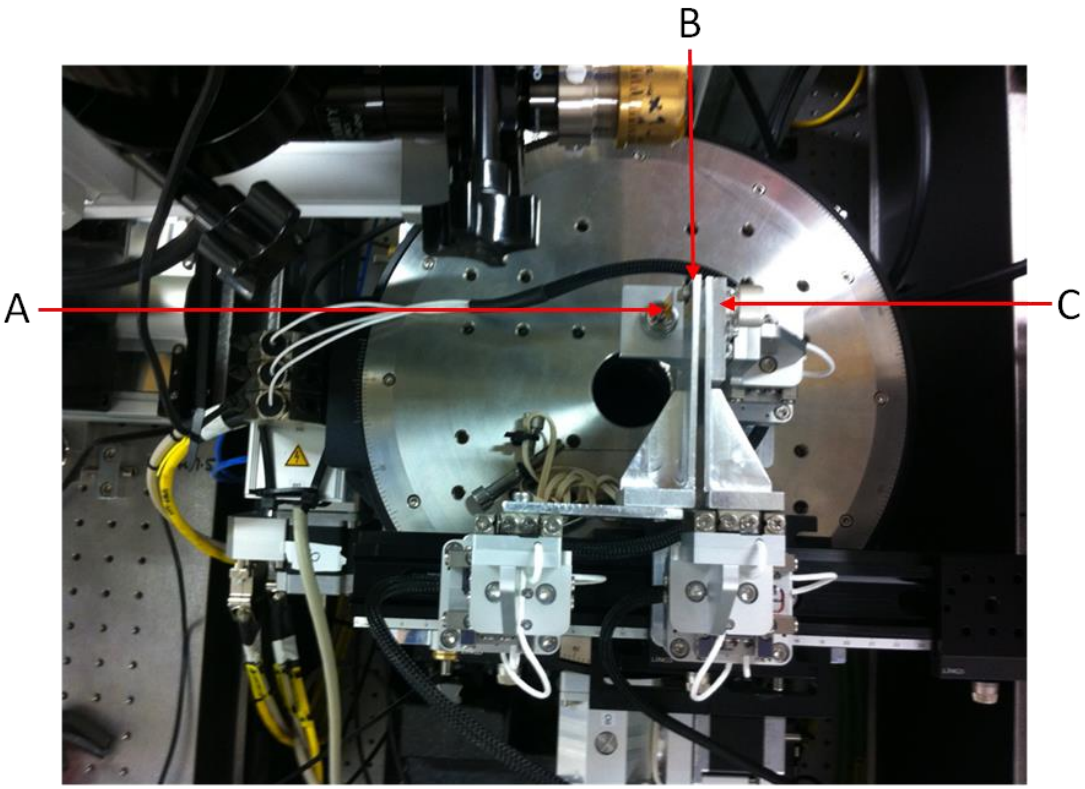

Figure 4.20: Experimental setup with the beam travelling from right to left. The specimen (a) is mounted behind a 10µm pinhole(c). A holder for a spatial diffuser (b) is sandwiched in between the two although this was eventually unused due to instability issues.

During this experiment a selection of soft matter specimens were examined, the results shown here are of starch granules and ferritin. A reconstruction of the ferritin specimen is shown in Figure 4.21. Unfortunately, there appears to have been an issue with the experimental setup during this experiment and all of the datasets originally reconstructed poorly. After closer analysis of the data

and the use of the position correction software (Maiden et al., 2012b), some of the datasets eventually produced the results shown in Figure 4.21, Figure 4.22, and Figure 4.23.

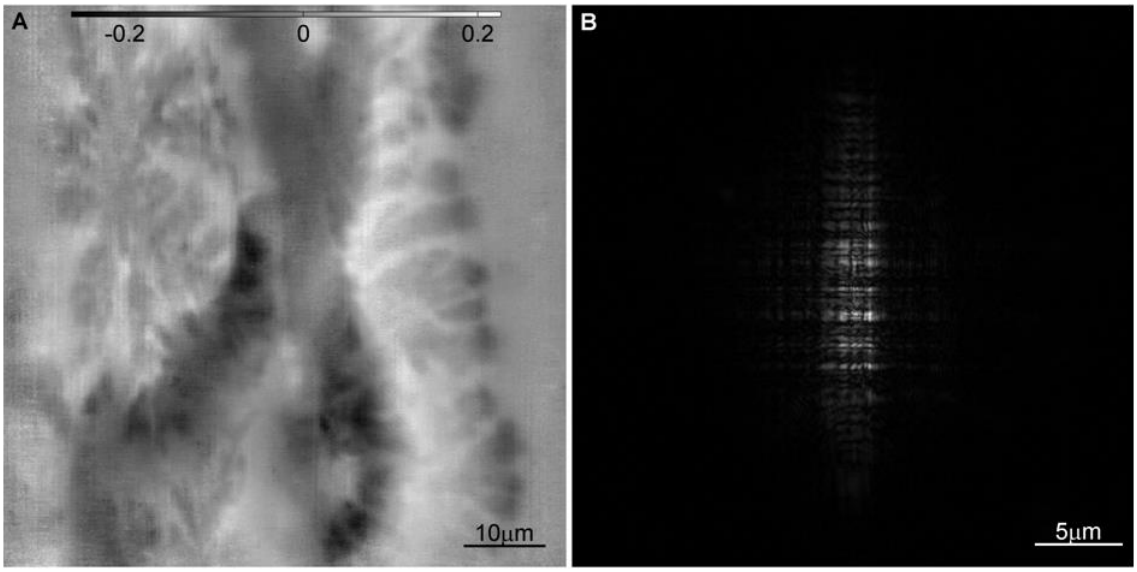

Figure 4.21: Reconstruction of a ferritin specimen (an iron storing protein). a) The phase of the object. b) The modulus of the probe function.

Along with the ferritin specimen, a selection of starch granules in different densities were also scanned. The result of the sparsest of these specimens is shown in Figure 4.22.

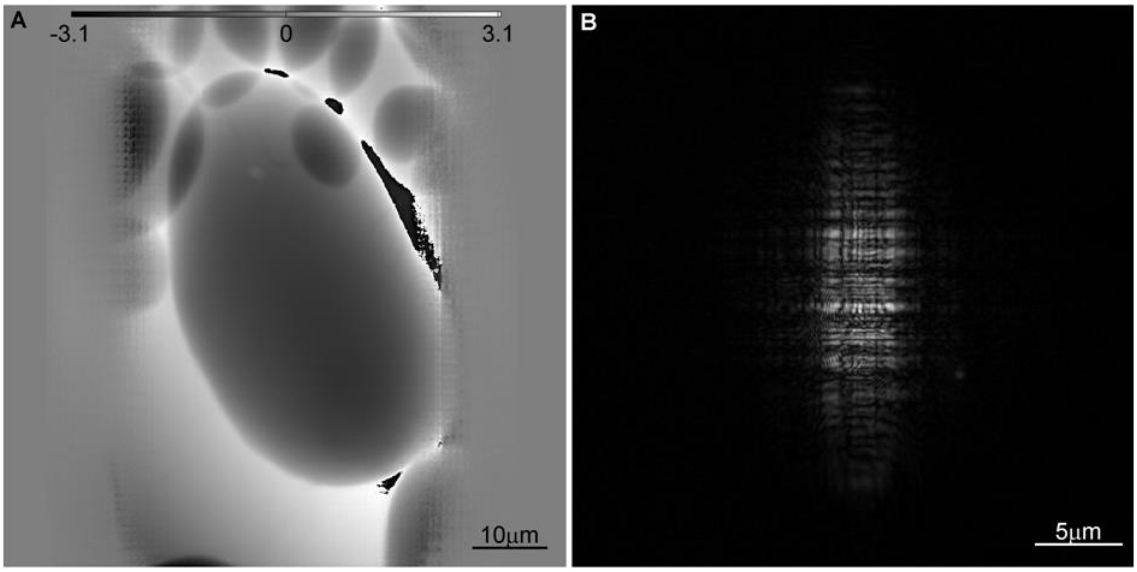

Figure 4.22: Reconstruction of sparsely packed starch granules. a) The phase of the object. b) The modulus of the probe function.

A more densely packed cluster of starch granules was reconstructed and is shown in Figure 4.23. Some of the original artefacts remain in the recontructed phase image (Figure 4.23a), where there is

a noticeable verticle stripe about one third of way from the right hand side. Aside from this however, the image produced is very good. The phase profile of the densely overlapping granules, which cause phase wraps throughout the image, have been reproduced with clarity.

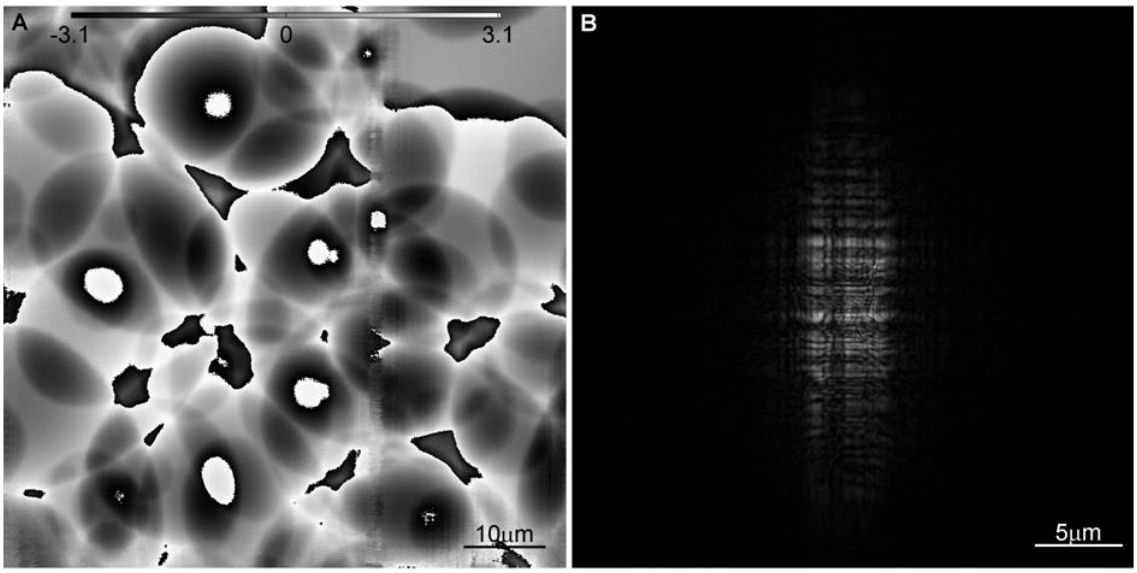

Figure 4.23: Reconstruction of densely packed starch granules. a) The phase of the object. b) The modulus of the probe function.

The structure seen in the probe functions of Figure 4.21, Figure 4.22, and Figure 4.23 is a result of the imperfections in the surface of the K-B focussing mirrors, which introduce severe aberrations. However, as noted earlier, one of the benefits of ptychography is the non-reliance on high quality optics. Reconstruction algorithms are able to refine the unknown structure within the illumination function during the reconstruction process, as demonstrated here.

4.3 Up-Sampling

In chapter 3, the sampling condition within a ptychographic dataset was discussed in terms of the number of intensity measurements and the requisite four dimensional spacings of them that are required in order to create a complex phase image from a set of diffraction intensity patterns. In this section the consequences of the theory is explored through the real experimental dataset that was recorded in the hard x-ray regime as used in the reconstruction of Figure 4.14.

The original dataset has a sampling factor (according to equation 3.7) of 2.94. As the single-shot CDI sampling factor of each individual diffraction pattern is 1.07 (approximately a factor of two below the current ptychographic limit), the dataset must be down-sampled by a factor of three in order to be comprehensively 'under-sampled' with respect to the current requirements. This does however place the dataset at just below the full requisite ptychographic sampling condition. As can be seen later, the data is still sufficient to convincingly demonstrate the applicability of the ptychographic sampling condition to real data. The principle is also then pushed to the extremal case of only four (2x2) detector pixels through a simulated dataset.

It was shown in section 3.3.1 that when an illumination with no isolation within the Fourier-repeat cell in real-space is used, and therefore no convolution has occurred within each diffraction pattern, the phase problem remains soluble so long as the sampling condition in equation 3.7 is satisfied. It is now shown that the data may be down-sampled further, such that the probe now extends beyond the Fourier-repeat unit cell in real-space, and still be successfully reconstructed using the convolution across R-space (the overlap of the illumination function in real space) alone.

In the most basic sense, reconstructing an array of measurements from a detector that can physically only record the intensity values of the incident wave-field into a complex image with half the number of pixels can be described as transforming each group of four pixels in the physical detector into one single synthetic complex pixel. The stitching of multiple single-shot reconstructions into one, forming a synthetic detector, is a form of up-sampling and relies upon the prior knowledge of the object-illumination shifts between exposures.

4.3.1 Sparse Pixels

Initially, the case of sparse detector pixels is examined (keeping in line with the simulations of chapter 3). The pixel-pitch of the recorded dataset is physically fixed at 55µm during the manufacturing of the chip. New subsets of the original dataset are formed such that the new pixel-pitches are 110 and 165 µm. This is achieved by sub-sampling each diffraction appropriately, as

shown in Figure 4.24. Down-sampling the diffraction patterns by 2x2 and 3x3 alters the overall sampling factor, $\hat{S}$, from the original 2.94 to 1.47 and 0.98, respectively.

ePIE processes the data as shown in Figure 4.24c, which introduces a false contraint and an incorrect repeating of the illumination function within the real-space array at each position. The results of the ePIE reconstructions are shown in Figure 4.25 and Figure 4.27 for the datasets with down-sampling of factors of 2x2 and 3x3 respectively.

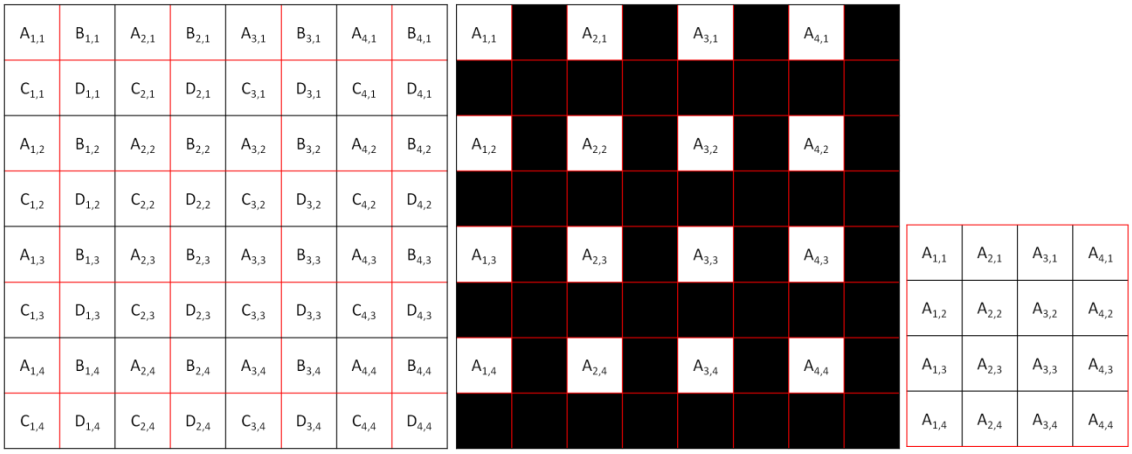

Figure 4.24: Down-sampling of original diffraction patterns. a) Example array represented by four subsets. b) Single subset as physically distributed on a sparsely sampled detector. c) Single subset for processing through ePIE.

Using the same reciprocal-space update step as equation 2.62, an interpolation algorithm is created named fPIE. fPIE begins with the data as in Figure 4.24b then preserves the estimates of the unkown pixels (respresented as black) in both modulus and phase. The measured pixels (repesented in white) are constrained as usual, with only the phase being preserved while the modulus is replaced with the square root of the recorded intensity. The same dataset as used in Figure 4.25 is now reconstructed on a synthetic detector using the fPIE algorithm and the results are shown in Figure 4.26.

The fPIE reconstruction has produced a similar result as the ePIE algorithm albeit with slightly increased contrast in the phase image. This is as expected though as it is already known that ptychography is able to accommodate an illumination function so long as it is confined within the Fourier repeat unit cell in real-space. Down-sampling further produces an ‘under-sampled’ dataset

which is, in the conventional sense, below that sufficient for ePIE to operate successfully. In order to achieve such a condition, the pixel-pitch is increased to 165μm for the following reconstructions. As increasing the pixel-pitch of the detector whilst preserving the pixel-size removes a significant amount of counts (in this case reduced to a ninth) this dataset will now intrinsically be degraded by shot noise along with the effects of down-sampling. The effects of shot noise can be seen in both of the reconstructions shown in Figure 4.27 and Figure 4.28. With that in mind it can still be seen that for the conventional ePIE reconstruction (which does not have a mechanism for detector interpolation) the illumination is falsely contrained within a real-space unit cell that is sufficiently smaller than the physical extent of the illuminating beam. The resultant phase image has little contrast and it is difficult to observe the finer details of the specimen. It is clear that ePIE is unable to process such data.

When the same dataset is processed through fPIE (after adding virtual pixels in between the measurements to allow for the interpolation) it can be seen that the illumination function now fits easily within the real-space unit cell (see Figure 4.28). The result of this process is an image which, although degraded by shot noise, is much improved from a sampling viewpoint. The contrast is sufficient so that features of the specimen may be seen at both large and small scales (the resolution is reduced but this will be severely affected by the reduction in counts).

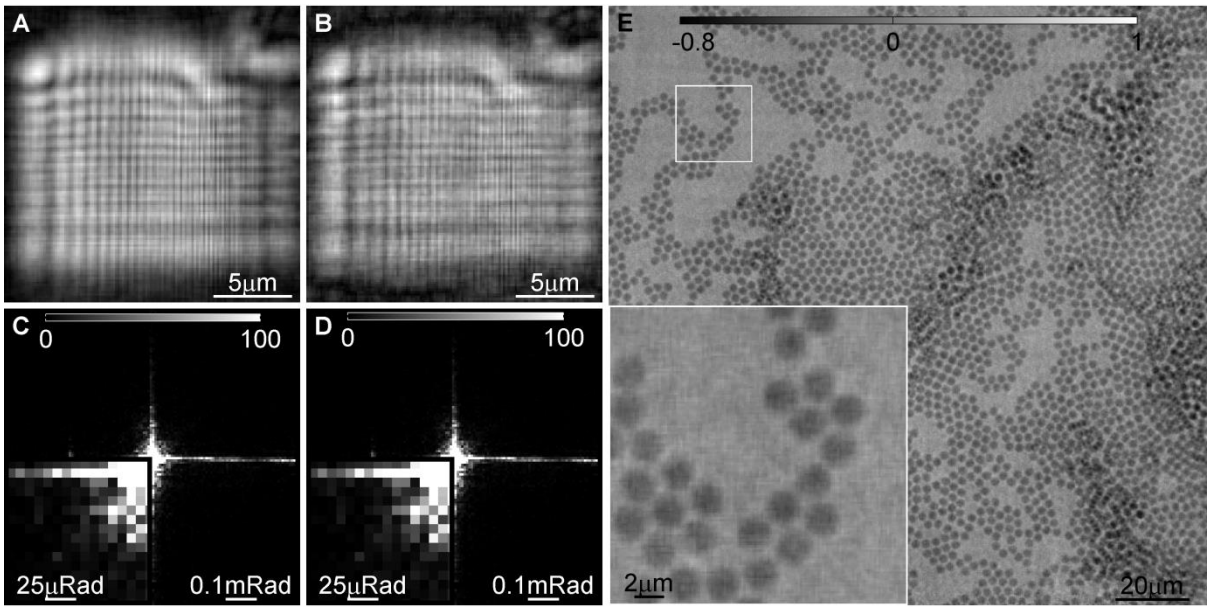

Figure 4.25: ePIE reconstruction of the data after down-sampling by a factor of 2x2. a) Input illumination function. b) Output illumination function. c) Typical input diffraction pattern. d) Corresponding output diffraction pattern estimate. e) Output phase image of the specimen. The diffraction patterns contain magnified inlays of the region underneath their top right corner.

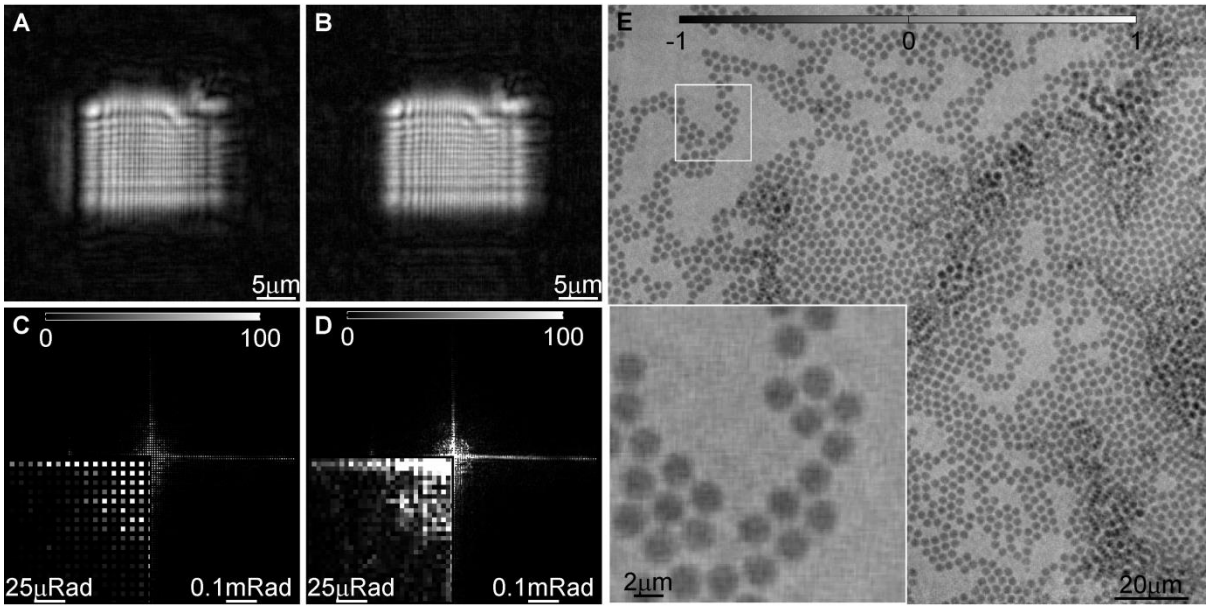

Figure 4.26: fPIE reconstruction of the data after down-sampling by a factor of 2x2. a) Input illumination function. b) Output illumination function. c) Typical input diffraction pattern. d) Corresponding output diffraction pattern estimate. e) Output phase image of the specimen. The diffraction patterns contain magnified inlays of the region underneath their top right corner.

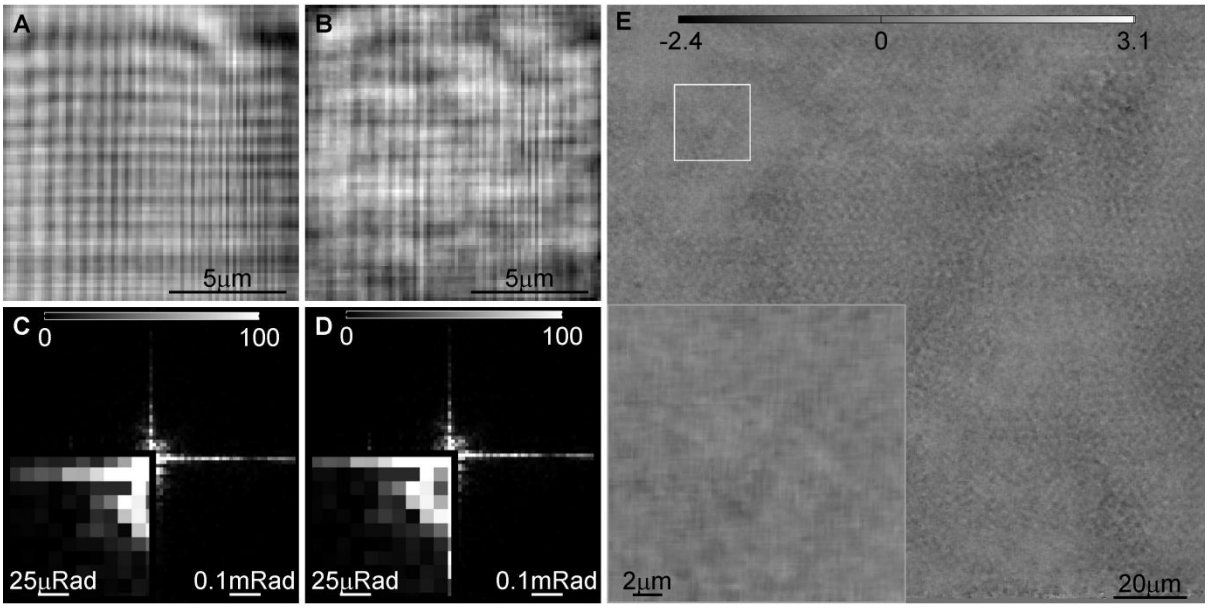

Figure 4.27: ePIE reconstruction of the data after down-sampling by a factor of 3x3. a) Input illumination function. b) Output illumination function. c) Typical input diffraction pattern. d) Corresponding output diffraction pattern estimate. e) Output phase image of the specimen. The diffraction patterns contain magnified inlays of the region underneath their top right corner.

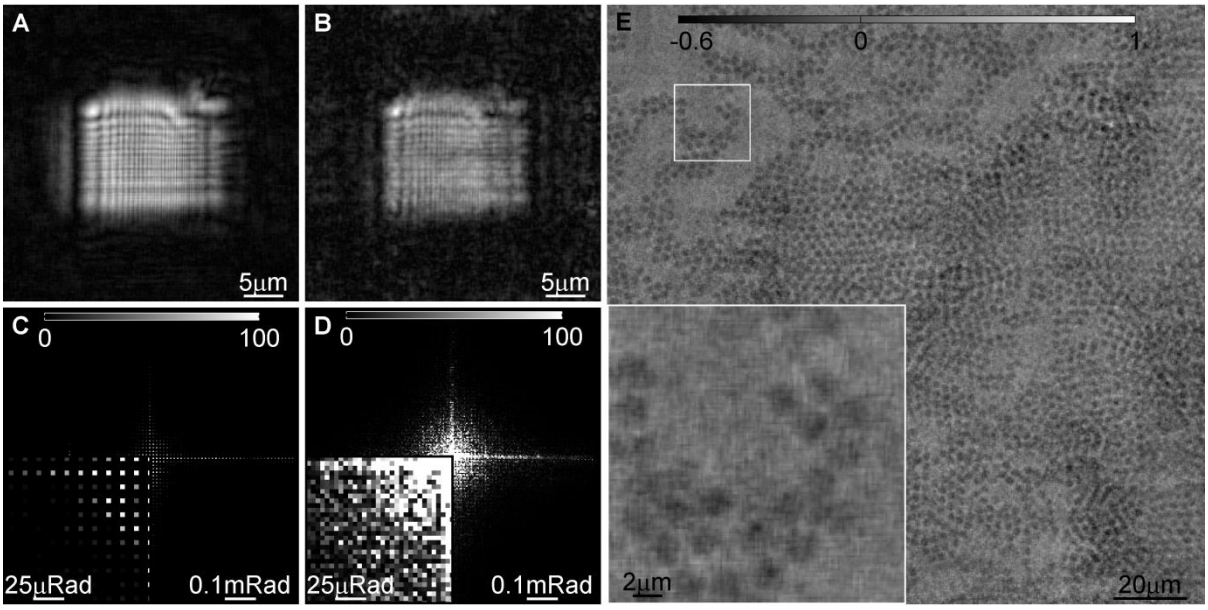

Figure 4.28: fPIE reconstruction of the data after down-sampling by a factor of 3x3. a) Input illumination function. b) Output illumination function. c) Typical input diffraction pattern. d) Corresponding output diffraction pattern estimate. e) Output phase image of the specimen. The diffraction patterns contain magnified inlays of the region underneath their top right corner.

4.3.2 Integrating Pixels

The discussion about the sampling condition required in a ptychographic imaging system has, so far, only considered the number of measurements in the form of single coherent points. In reality these 'coherent' points are blurred out by an incoherent integration of those points in a convolution operation. This is due to the detector pixel-size being of sufficient size so that the detection area of the pixel fills the whole gap (or a significant amount of the gap) between measurement points. This binning operation is an incoherent addition of the coherent states that exist within each pixel. So long as the pixel-pitch is sufficiently fine, such that the sampling condition is satisfied, then any pixel-size between zero and the pixel-pitch does not affect the sampling condition.

The sparse sampling example described above is now extended to the more practical situation of large integrating detector pixels. The same dataset is again used to demonstrate this principle. The pixels already integrate over the whole pixel-pitch of the detector and instead of removing subsets of pixels, subsets of pixels are integrated in intensity so that the pixel-size increases along with the pixel-pitch. The effect of increasing the fill factor from a sparse case to a practical case is shown in Figure 4.29.

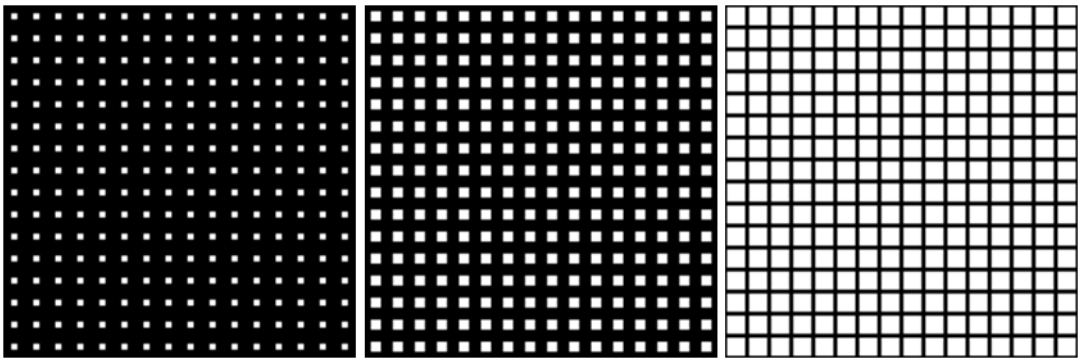

Figure 4.29: Measured pixels (white) with varying fill factors. a) 0.3. b) 0.5. c) 0.9.

The binned reciprocal-space sampling condition is important in the x-ray regime as the high quality, photon-counting detectors currently available have relatively large pixel-sizes (as with the current detector with a pixel-size of 55µm). As the focussing and characterisation of hard x-ray beams is

difficult (Schropp et al., 2010), satisfying the conventional single-shot sampling condition is an experimental difficulty.

As well as having large pixel-sizes, the direct x-ray photon counting detectors also have limited flux rates and finite regions of linearity. It is therefore often advantagous to employ a diffuse illumination function (Guizar-Sicairos et al., 2012, Maiden et al., 2013). Diffuse beams spread out quickly along the optic axis and so without a sufficiently considered setup of the specimen and probe forming optics, the illumination function under these conditions will become too large at the specimen plane. The ability to meet the sampling condition and maximize the number of photons recorded during the exposure time is an important aspect of optimising ptychographic imaging in the x-ray regime.

The above issues are exacerbated when performing Bragg angle ptychography (Hruszkewycz et al., 2012). The recording of Bragg reflections requires that the detector be positioned at steep angles away from the optic axis and so the height of the experimental hutch, along with its length, contrains the localization required of the illuminating beam in the specimen plane. Relaxing the single-shot sampling condition, through a reduction in real-space step size, allows for fundamental changes to be made to the ptychographic imaging setup, greatly relaxing many of the most problematic contraints.

The increase in pixel-size when moving from a sparse detector to more practical pixel-sizes, introduces the recorded measurement with an incoherent sum of coherent values,

$$I^m = \sum_{n=1}^{N} |\Psi|^2_{m,n} \,, \tag{4.3}$$

where m indexes the measured pixel coordinates, n indexes the virtual sub-pixel coordinates within this measured pixels, and I^m represents the measured intensities. The process is shown in Figure 4.30.

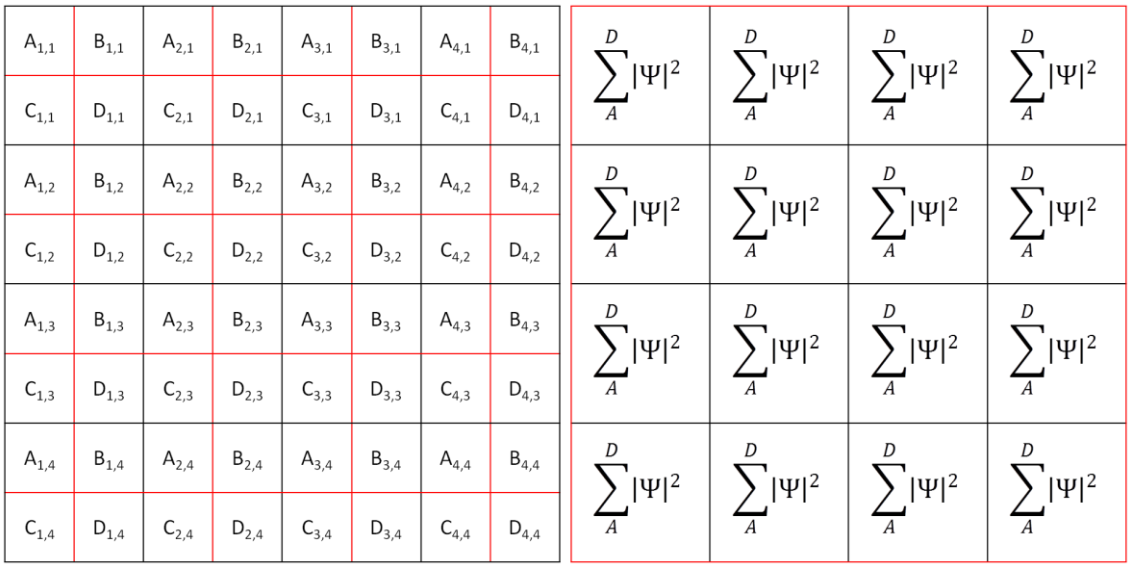

Figure 4.30: Down-sampling of original diffraction patterns. a) Example array represented by four subsets (a,b,c,d). b) Incoherent sum of the subsets create a down-sampled version.

An existing method of improving the sampling condition is achieved by physically scanning the detector on a sub-pixel grid (Chushkin and Zontone, 2013). Such a method does however require a second scanning stage for the detector with the accuracy to scan the detector on a sub-pixel grid. The ptychographic sampling condition suggests that the existing real-space scanning stage may be exploited in order to overcome the issue, without requiring sub-pixel accuracy of a detector scanning stage.

Datasets which have been under-sampled in reciprocal-space must be computationally interpolated such that the illumination function at least fits within the Fourier-repeat unit cell in real-space. A new algorithm, named sPIE, achieves this by employing a synthetic detector made up of 'virtual' pixels. The virtual pixels are of a pixel-size and spaced at a pixel-pitch that meets the Nyquist sampling condition of the complex wave-field. The real-space ptychographic interference is then used to unlock the incoherent convolution within the datasets and ultimately the relative phase of all the pixels. Unlike previously with sparse detectors, such an integrating detector consists of no recorded measurements directly. Instead each area of the synthetic detector should be constrained by a single measurement from the physical detector. Figure 4.31 shows how the synthetic detector, which has a finer pixel-size than its physical counterpart, may be rearranged into a stack of estimates

that each matches the properties of the physical detector. Each stack of pixels may then be constrained by the corresponding intensity measurement recorded on the physical detector.

The interpolation process requires that the original dataset is expressed on a synthetic detector with a reduced pixel-pitch. For the sparse example used with the fPIE algorithm this required taking only the measured set of pixels, A, and padding them with virtual pixels. For the situation of interpolating large pixels the update step has a mismatch between the estimated pixel-pitch and the physical, measured, pixel-pitch. In order to process such data the synthetic detector is again segmented into several subsets. However, unlike previously, all of these subsets are to be constrained by the measured data and no virtual pixels are to float directly. Instead the ratio between the measured intensities and the sum of squares of the subsets is used as a scaling parameter such that after the reciprocal-space update the sum of squares of the virtual pixels that are within each of the measured pixels are equal to the measured intensity value over that region.

The synthetic diffraction estimate may be expressed through subsets by shifting the virtual pixels into stacks. The sum of intensities along the new dimension gives the estimate of the measured intensity values. Figure 4.31 shows how the single exit-wave is reshaped into a stack of exit-waves which each match the size of the physical detector.

Constraining a set of complex numbers from the sum of their squares is achieved by applying a constant scaling factor to each sub-pixel such that the sum of their squares matches that of the measured intensity whilst the internal distribution within the measurement area is preserved. This is achieved with a generalisation to the reciprocal-space intensity contraint of the sPIE algorithm,

$$\Psi'_{m,n} = \frac{\Psi_{m,n}\sqrt{I_m}}{\sqrt{\sum_{n=1}^{N}|\Psi|^2_{m,n}}}, \qquad 4.4$$

where Ψ and Ψ' represent the complex value at each synthetic pixel before and after the update step respectively, I represents the intensity value of the recorded pixel, m addresses the recorded

pixel coordinate, n addresses the synthetic sub-pixel coordinates, and N is the number of synthetic sub-pixels per recorded pixel.

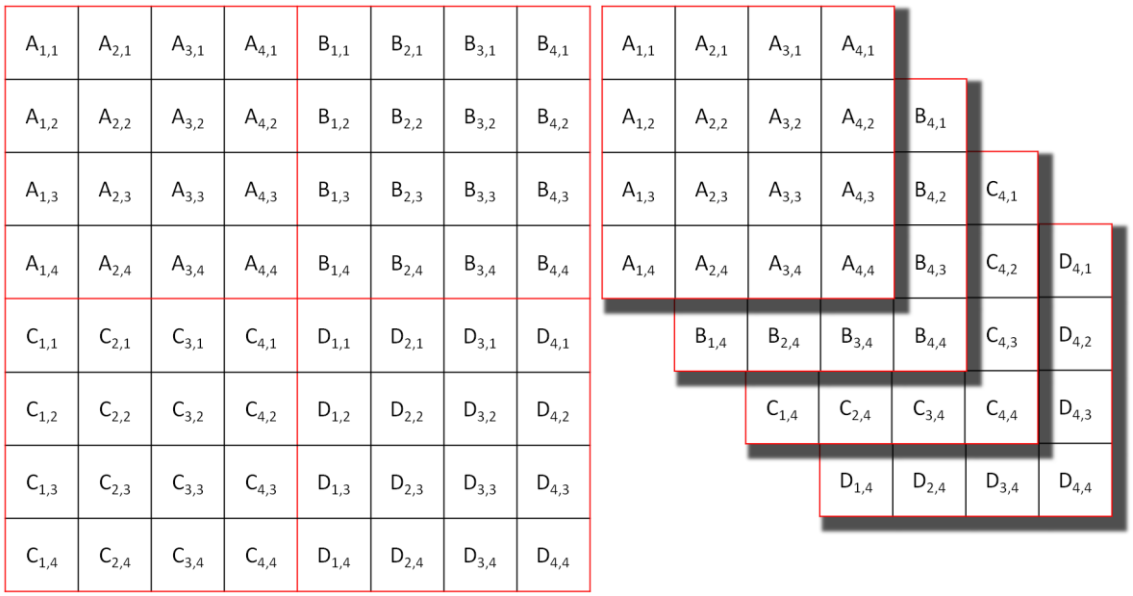

Figure 4.31: The reshaping operation for binned pixels from (a) the synthetic detector to (b) a group of subsets that each matches the physical detector.

As well as improving the ability to reconstruct poor quality datasets, the princinple of up-sampling allows for a much larger illumination function than has previously been possible. In order to explore this, the same dataset is computationally binned down (as in Figure 4.30) before processing through the sPIE algorithm.The binning is applied in two stages (a factor of 2x2 and 3x3) until the dataset is critically under-sampled, below the conventional, single-shot CDI, condition. Figure 4.32(a1-c1) shows a typical diffraction pattern from each of the datasets, that are subsequently processed through the sPIe algorithm, with pixel-sizes of 55, 110, and 165µm.

Figure 4.32(a2-c2) shows the corresponding reconstructed diffraction patterns after up-sampling (through sPIE) to the original pixel-pitch of 55µm. Figure 4.32(a3-c3) shows the reconstructed diffraction patterns after up-sampling the the same three datasets (through sPIE) to half of the physical pixel-pitch of the originally recorded data (27.5µm). Some structure (principally in the form of horizontal and vertical fringes) emerges beyond that which was physically measured.

Figure 4.32(a4-c4) shows the reconstructed diffraction patterns after up-sampling (through sPIE) to a quarter of the physical pixel-size of that which was originally recorded (13.75μm). The structure that began to emerge in Figure 4.32(a3-c3) is now clearer and resembles genuine structure. This suggests that the original 'well sampled' data was actually being restricted by the pixel-size. It is also interesting to note that even the data that was severely binned (actually just below the fundamental ptychographic sampling limit) may be successfully up-sampled by a factor 12x12 (see Figure 4.32(c4)), this reconstruction is solving for the distribution across 144 synthetic pixels for every single pixel intensity recorded.

Computational interpolation of the measured diffraction patterns does not necessarily guarantee an improvement to the quality of the reconstruction. Instead, the fundamental criteria by which the reconstruction algorithm should be judged is the quality and information content of the reconstructions. Such properties may be more clearly evaluated from the reconstructed specimen phase images that are shown in Figure 4.33. Each element of the figure corresponds to the equivalent element position of the diffraction patterns shown in Figure 4.32.

The ePIE reconstructions become very low quality at a binning factor of 2x2 and any useful information is completely destroyed at a binning factor of 3x3. The sPIE algorithm handles the data with a binning factor of 2x2 well (see Figure 4.33(b2)), with an improvement in quality above even that of the ePIE reconstruction of the original data (Figure 4.33(a1)).

The apparent improvement from up-sampling when the data is within the single-shot sampling condition either suggests a weakness in the current setup (the current constraints are not strict enough) or that other forms of incoherent addition (such as that due to the partial spatial and temporal coherence within the experiment) is present. Such effects may be somewhat accounted for by the interpolation step. The incoherent addition that would originally have existed across measured pixels (and so not accounted for by up-sampling) is, after the binning operation, largely an incoherent addition within the pixel-size and so is now in the realm of the up-sampling process. As a

result, sPIE attempts to account for these artefacts as a distribution across the synthetic pixels. It is worth noting that a distribution on such a scale in reciprocal-space is expressed at the edges of the real-space window, an effect that can be seen in the up-sampled probes of Figure 4.34 (rows 3 and 4).

The binning effect is resulting in a different reconstruction from the fPIE reconstruction of the data which has been down-sampled by the same amount (same increase in the pixel-pitch), the difference being in the pixel-sizes. For example, Figure 4.33(c4) is a better reconstruction than the fPIE equivalent shown in Figure 4.28. One possible contributing factor to this is that where the sparse example only records those photons that are incident on those pixels, the integrating pixels capture all of the counts within the pixel-pitch of the detector. In general, so long as the sampling condition is satisfied, increasing the pixel-size will always act to improve the signal-to-noise ratio (SNR) of the dataset.

The corresponding reconstruction of the illumination functions are shown in Figure 4.34. The aliasing effect from the down-sampling is clearly visible in Figure 4.34(c1) and are largely relieved by the up-sampling process, shown in Figure 4.34(c2).

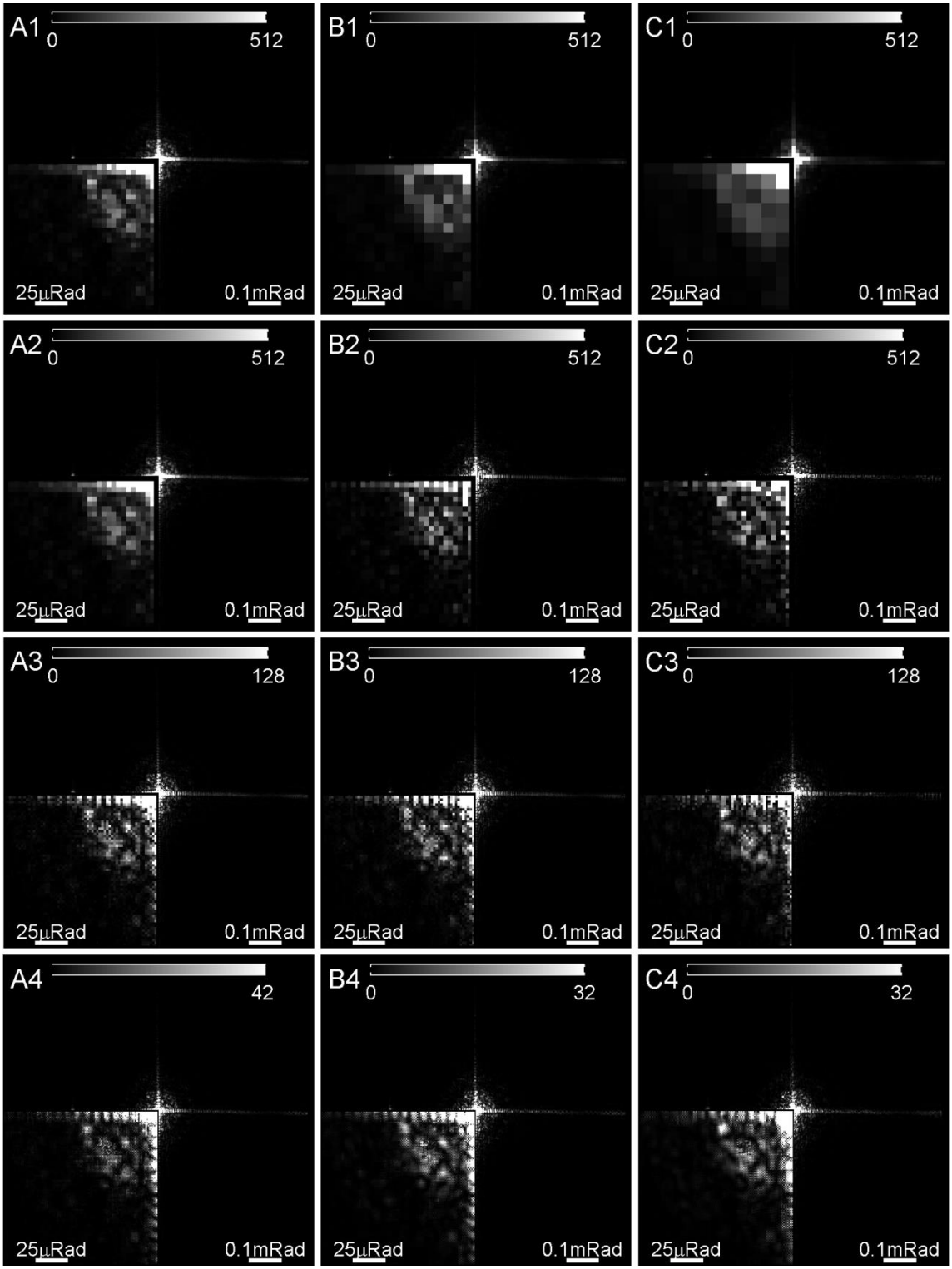

Figure 4.32: Typical diffraction patterns with magnified inlays of the region underneath their top right corner. (a-c) represent reconstruction with input diffraction patterns of 256x256,128x128, and 85x85 pixels, respectively. 1) ePIE reconstruction, 2) sPIE reconstruction to original pixel-size, 3) sPIE reconstruction to a quarter of the pixel-size, 4) sPIE reconstruction to an eighth of the original pixel-size.

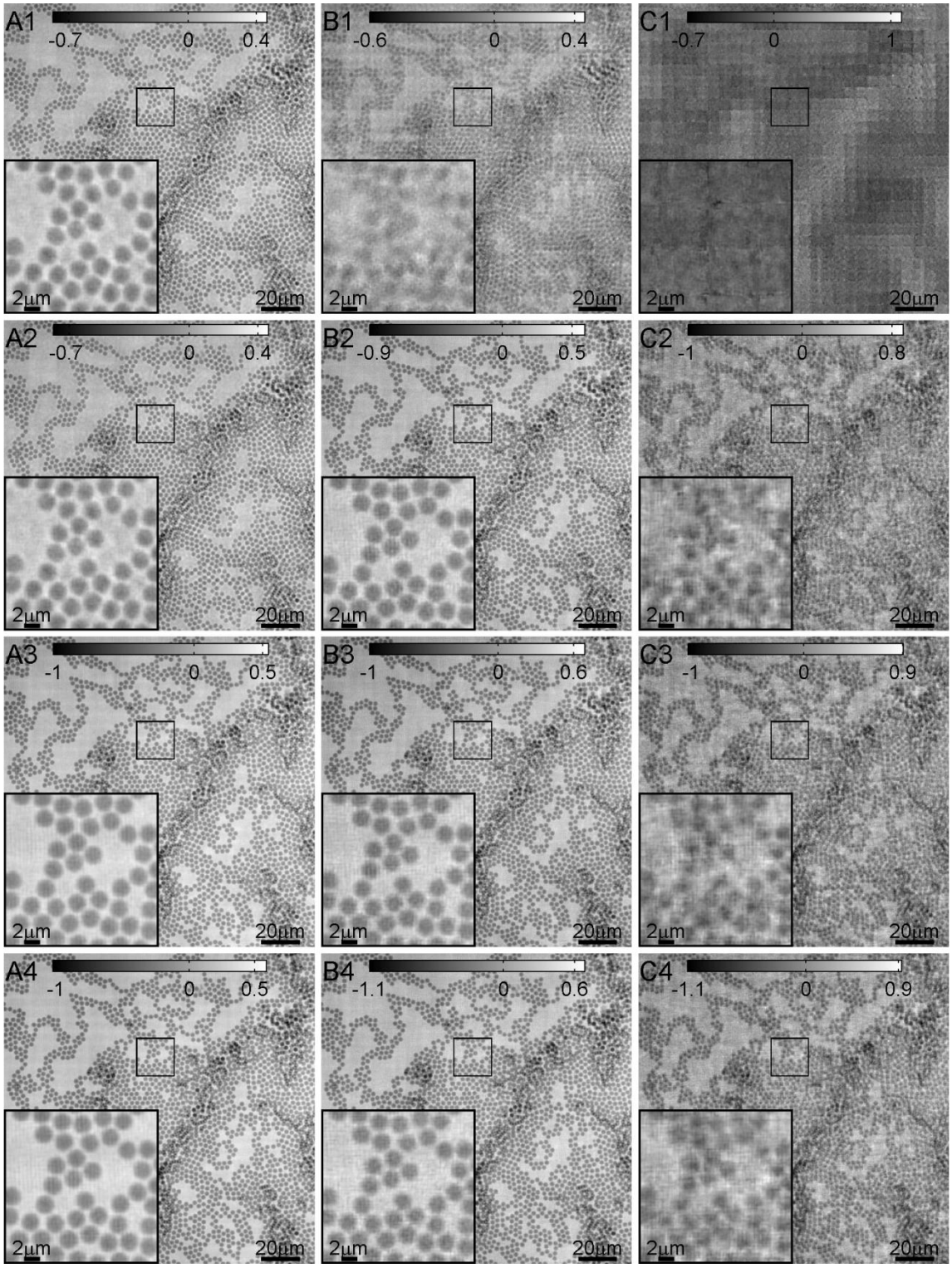

Figure 4.33: Reconstructed phase images with magnified inlays of the region within the black box. a-c) Reconstructions of the data shown in Figure 4.32 (a-c). 1) ePIE reconstructions 2) sPIE reconstruction to the original pixel-size, 3) sPIE reconstructions to a quarter of the original pixel-size, 4) sPIE reconstructions to an eighth of the original pixel-size.

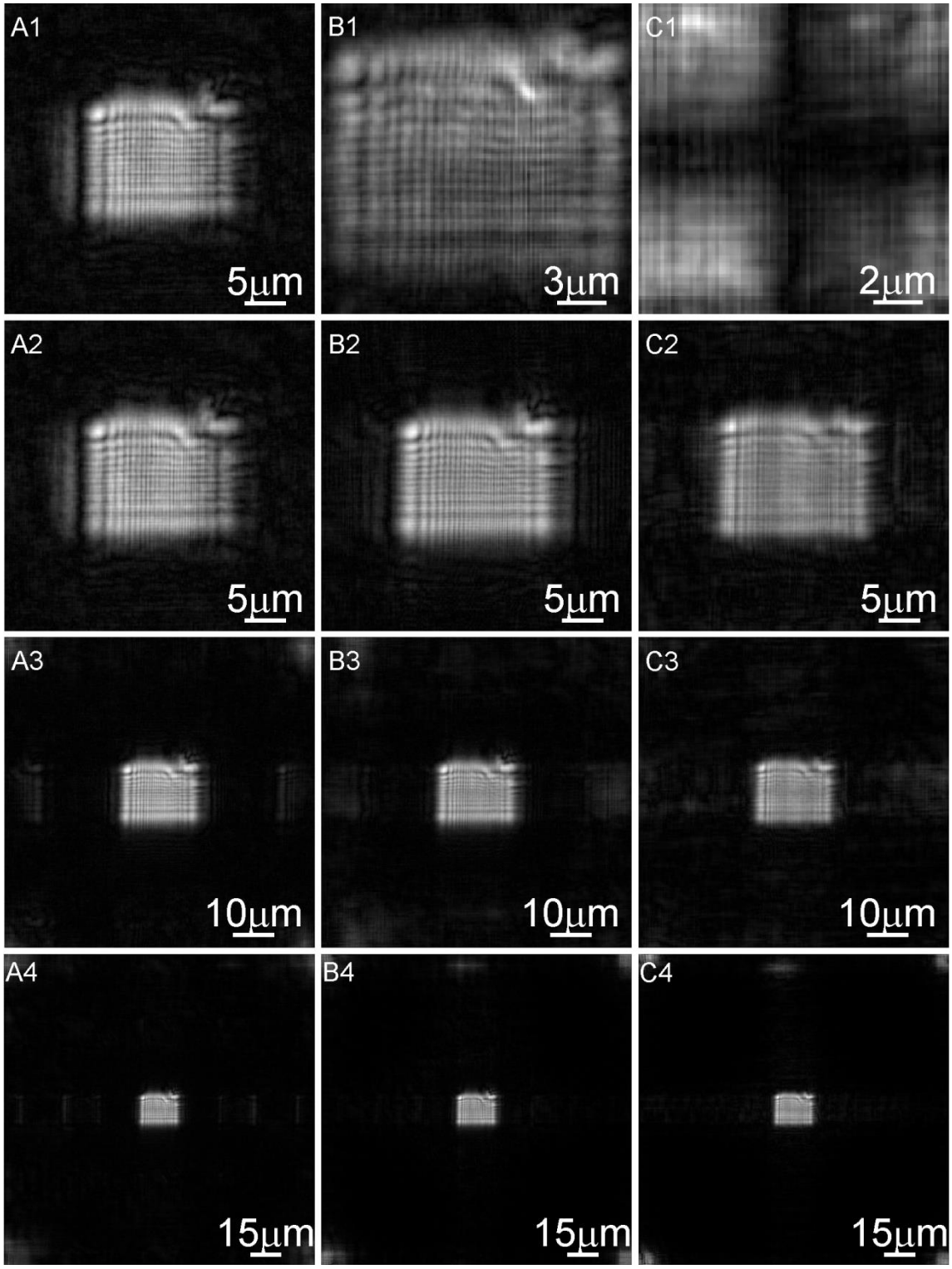

Figure 4.34: ***Reconstructed probes in modulus. (a-c) Reconstructions of the data shown in Figure 4.32 (a-c), respectively. 1) ePIE reconstructions 2) sPIE reconstruction to the original pixel-size, 3) sPIE reconstructions to a quarter of the original pixel-size, 4) sPIE reconstructions to an eighth of the original pixel-size. Note that the probes in rows 3 and 4 contain some low level intensity in the corners, as discussed above.***

4.3.3 Simulations

Although the sampling condition shown in section 3.2 has been shown to hold true for practical x-ray data, the factor of three is not sufficient in isolation to significantly change the manner in which x-ray (and other) ptychographic microscopes are set up. In order to show the potential of the technique proposed here, some simulated datasets are processed through sPIE which are at the limit of the sampling condition. The sampling factor, $\hat{S}$, of the datasets is only two and one. Each diffraction pattern is also at the limit of the required number of detector pixels, 16 and 4. In order to achieve such datasets, a large original dataset with a sampling factor of 32 (with 64x64 pixels in the detector) is simulated and subsequently binned by factors of 16 and 32. The 4x4 pixel dataset along with the sPIE reconstruction is shown in Figure 4.35. It can be seen that such a dataset is adequate to produce a good reconstruction of the original image.

Comparing Figure 4.35 to Figure 3.11, it can be seen that the sampling condition is not the full story. By expressing the same dataset across pixels of different sizes (but importantly the same pitch) the reconstruction can be affected. The result here is showing that the 'coherent' imaging technique can actually be improved by introducing some levels of incoherence, where that incoherent addition takes place within a region less than the required sampling pitch (determined by $\hat{S}$). This is already understood within the realm of the single-shot CDI sampling condition, as increasing the fill factor of a detector offers an increased signal to noise ratio. Here the same principle is shown to extend into the more general ptychographic sampling condition, where the incoherent integration spreads across the pixel-pitch required by the single-shot sampling condition but remains within that required by the ptychographic sampling condition.

The ultimate limit of the technique is to reduce the number of pixels in each orthogonal direction down to just two. Ptychographic data can in principle be recorded with a three pixel detector, as shown for the non-iterative method (McCallum et al., 1995), but in order to keep to the sampling framework as outlined in section 3.2, a four pixel detector is used. The resultant dataset, with a

sampling factor of only 1, is reconstructed using the sPIE algorithm and the result is shown in Figure 4.36.

The illumination function is 16 times the width of the real-space Fourier-repeat cell captured by the pixel-pitch. As such the diffraction patterns must be up-sampled by at least a factor of 16x16 in order to house the illumination function in real-space. Here the diffraction patterns are up-sampled by a factor of 32x32 - bringing the completed reconstruction in line the single-shot sampling condition. The reconstruction does successfully recover the object although it is slightly degraded by some unwanted structure in both the object and the illumination. Low-level structure is observable and some detail within the face of the cameraman and the camera itself is just about resolvable.

Reconstructing images with a detector consisting of only four pixels, as described above, is similar to other sector detector methods (Hornberger et al., 2008, McCallum et al., 1995). These methods do however require a focussed probe, here though the probe is much greater than the image resolution. Although the current algorithm may still not be entirely optimised for such data, the simulations do show that the factor of three up-sampling described above is far from being the limit of the reciprocal-space up-sampling technique offered by ptychography.

In these demonstrations the detector pixels have been computationally binned such that the reciprocal-space sampling condition is reduced, future experiments can exploit the same principle in order to move the detector closer to the specimen. Reducing the specimen to detector distance extends the total angular range captured by the detector and therefore dramatically improves the potential resolution limit of any given setup. For the x-ray example above, the resolution improvement would be approaching a factor 3, which takes this rather sub-optimal setup into the 50nm resolution regime. It is entirely conceivable that with a further reduction in the specimen to detector distance, employing some condensing optics, along with a reduction in the specimen scanning pitch, the resolution could be pushed significantly higher.

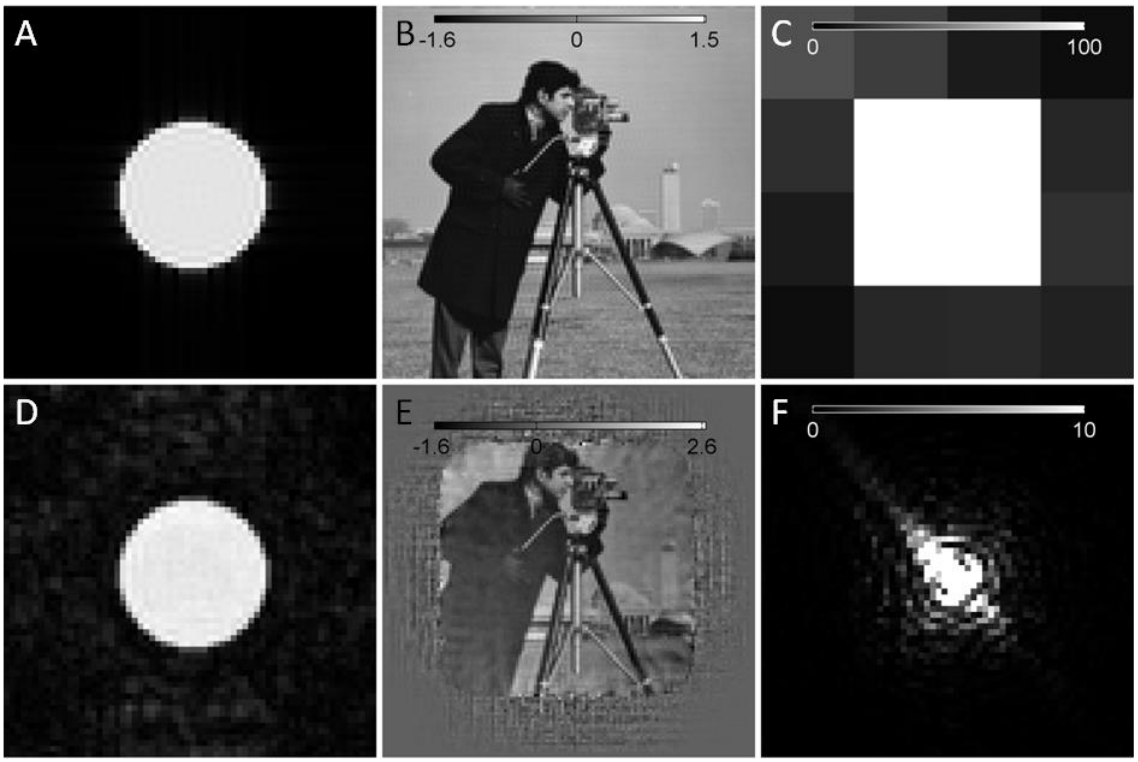

Figure 4.35: sPIE reconstruction of sparsely sampled data with $\hat{S}$=2. a) Original probe modulus. b) Original phase image. c) Input diffraction pattern with 16 large pixels. d) Reconstructed probe modulus. e) Reconstructed phase image. f) Reconstructed diffraction pattern with 1024 reconstructed smaller pixels.

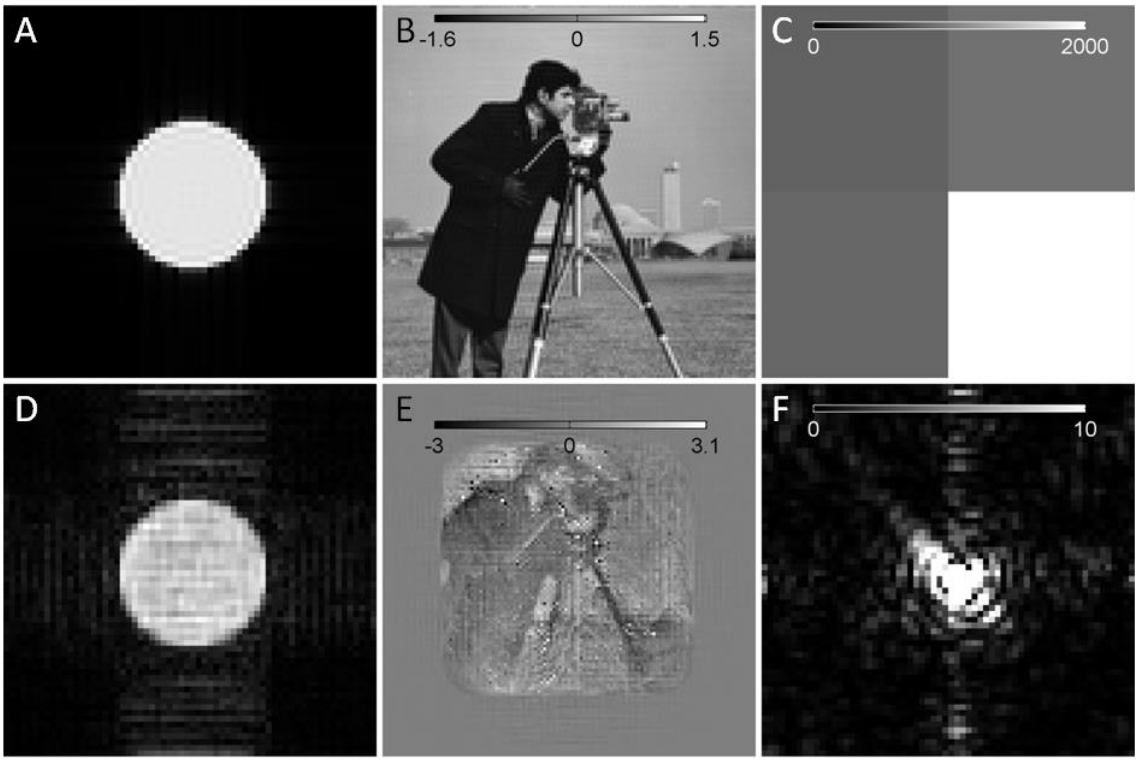

Figure 4.36: sPIE reconstruction of sparsely sampled data with $\hat{S}$=1. a) Original probe modulus. b) Original phase image. c) Input diffraction pattern with 4 large pixels. d) Reconstructed probe modulus. e) Reconstructed phase image. f) Reconstructed diffraction pattern with 1024 reconstructed smaller pixels.

4.3.4 Summary

In summary, this chapter has covered three sets of experimental runs at a newly commissioned beam line. Due to the nature of working on such a young beam line, the initial run did not yield adequate results. However, the issues that came to light during that experiment raised questions about the algorithm and in particular about the ability to handle under sampled diffraction patterns.

For the second run, the two main issues from the first run were rectified. A monochromator was installed and there was the ability to position the detector at the far end of the hutch, an adjustment of the specimen to detector distance from the original 6m to 14m. These improvements, along with a simplification of the setup, allowed for some good quality data to be recorded. From that data a large field of view image of a test specimen was produced and a basic comparison to theoretical values showed that the phase was quantitative across the whole image. Obtaining a quantitative phase image across a region larger than the coherence width of the beam demonstrated the ability that ptychography has to synthesise an extended illumination function. Employing the theory outlined in chapter 2.3, this principle was pushed still further. Binning the recorded diffraction patterns down below the conventional diffractive imaging limit reduced the real-space window to a width smaller than that of the physical beam. Recovering from that position to produce a clean, high quality reconstruction showed that ptychography was not tied to the same sampling constraints that had previously been thought essential.

As the dataset used was only able to demonstrate a modest level of up-sampling, a simulation was employed that, by recovering from as few as 4 pixels in the detector, showed that ptychography truly breaks free from the conventional sampling wisdom of single-shot CDI.

5 Visible Light Ptychography

The previous chapters have described how ptychography offers a rich sampling framework and how that may be used in order to extend the effective coherence width of a microscope. The phenomenon of coherence is one of making repeated measurements from a beam of individual photons (or other quanta) after emission from a source, where each photon is emitted in (and arrives in) the same state. That is to say that each emission (and propagation) is identical to all others. Coherent diffraction relies upon passing a beam of such radiation through a specimen and integrating their intensities over time. After a sufficiently high dose, the recorded pattern resembles the probability distribution of arrival of any single photon. The modulus of the underlying wave function is related to the intensity pattern by a power of two and so unlocking the phase portion of the wave allows propagation back to the complex image in real-space.

The binned pixels problem described in section 4.3 is an example of separating out a distribution of incoherently mixed coherent modes. There are however many other contributors to the incoherent addition in the detector plane of a ptychographic dataset and they are very much dependent upon the experimental setup. Other forms of incoherence come from the source (both spatial and temporal) and the stability of the optics, specimen, scanning stage, and detector (points spread functions). These contributors, unlike the large pixel case, have incoherently mixed terms across detector pixel boundaries (not only within them). This chapter is concerned with the expression of, and more importantly the computational decomposition of, these incoherently mixed terms within a ptychographic dataset.

A diffractive imaging setup may be considered perfectly coherent only when the source emits the radiation in identical states, the specimen remains stable (in the same state), and the response of all optical elements remain fixed throughout the data acquisition time. Coherence is washed out by changes of state in each of the above three elements during the acquisition time and any factor which contributes towards the lack of coherence will be referred to as adding incoherence into the system.

Each form of incoherence may be described as an incoherent convolution of some kind. For example, large integrating pixels can be viewed as a convolution of sparse detector pixels with a point-spread function whose width is less than the pixel-pitch of the detector. This may also arise from lateral movements of the detector or the source during the exposure time but is only distinguishable from binning when the effective envelope of incoherence in the detector plane is greater than the pixel-pitch of the detector. As from the dataset's point of view these are entirely indistinguishable, they will all be referred to as a binning effect with an equivalent pixel-size in the detector plane. The dataset is only degraded by incoherent addition when the interaction crosses over measurement points. In some experimental setups the source is imaged into the detector plane, where the effect of an extended source is relative to the detector’s pixel pitch. In others (for

example, STEM) the source is imaged onto the specimen plane, where the effect of an extended source is relative to the real-space step size.

Single-shot CDI relies entirely on the radiating beam having a coherence width in reciprocal-space greater than the pixel-pitch of the detector (due to the requirement on a coherent convolution of object Fourier components). In such a regime, any form of incoherent convolution increases the constraints on the probe size in real-space. Ptychography introduces a real-space scan which, when is suitably precise and remains stable, may be considered as introducing a coherent convolution operation: the scan step (or pitch) is less than the coherence width of the beam such that subsequent exposures overlap and separate measurements are then made at each position. Section 4.3.2 shows how reducing the real-space scan pitch is enough to solve for the phase problem when the levels of coherent interference in the detector plane are extremely low (see Figure 4.35 and Figure 4.36). Handling a dataset that is recorded with pixels too large to satisfy the conventional sampling limit is a further demonstration of ptychography's robustness to experimental issues.

So far, only the improvement to current ptychographic images has been considered, where instrumental imperfections are decoupled from the coherent experiment. However, other forms of mixed states caused by multiple modes within the illuminating beam (i.e. probing a specimen with a mixture of photon energies) are recorded at the detector plane in a similar way to the binned pixel elements, through an incoherent summation. Alterations to the real-space update process allows the mixed states to be decomposed in much the same way as the internal distributions of large pixels have been in section 4.3.2. A full decomposition of these mixed states within such datasets not only allows for cleaner reconstructions but also paves the way for the imaging of spectral responses, dynamic events, and other mixed states. These effects are not limited to the specimen and so decomposition of modes within the illumination would allow for instrument characterisation, such as source distribution and lens behaviour.

5.1 MS-PIE

The sPIE algorithm exploits a modification to the reciprocal-space constraint in order to constrain a group of complex estimates that exist within an area of the detector that were recorded as an integration of their intensities. The other forms of incoherence and mixed states are also integrated in intensity at the detector plane. Instead of across an area though, the integration occurs across all dimensions such as photon energy and specimen state. Incorporating the various dimensions into the algorithm requires modifications in the real-space updates. Each modal contribution must be tracked, propagated, and updated individually. The requirement on the real-space expansion can be seen in Figure 5.1 where a source function, S, is added and the previously single probe, P, and object, O, functions have been extended into three-dimensional stacks.

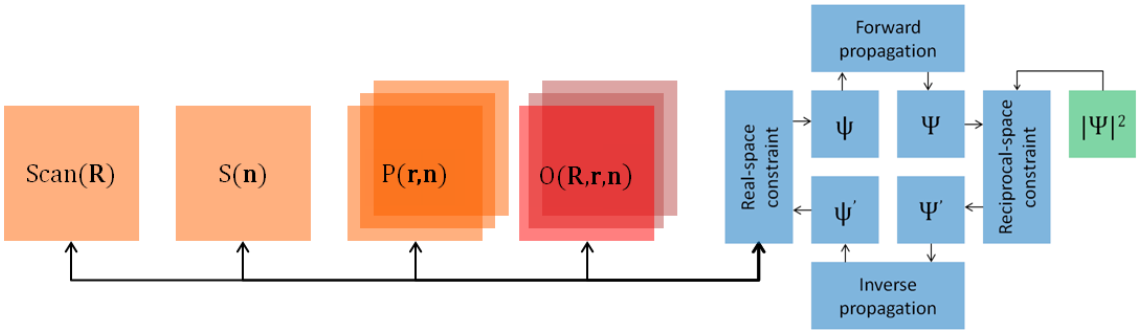

*Figure 5.1: A flow diagram of the MS-PIE reconstruction algorithm for a single iteration at scan position **R**, where **n** represents the source coordinates and **r** represents the real-space coordinates. The kernel of the algorithm (shown in blue) feeds from the known values, $|\Psi|^2$, (shown in green) in order to solve for the unknown object(s) (shown in red), and the partially known probe(s), P, scan, and source, S, (shown in orange).*

5.1.1 Multi-Dimensional Kernel

The reconstruction process follows the same basic structure as sPIE, with several separate modes being processed in parallel in a multi-dimensional array. In order to minimise the reconstruction time when transforming many exit-waves back and forth to the detector plane, the parallelisation power of the readily available NVIDIA graphics cards and CUDA library have been employed in these algorithms. The NVIDIA graphics cards are originally designed for the gaming industry, their power in parallel computation has however made them an extremely valuable tool for many science and engineering algorithms. The CUDA library opens up the GPU's (graphics processing unit) power to

the scientific community and in this case dramatically reduces the execution time required for a Fourier transform, and so reduces the overall reconstruction time. Through the construction of the MS-PIE algorithm, I have allowed the extra dimensions that are introduced by the incoherent modes and annealing estimates to be processed in one streamlined operation.

Each modal contribution must be coherently propagated through the system before all contributions are incoherently summed in the detector plane to give the current estimate of the recorded diffraction pattern. The propagation of each such mode between planes must be performed within a two dimensional array that satisfies the Nyquist condition. Beyond that the modal contributions and annealing estimates may be expressed along a further two dimensions. The indexing of dimensions is used when the dimensionality of the modal contribution exceeds one, when the source is extended both spatially and temporally for example. After incorporating the real-space scan, the algorithm is constructed around a five-dimensional array, two for the spatial dimensions, one for the real-space scan, one for the incoherent modes, and one for the annealing estimates. The wave function is then described as,

$$\psi(r_x, r_y, \boldsymbol{R}, \boldsymbol{\eta}, \boldsymbol{\xi}) = \frac{\sqrt{S(\boldsymbol{\eta})}}{\sqrt{\sum_{r_x}\sum_{r_y}\left[\left|P(r_x, r_y, \boldsymbol{R}, \boldsymbol{\eta}, \boldsymbol{\xi})\right|^2\right]}} \cdot P(r_x, r_y, \boldsymbol{R}, \boldsymbol{\eta}, \boldsymbol{\xi}) \cdot O(r_x, r_y, \boldsymbol{R}, \boldsymbol{\eta}, \boldsymbol{\xi}), \quad 5.1$$

where r_x and r_y represent the real-space coordinates in the x and y directions respectively, $\boldsymbol{R}$ indexes the real-space positions, $\boldsymbol{\eta}$ indexes the modal contributions, $\boldsymbol{\xi}$ indexes the drift estimates, and S is the source function. The real-space wave function may be propagated to the Fraunhofer plane through a Fourier transform applied to this array along the two real-space dimensions as follows,

$$\Psi(u_x, u_y, \boldsymbol{R}, \boldsymbol{\eta}, \boldsymbol{\xi}) = \sum_{r_y}\left[\sum_{r_x}\left[\psi(r_x, r_y, \boldsymbol{R}, \boldsymbol{\eta}, \boldsymbol{\xi}) e^{\frac{-i2\pi(r_x \cdot u_x + r_y \cdot u_y)}{N}}\right]\right], \quad 5.2$$

where u_x and u_y represent the reciprocal-space coordinates in the x and y directions respectively (see Figure 3.3). Note that the $\boldsymbol{R}$ dimension is only included here for completeness. It is required when performing parallel updates as used in some algorithms, however for the serial PIE on which the MS-PIE algorithm is based each update step is executed on a single scan position at a time.

The group of incoherent estimates (that is estimates of the recorded intensity pattern at each position) can then be computed as a sum of intensities along the fourth dimension as follows,

$$I^e(u_x, u_y, \boldsymbol{R}, \boldsymbol{\xi}) = \sum_{\boldsymbol{\eta}} \left[\left| \Psi(u_x, u_y, \boldsymbol{R}, \boldsymbol{\eta}, \boldsymbol{\xi}) \right|^2 \right], \tag{5.3}$$

and the error associated with each annealing estimate is then computed as follows,

$$\Psi(\boldsymbol{\xi})_{error} = \sum_{\boldsymbol{u}} \left[\left| \sqrt{I^m(\boldsymbol{u}, \boldsymbol{R})} \right| - \left| \sqrt{\sum_{\boldsymbol{\eta}} |\Psi(\boldsymbol{u}, \boldsymbol{R}, \boldsymbol{\eta}, \boldsymbol{\xi})|^2} \right| \right]^2 . \tag{5.4}$$

The estimate associated with the lowest error is selected, with all other possibilities being abandoned. The selected set of incoherent modes can now be updated using the reciprocal-space update step,

$$\Psi'(\boldsymbol{u}, \boldsymbol{R}, \boldsymbol{\eta}) = \Psi(\boldsymbol{u}, \boldsymbol{R}, \boldsymbol{\eta}) + \alpha_\Psi \beta_\Psi \left([\gamma(\boldsymbol{u}, \boldsymbol{R}) \cdot \Psi(\boldsymbol{u}, \boldsymbol{R}, \boldsymbol{\eta})] - \Psi(\boldsymbol{u}, \boldsymbol{R}, \boldsymbol{\eta}) \right), \tag{5.5a}$$

$$\gamma(\boldsymbol{u}, \boldsymbol{R}) = \sqrt{\frac{I(\boldsymbol{u}, \boldsymbol{R})^m}{\sum_{\boldsymbol{\eta}} |\Psi(\boldsymbol{u}, \boldsymbol{R}, \boldsymbol{\eta})|^2}} . \tag{5.5b}$$

The back propagation can now be performed in the same fashion as the forward propagation, with the inverse Fourier transform being applied along the two reciprocal-space dimensions as follows,

$$\psi(r_x, r_y, \boldsymbol{R}, \boldsymbol{\eta}) = \frac{1}{N} \sum_{u_y} \left[\sum_{u_x} \left[\Psi(u_x, u_y, \boldsymbol{R}, \boldsymbol{\eta}) e^{\frac{i2\pi(r_x \cdot u_x + r_y \cdot u_y)}{N}} \right] \right]. \tag{5.6}$$

5.1.2 Real-Space Updates

The real-space updates for an experimental setup with mixed states in the object and illumination functions is more generally stated as,

$$O'(\boldsymbol{r},\boldsymbol{R},\boldsymbol{\eta}) = O(\boldsymbol{r},\boldsymbol{R},\boldsymbol{\eta}) + \mathbb{U}_O(\boldsymbol{r},\boldsymbol{\eta})[\psi'(\boldsymbol{r},\boldsymbol{R},\boldsymbol{\eta}) - \psi(\boldsymbol{r},\boldsymbol{R},\boldsymbol{\eta})]\,, \tag{5.7a}$$

$$P'(\boldsymbol{r},\boldsymbol{R},\boldsymbol{\eta}) = P(\boldsymbol{r},\boldsymbol{R},\boldsymbol{\eta}) + \mathbb{U}_P(\boldsymbol{r},\boldsymbol{\eta})[\psi'(\boldsymbol{r},\boldsymbol{R},\boldsymbol{\eta}) - \psi(\boldsymbol{r},\boldsymbol{R},\boldsymbol{\eta})]\,, \tag{5.7b}$$

where the update equations , $\mathbb{U}$, are defined as,

$$\mathbb{U}_O(\boldsymbol{r},\boldsymbol{\eta}) = \alpha_O\beta_O\frac{P^*(\boldsymbol{r},\boldsymbol{R},\boldsymbol{\eta})}{|P(\boldsymbol{r},\boldsymbol{R},\boldsymbol{\eta})|^2_{max}}, \tag{5.8a}$$

$$\mathbb{U}_P(\boldsymbol{r},\boldsymbol{\eta}) = \alpha_P\beta_P\frac{O^*(\boldsymbol{r},\boldsymbol{R},\boldsymbol{\eta})}{|O(\boldsymbol{r},\boldsymbol{R},\boldsymbol{\eta})|^2_{max}}. \tag{5.8b}$$

The distribution of power across the modes, for example the energy spectrum of illumination, is obtained as a source function, S, and the update of the source function is,

$$S'(\boldsymbol{\eta}) = S(\boldsymbol{\eta}) + \alpha_S\left(\sum_{r_x}\sum_{r_y}\left[\left|P(r_x,r_y,\boldsymbol{R},\boldsymbol{\eta})\right|^2\right] - S(\boldsymbol{\eta})\right) \tag{5.9}$$

5.1.3 Reciprocal-Space Error Metric

The reciprocal-space error metric for single mode ptychography (see equation 2.53) is also generalised in a similar manner such that,

$$\Psi_{error} = \sqrt{\frac{\sum_{\boldsymbol{R}}\left[\sum_{\boldsymbol{u}}\left[\left|\sqrt{I^m(\boldsymbol{u},\boldsymbol{R})}\right| - \left|\sqrt{\sum_{\boldsymbol{\eta}}|\Psi(\boldsymbol{u},\boldsymbol{R},\boldsymbol{\eta})|^2}\right|\right]^2\right]}{N_R N_u}}. \tag{5.10}$$

5.2 Multiple Wavelength Ptychography

For a lens-less setup (as used for the x-ray experiment shown in Figure 4.13) the source is imaged onto the detector plane. Introducing an energy spread within the source under such a setup

therefore produces a blurring effect, as shown in Figure 4.6. In this section, an experimental situation is manufactured in order to investigate multiple wavelength illumination within ptychography in the optical regime. A multiple wavelength source is a good experiment as it examines modal responses in three planes, the source (temporal spread), the probe (optics wavelength response), and object (specimen wavelength response). An illuminating beam consisting of photons that are in three separate states (energy levels) are passed through an energy dependant optical element (in this case an aperture with a diffuse membrane) onto a specimen which has features within it that have a different complex refractive index at different photon energy levels.

The theory of the four-dimensional sampling within a ptychographic dataset is discussed in detail in chapter 3. In chapter 4, a practical application is demonstrated for x-ray imaging in terms of the up-sampling of large detector pixels. Until recently, the presence of incoherence in ptychography (and diffractive imaging in general) has been seen as a nuisance. Although the up-sampling technique (and other work (Thibault and Menzel, 2013)) shows that this no longer need to be a major issue, this chapter describes work which has shown for the first time that incoherence effects can in fact provide a much richer dataset. When such a dataset is processed correctly, the reconstructions can in fact contain much more information than a perfectly coherent experiment. The principle of modal decomposition is somewhat generalised, from the up-sampling example, such that several entirely uncorrelated experimental setups (that is different source, illumination, and object functions) can be recorded together as an incoherent sum and successfully separated into their constituent coherent modes.

This chapter concentrates on the demonstration of illuminating specimens with a beam of photons composed of multiple wavelengths that are recorded in transmission mode. The technique is in fact much broader though and other forms of information multiplexing can be achieved in the same manner, for example using different polarisations of light and dual wavelength tomography (exploiting the phase multiplexing in reflection mode). Each wavelength interacts differently with the

specimen (due to the difference in the complex refractive index at different photon energies) and applying the new reconstruction algorithm allows the recovery of each of the wavelengths - the object and illumination both have a different response at the different wavelengths. For the case of a biological specimen, a colour image is successfully produced even though the detector used only measured greyscale intensities. The resultant colour image is then compared to its white light counterpart.

Some work has been carried out on multiple wavelength diffractive imaging within the x-ray community (Whitehead et al., 2009, Chen et al., 2009) that indicates the applicability of MS-PIE to that regime. Indeed the elemental analysis of specimens has recently been demonstrated using separate ptychographic scans across the absorption edges of materials within a biological cell (Maiden et al., 2013). The work shown here is principally designed to be a proof of principle for the general decomposition of mixed states throughout a microscope, showing the ability of the technique across a range of specimens and examining the performance of the reconstruction algorithm for each.

The experiments shown in this chapter were carried out on an optical bench with lasers producing photons in the visible light regime (410-633nm). The effects of multiple wavelength illumination is explored, from the effects that such illumination has on the dataset (diffraction patterns) to how the four dimensional sampling framework within ptychography allows for the solution of each coherent mode. Again, both the specimens and the probe forming optics respond differently to each wavelength and so the spectral response of each must be recovered.

5.2.1 Experimental Setup

The instrumentation for the visible light experiments described in the chapter was assembled by Dr Daniel Claus as part of a joint piece of work in which I developed the algorithms and performed the reconstructions. The general experimental setup employed was the same for the acquisition of each of the datasets. For single wavelength experiments the lasers where blocked as required and

different apertures where used (these will be stated where appropriate for each dataset below). The full setup consists of red (633nm), green (530nm), and blue (410nm) lasers combined, as shown in Figure 5.2. The three lasers were launched through separate optical fibres into an arrangement of beam splitters, where the three separate light beams were combined and passed onto an aperture. The aperture was combined with a spatial diffuser (tissue paper) to create the illumination function (or probe, P). The spatial diffuser is added to maximise the dynamic range of the detector and, as discussed in section 2.4.1, to increase the information content of the dataset. All diffraction patterns are recorded on a CCD detector (Kodak KAI-04022) with a pixel pitch of 7.4µm. While the detector contains 2048x2048 pixels, in order to significantly reduce the computation time and required processing power, the datasets were all cropped about the centre to 1024x1024 pixels. The specimens were mounted on a scanning stage (Physik Instrumente M-686) with a scan position accuracy of 0.1µm.

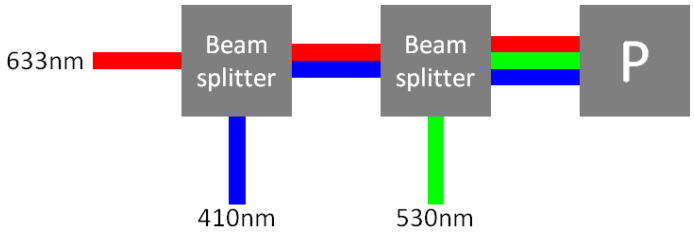

Figure 5.2: Schematic representation of the multiple wavelength experimental setup. Three lasers are combined through two beam splitters, forming a polychromatic illumination function (P).

The resultant illumination function contains all three wavelengths. A normalised plot of the wavelength spectrum of the illuminating beam is shown in Figure 5.3. It can be seen that the 410nm mode is broader than the other two, with substantial side lobes that extend at least into the region of influence of the 530nm mode.

In order to demonstrate both the usefulness of the technique and quality of the reconstruction algorithm under different circumstances, three different specimens are used to test the MS-PIE algorithm. Initially a manufactured colour projector slide (composed of three different digital greyscale images) is used in order to demonstrate the ability of the algorithm to separate three coherent spectral responses for both the specimen and probe forming optics when only their

incoherent sum is recorded. In order to demonstrate the applicability of the technique to biomedical imaging, a second specimen (a stained biological slide, Cushaw Stem L.S. obtained from Brunel Microscopes Ltd.), is processed through the multiple wavelength system. In order to show that the separation of spectral responses within the biological specimen is accurate, the resulting specimen responses are used to produce a colour image, which is then compared to its conventional white light counterpart. Finally, in order to examine the loss in resolution and general image quality due to the combination and decomposition of the multiple wavelengths, a standard USAF test target is imaged with both the single wavelengths and the multiple wavelength illuminations.

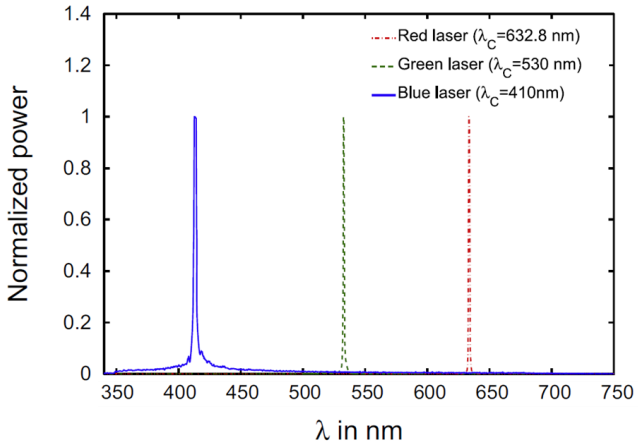

Figure 5.3: Normalized power spectrum of the illuminating beam showing three peaks, corresponding to the red, green, and blue lasers.

5.3 RGB Projector Slide

This section deals with a test experiment using a colour positive projector slide (120 lines/mm resolution) as a specimen. Four ptychographic datasets are recorded, one for each wavelength (red, green, and blue) and one with all three wavelengths present in the illuminating beam. The specimen was created from three separate greyscale images, which were converted into the RGB channels. The resultant colour image is shown in Figure 5.4.

The visible light experiments were all carried out under the simple, aperture only, setup in a similar manner to that employed in the x-ray experiment from section 4.2.1. For the projector slide dataset,

a 1.6mm square aperture was used with a nominal step size of 160µm (90% overlap) and the detector was positioned 78mm away from the specimen.

Figure 5.4: The digital RGB image used to generate the colour positive projector slide used to test the separation of spectral states (scale bar represents 500µm).

5.3.1 Single Wavelengths

Initially, ptychographic scans of the specimen are recorded under the three distinct wavelengths separately. The results of these reconstructions can be seen in Figure 5.5. It can be seen that there is some cross talk between the three object modulus reconstructions. As the images have each been taken under single wavelength illumination it suggests that the manufacturing of the projector slides has not reproduced the three separate digital images perfectly into the desired RGB channels. The important point is that the following multiple wavelength reconstructions should be compared directly to the reconstructions in Figure 5.5. Also note that the illumination functions have different structure, the probe forming diffuser is also wavelength specific. The apparent size difference between the illumination functions in these images is mainly due to the difference in real-space pixel size for each wavelength. For display purposes the objects have been rescaled but the illumination functions have not, the scale bars reflect this.

It is also interesting to see how the algorithm is able to reconstruct the phase response of the specimen across the energy spectrum. Imaging an energy sensitive specimen across a range of

photon energy levels, has been demonstrated successfully in the soft x-ray regime (Maiden et al., 2013, Beckers et al., 2011, Takahashi et al., 2011).

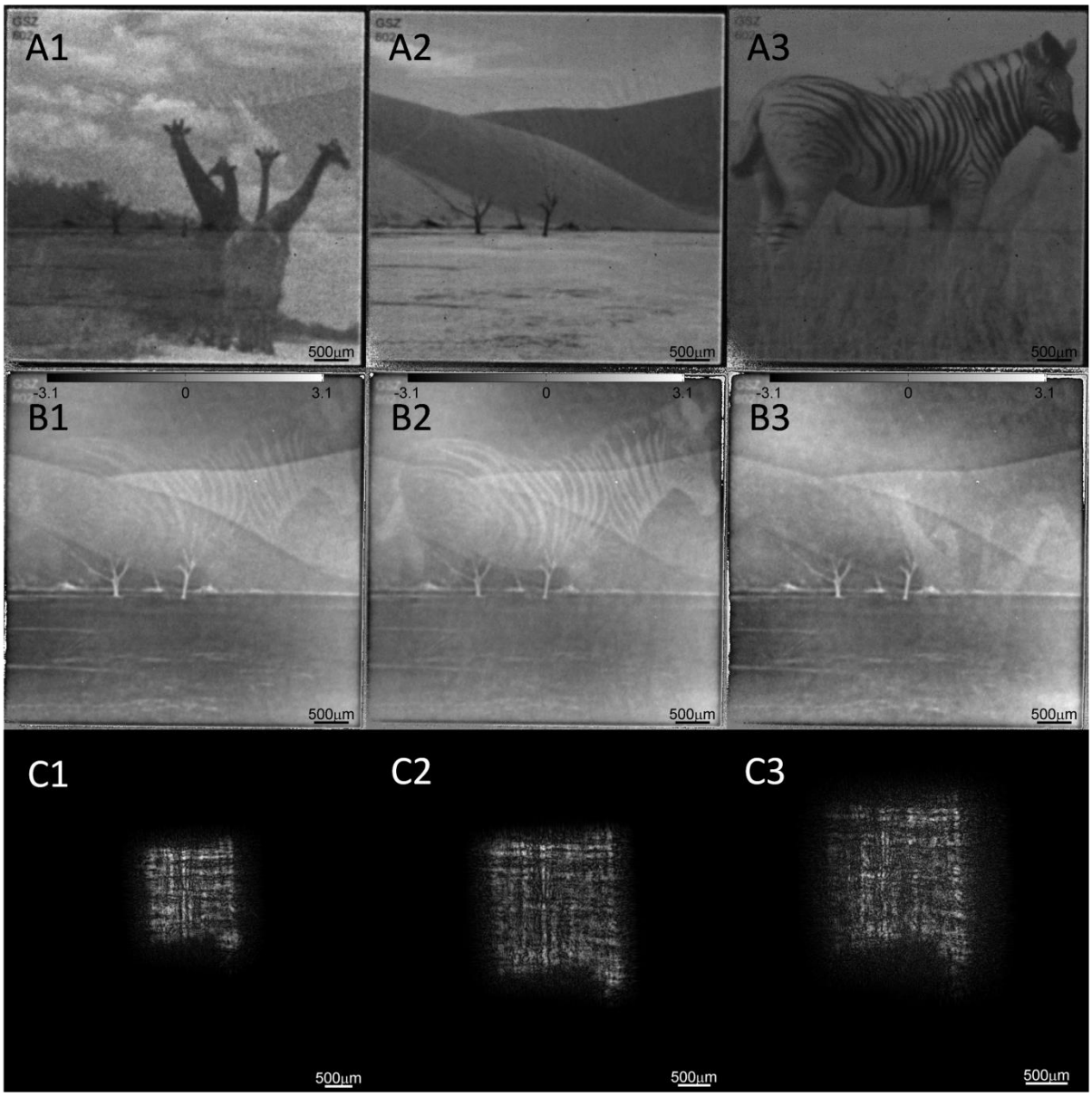

Figure 5.5: The ePIE reconstructions from three separate, single wavelength, datasets. Column 1) 633nm. Column 2) 530nm. Column 3) 410nm. Row A) The object's modulus response. Row B) The object's phase response. Row C) The modulus of the illumination function at the object plane

5.3.2 Multiple Wavelengths

Rather than relying on the recording of separate datasets, during which time the specimen may alter its state, the same specimen is now flooded with the three separate illuminations simultaneously. A single ptychographic scan (under the same parameters) is then recorded. The resulting dataset is effectively an incoherent superposition of the individual single wavelength datasets and the

separation of such individual states may be achieved using the MS-PIE algorithm. The multiple wavelength dataset is reconstructed firstly with the conventional ePIE algorithm before processing through the MS-PIE algorithm.

The ePIE algorithm assumes perfect coherence and so a single illumination function is required as the input, here the red (633nm) illumination function from Figure 5.5 is used as the initial illumination estimate. The result of the reconstruction is shown in Figure 5.6. The same combined, incoherent, dataset is then reconstructed using the new algorithm. In order to keep the comparisons fair, the algorithm takes only the same red illumination function as shown in Figure 5.5 as the initial estimate of the illumination functions. The green and blue initial estimates are produced by scaling the red estimate in such a way as to match the real-space pixel size of their corresponding wavelengths and are otherwise unaltered. The output of the MS-PIE algorithm after processing the combined dataset is shown in Figure 5.7.

In order to compare the measured data with estimated data, diffraction pattern estimates from each wavelength at a single position can be incoherently summed. A typical recorded diffraction pattern under multiple wavelength illumination, along with the combined estimates from the MS-PIE algorithm at that position, is shown in Figure 5.8. The likeness of these images demonstrates that all of the data is being taken into account by the algorithm correctly and in line with the experiment. The individual diffraction patterns are also now compared. Figure 5.9 shows typical diffraction patterns when the specimen is scanned with each wavelength individually (top row) and the corresponding estimated diffraction patterns from the MS-PIE algorithm when the input is the combined dataset (a typical diffraction pattern from which is shown in Figure 5.8). Just as Figure 5.8 shows that the combined data is consistent with the experiment, Figure 5.9 shows that the MS-PIE algorithm is able to separate the contribution out from each individual wavelength from a polychromatic dataset very effectively.

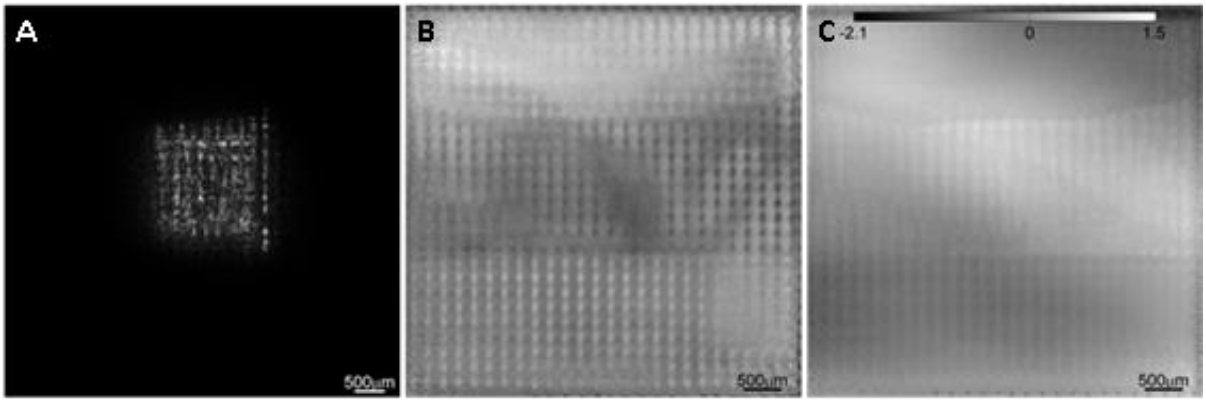

Figure 5.6: ePIE reconstruction of the multiple wavelength dataset, the known red (633nm) probe from Figure 5.5 is used as the probe estimate. a) The modulus of the output probe. b) Modulus of the output object. c) Phase of the output object.

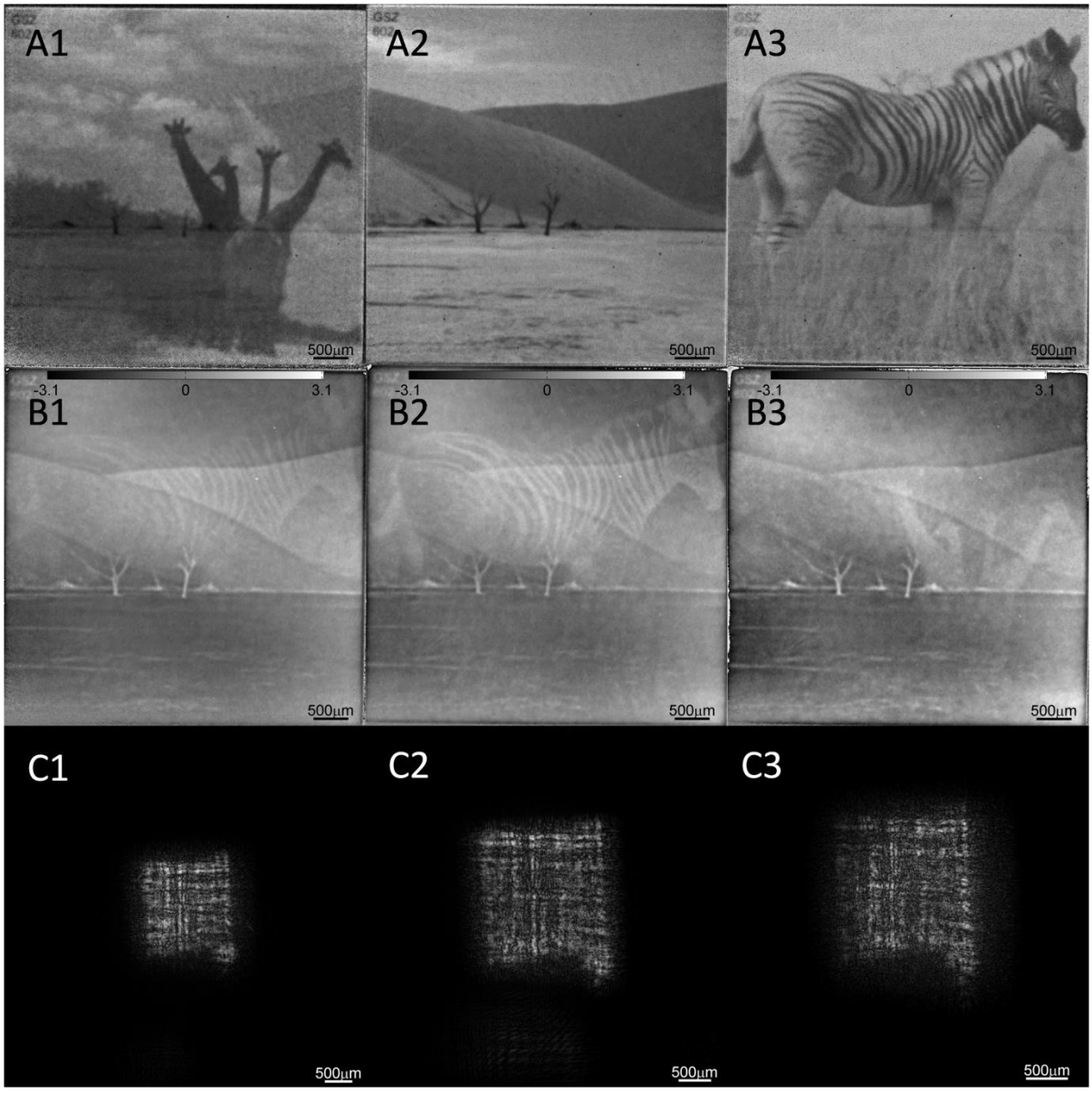

Figure 5.7: The MS-PIE reconstruction from the multiple wavelength dataset. Column 1) 633nm, Column 2) 530nm, Column 3) 410nm. Row 1) the object's modulus response, Row 2) the object's phase response, Row 3) the modulus of the illumination function at the object plane.

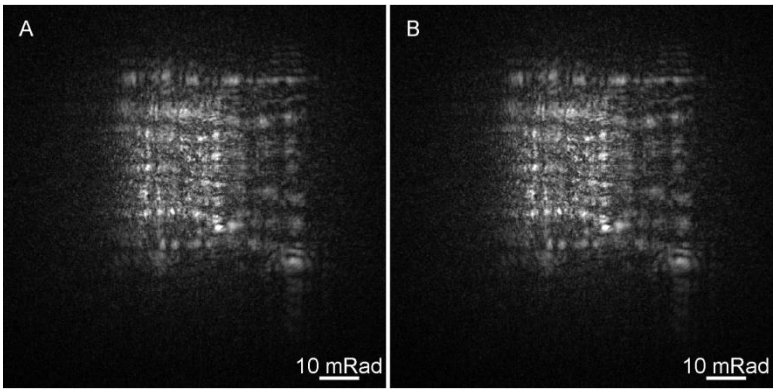

Figure 5.8: Typical diffraction patterns from the multiple wavelength dataset in modulus. a) As recorded. b) Created form the outputs of the MS-PIE reconstruction.

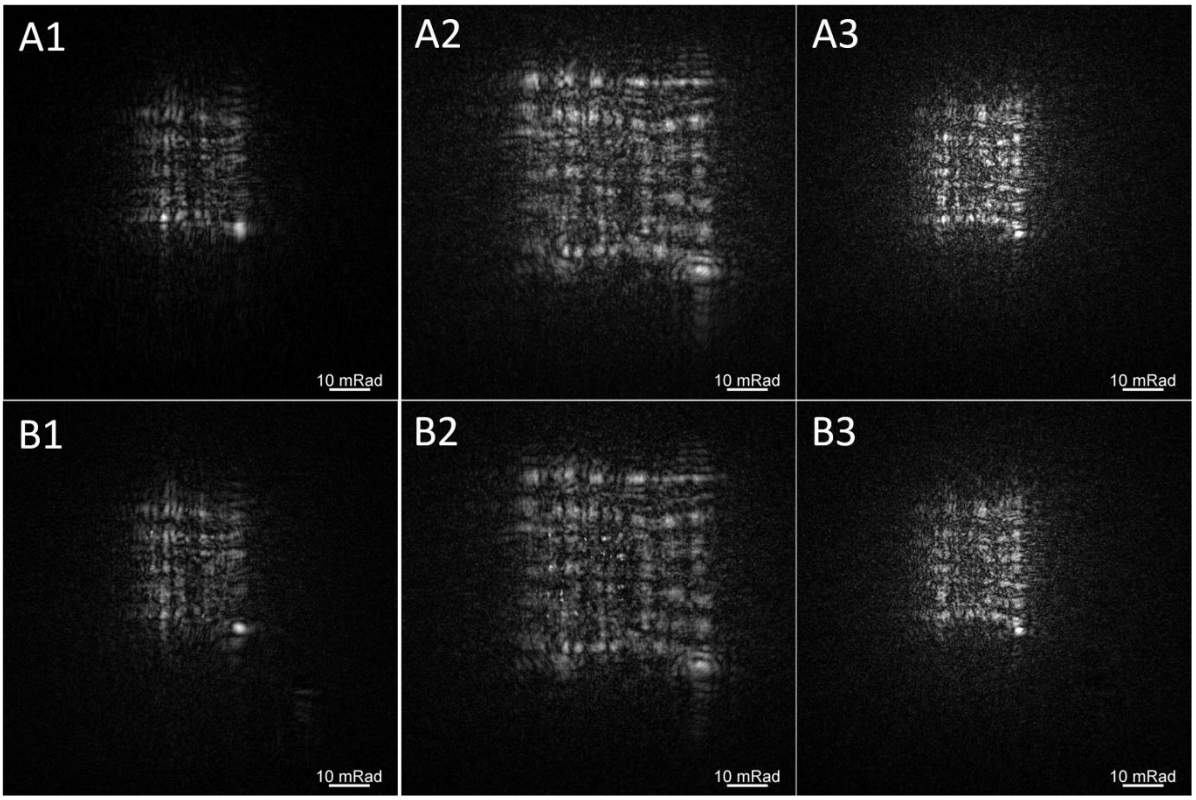

Figure 5.9: Row A) Typical recorded diffraction patterns from the single wavelength datasets in modulus. Row B) The corresponding estimated diffraction patterns as outputted from MS-PIE. Column 1) 633nm. Column 2) 530nm. Column 3) 410nm.

5.4 Biological Specimen

The procedure described for the projector slid above is now applied to a stained biological specimen. The aperture is changed to a circular aperture with a diameter of 500µm, which is mounted along with the same spatial diffuser. The specimen is scanned in steps of 100µm (80% overlap) and the detector is positioned 60mm away from the specimen.

5.4.1 Single Wavelengths

The change in structure at different wavelengths for this specimen is not as obvious as with the projector slides and so the separation process is perhaps not as straightforward. It does though apply the technique to a more scientifically interesting specimen. Initially a scan of the specimen is recorded, and reconstructed, at each individual wavelength with the results shown in Figure 5.10.

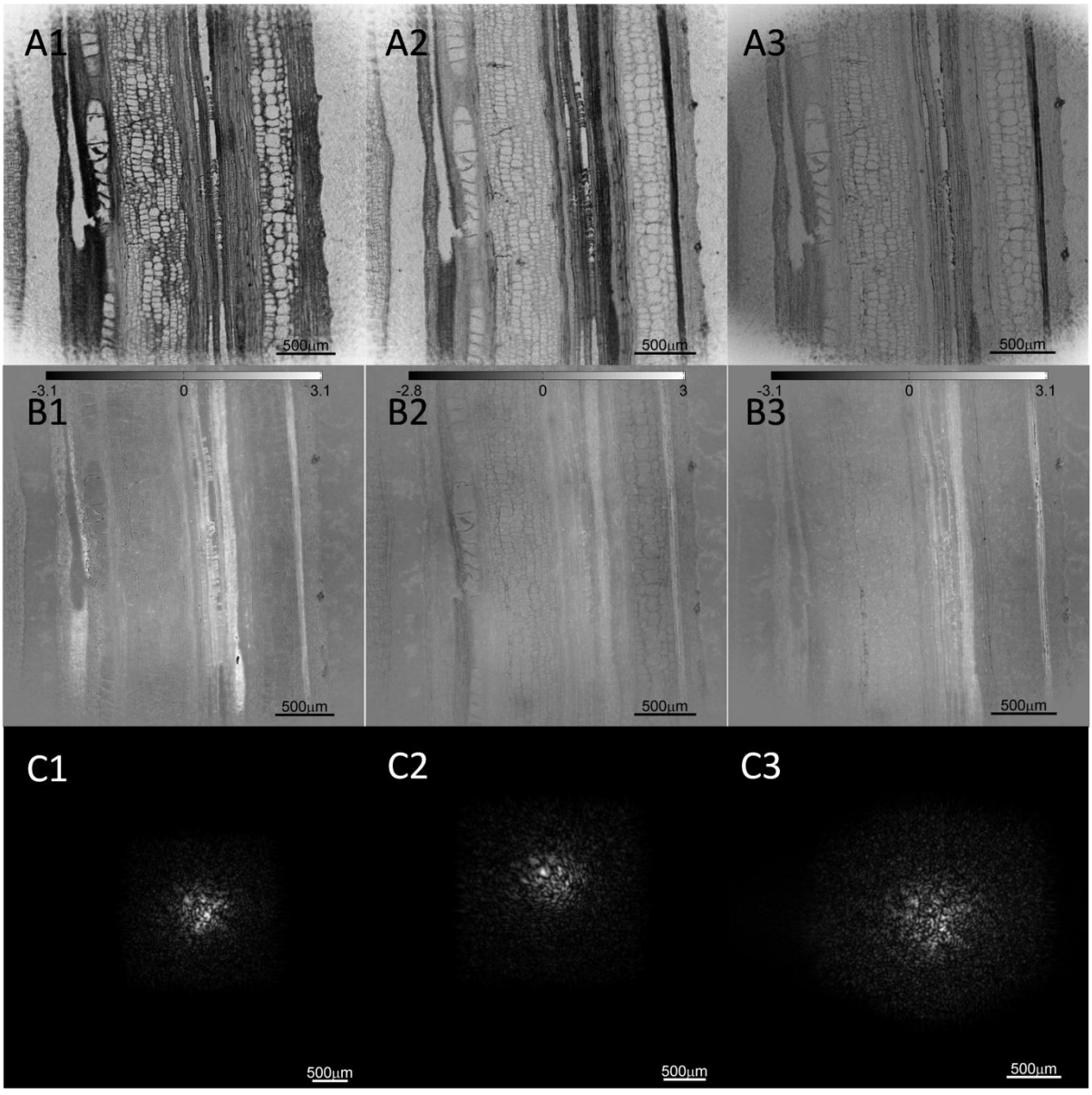

Figure 5.10: The ePIE reconstructions from three separate, single wavelength, datasets, where columns separate the different wavelengths; column 1) 633nm, column 2) 530nm, and column 3) 410nm. Row a) The object's modulus response. Row b) The object's phase response. Row c) The modulus profile of the illumination function at the object plane.

5.4.2 **Multiple Wavelengths**

A dataset is now recorded with all three wavelengths present in the illuminating beam. This incoherent dataset is firstly reconstructed using the conventional ePIE algorithm and then using the MS-PIE algorithm. As with the projector slides, the combined dataset is reconstructed using the conventional ePIE algorithm assuming that a single wavelength (red) is present in the illuminating beam. The results of the ePIE algorithm reconstruction, when the known red illumination function (taken from Figure 5.10c1) is used as the initial illumination estimate, is shown in Figure 5.11. The combined dataset is then processed using the new algorithm, again with the known red illumination function scaled appropriately as initial estimates for the three wavelengths. The results of the new algorithm when processing the combined dataset is shown in Figure 5.12.

A typical recorded incoherent diffraction pattern is compared with the incoherent sum of the three corresponding coherent diffraction patterns, of which it is composed, as produced from the MS-PIE algorithm. The results can be seen in Figure 5.13, which shows an excellent correlation. Such similarity demonstrates that the algorithm is indeed handling the data in a meaningful manner and one which is in agreement with experiment. Typical recorded diffraction patterns from each single wavelength dataset (as in Figure 5.13) are compared to the three corresponding coherent diffraction patterns that result when the MS-PIE algorithm separates out the three individual wavelengths from the multiple wavelength dataset. Figure 5.14 shows the comparison and the results show a high level of correlation.

The comparison between the MS-PIE outputs and the experimental measurements for the individual modes along with the equivalent comparison for the multiple wavelength diffraction patterns suggest that the technique is indeed functioning as desired. There is no appreciable loss in reconstruction quality at all.

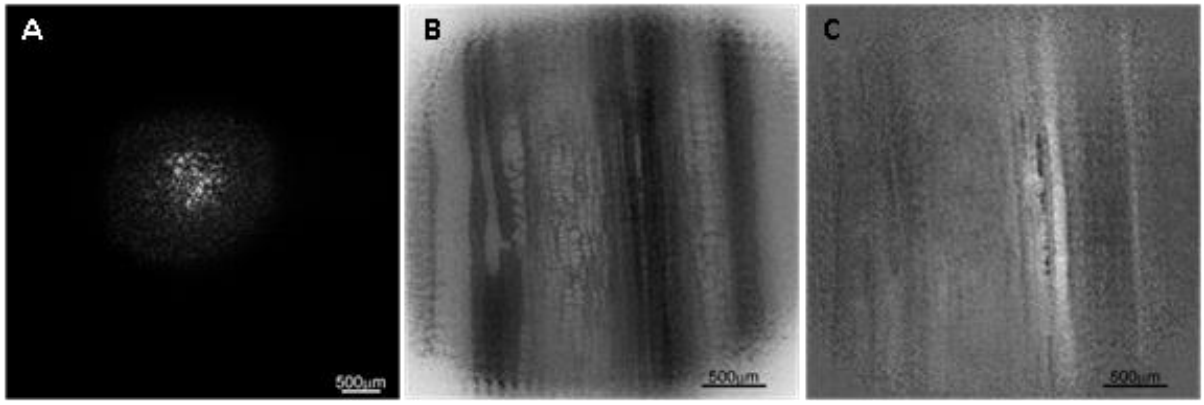

Figure 5.11: ePIE reconstruction of the multiple wavelength dataset with an initial probe function estimate of the known red (633nm) output from Figure 5.10(c1).

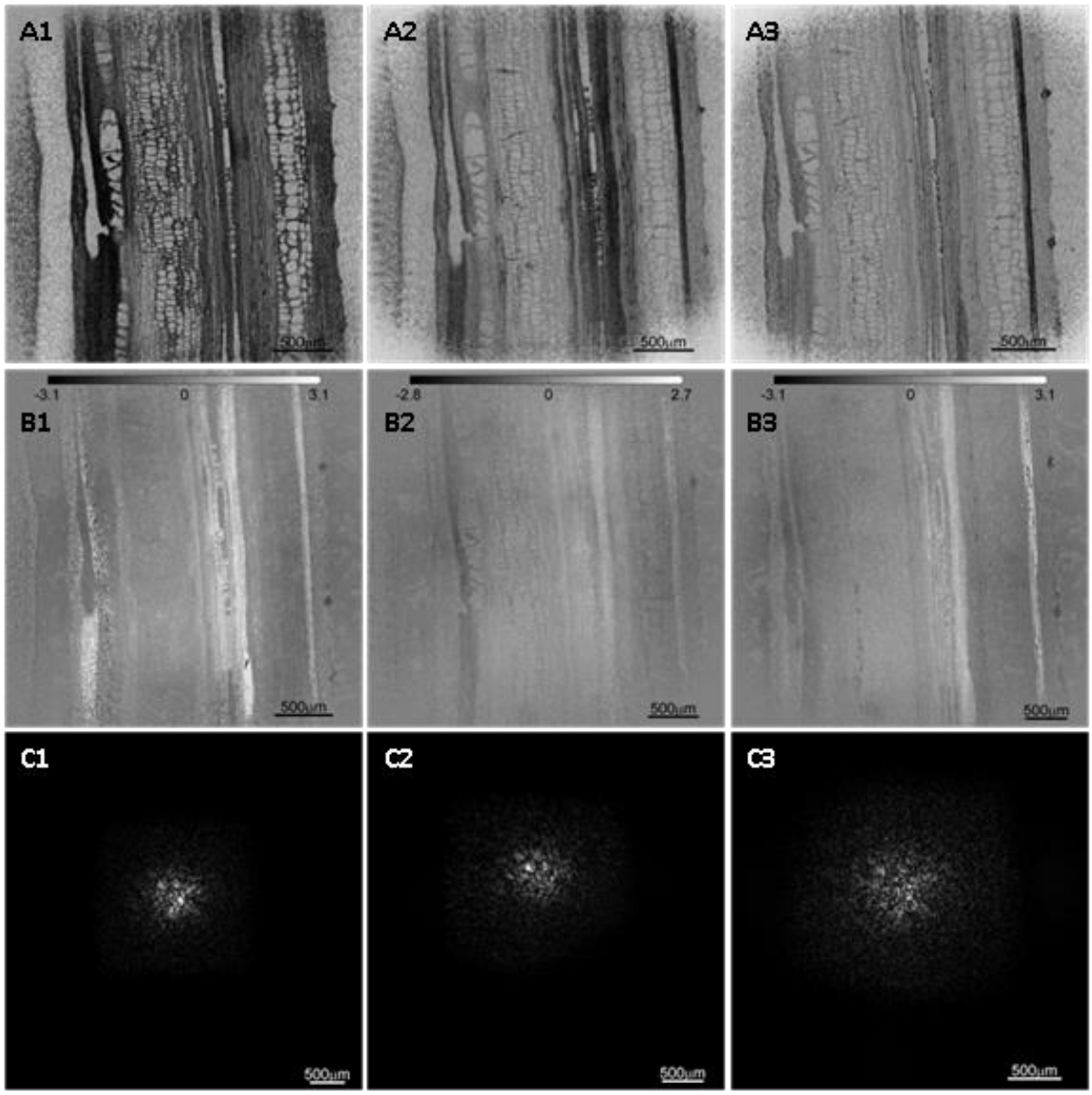

Figure 5.12: The MS-PIE reconstruction of the multiple wavelength dataset, where columns separate the different wavelengths; Column 1) 633nm, column 2) 530nm, and column 3) 410nm. Row a) The object's modulus response. Row b) The object's phase response. Row c) The modulus profile of the illumination function at the object plane.

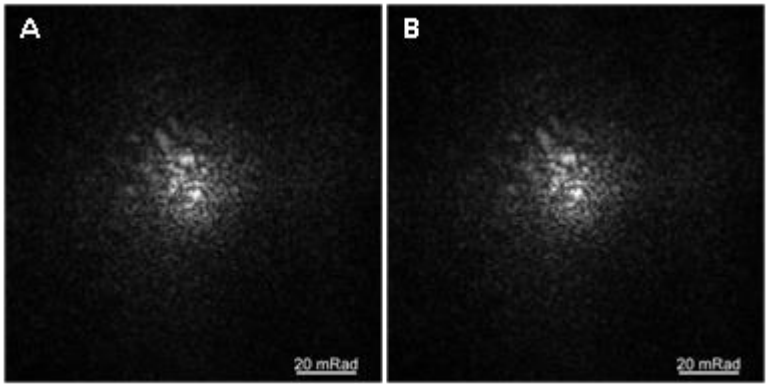

Figure 5.13: Typical diffraction patterns from the multiple wavelength dataset in modulus. a) As recorded. b) Created form the outputs of the MS-PIE reconstruction.

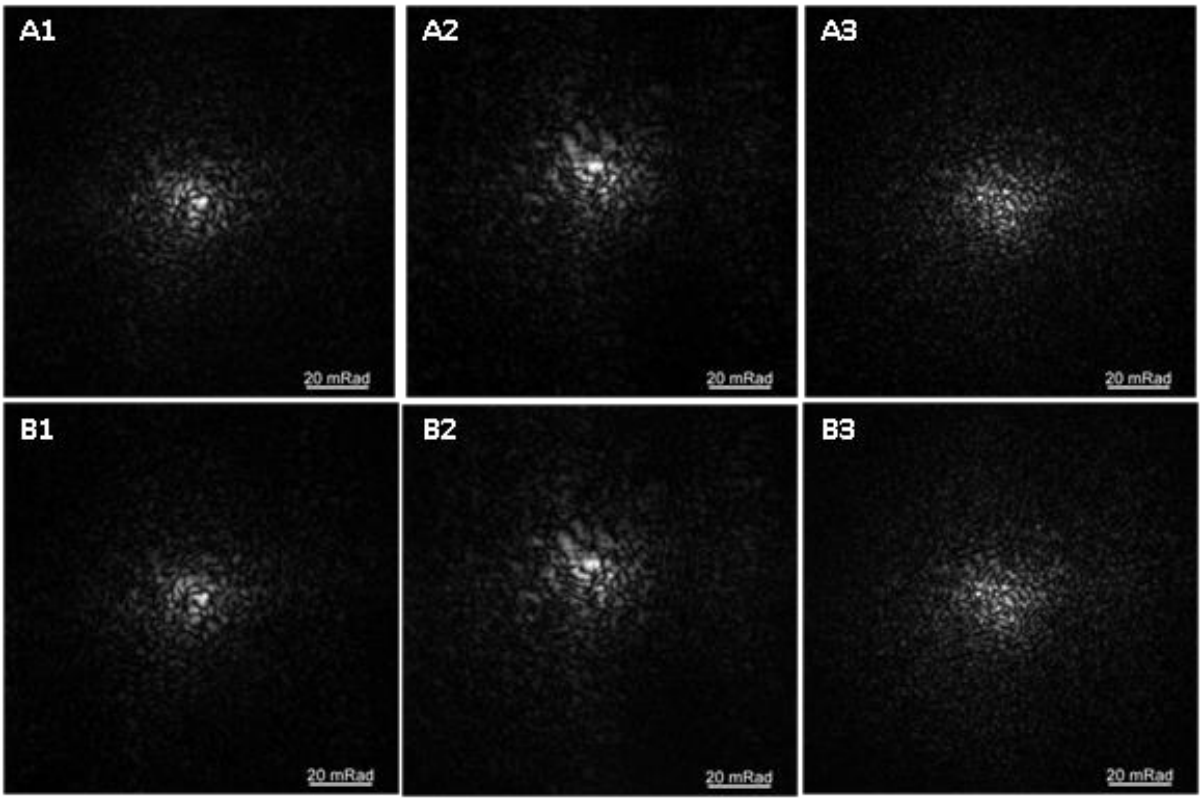

Figure 5.14: Typical recorded diffraction patterns from the single wavelength datasets in modulus (row a) and corresponding estimated diffraction patterns outputted from MS-PIE (row b) for the three wavelength, 633nm (column 1), 530nm (column 2), and 410nm (column 3).

5.4.3 Spectral Weights and Colour Imaging

The influence of the initial estimate of the relative spectral weights on the recovered spectral weights is now investigated. Twenty-eight different distributions of spectral weights are used as initial spectrum estimates for the reconstruction of the biological sample. The normalized outputted spectral weights are plotted against the distribution of inputs, shown in Figure 5.15. Regardless of

input estimate, the recovered spectral weights all converged to the same discrete values and so *a priori* knowledge of the spectral weights is not a requirement for the this method.

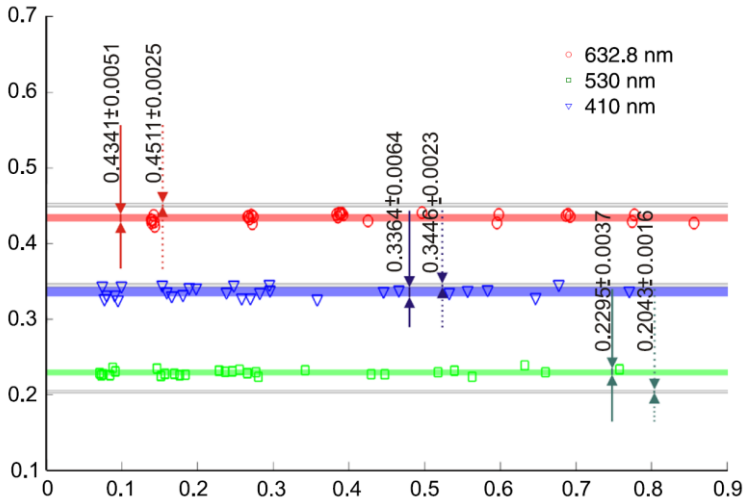

Figure 5.15: A variety of Input spectral weights (normalized) against output normalized spectral weights from the MS-PIE algorithm for the biological specimen (normalized against the sum of power of the three wavelength specific probes).

As the reconstructed object is sampled with red, green, and blue lasers, it is possible to combine the modulus images (which represent the absorption of the specimen at each wavelength) into a composite RGB image. The result is shown in Figure 5.16, alongside a conventional white light transmission image of the specimen for comparison.

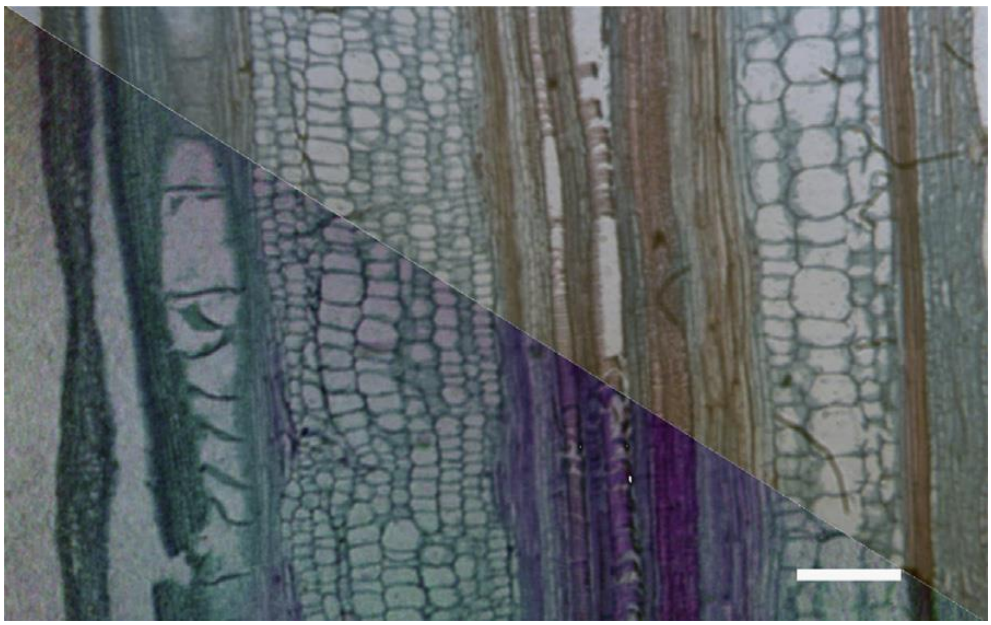

Figure 5.16: A conventional white light transmission image taken with Olympus SPlan 4PL microscope objective (top right) with the MS-PIE reconstruction combined into an RGB image (bottom left). Scale bar represents 500µm.

The RGB colour representation of the MS-PIE reconstruction in Figure 5.16 shows the brown regions from the conventional white light microscope as more purple. This is likely to be as a result of either the sparse sampling of the energy spectrum, the alteration of the laser light into the RGB gamut, or a combination of the two. The details of this have not been explored a great deal as the production of the colour image is mainly to show that the correct wavelengths are being absorbed in the correct locations and it is the individual specimen response images that are providing the important scientific information.

The specimen here was stained although ptychography does not require staining in order to reveal the structure of biological specimens due to its achievable phase sensitivity (Claus et al., 2012, Marrison et al., 2013). Applying this technique to such specimens opens up the possibility of performing spectroscopy of stain-free, live, *in situ* biological specimens.

5.5 USAF Test Target

In order to more precisely examine the performance of the MS-PIE algorithm, a standard USAF test target is now imaged. The experimental setup is as with the biological specimen, with a slightly reduced specimen-detector distance of 57mm. Figure 5.17(a-c) shows the individual reconstructions using the ePIE algorithm. As expected due to the diffraction limit of the different wavelengths, the obtained resolution increases as the wavelength of the incident illumination is decreased from 633nm to 410nm.

The corresponding multiple wavelength dataset is reconstructed using the MS-PIE algorithm for comparison and the results are shown in Figure 5.17(d-f). The MS-PIE reconstructions have retained the resolution levels seen in the single wavelength reconstructions extremely well, once again demonstrating the ability of MS-PIE to separate mixed states from a single incoherent dataset without a loss of quality.

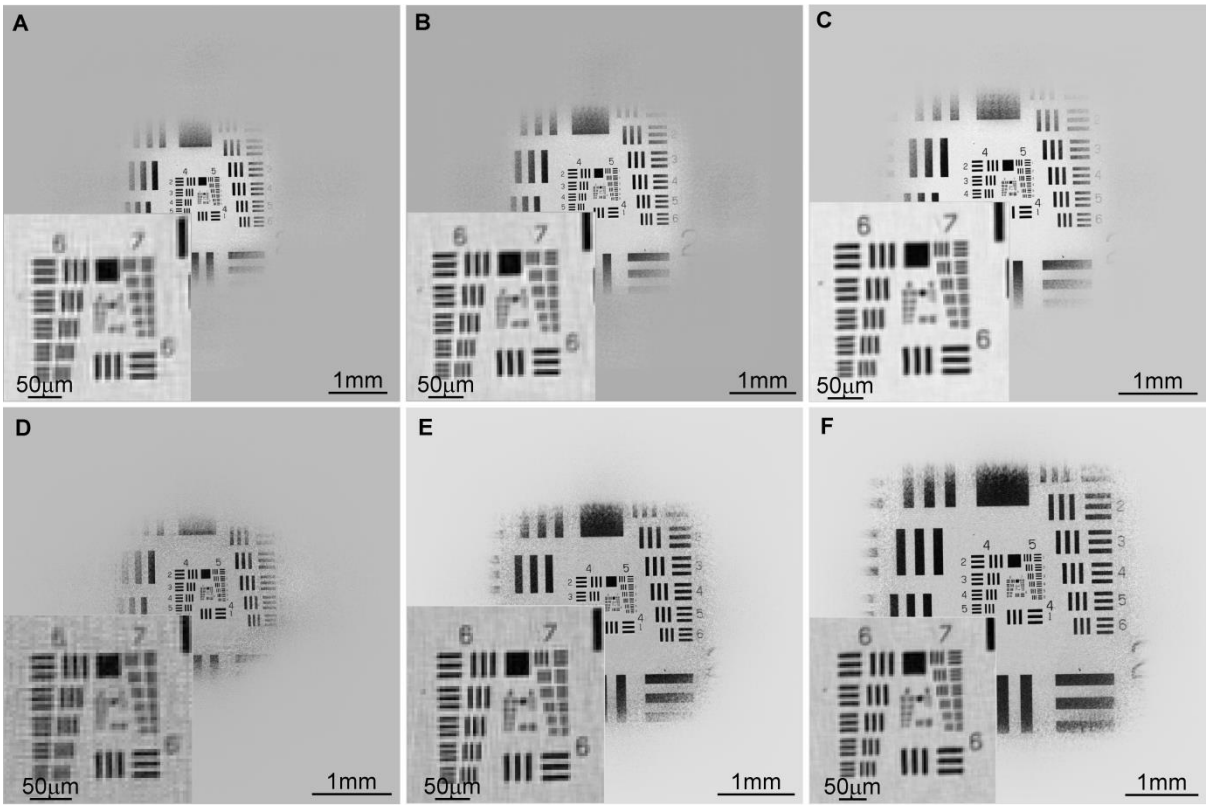

Figure 5.17: Reconstructed modulus images of a USAF test target. a-c) ePIE reconstructions of the individual object responses to the red, green, and blue wavelengths, respectively. d-f) MS-PIE reconstruction of the combined dataset, showing the object response to the red, green, and blue wavelengths, respectively.

5.6 Summary

This work outlined in this chapter is designed to be a proof of principle for the general principle of imaging mixed states. The results shown are important in their own right, although the real scientific advantages are to be made by implementation of the technique in both the x-ray (for elemental analysis) and electron (for instrument instabilities) regimes.

An advantageous feature of ptychographic spectroscopy is that the full refractive index is recovered - this includes the phase change across an energy range along with the absorption coefficient. The method of ptychographic spectroscopy has indeed been demonstrated in the soft x-ray regime (Maiden et al., 2013). In this case though, separate scans were required for each illumination energy. Combining these into a single exposure of the specimen would be of advantage in ensuring the elements across reconstructed energy levels remain in the same location and that the total number of photons can be reduced (important for beam sensitive specimens and time critical analysis).

The experimental proofs outlined above have so far been limited to three distinctly separate wavelengths. Applying the technique in a more practical setting will likely rely on the ability to extend the number of modes present and in some situations (for example, chemical contrast imaging in the x-ray regime across absorption edges within a specimen) a significant increase in the energy resolution (the experiment described above has a $d\lambda/\lambda$ of 0.2. The sampling requirements for an increase of the number of modes present, and indeed the separation of them, is still ill defined and should be the subject of future work.

6 Electron Ptychography

Although photon imaging via the ptychographic method has been shown to work well over a wide range of energies, the electron regime has so far not produced results that improve upon the conventional STEM resolution. There are problems that arise in the electron regime that do not necessarily arise in the visible light and x-ray regimes such as, illumination stability, sample stability, and inelastic scattering. These problems must be overcome to achieve wavelength limited resolution in electron ptychography.

As it is difficult to measure exact form of the illumination in the specimen plane, for the electron case it is crucial to be able to reconstruct the probe function (for example with the ePIE or difference map algorithms) in order to reconstruct the object. Ptychography principally solves for the exit wave emanating from the object function, which is irradiated by the illumination function. ePIE can solve

for both the object function and the illumination function because the illumination remains constant at each position but the object at each position changes. This process therefore requires good stability of the STEM probe during the acquisition time.

As well as having a constant illumination function it is also crucial to know accurately its position as it is scanned over the object. This is often very hard to achieve practically in an electron microscope due to such issues as hysteresis in the scanning coils and specimen drift. The problem of thick specimens and the resulting effects of dynamical scattering on the PIE algorithm have also been briefly explored (Liu et al., 2009). The adverse effects due to experimental instabilities can to some degree be negated by reducing the acquisition time, however the quality of the reconstruction is ultimately limited by the number of counts incident upon the detector per exposure (the results of chapter 3 may solve this problem). The balance between these two conflicting requirements is an important factor to consider when executing an electron ptychography experiment.

6.1 STEM Ptychography

High energy electron ptychography is essentially a hybrid technique - the microscope is operated in STEM mode (with a near focus beam scanned relative to the specimen) but the STEM detector is replaced with an array TEM detector. In this manner the whole diffraction pattern, including all of the interference and structure, is recorded (unlike the annular detectors used in traditional STEM imaging, which record a single amount of electrons per position). It is this setup which provides ptychography with the four-dimensional dataset and the ability to produce a complex image of the specimen instead of simply an intensity distribution.

6.1.1 Experimental Issues

There are many experimental parameters to consider when setting up a ptychography experiment in a transmission electron microscope. Many of the lenses that are so crucial in conventional high resolution TEM and STEM imaging only act as a problem for the ptychographic setup. It is the post

specimen lenses that are a particular hindrance, although any lens that is surplus to requirement is liable to introduce unnecessary drift and instabilities into the setup.

The specimen is also a major consideration in electron ptychography (as indeed in any electron microscopy technique). Issues such as specimen contamination due to the highly focussed charged beam that attracts hydro carbons to build up on the specimen, knock-on damage and other beam sensitive effects are all inevitable and must be suppressed as much as possible (Williams, 2009). Other issues occur in electron ptychography such as specimen drift and stage movement inaccuracies. All instabilities have a detrimental effect on the ptychographic imaging process as they violate the requirement that the experiment is constant over the acquisition time. Another problem that is associated with the characteristics of the specimen is that of its thickness, multiple scattering effects can begin to dominate when the specimens becomes sufficiently thick. The work on three-dimensional imaging from ptychographic data using the multi-slice methods (Maiden et al., 2012a), as discussed in chapter 2, may help but has not yet been successfully demonstrated in the electron regime.

Some of the problems associated with electron ptychography have been explored previously (Hue et al., 2011). As described in section 2.4.1, the scan position errors may now be alleviated to some degree during the reconstruction process (Maiden et al., 2012b, Zhang et al., 2013). However, the correction methods have a limited ability and minimizing the errors experimentally is always beneficial.

A further intricacy that presents itself in high resolution electron ptychography is that of periodicity in the specimen. Electron ptychography relies heavily on the ability to refine the probe function from a rough initial estimate, which in turn relies on specimen structure to sample the whole probe as is scanned across the region of interest. In most other applications this is not an issue, with a periodic specimen though ensuring that the entire probe is sampled sufficiently is an important factor to consider. For example, when the scan is small (relative to the specimen) so that no edges of a crystal

are in the field of view and the step size of the scan is matched to the periodicity within the specimen, shifting the beam has no meaning at all. Solving for the probe function relies on there being sufficient structure within the specimen across the field of view - something not guaranteed in situations such as STEM mode ptychography. Scanning over a large field of view will greatly increase the effectiveness of the ePIE algorithm as many particles may then be captured, each in a variety of different orientations.

In the visible light and x-ray regimes the localisation of the illuminating radiation can be achieved with apertures very close to the specimen plane, however due to the physical configuration of the electron microscope this is not possible. A localised spot on the specimen is instead created in STEM mode with the objective lens defocused, as shown in Figure 2.5. The size of the probe at the specimen, which is determined by the convergence angle of the beam and the amount of defocus, is very important and is limited by the sampling of the diffraction data at the detector. Unlike conventional STEM, where the side lobes of the beam may have small but significant amounts of flux so long as they are spread out sufficiently, great care must be taken in ptychography to ensure that the majority of the electron flux is localised with the Fourier repeat unit cell defined by the angular range of the detector pixels.

6.1.2 Data Collection

Such a STEM experiment as described above was carried out on a 300keV JEOL R005 electron microscope via collaborators at Oxford University as part of the PI-PHI project, which was funded by the EPSRC Basic Technology Grant scheme. The following sections describe the details of that experiment along with the issues that had to be confronted and that should be learned from in order to improve future experiments. Although the principle aim of electron ptychography has been to improve upon the resolution limit of the electron lens (without the requirement on high quality aberration corrected lens systems), the high-end microscope was chosen for other benefits such as high stability and the cold FEG source that produces a highly coherent beam with high levels of flux.

A JEOL R005 microscope is also installed at the University of Sheffield and I have recorded and reconstructed some ptychographic datasets from that machine. However, as it was still not possible to increase the number of scan positions beyond a 7x7 scan (due to computational limits on the data acquisition computer), no improvement has yet been made upon the result shown here.

The specimen chosen was Ceria particles (CeO_2) dispersed across a support film - a single particle was selected overhanging free space such that the edge could be scanned without potential issues associated with support films. A conventional high angle annular dark field (HAADF) image of the specimen is shown in Figure 6.1.

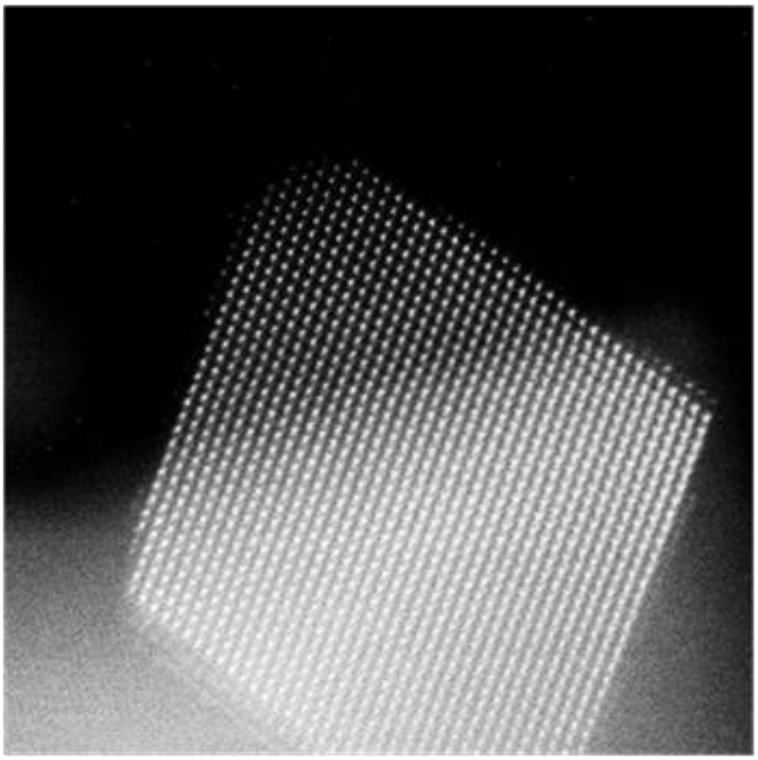

Figure 6.1: Survey STEM image (HAADF) of the CeO_2 particle orientated on a <110> axis

Once in STEM mode, the probe is defocused by changing the strength of the objective lens. The same scanning coils as used for conventional STEM to steer the electron beam were used to position the probe as it traversed the 25 overlapping positions (5x5) across the specimen.

The detector used is a Gatan UltraScan, which has 2048x2048 pixels each of 14μm x 14μm.The detector is shown capturing a highly defocused shadow image in Figure 6.2a before the objective

lens is shifted towards focus in Figure 6.2b. An aperture is placed in the back focal plane of the condenser lens, which on the STEM configuration is also the detector plane. The result is a sharp disc in the detector plane as shown in Figure 6.2c.

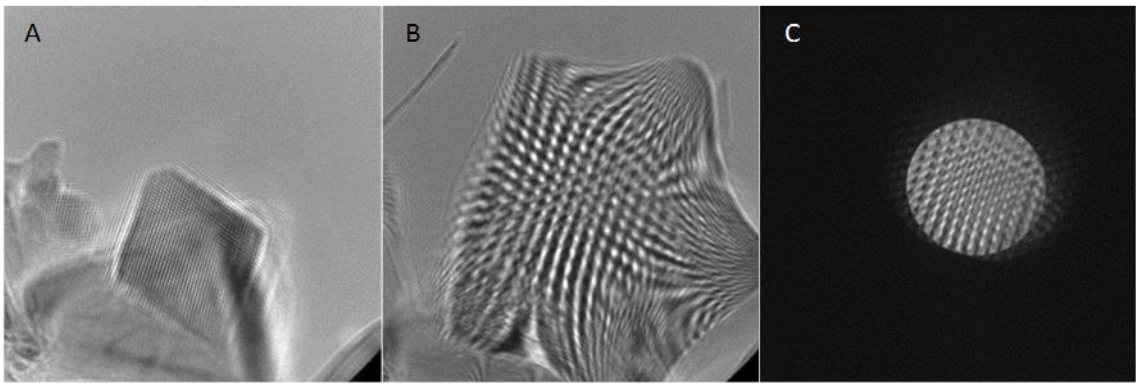

Figure 6.2: Capturing a localised, defocused, Ronchigram in reciprocal-space in STEM mode. a) Large defocus, b) 91nm defocus, 91nm defocus with condenser aperture inserted.

Switching the intermediate lenses into image mode brings real-space into focus at the detector plane. The result of this when the specimen is moved out of the beam is a free-space image of the probe function as shown in Figure 6.3.

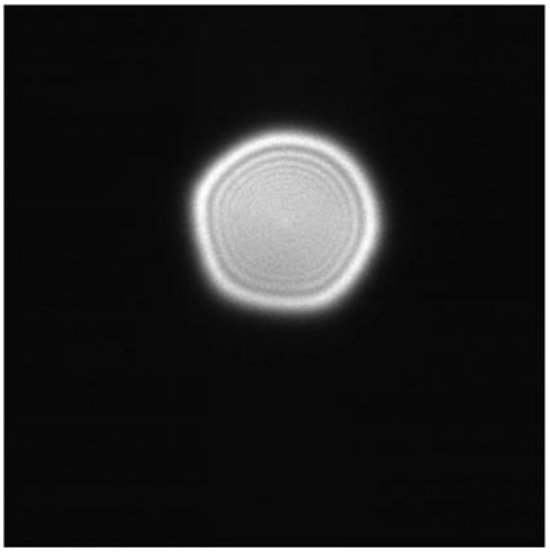

Figure 6.3: Real space image of the electron beam as used to form the diffraction pattern in Figure 6.2c.

6.1.3 ePIE Reconstruction

The raw data as captured is shown in Figure 6.4a and, unfortunately, appears to be sub optimal in several ways. The most striking problem at first glance is the variation in intensity between the diffraction patterns. Taking regions from the top left corner of each diffraction pattern, where there

is deemed to be no scattering present, shows the extent of the problem (see Figure 6.4b). In an effort to alleviate this flaw, the cut outs where averaged and their mean values were subtracted from the datasets. (Any resultant negative numbers were set to zero.) The result can be seen in Figure 6.4c, where the dark-field now appears uniformly dark. On top of the dark-field imperfections, the total flux within the central discs also varies. Some variation is expected at focus, which is what gives rise to a bright-field STEM image, but for a defocused probe the dips in intensity are too great to be real specimen structure. An assumption is made that the total flux in each recorded diffraction pattern should be equal and so each is scaled to contain the same total counts as that in the top left corner (almost free space). Also, as there is very little signal in the outside regions of the diffraction patterns, cutting out the central region effectively increases the signal to noise ratio. The results of the flux correction and cropping operations are shown in Figure 6.4d.

Before processing the data through the ePIE algorithm, an initial estimate must be made for the probe function. An estimate of the probe at the specimen plane may be generated from the Ronchigram. For a given camera length and detector pixel-size, the convergence angle of the beam may be deduced (this data has a convergence half angle of 15mRad). The value of defocus may also be found if the defocused Ronchigram, which is essentially a shadow image, contains a feature of known size. The total power of the illumination function can be taken as an average of the total counts per diffraction pattern. The illumination function estimate may be initially formed in reciprocal-space, where an aperture of the correct angular range is created with the total number of counts matched to the experimental data. Taking a Fourier transform produces a diffraction limited probe at focus, applying the angular spectrum propagation method (see section 2.1.7), with the required values of defocus, produces a model probe function at the specimen plane.

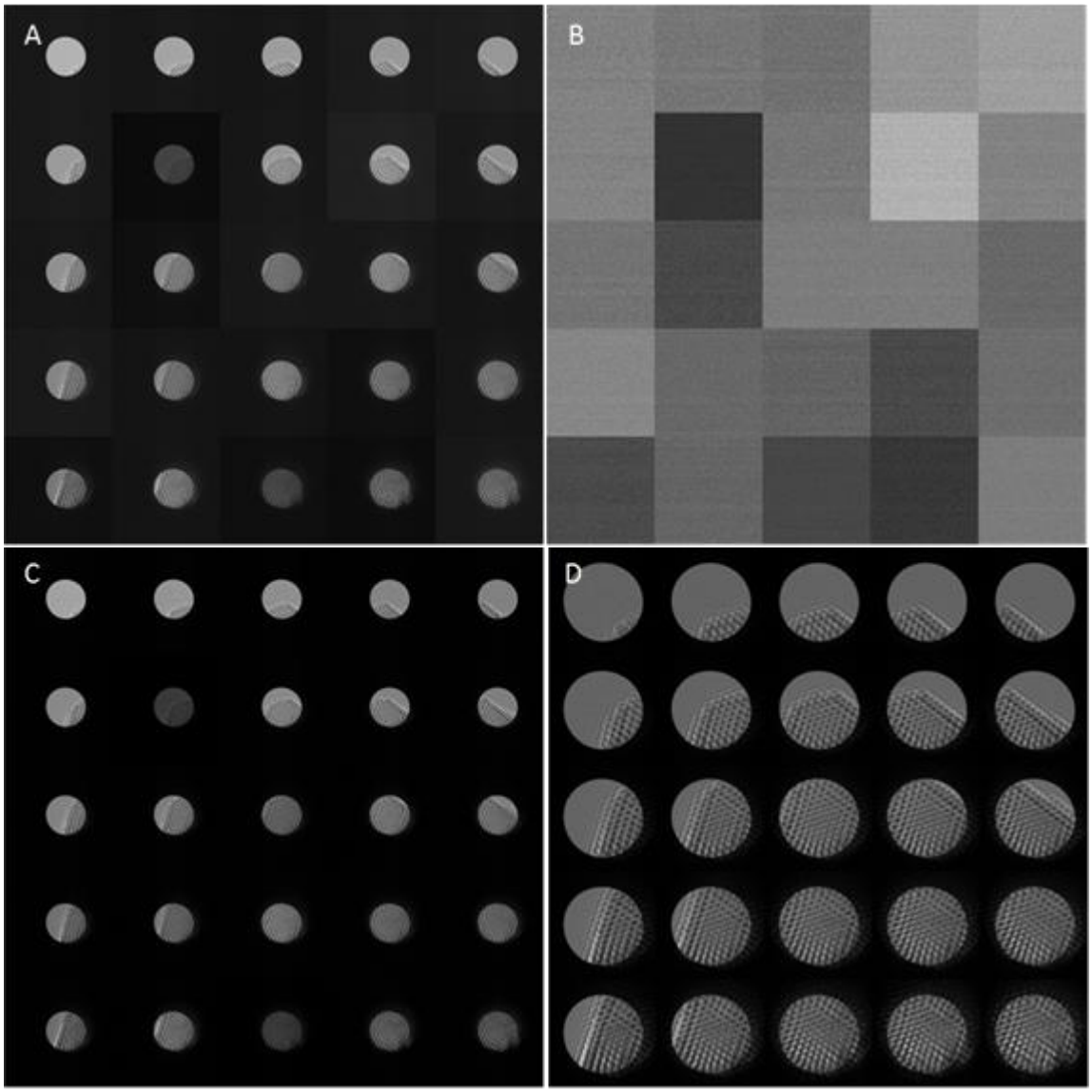

Figure 6.4: The pre-processing of the dataset. a) Original dataset. b) Cut out of top left corner of each diffraction pattern in (a). c) Dark-field corrected version of (a) using the average dark-field values in (b). d) The final dataset after normalisation of the total power in each diffraction pattern to be the same and cropping out of the central section.

Starting with such an initial model probe and with an estimate of free-space for the object, the data was processed through the ePIE algorithm, producing the reconstruction shown in Figure 6.5. Although an atomic resolution image of the specimen has been produced, note that the probe function contains some false features. Such artefacts within the illumination are indicative of inconsistencies between the reconstruction constraints applied to, and the measurements within, the dataset. The algorithm settles on the most globally consistent solution in such situations by introducing a secondary contribution to each exit-wave, one which reduces the difference between forward estimates and measured data whilst having the least effect on the main consistent region.

Due to the periodic nature of the crystal, the illumination function has come to a solution that contains false peaks within the main probe as well as a 'secondary' peak just below. These false peaks in the probe function have been carried across and ‘punched’ into the object function in areas of free space. The punching across of peaks comes from the real-space update, where an updated exit-wave is used to update the object and probe in a parallel operation. If the object is free-space and the probe contains an artefact which is not present in the updated exit-wave then the algorithm is forced to compensate somewhat with an attenuating region in the specimen. This problem lowers the contrast of the image within the crystal region and adds artefacts across the rest of the image.

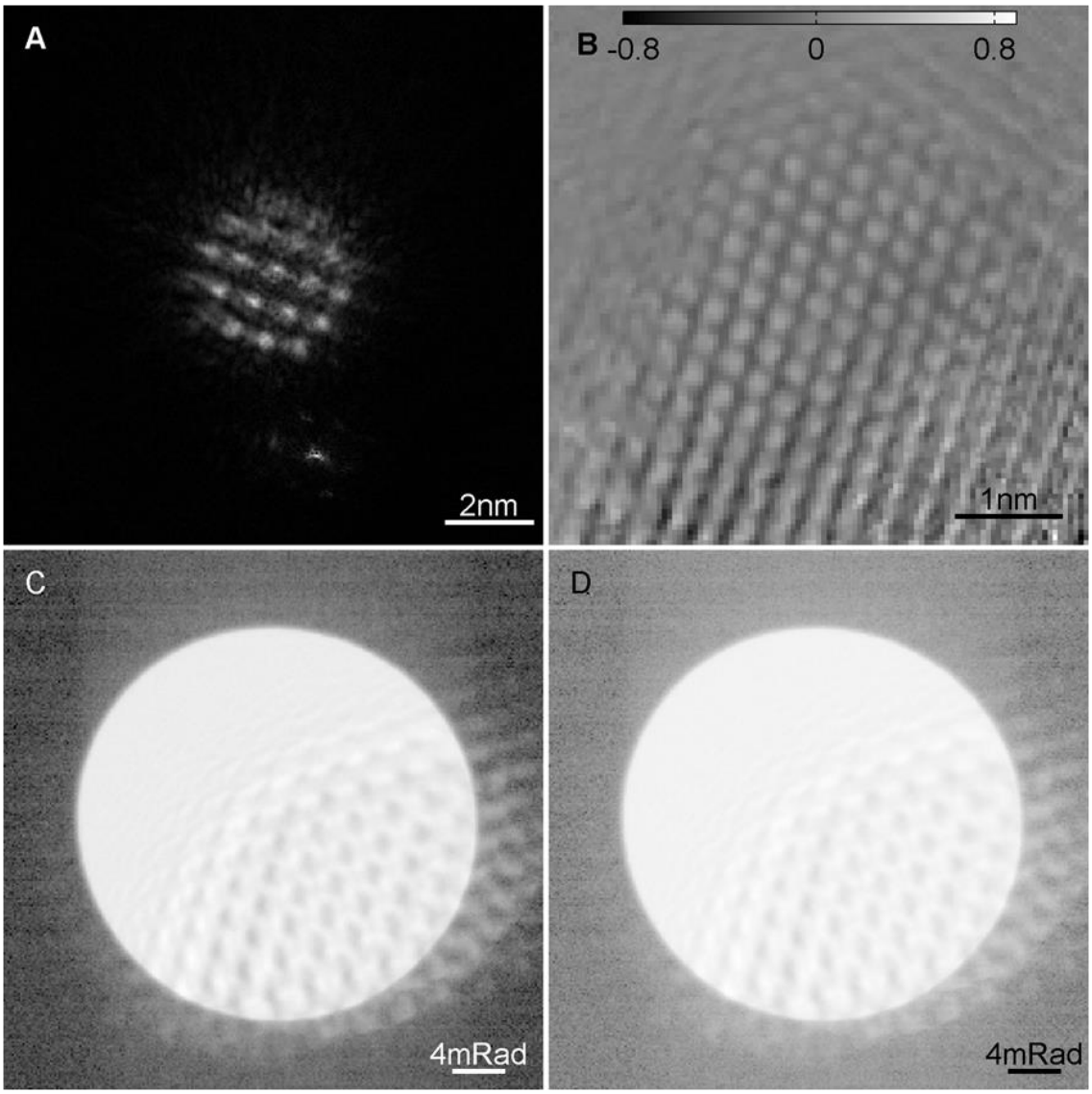

Figure 6.5: Initial reconstruction of the dataset from Figure 6.4d through ePIE. a) Modulus of the probe, b) Phase of the object, c) Intensity of a typical diffraction pattern (log scale), d) the output diffraction pattern (log scale).

6.1.4 MS-PIE Reconstructions with Detector Extrapolation

The secondary probe in Figure 6.5a could represent a myriad of inconsistent contributions to the dataset. There are several sources of incoherence in the electron microscope, from the source of electrons itself, the stage and specimen, to the lenses and coils throughout the column. None of these elements remain entirely stable throughout the acquisition time and each can be treated as a separate contribution to the diffraction pattern – via an incoherent addition of intensities.

The dataset is re-run through the MS-PIE algorithm with two full modes (two probes and two objects) of equal wavelength. The first probe mode is the usual initial estimate and the second probe mode is taken from the secondary probe peak in Figure 6.5a. The primary reconstructed mode is shown in Figure 6.6. It is quite clear that the probe function is much cleaner, the secondary peak is gone and the main probe is generally more complete. Although not at first obvious, the contrast of the object's phase (Figure 6.6b) is increased (see colour bars). The removal of the problematic peak from the experiment has therefore definitely improved the reconstruction of the remaining mode. The diffraction pattern however seems aliased (the ripples in between the disc and the edge). As the wave-field at the detector plane is formed from a convolution of the probe and the object function after propagation to the detector plane (in the far field), it will always be a requirement that a region outside of the diffraction pattern (which corresponds to the maximum width of the smaller of the two functions) is allowed to update during the reconstruction. In this case, as the probe is known to be localised in the detector plane, it is sensible to add a border which corresponds to the width of the bright-field disc. Using the detector extrapolation method outlined in section 2.4.1 it is possible to computationally extrapolate out into this region and in so doing prevent aliasing effects. The dataset is reconstructed once again with the two-mode MS-PIE arrangement as for Figure 6.6 along with the detector extrapolation update in reciprocal-space and the result is shown in Figure 6.7.

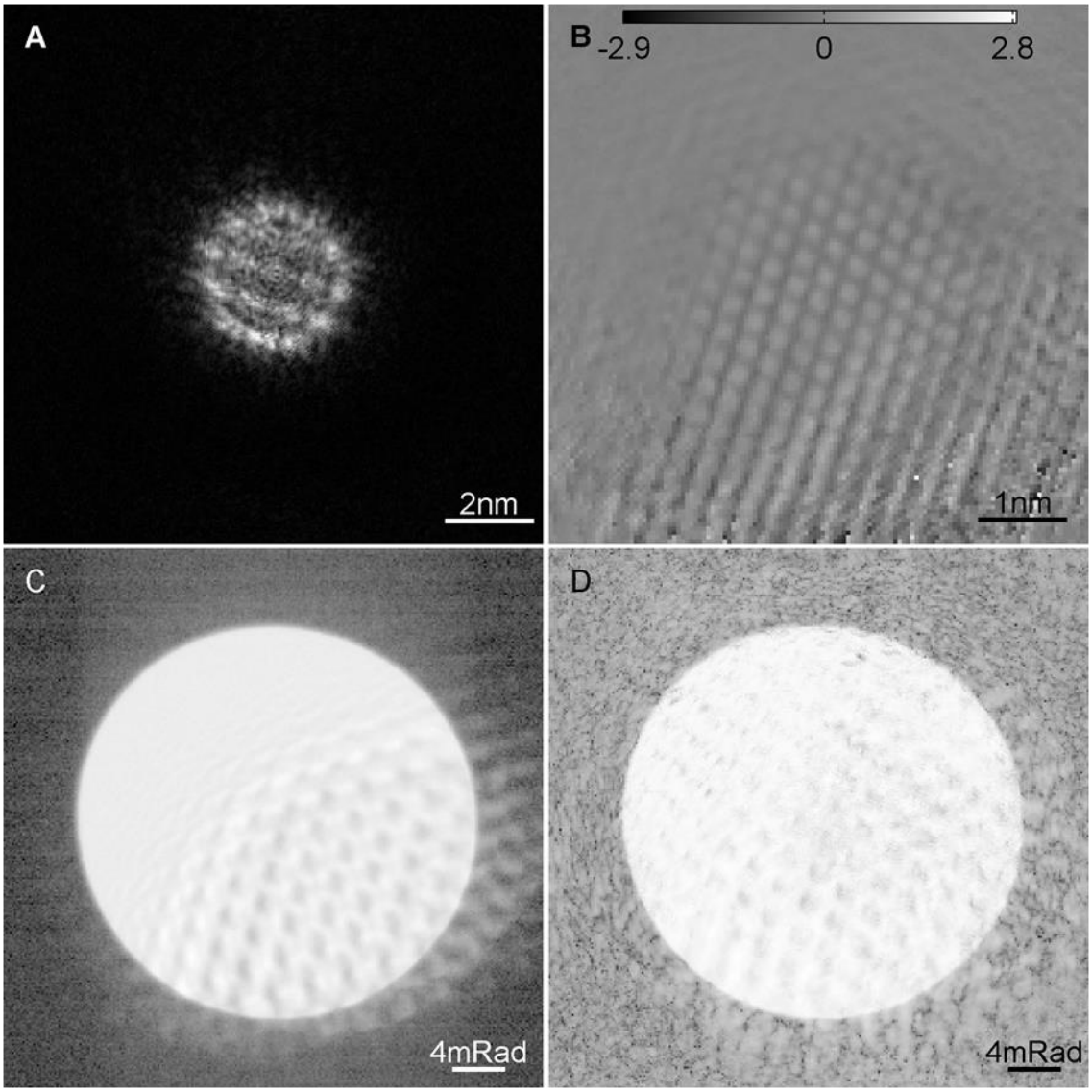

Figure 6.6: Reconstruction of the dataset from Figure 1.4d through MS-PIE with two modes of equal wavelength. The dominant mode is shown. a) Modulus of the probe, b) Phase of the object, c) Intensity of a typical diffraction pattern (log scale), d) the output diffraction pattern (log scale).

The reconstruction of the main mode is improved yet further (albeit only slightly). The main effect on the reconstruction is that the probe function is more complete, with less structure imprinted from the specimen. It can be seen from the output diffraction pattern (Figure 6.7d) though that the detector extrapolation has allowed for some of the aliased structure from Figure 6.6d to spill out beyond the recorded region. This is the first time the super-resolution technique has been applied to electron ptychography and shows that such principles may be used under more ideal circumstances in the future.

These results demonstrate sub-nanometre phase imaging within a high energy TEM/STEM, an important result in the development of high resolution electron ptychography. Unfortunately though the requirements on data acquisition were not fully appreciated at the time of recording and the dataset is subsequently far from ideal. Although the algorithm is powerful enough to massage out a fairly clean and self-consistent reconstruction it is heavily limited by the total size of the scan. It is now understood that a 5x5 scan is quite severely smaller than the simultaneous recovery of the probe function requires.

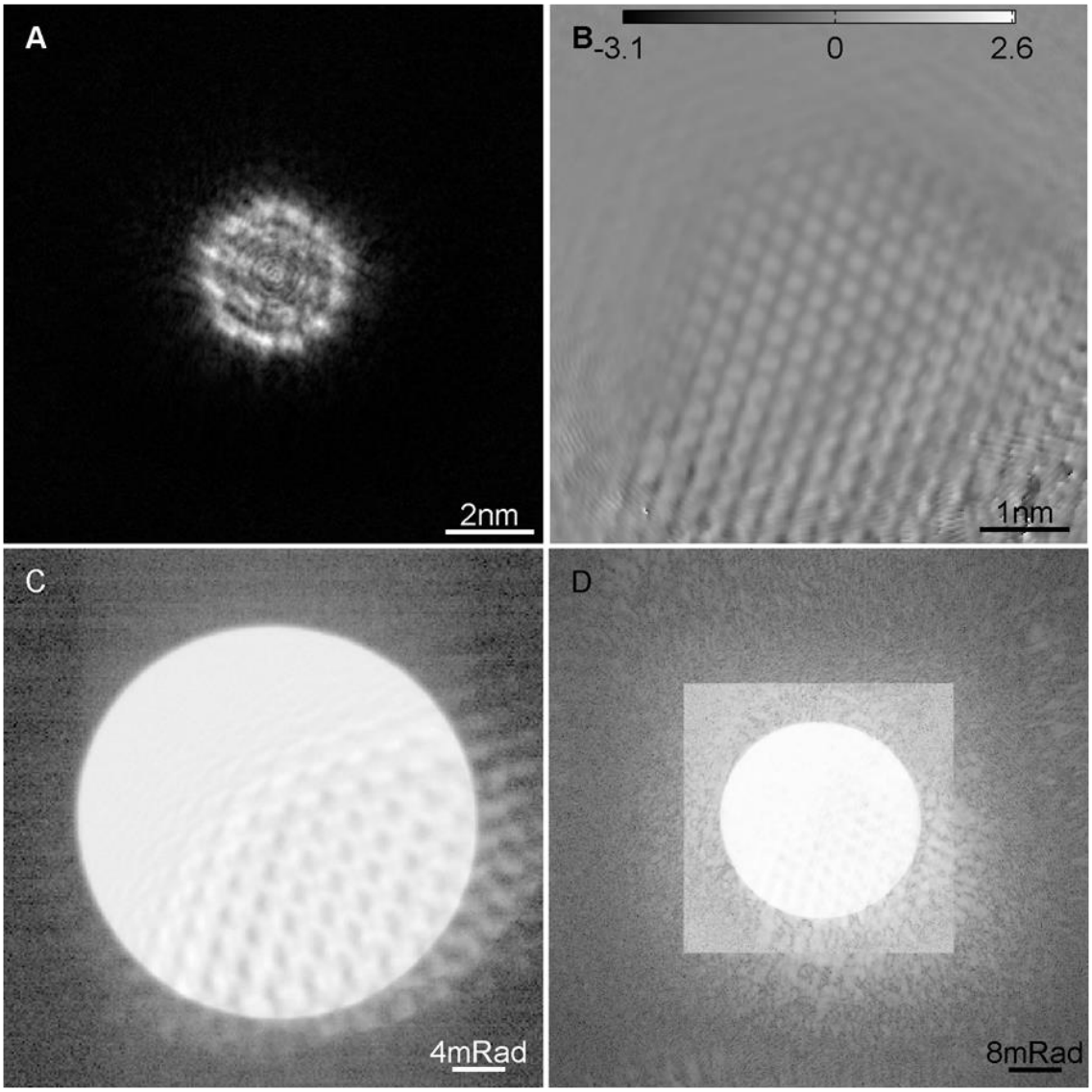

Figure 6.7: Reconstruction of the dataset from Figure 1.4d through MS-PIE with two modes of equal wavelength and the detector extrapolated to accommodate the convolution of the central disc. The dominant mode is shown. a) Modulus of the probe, b) Phase of the object, c) Intensity of a typical diffraction pattern (log scale), d) the output diffraction pattern (log scale).

Some of the experimental issues that have been prohibiting the progress of electron ptychography may be alleviated by exploiting the sampling condition discussed in chapter 3. Building on from the real-space considerations of mixed state imaging in chapter 5, the following section describes extensions to the PIE algorithm which I have developed in order to overcome some of the experimental hurdles.

6.2 Detector Imperfections

The principle aim of ptychographic imaging is to replace, and improve upon the functionality of, the imaging lens. More specifically, the lens is replaced by a scanning stage along with a detector. The quality of the reconstructed images is now limited by the properties not of a lens but of those two elements. One of the limits of current detectors is that the response is imperfect. Many detectors suffer from background noise, coupling issues with the scintillator, saturation, and limited regions of linearity. In order to overcome this, images are currently recorded as dark-field (false signals on the detector when no beam is present) and gain (the amplification or attenuation of the signal) references which are then applied post acquisition to correct the raw data. When recording diffraction data that is subsequently used in a ptychographic reconstruction, the sensitivity to these imperfections is much higher than in a conventional image.

An example of the effect that imperfect detection has on a recorded image is shown in the response functions of Figure 6.8, where the offsets are some background noise and the gain in one corner represents a four chip configuration where the top left corner has a higher gain response than the other three.

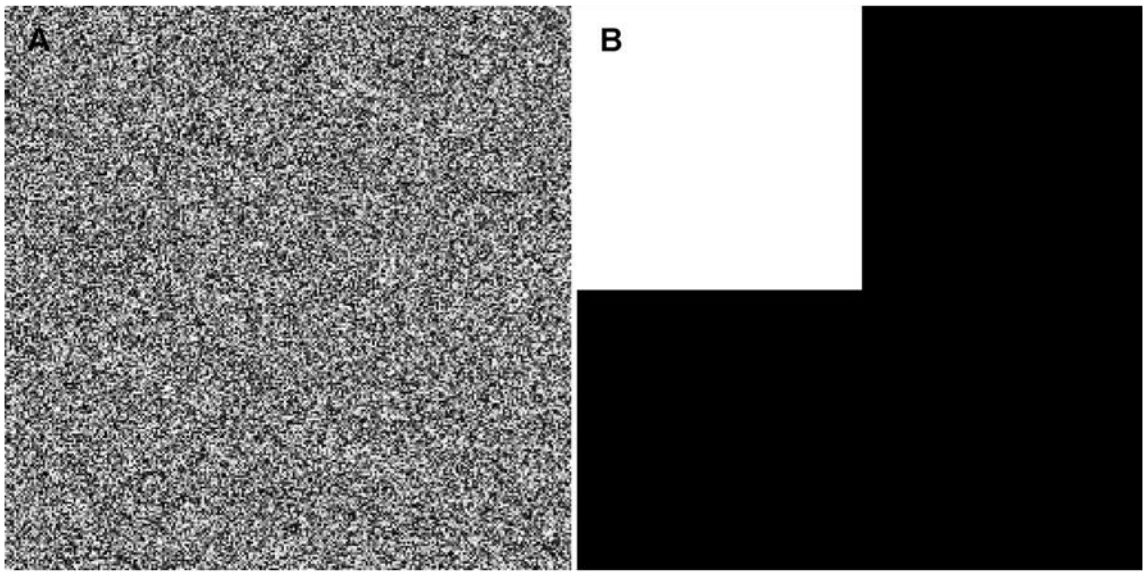

Figure 6.8: A typical imperfect detector response, used to corrupt ideal diffraction patterns. a) Offsets (values between 0 and 200). b) Gains (values between 1 (black) and 1.5 (white)).

6.2.1 ePIE Reconstruction

A model dataset is simulated (the same dataset is used again in later sections) and each diffraction pattern is subsequently modified by the response in Figure 6.8. The modified dataset is processed through the ePIE algorithm so that the effects that the imperfect detector response has on current reconstructions may be seen. The real-space outputs are shown in Figure 6.9.

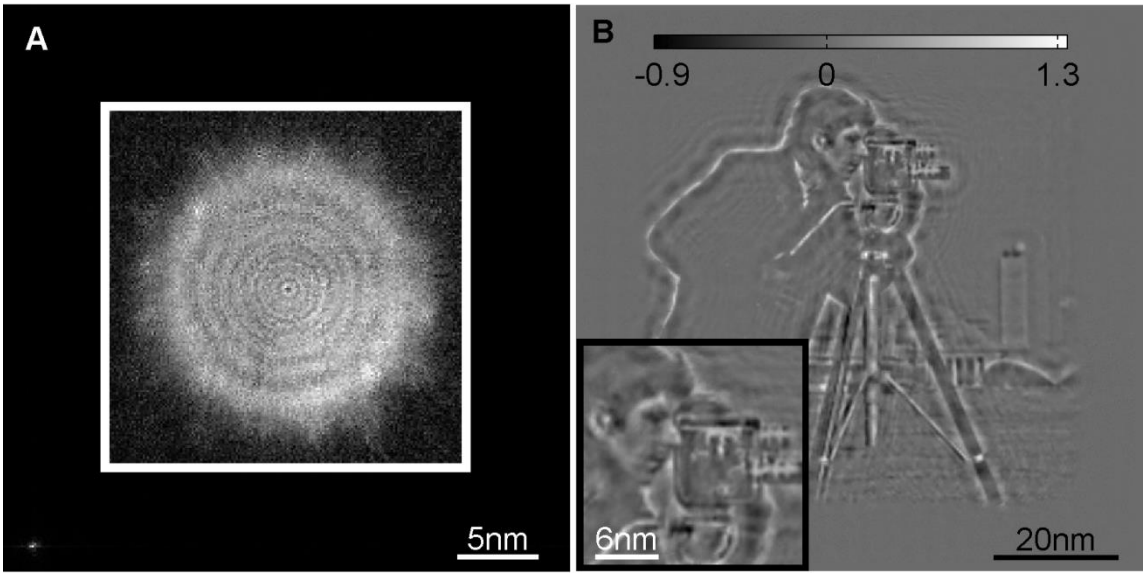

Figure 6.9: Reconstructed outputs from the modified dataset. a) The modulus of the probe. The region within the box within a white border has a gain of 41 so that it may be seen alongside the bright peak in the bottom left corner. Note the peak in the bottom right corner, which is at a gain of 1 and dominates the probe reconstruction. b) The phase of the object with magnified inlay.

Although the object has reconstructed to some extent, the contrast is low and the general quality is poor. The probe function has converged to a solution with a significant peak in the bottom left corner, a phenomena that is often observed in the reconstruction of poor quality datasets. Essentially the most consistent solution is reached by dumping other false contributions in a small peak in a region which has as little interaction with the object structure as possible.

A typical diffraction pattern from the dataset along with the corresponding output from ePIE is shown in Figure 6.10. Although ePIE struggled to recover the real-space functions, an estimate of the actual diffraction pattern has still been produced very accurately, a common property of ePIE as the constraint in reciprocal-space is very strong.

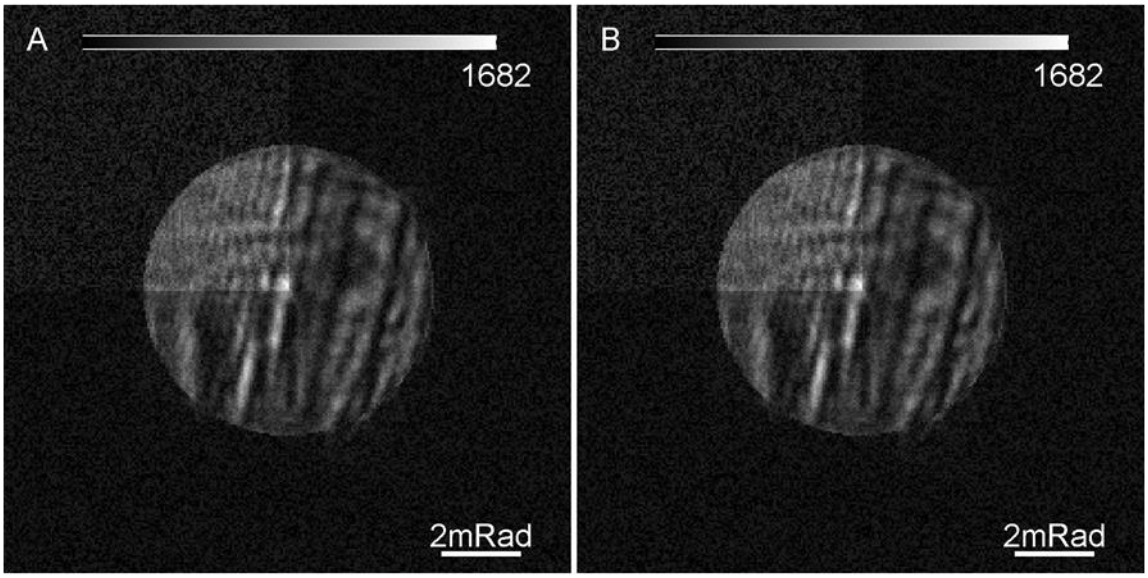

Figure 6.10: Typical diffraction pattern. a) From the modified dataset. b) Corresponding diffraction pattern as reconstructed from the ePIE algorithm.

6.2.2 DR-PIE

As the reconstruction in Figure 6.9 shows, the ptychographic dataset is more sensitive than direct imaging techniques to imperfections in the detection processes. This is not surprising as in ptychography the detector is a major part of the processing, not merely a detection of the result. In an effort to improve this aspect of the ptychographic imaging method (particularly with electron ptychography in mind) a detector response recovery algorithm is now described.

Rather than always using the same potentially corrupted recorded data, I^M, to modify the current estimate of the wave-field in the detector plane (reciprocal-space constraint), the DR-PIE algorithm uses a corrected dataset, I^A. The corrected dataset is related to the original dataset by a detector response function, DR. The estimated detector response is an array of values, one for each order of distortion (offset, gain, and higher order terms) for each physical detector pixel. Each update step is performed using the adjusted dataset, I^A, which is calculated (typically every few iterations) from the current set of estimates and the full set of original measurements. This is possible because of the large range of intensities at which many of the detectors pixels are subjected to during a scan: many pixels are exposed to a range of incident intensities. The detector response update element is added in between the reciprocal-space update step and the recorded dataset, as shown in Figure 6.11.

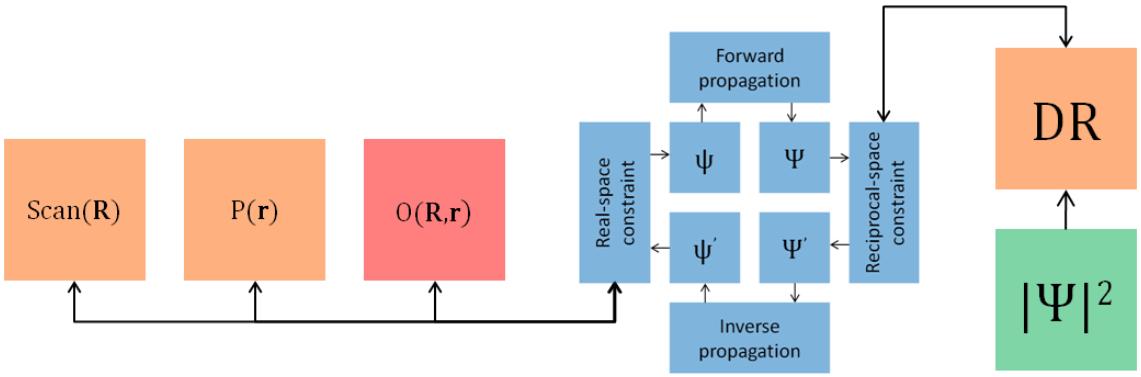

*Figure 6.11: A flow diagram of the DR-PIE reconstruction algorithm for a single iteration at scan position **R**, where **r** represents the real-space coordinates. The kernel of the algorithm (shown in blue) feeds from the known values (shown in green) in order to solve for the unknown object (shown in red) and partially known probe, P, and scan (shown in orange). Added as an unknown here is the detector response, DR, which is updated periodically throughout the iterations. The reciprocal-space update step is performed on the measured data after correction through the detector response.*

As each detector pixel records a range of intensity values at each pixel throughout a ptychographic dataset, it is possible to correct for systematic errors within the recording of the intensity values for each pixel. Plotting the measured values against the recorded values of each pixel at each scan position over an iteration it is possible to fit a polynomial (see Figure 6.15). In the case examined here the polynomial consists of two terms, the zero and first order. There is no reason why higher orders couldn't be added to account for non-linearity. The polynomial is fitted to the distribution through a least squares fitting procedure via the polyfit() function available in MATLAB.

Once the detector response estimate has been updated, the adjusted dataset must be re-computed. The reciprocal-space update step is then performed using the adjusted dataset, I^A, where previously the recorded measurements, I^M, where used. The adjusted dataset is computed using the DR such that,

$$I^A = \frac{I^M - DR(0)}{DR(1)}, \tag{6.1}$$

where $DR(0)$ and $DR(1)$ are the offset and gain of the detector response.

6.2.3 DR-PIE Reconstruction

The DR-PIE algorithm, as outlined above, is used to process the same dataset as used to produce Figure 6.9. The detector response is updated every 5 iteration throughout the reconstruction and the algorithm converged to the solution shown in Figure 6.12. The corresponding detector response as calculated by the algorithm is shown in Figure 6.13 and a typical diffraction pattern from the dataset along with the corresponding reconstruction estimate from DR-PIE is shown in Figure 6.14.

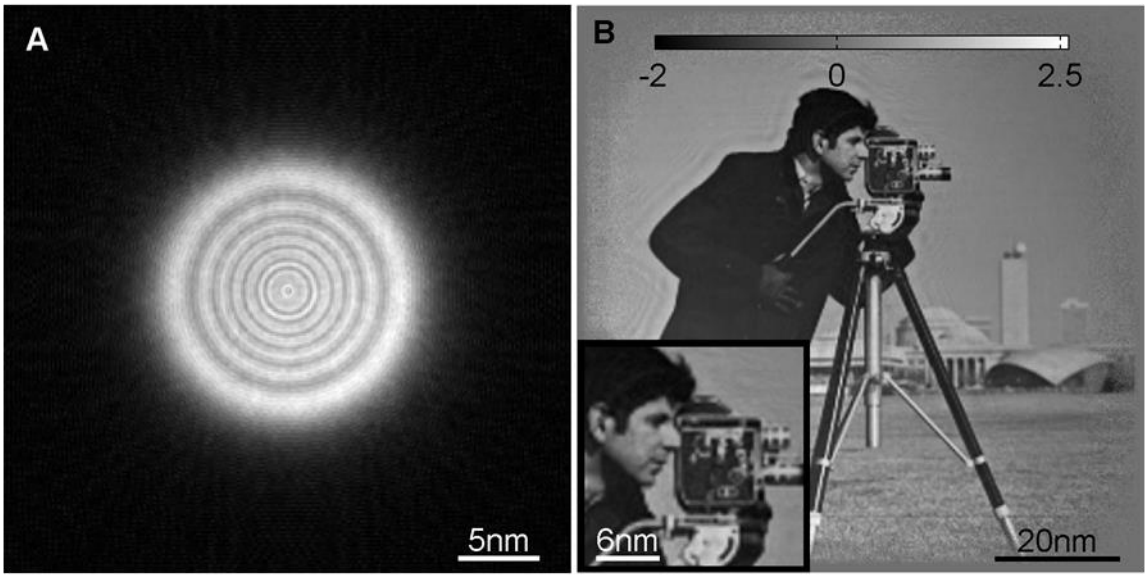

Figure 6.12: Reconstructed outputs from the modified dataset after using the DR-PIE algorithm. a) The modulus of the probe. b) The phase of the object.

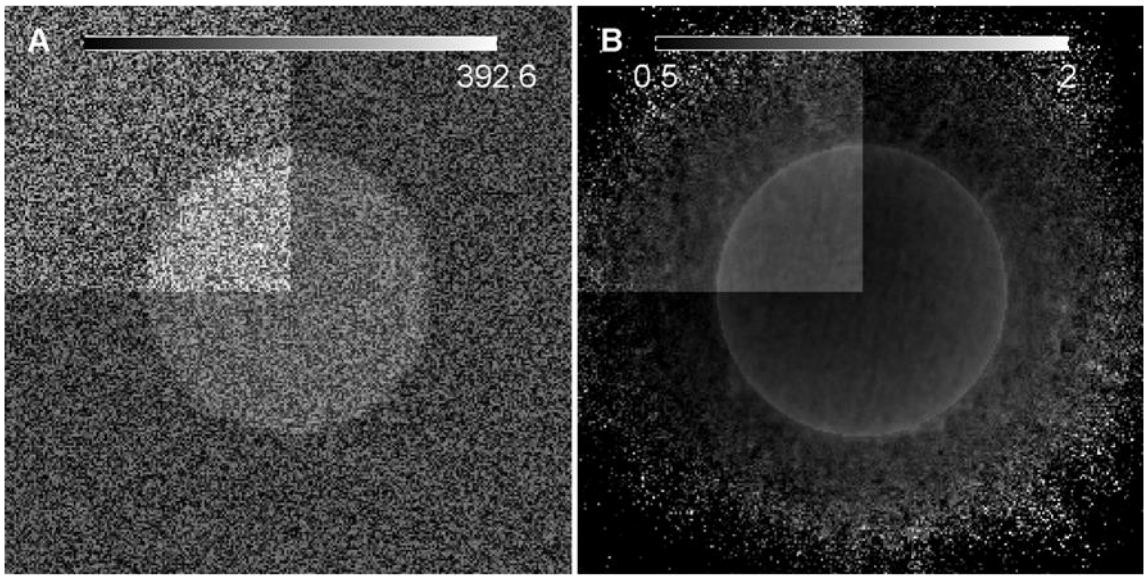

Figure 6.13: The detector response as outputted from the algorithm during the reconstruction shown in Figure 6.12. a) Offsets. b) Gains.

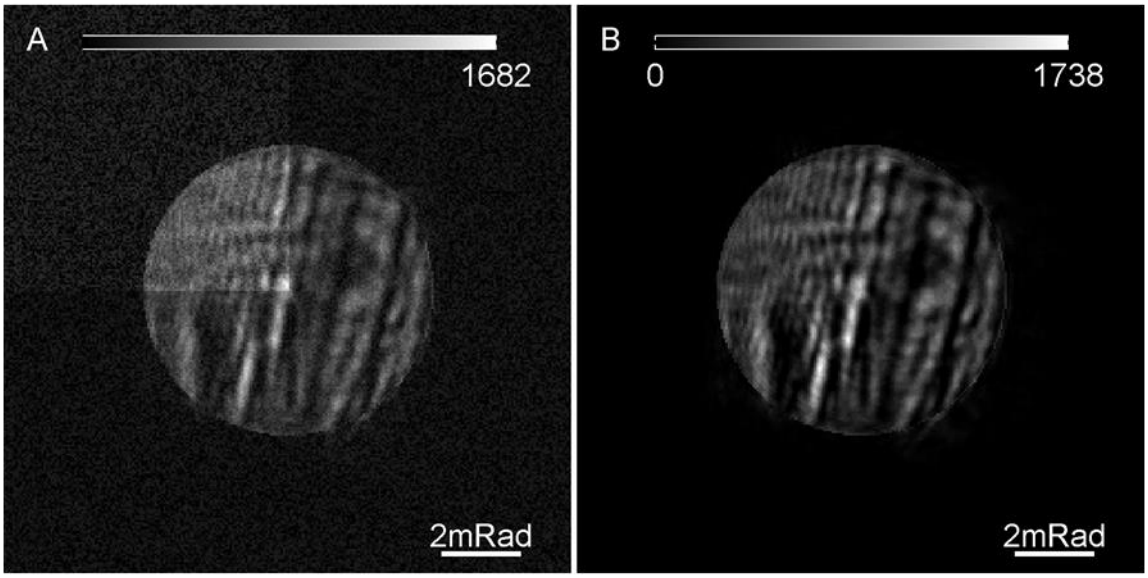

Figure 6.14: Typical diffraction pattern. a) From the modified dataset. b) Corresponding diffraction pattern as reconstructed from the DR-PIE algorithm.

Unlike Figure 6.10, the estimated diffraction pattern is now much cleaner and shows none of the effects of the detector imperfections. Instead, the estimate more accurately represents what would have been recorded on a perfect detector – a result which promises to reduce the requirement on high quality detectors for ptychographic imaging.

In order to more easily observe the workings of the detector correction process a plot is shown in Figure 6.15 which shows a snapshot for a single pixel at a single point (fifth iteration) during the

reconstruction. The same analysis is also performed at the 50th iteration, the result of which is displayed in Figure 6.16. The estimated response is clearly moving towards the actual detector response. The offset values are good while the gain is slower to converge. The algorithm is allowed to continue for a further 350 iterations at which point the analysis is performed a final time, the result is shown in Figure 6.17. The estimates response has converged further still towards that of the true detector response. The gain also appears to be beginning to converge at this point.

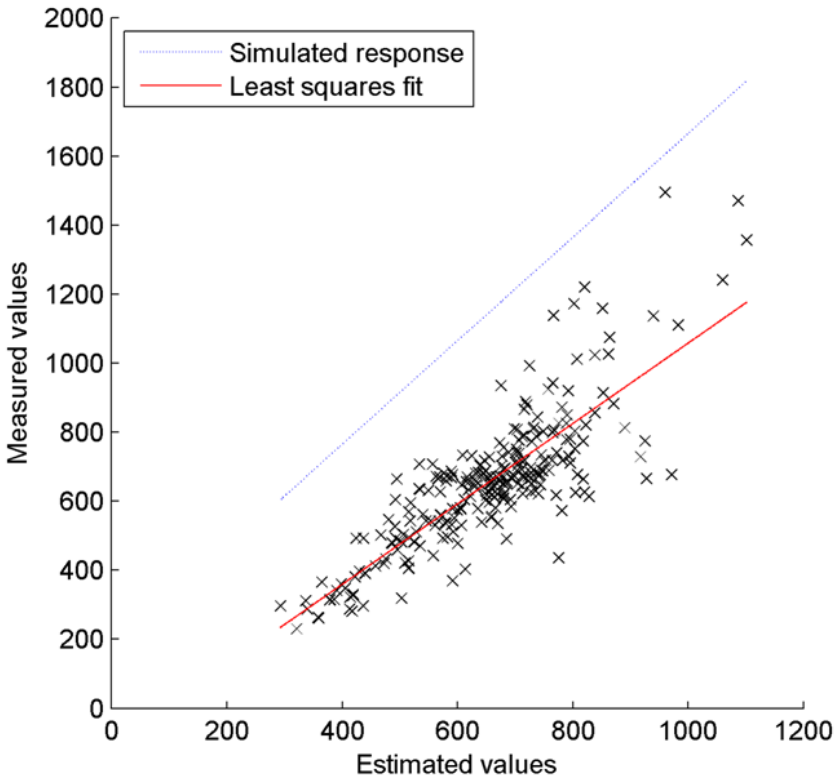

Figure 6.15: The response profile of a typical pixel after 5 iterations along with the artificially added response (dotted blue line) and the computed first order polynomial fit (solid red line).

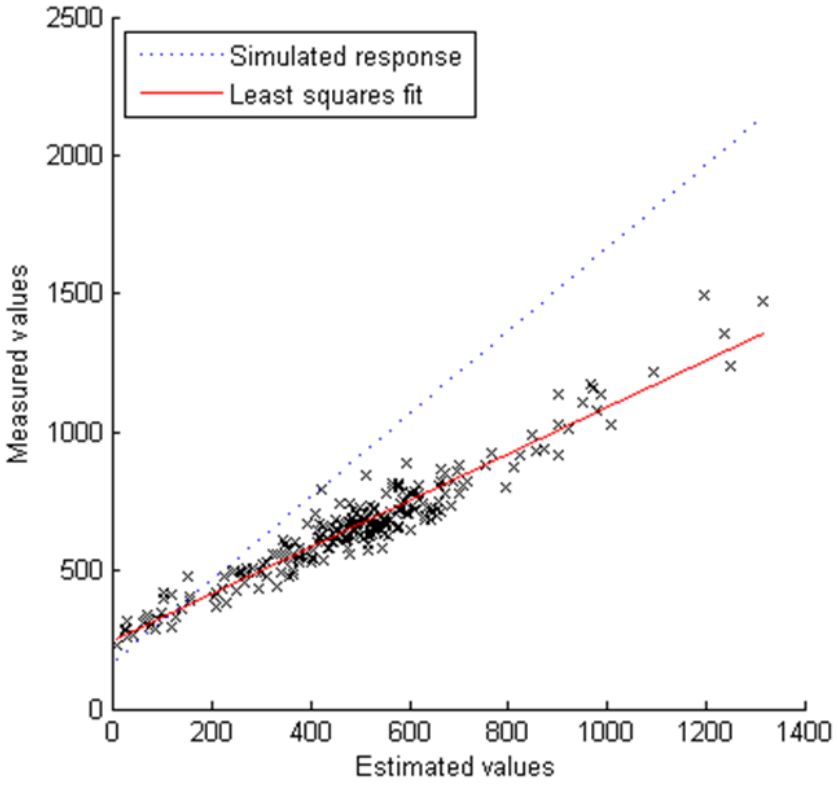

Figure 6.16: The response profile of a typical pixel after 50 iterations along with the artificially added response (dotted blue line) and the computed first order polynomial fit (solid red line).

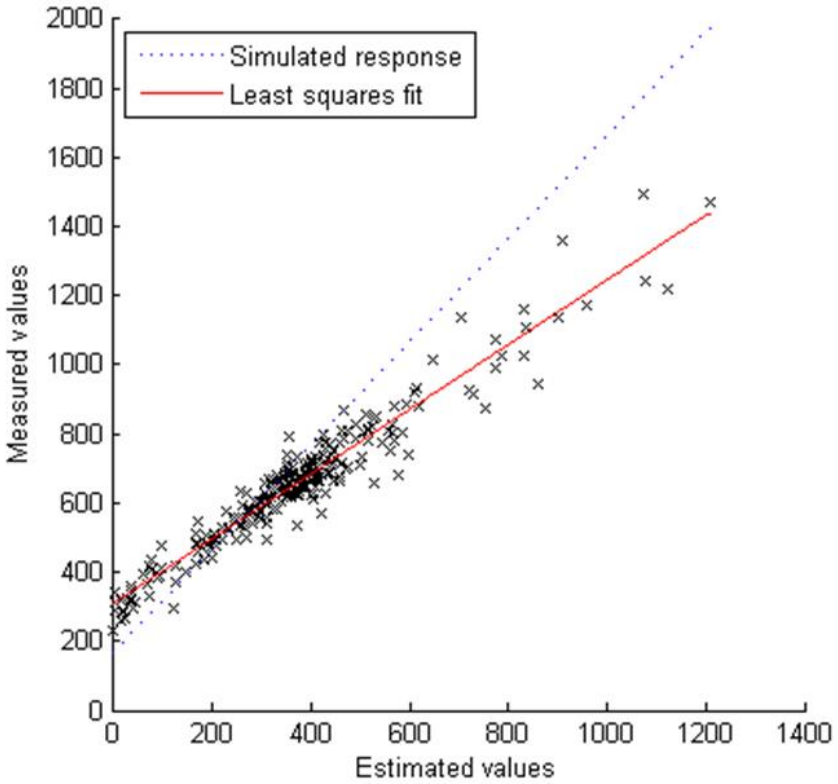

Figure 6.17: The response profile of a typical pixel after 400 iterations along with the artificially added response (dotted blue line) and the computed first order polynomial fit (solid red line).

6.3 SEM Ptychography

The SEM (modified to operate in transmission mode) offers a simpler experimental setup than the higher energy TEM/STEM microscopes. The most obvious difference is in the accelerating voltage of the electrons, the SEM used to record the data in this section was at 30keV whereas the above mentioned STEM experiments were conducted at 300keV. Lower energy electrons have a longer associated wavelength and so offer a lower intrinsic resolution. However, as the electron microscope is yet to enter the diffraction limited region, this is not the main consideration for the progression of electron ptychography at this time. One of the issues that ptychography faces in the TEM/STEM is from the post specimen lenses (intermediate and projector). These lenses introduce instabilities into the recording of the diffraction patterns such as pincushion distortion, rotations, as well as the above mentioned drift. The SEM does not have these lenses and so the experiment has fewer potential instabilities and distortions.

6.3.1 ePIE Reconstruction

The data used in this section is the same as that used to produce the first demonstration of ptychography in the SEM (Humphry et al., 2012). The reconstructed specimen from that publication is shown in Figure 6.18 and represents a significant step forward in electron ptychography as it extends the resolution of the SEM microscope beyond the limit of the lens.

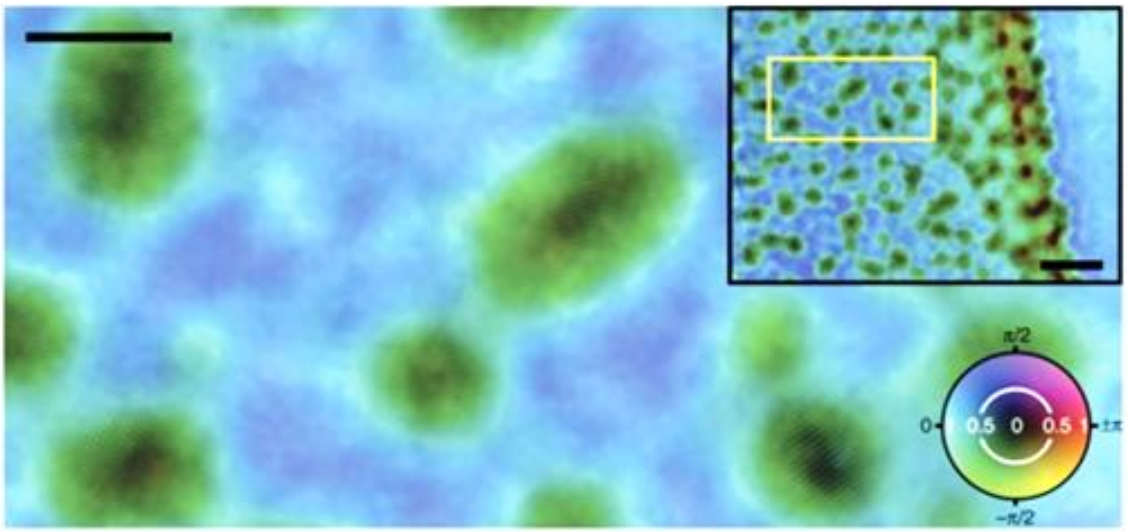

Figure 6.18: ePIE reconstruction of gold particles from data recorded in an SEM (Humphry et al., 2012). The main scale bar represents 5nm and the wider field of view inlay has a scale bar of 15nm.

6.3.2 DR-PIE Reconstructions

The original dataset used for Figure 6.18 was cropped down to 512x512 for processing reasons and so in order to compare the DR-PIE algorithm reconstruction directly with the current state-of-art result, a similarly cropped dataset is processed.

The detector response, as produced from DR-PIE during the reconstruction, is shown in Figure 6.19. The bright areas around the edge are as a result of the convergent form of the beam and the higher frequency components within the specimen. As in Figure 6.7, an extrapolation, determined by the size of the illumination in reciprocal-space, must be performed for the convolution to be valid. A consequence of not employing detector extrapolation can be seen in Figure 6.19b. The flux which should be distributed outside of the detector is forced to be expressed inside (satisfying Parseval's theorem as in section 2.1.8) and the algorithm expresses as an increase in the gain in some regions. Figure 6.19a shows that an offset has been removed from the area that is exposed to the central disc, which suggests that the scintillator is producing a continuous background of photons in this region. A process which is seen as an afterglow on the detector when the beam is blanked.

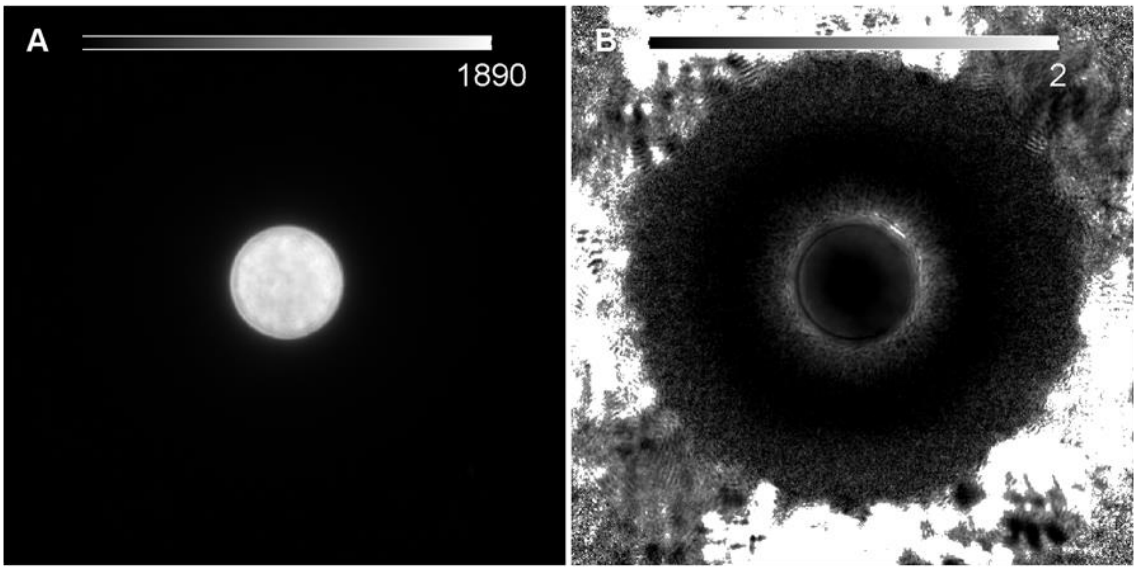

Figure 6.19: The detector response, DR, as outputted from the DR-PIE algorithm during the reconstruction of Figure 6.20. a) Offsets. b) Gains.

The complex image of the object that is produced during this reconstruction is shown in Figure 6.20. Although some atomic fringes are visible in the original reconstruction, the contrast is low (see Figure 6.18). After processing the same, cropped, dataset through DR-PIE the contrast is improved and similar structure can be seen in all of the particles. It can also be seen that some of the particles that appear as oval in Figure 6.18 are actually overlapping spherical particles, the phase doubles accordingly in such regions.

The reconstruction is re-run on the full dataset with a suitable border of unconstrained pixels outside of the known regions of values (see Figure 6.22). The new reconstruction of the specimen is shown in Figure 6.21. The quality of the reconstruction is a great improvement upon the original (Figure 6.18). The increase in resolution and contrast reveals the atomic planes and columns in all of the gold particles with clarity. The reconstruction has clearly resolved the sub-nanometre atomic distances although some delocalisation between the particles and some of those planes remain. This may be due to inaccuracies in electron energy, camera length, scan steps, or other parameters which give rise to a defocused reconstruction.

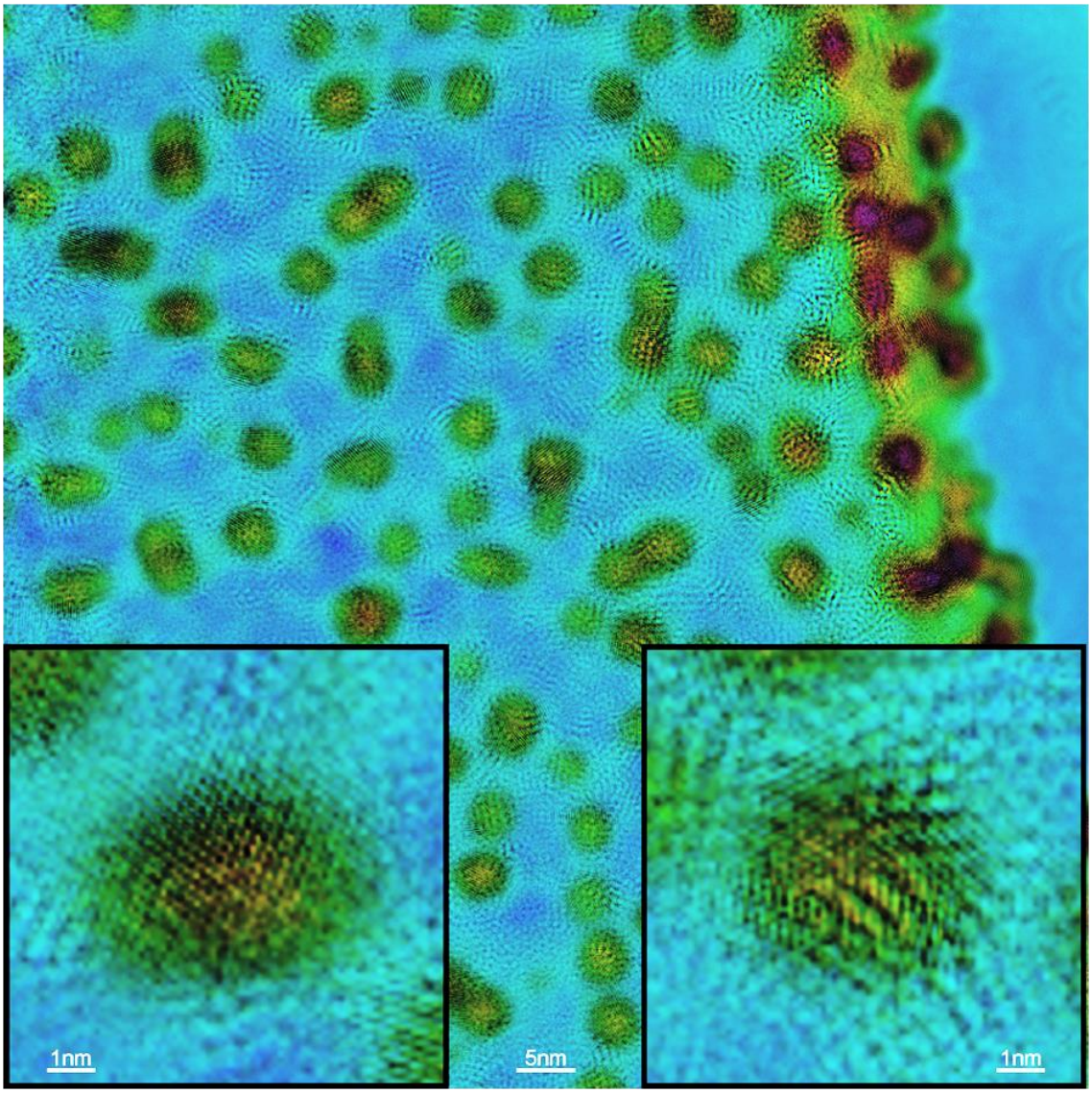

Figure 6.20: DR-PIE reconstruction of the object from the cropped SEM dataset, showing gold particles in a variety of orientations. Two selected regions are shown again in magnified inlays. The colour wheel is as in Figure 6.18.

In the improved reconstructions (see Figure 6.20 and Figure 6.21), a speckle structure is present across the carbon film. As this does not exist in the area of free space (on the right of the image) it seems as though this could be real structure in the carbon support film. A similar structure can be seen in amorphous carbon films in bright field images at similar length scales, see (Howie, 1978). It should be understood that when dealing with diffractive imaging, such effects may also arise from removing or adding Fourier components, in this case by an artificial truncation of the effective transfer function. For an example see figures 8 and 10 in (Maiden et al., 2011). This clearly requires further investigation.

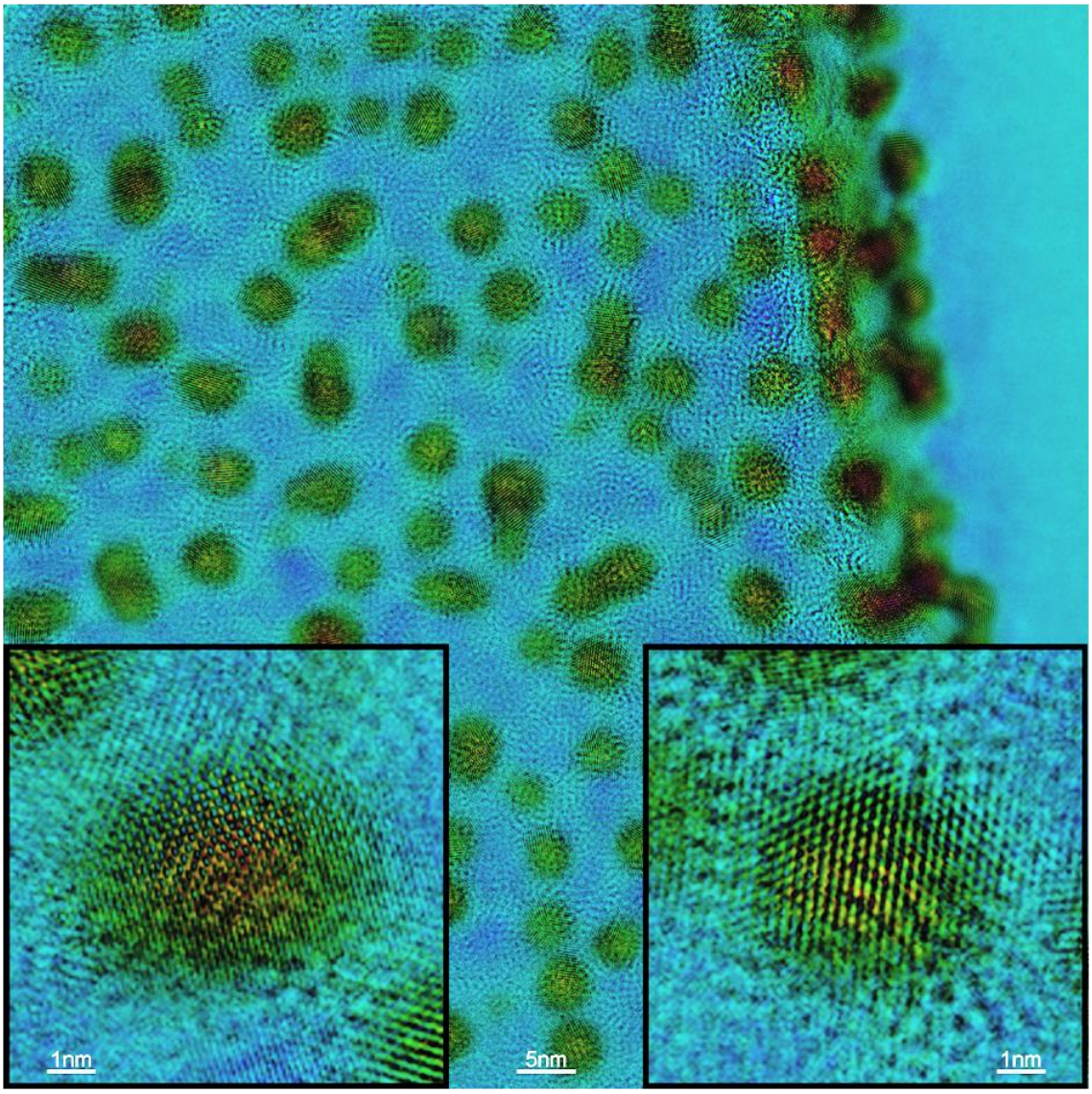

Figure 6.21: DR-PIE reconstruction of object from the binned SEM dataset, showing gold particles in a variety of orientations. Two selected regions are shown again in magnified inlays. The colour wheel is as in Figure 6.18.

The estimated detector response from the reconstruction is shown in Figure 6.22. The outer region of black in Figure 6.22b comes from the padding of the original data to 1024x1024, for reasons of computational efficiency, and the intermediate border of no structure is the region of unconstrained pixels. The unconstrained region has no physical measurements and so the detector response cannot be deduced and is forced to have zero offsets and a gain of unity. The input diffraction pattern is shown alongside the corresponding estimate of the diffraction pattern from the reconstruction in Figure 6.23. Note that some of the peaks that are visible in the corrected diffraction pattern do not appear in the corresponding recorded pattern and although the background appears brighter, the signal to noise ratio is increased.

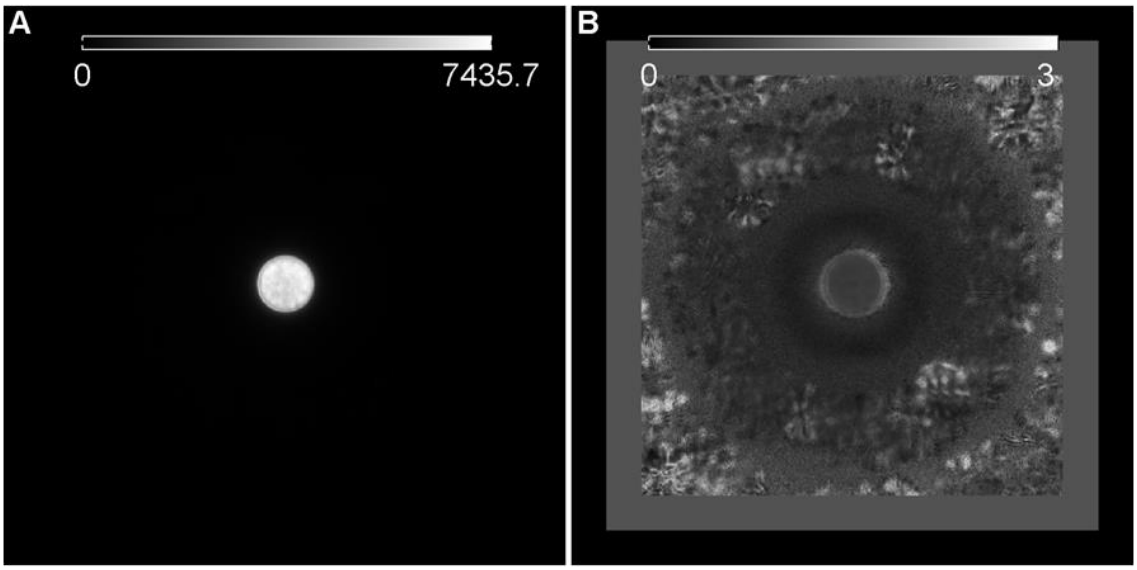

Figure 6.22: The detector response, DR, as outputted from the DR-PIE algorithm during the reconstruction shown in Figure 6.21. a) Offsets. b) Gains.

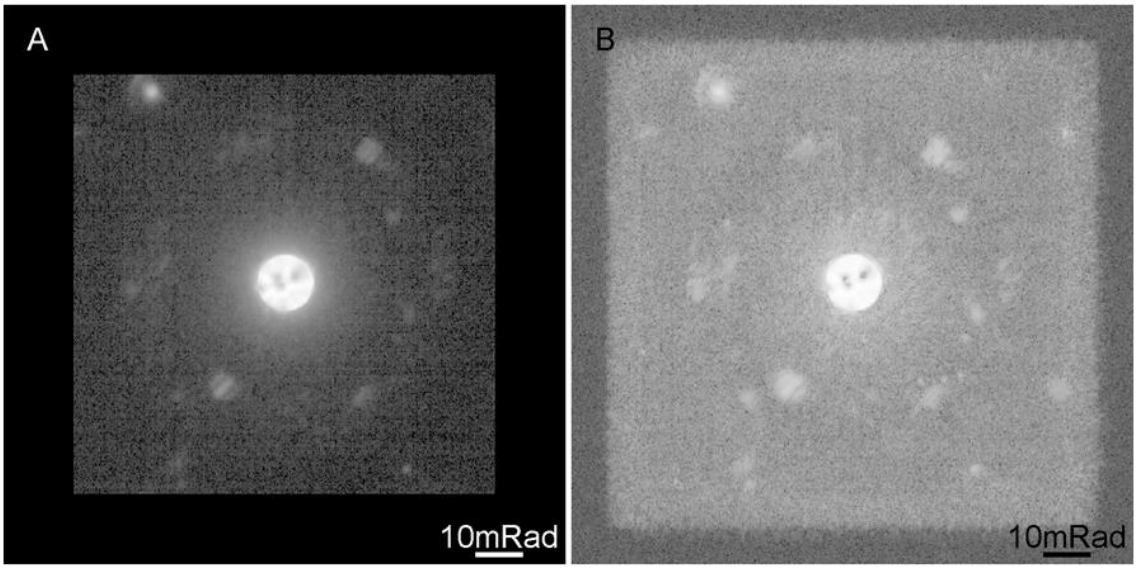

Figure 6.23: Typical diffraction pattern from the binned SEM dataset. a) The recorded dataset. b) Corresponding diffraction pattern as reconstructed from the DR-PIE algorithm. Both are displayed on a log scale.

As well as an improvement to the object reconstruction, the reconstructed probe function is also altered from that in the original image (see (Humphry et al., 2012)). The reconstructed probe, along with slices through the x and y planes after computational propagation through z, is shown in Figure 6.24. The two planes come to focus at different heights, showing the effects of two-fold astigmatism in the probe forming lens.

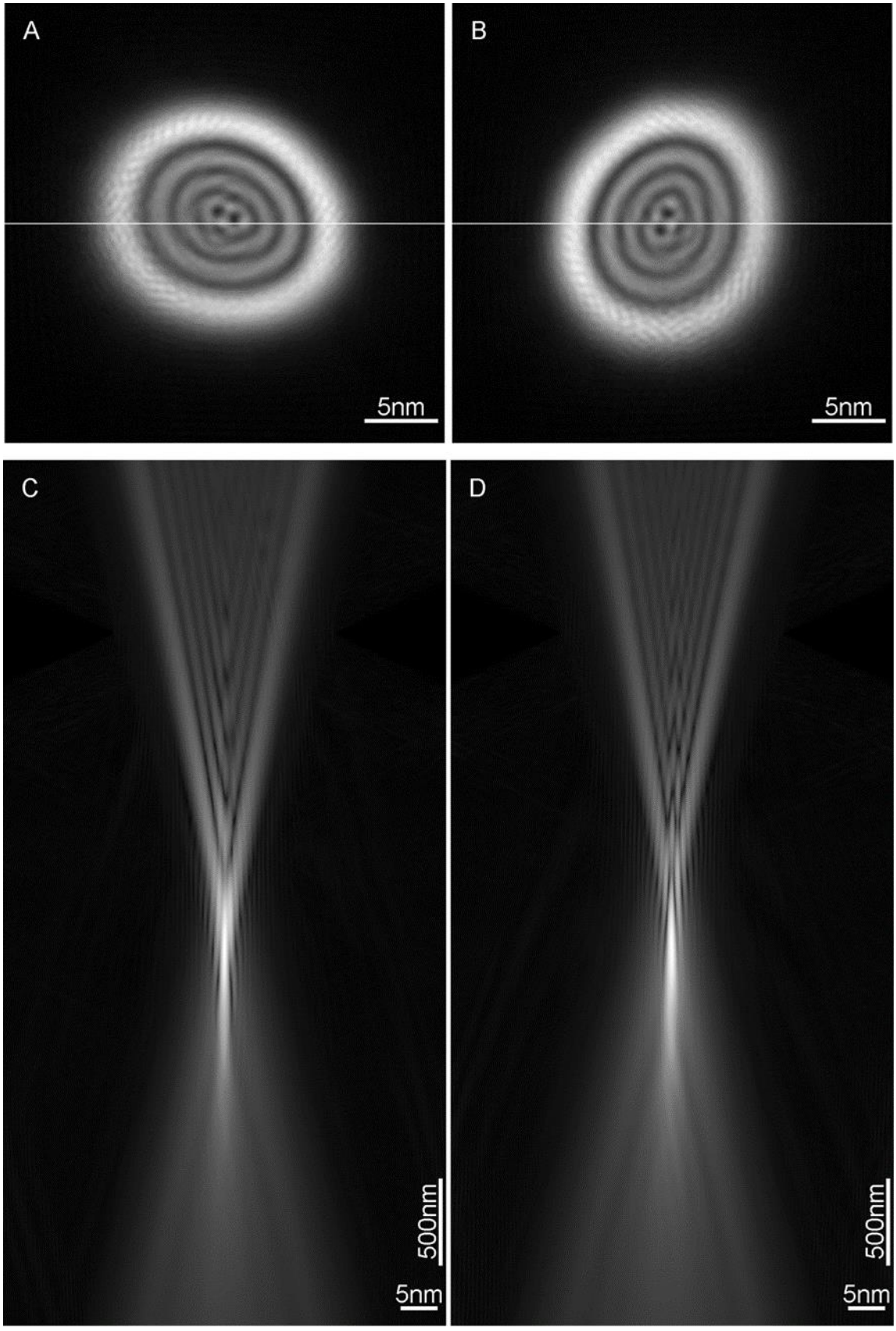

Figure 6.24: Profile of the electron beam as propagated through focus. a) an xy slice through the beam profile at the specimen plane. b) a yx slice through the beam profile at the specimen plane. c) an xz slice through the beam cutting through the focal point. d) a yz slice through the beam cutting through the focal point. (a and b are shown in modulus with the square root of the modulus used for c and d to display the dynamic range.)

6.4 Partial Spatial Coherence

Another one of the experimental issues facing electron ptychography is the level of stability and coherence offered by the source of electrons. Ptychography in STEM mode requires a defocused probe (a defocused source image) in order to sufficiently overlap the illuminated areas in the specimen plane as the scan progresses. The ability of ptychography to overcome the effects of partial coherence in the electron microscope has been described previously with regard to the Wigner-distribution deconvolution, where the 'stepping out' across points in reciprocal-space gave access to higher frequency information than the partial coherence within the probe scan could provide alone (Rodenburg and Bates, 1992). Unfortunately, the solution required recording a diffraction pattern on an array detector as the probe was scanned to every object element and, due to the levels of data processing required, was not entirely practical at the time. The principle remains sound though and here the situation is addressed in terms of the more recently developed iterative methods where fewer, sparser, steps are required in the real-space scan.

The case of an incoherent convolution operation occurring in the detector plane has been discussed in previous chapters. (Both the pixel up-sampling of section 4.3.2 and the effects of a multiple wavelength source under a simple aperture configuration from chapter 5 are examples of this.) However, when the probe is defocused, the source convolution with the probe (a function of the optical elements) occurs in neither the specimen or detector plane (as in conventional STEM and TEM respectively) but in some intermediate plane, as depicted in Figure 6.25.

6.4.1 Ideal Source

Initially, for comparison purposes, a point source dataset is generated and reconstructed through the ePIE algorithm. The outputs are shown in Figure 6.26. As would be expected, the ideal setup yields a very good reconstruction of both the probe and object functions. It is the probe and object functions shown in Figure 6.26 that should be used as a reference point for comparisons with later reconstructions executed under a partially coherent setup. Also required for a full comparison is a

typical model diffraction pattern and the corresponding reconstructed diffraction pattern, these are shown in Figure 6.27. As with the real-space reconstructions, it is not surprising that the single mode algorithm has produced a final diffraction pattern estimate that matches the model data very accurately.

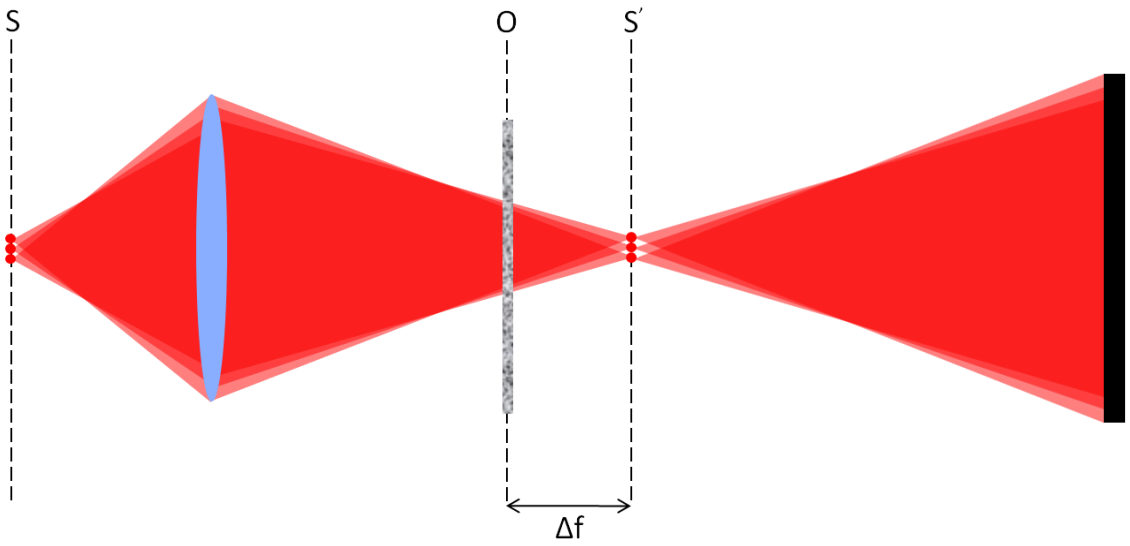

Figure 6.25: Schematic diagram of a defocused STEM setup in the presence of an extended source in the source plane, S. The object, O, placed at a defocused position away from the source image plane, S'.

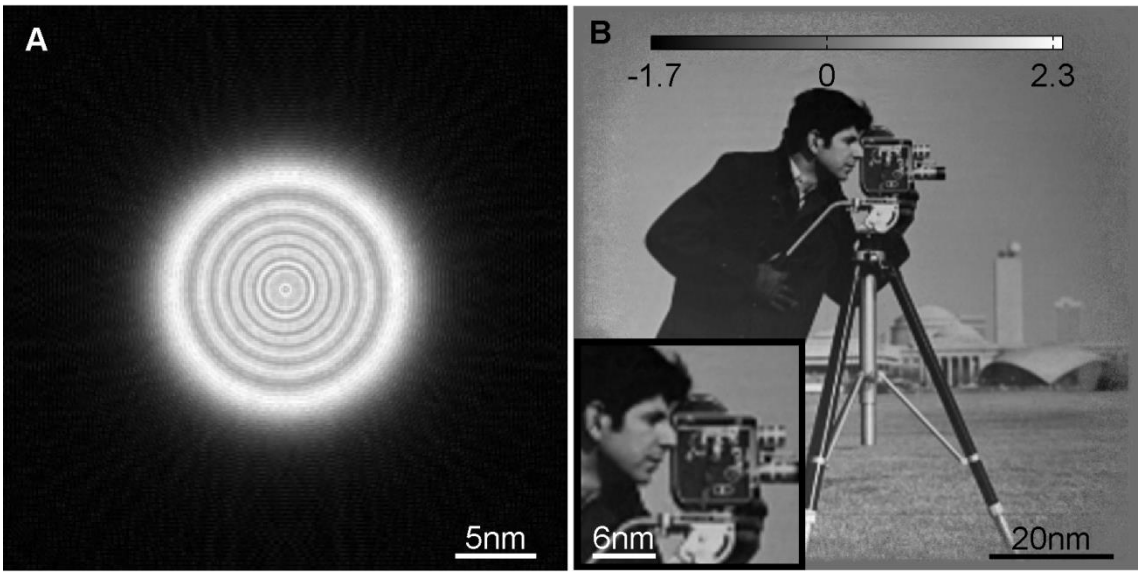

Figure 6.26: Reconstruction outputs from ePIE. a) Modulus of the illumination function, b) Phase of the object with magnified inlay.

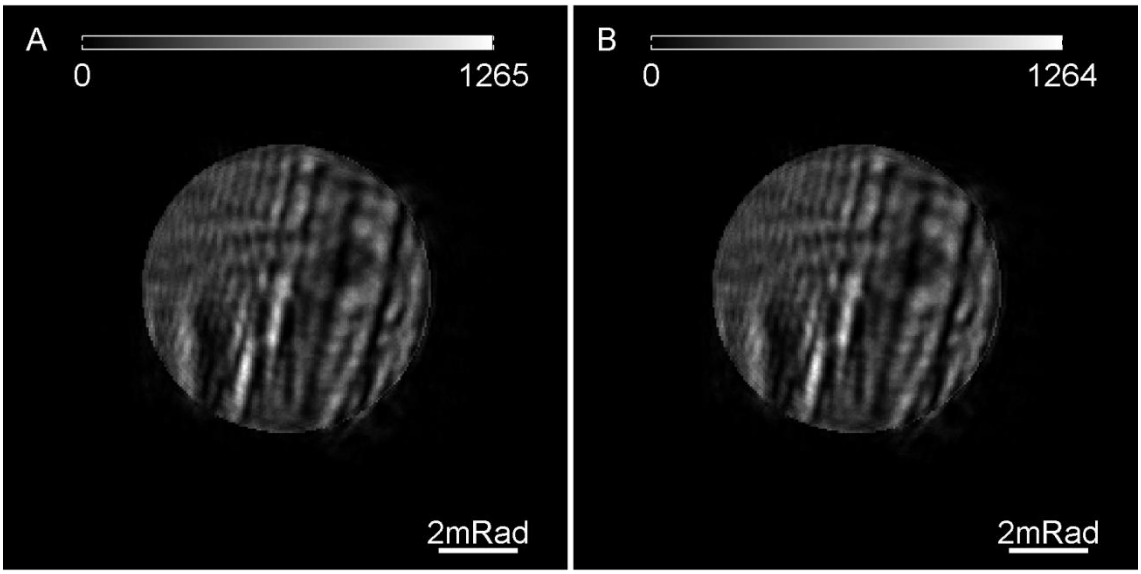

Figure 6.27: Typical diffraction patterns from a point source dataset. a) Inputted model diffraction pattern, b) corresponding reconstructed diffraction pattern.

6.4.2 Extended Source

The case of an extended source is now examined. Firstly, the generation of a dataset in the convergent beam STEM configuration with partial spatial coherence in the source plane is discussed. The simulation of a ptychographic dataset requires the computational propagation of an illumination function and resultant exit-wave between various planes. Such computational propagation relies on coherent interference effects and so the propagation of an incoherent beam is not directly possible. Instead, each coherent mode within the simulation must be simulated individually and the result integrated in intensity at the detector plane. Firstly, each source mode must be propagated through the probe forming optics, and then multiplied with the specimen before propagation into the detector plane. Propagating the source modes into the object plane is achieved through a modification of the probe estimate. The probe (Figure 6.28a) is propagated to focus (Figure 6.28b - the focal plane is effectively the conjugate plane of the source) where several shifted versions may be created. The power distribution may then be set by the source distribution and after a summation of intensities an extended source function is created (Figure 6.28c). The effect that the extended source has on the illumination function in the specimen plane is also shown in Figure 6.28d. The resulting patch of illumination that is incident upon the specimen when the source distribution of Figure 6.28c is passed through an optical system with an impulse response of that

shown in Figure 6.28a is the incoherent illumination function shown in Figure 6.28d. Although the loss of fringe visibility is dramatic, the following reconstruction algorithm is nevertheless able to deconvolve the impulse response of the optics from the extended source, producing a coherent reconstruction.

The extended source is modelled as a Gaussian distribution of emission intensity. The full width at half maximum (FWHM) is 3nm. Although 3nm is extremely large, especially in relation to modern microscopes, such a source is required to fully demonstrate the capabilities of the technique. It follows that recovering from less severely corrupted datasets is also possible, a principle tested later when the new algorithm is shown to converge when the source is actually ideal. The computational modelling requires a discretization of the source and a pitch between source elements of 4 Ångström is used to span an array of 15x15 individual elements. It is this limitation of the computational model which causes the source in Figure 6.28c to appear to be made of separate dots, they are in fact overlapped such that there are no zeros within the source. The resultant four-dimensional set of diffraction patterns (for a single scan position) along with the resultant sum of intensities across source modes (see equation 6.2) is shown in Figure 6.29. The total flux across the field of view in this simulation is 10^9 electrons and this is reflected in the shot noise present in the final diffraction pattern.

Each coherent mode (one from each discrete source element) is shown in Figure 6.29a. The resultant incoherent diffraction pattern at each scan position is taken from the sum of intensities across the source modes,

$$I^m = \sum_{\boldsymbol{\eta}} |\Psi(\boldsymbol{u}, \boldsymbol{\eta})|^2 \,, \tag{6.2}$$

as shown in Figure 6.29b. Note that the formation of the pixel intensity for spatial coherence shares a great similarity with that for the case of large pixels (see equation 4.4). The coordinate system for the four-dimensional set of diffraction patterns shown in Figure 6.29a is as described in Figure 3.3.

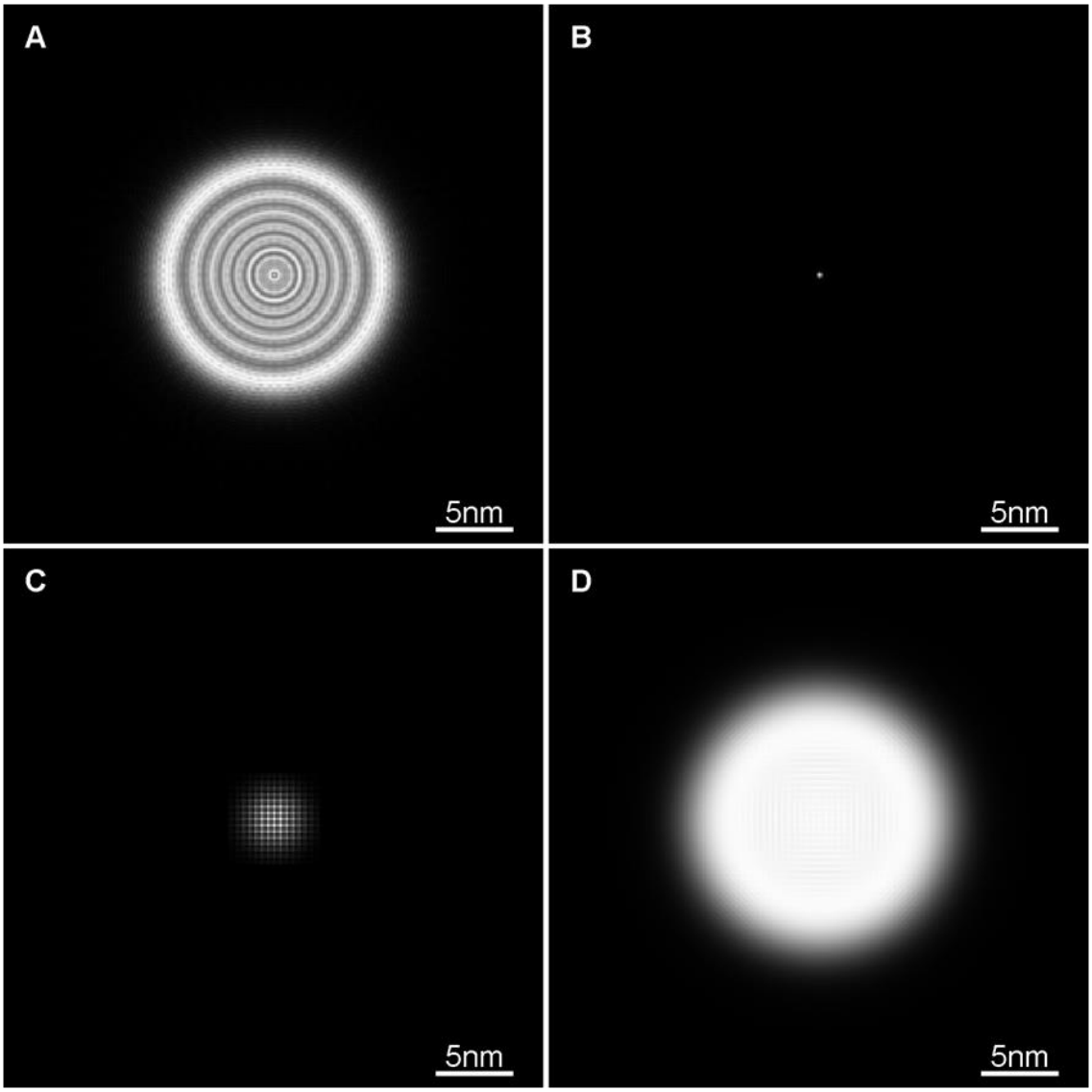

Figure 6.28: The simulated partially coherent illumination function from an extended source. a) A typical coherent probe function, b) The focal point of the probe in (a) which is an image of the source through the probe forming optics, c) The extended source as an incoherent sum of shifted versions of the single source from (b), d) the incoherent sum of the shifted source functions after propagation to the object plane (as in (a)). All images are of intensity profiles.

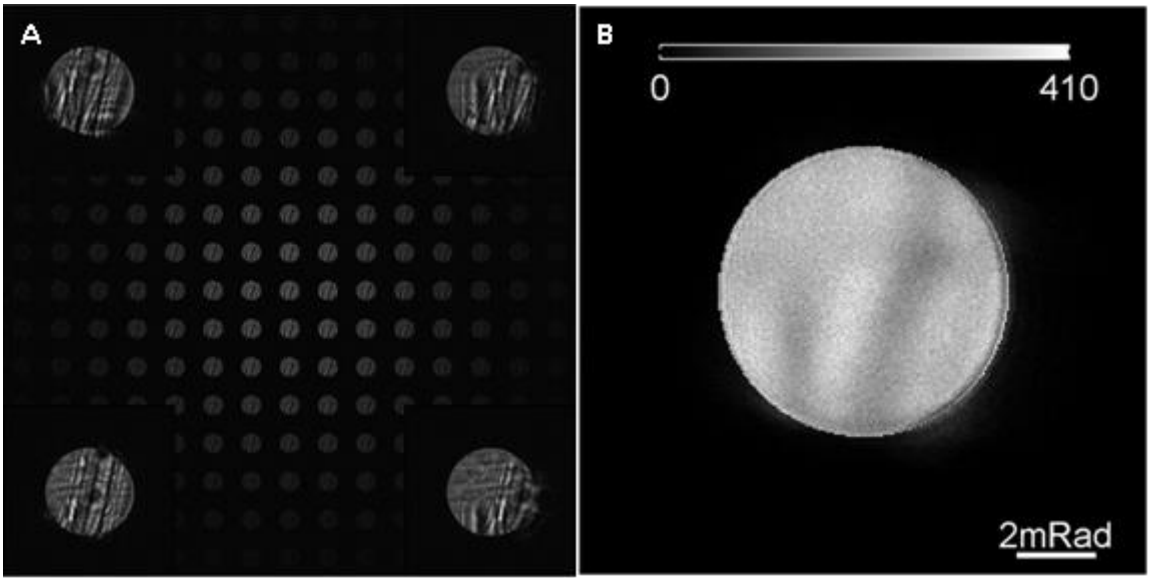

Figure 6.29: Generation of a typical partially coherent diffraction pattern from a set of coherent modes. a) Four-dimensional coherent set of diffraction patterns, where the four magnified inlays show rescaled versions of the diffraction modes from the corresponding four corners of the source distribution. b) Two-dimensional partially coherent diffraction pattern as generated from the incoherent summation of (a) across all source modes.

6.4.3 ePIE Reconstruction

The dataset generated from the extended source function is processed through the ePIE algorithm. Such an algorithm assumes complete coherence and the reconstructed outputs shown in Figure 6.30 are a representation of how the conventional reconstruction algorithm would currently handle such levels of coherence within the microscope setup.

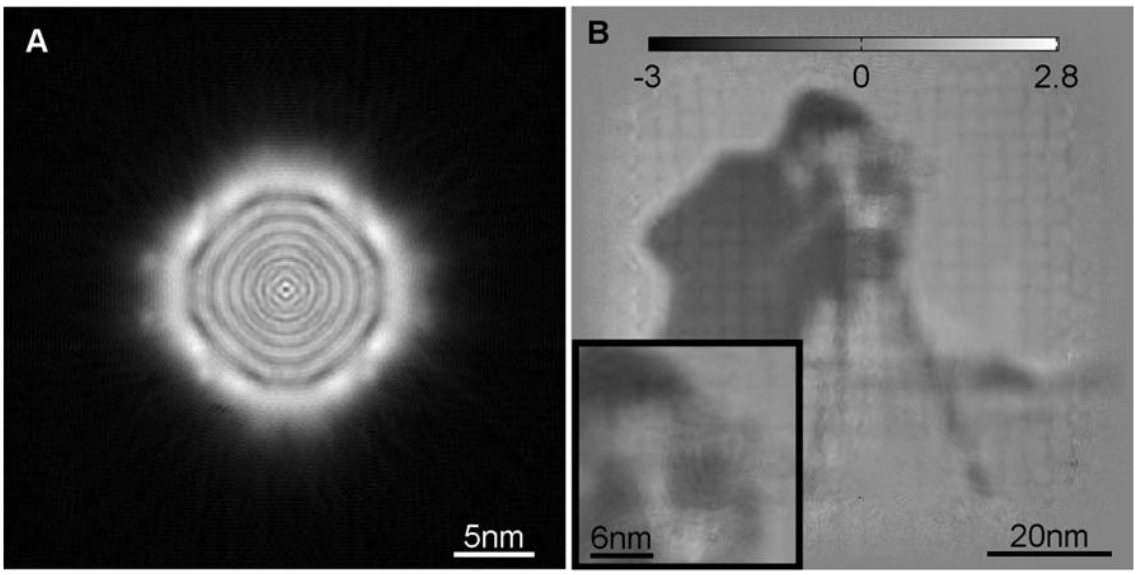

Figure 6.30: Reconstruction outputs from ePIE. a) Modulus of the illumination function. b) Phase of the object with magnified inlay.

The reconstruction is clearly degraded, only very broad features are visible and the illumination function is deformed. The nature of the PIE reconstruction algorithm (and others based on similar principles) in general is such that the diffraction plane is strongly constrained. It can be seen from Figure 6.31 that the reconstructed diffraction pattern matches the corresponding pattern from the dataset. The algorithmic constraints are clearly insufficiently configured for partially coherent data.

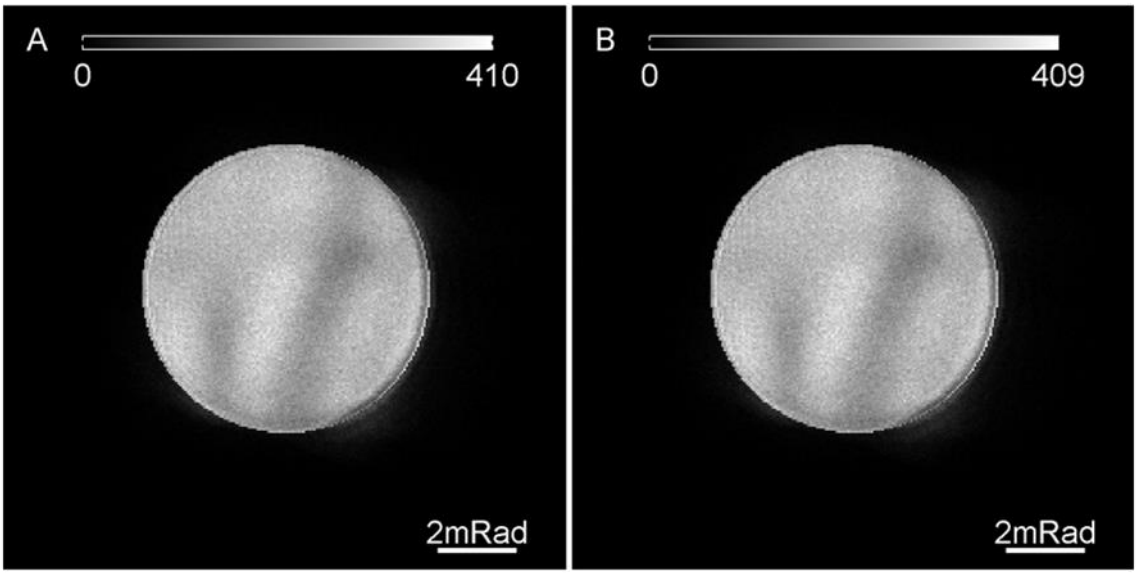

Figure 6.31: Typical diffraction pattern from incoherent dataset. a) Simulated dataset. b) Corresponding reconstruction from a single source mode PC-PIE.

6.4.4 PC-PIE

A new algorithm (named PC-PIE for partial coherence PIE) is proposed which, in a similar fashion to MS-PIE in section 5.1, is able to process several coherent modes in parallel. For MS-PIE, all modes from a single position are constrained by the same incoherent diffraction pattern in reciprocal-space. When the source is emitting several spectral modes, the response of the optical elements and specimen from each of those modes may be independent and so a separate probe and object function is required for each such mode. Unlike the general MS-PIE algorithm though, here the solution is much more constrained because there only exists a single object, single probe, and a single source distribution. The response of the probe forming optics and of the specimen is assumed to be constant for the different source modes. The PC-PIE algorithm is not only able to alleviate the effects of partial coherence but also recover the shape and distribution of emission from the source.

An extra deconvolution step is added for the source function, which with the addition of a propagation step may be in a plane other than that of either the object or detector.

The ability to constrain the solution more heavily comes from assumptions about the response of the optical elements and the specimen to the different source modes. For sufficiently small angles subtended by the condenser aperture at the source plane, the set of source points can be assumed to be related by a single shift at the source plane (the focal plane of the condensing optics), S'. It is therefore possible to constrain the set of source modes with the *a priori* knowledge that the condensing optics are independent of source shifts.

In principle an extended source only needs to add a single array of unknown values to the reconstruction process. Indeed, it is now shown that alterations to the architecture of the real-space updates allows for the simultaneous solution of many more source modes than for the multiple wavelength case. The modifications to the MS-PIE flow diagram (Figure 5.1) may be seen in Figure 6.32, where the probe and object functions are now independent of source coordinates. (Note that there is no longer multiple probe, P, or object, O, modes.)

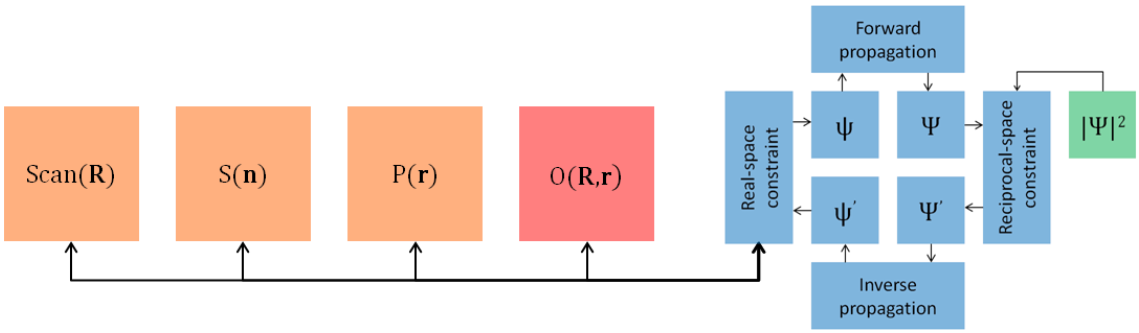

*Figure 6.32: A flow diagram of the PC-PIE reconstruction algorithm for a single iteration at scan position **R**, where **n** represents the source coordinates and **r** represents the real-space coordinates. The kernel of the algorithm (shown in blue) feeds from the known values (shown in green) in order to solve for the unknown object (shown in red) and the partially known probe(s), P, scan, and source, S, (shown in orange). Note that unlike Figure 5.1, the probe and object functions are no longer a function of source coordinate.*

The modified real-space update process through which the source, probe, and object functions may be deconvolved from each other is now described. Each illumination mode is updated in parallel following the same equation as in section 5.1.2.

$$P'(\boldsymbol{r},\boldsymbol{R},\boldsymbol{\eta}) = P(\boldsymbol{r},\boldsymbol{R},\boldsymbol{\eta}) + \mathbb{U}_p[\psi'(\boldsymbol{r},\boldsymbol{R},\boldsymbol{\eta}) - \psi(\boldsymbol{r},\boldsymbol{R},\boldsymbol{\eta})]\,. \tag{6.3}$$

The difference here is that each probe mode can be constrained such that when they are shifted into the same position in the source plane (focal point of the probe) they should be equivalent except in the amount of flux. A single coherent illumination function which has all the flux of the extended source may be extracted by taking the sum of the separate probe modes under such a condition. Propagation back to the object plane produces an illumination function that is related only to the probe forming optics and is decoupled from the source function. In short, the four-dimensional illumination function is split into two, two-dimensional, functions for the source and the probe.

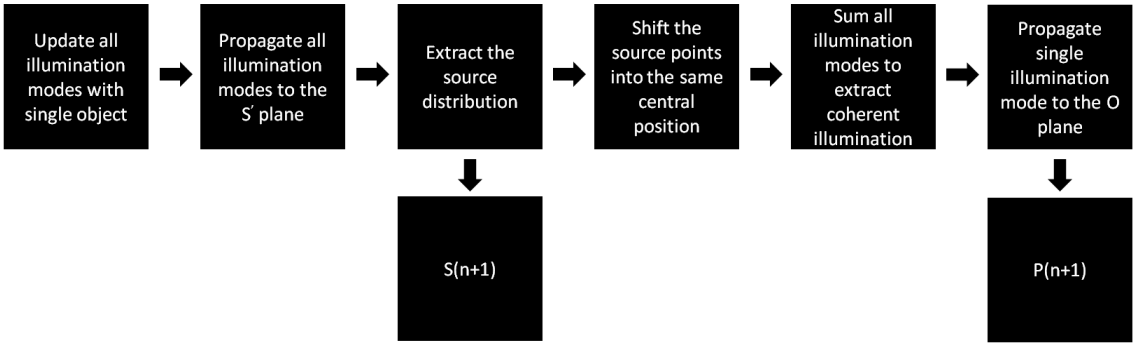

Figure 6.33: Flow diagram of the extraction of the two two-dimensional source and probe functions from the four-dimensional illumination.

Unlike the object update in equation 5.7b, in this situation the object may be assumed to be independent of a shift in the source plane and so a single object function can be extracted from the update step using a weighted sum,

$$O'(\boldsymbol{r},\boldsymbol{R},\boldsymbol{\eta}) = \sum_{\boldsymbol{\eta}} \left(\frac{S(\boldsymbol{\eta})}{\sum_{\boldsymbol{\eta}} S(\boldsymbol{\eta})} \right) \left[O(\boldsymbol{r},\boldsymbol{R}) + \mathbb{U}_o(\boldsymbol{\eta})[\psi'(\boldsymbol{r},\boldsymbol{R},\boldsymbol{\eta}) - \psi(\boldsymbol{r},\boldsymbol{R},\boldsymbol{\eta})] \right]. \tag{6.4}$$

A finite source may be viewed as an array of point emitters that emit radiation independently, that is to say they share no phase relationship. If the source may be considered as a two-dimensional array of such emitters then the illumination irradiating the specimen can be seen as a four-dimensional function, which is coherent across the two real-space dimensions but incoherent across the two

source-plane dimensions. Such an illumination function can be separated into its coherent and incoherent parts as follows,

$$S(s_x, s_y) = \sum_{r_x} \sum_{r_y} \left| a(r_x, r_y, s_x, s_y) \right|^2 , \tag{6.5}$$

and

$$P(r_x, r_y) = \sum_{s_x} \sum_{s_y} a(r_x, r_y, s_x, s_y) , \tag{6.6}$$

where a is the four-dimensional probe, s_x and s_y are source-plane coordinates, and r_x and r_y are real-space coordinates.

The algorithm is able to constrain the illumination to a single function as long as all the optical elements of the microscope are source position independent. This reduces the amount of information that must be recovered by the algorithm from N^2S^2 to only N^2+S^2, a significant decrease when the number of source pixels reaches any meaningful number. In the following simulations, the number of source elements, S^2, reaches 225.

6.4.5 PC-PIE Reconstructions

The dataset shown in Figure 6.29b is processed through the PC-PIE algorithm with a source array of initially 3x3 pixels, then, in order to show the improvement as more modes are added, this is increased to 9x9, then 15x15. For each reconstruction, the initial source estimate is a uniform distribution of intensities across all elements. The coherent probe and object functions are shown in Figure 6.34.

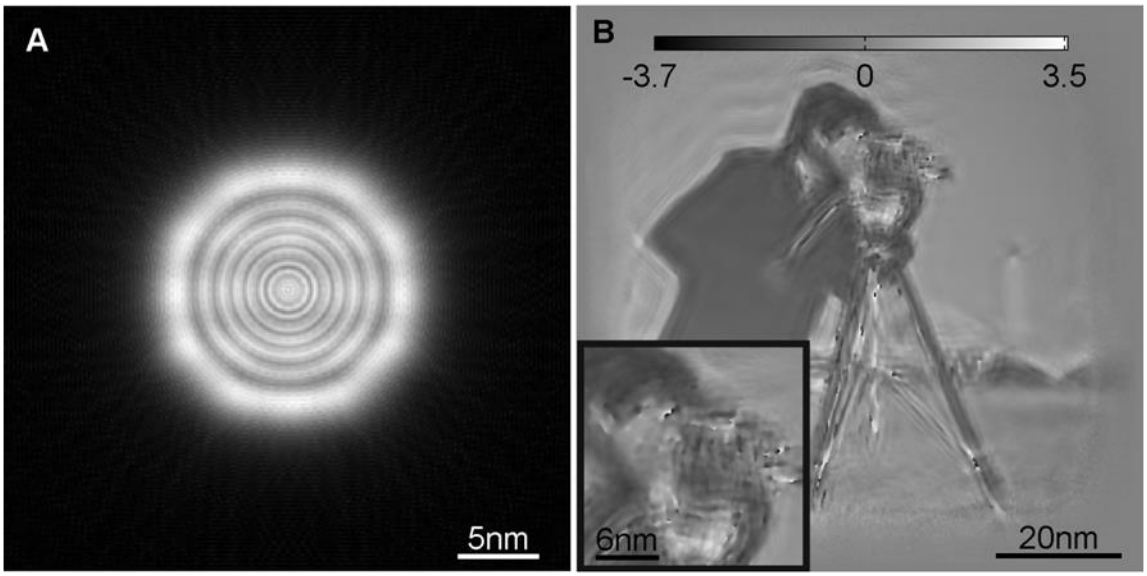

Figure 6.34: Reconstruction outputs from PC-PIE with 9 source elements. a) Modulus of the illumination function, b) Phase of the object with magnified inlay.

Comparing the 3x3 source mode reconstruction (Figure 6.34) to the single mode reconstruction (Figure 6.30) it can be seen that PC-PIE has been able to produce both a cleaner probe and object reconstruction that, although not an ideal representation of the original object, is improved from the single mode case. Although only 3x3 pixels have been reconstructed, the distribution converged to a similar shape as that used to generate the dataset. As each source point is associated with a separate coherent mode, each source point also has a corresponding probe and diffraction pattern estimate. A typical set of such probe and diffraction pattern modes is shown in Figure 6.35.

The source function is also reconstructed (in the same manner as that in Figure 6.28c) so that the distribution of emission in the source plane may be seen and is shown in Figure 6.36a along with the corresponding distribution of electrons at the specimen plane, shown in Figure 6.36b.

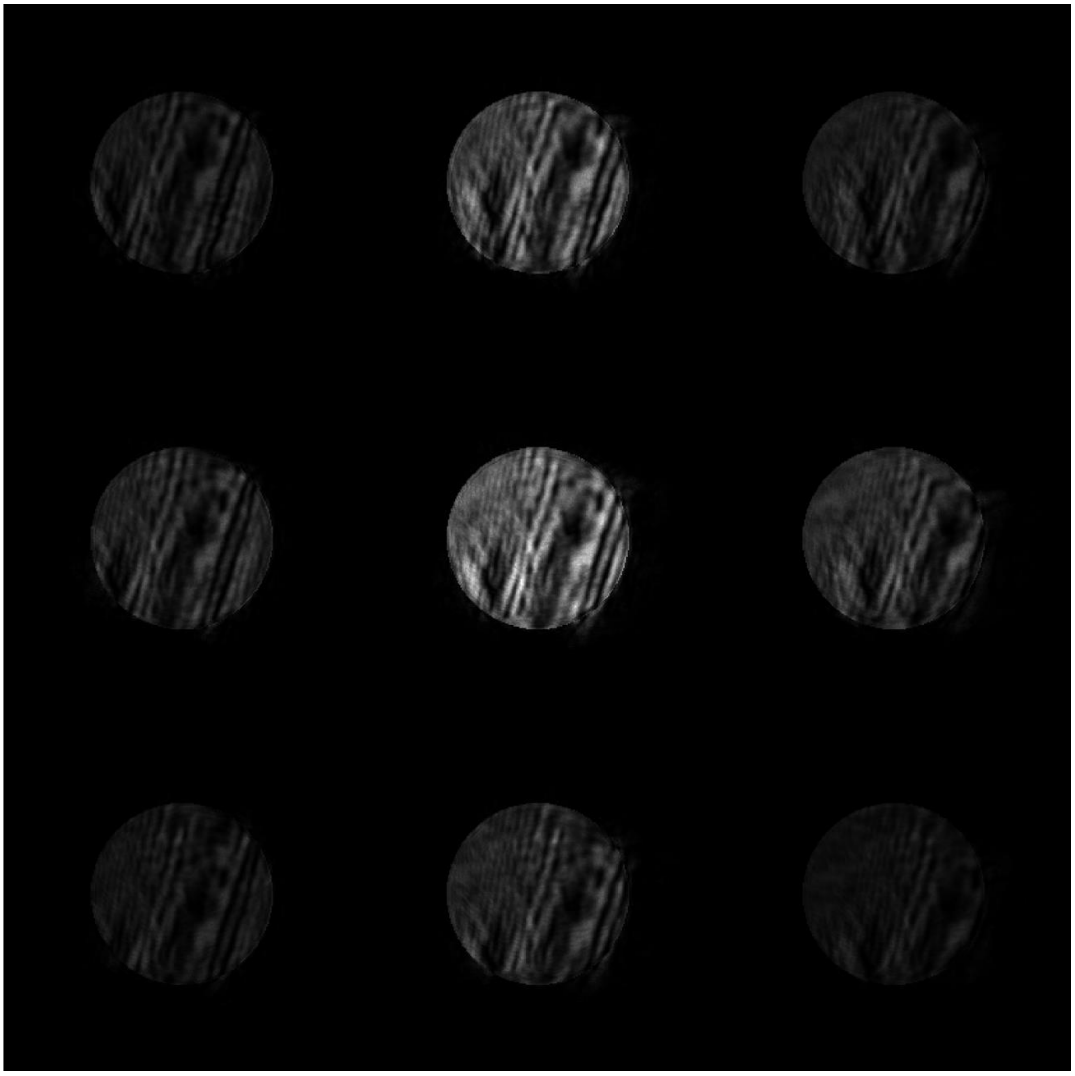

Figure 6.35: Four-dimensional distribution of electrons in reciprocal-space.

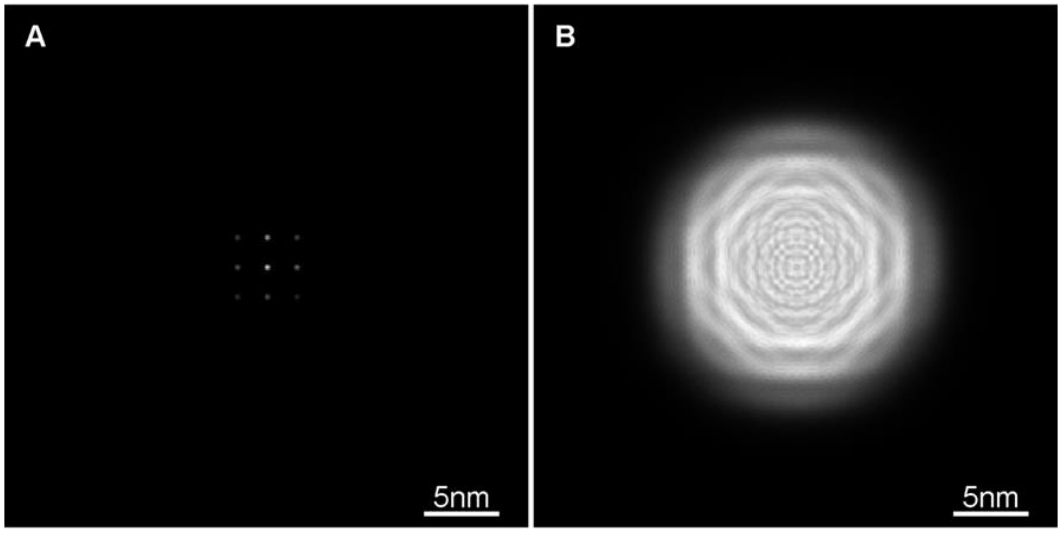

Figure 6.36: Reconstructed distribution of flux as outputted from the PC-PIE algorithm for the 3x3 dataset. a) The distribution of intensity in the source plane, showing the 9 separate points of emission. b) The illumination as seen by the specimen over the exposure time, each source mode has been propagated to the specimen plane and integrated in intensity.

The same reconstruction procedure is now performed with a source array of 9x9 pixels, again the pitch is altered to cover the model source size. The resultant reconstructions of the coherent probe and object functions are shown in Figure 6.37.

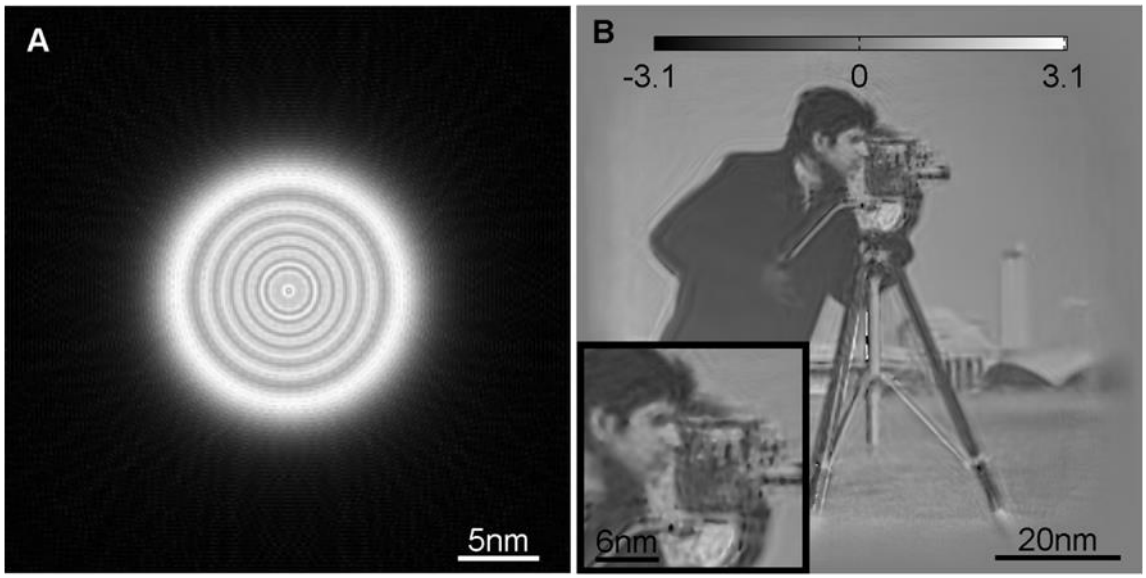

Figure 6.37: Reconstruction outputs from PC-PIE with 81 source elements. a) Modulus of the illumination function, b) Phase of the object with magnified inlay.

Introducing more source modes has significantly improved the reconstruction quality. The probe is now circular and matches that of Figure 6.26 almost perfectly. The object still has some minor artefacts at the edge of the features but nevertheless does reveal a substantial amount of structure and information that is not revealed by the current algorithm (see Figure 6.30).

The resultant distribution of coherent diffraction patterns, showing their relative weights, as computed by the PC-PIE algorithm is also shown in Figure 6.38. Note that the shadow image in the central disc is shifting with source position: in STEM mode the source plane is near to the object plane and so a shift in the source plane translates as a shift in the object plane. As with Figure 6.36, the incoherent distribution of intensity at both the source and object plane is also produced. These are shown in Figure 6.39.

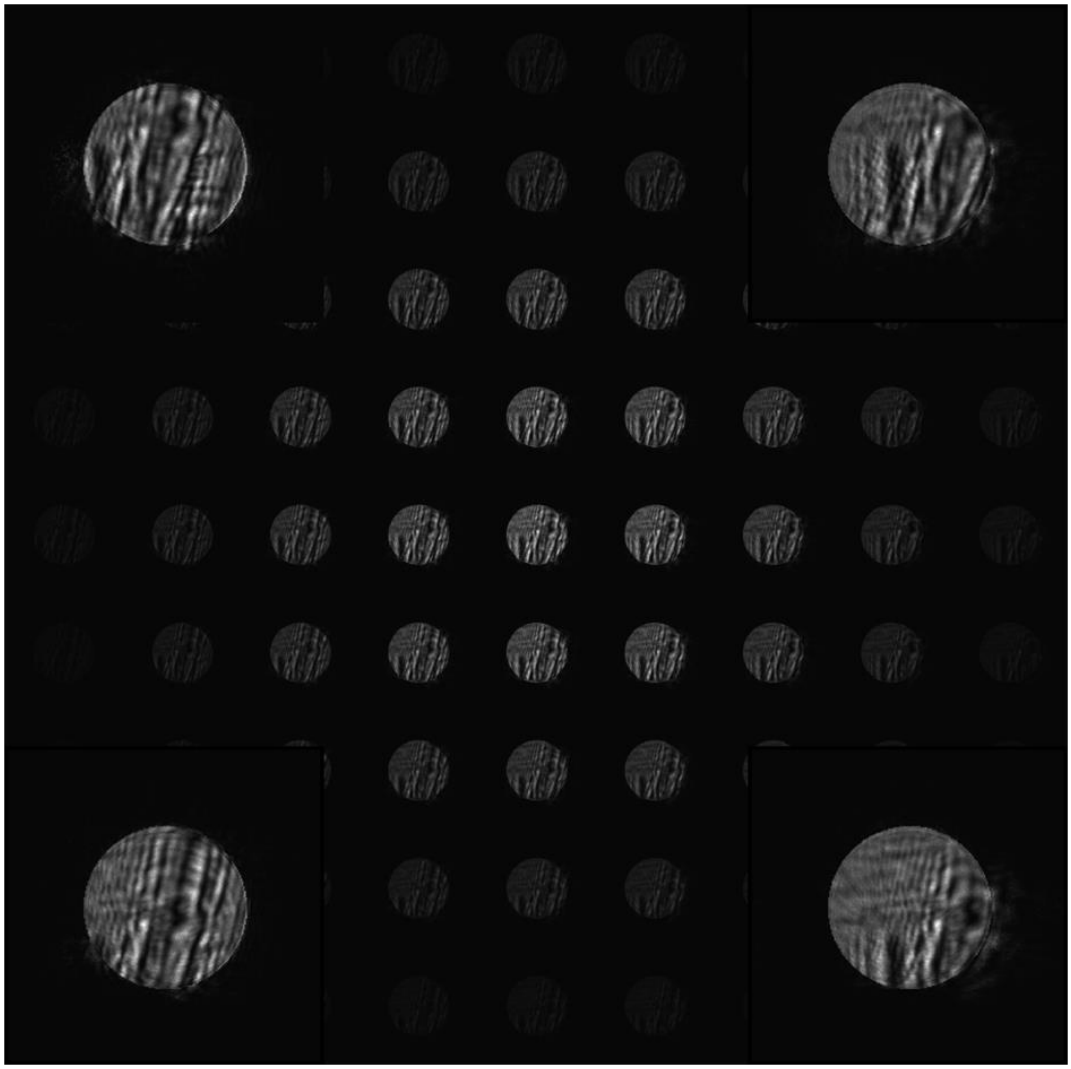

Figure 6.38: Four-dimensional distribution of electrons in reciprocal-space. The four magnified inlays show rescaled versions of the diffraction modes from the corresponding four corners of the source distribution.

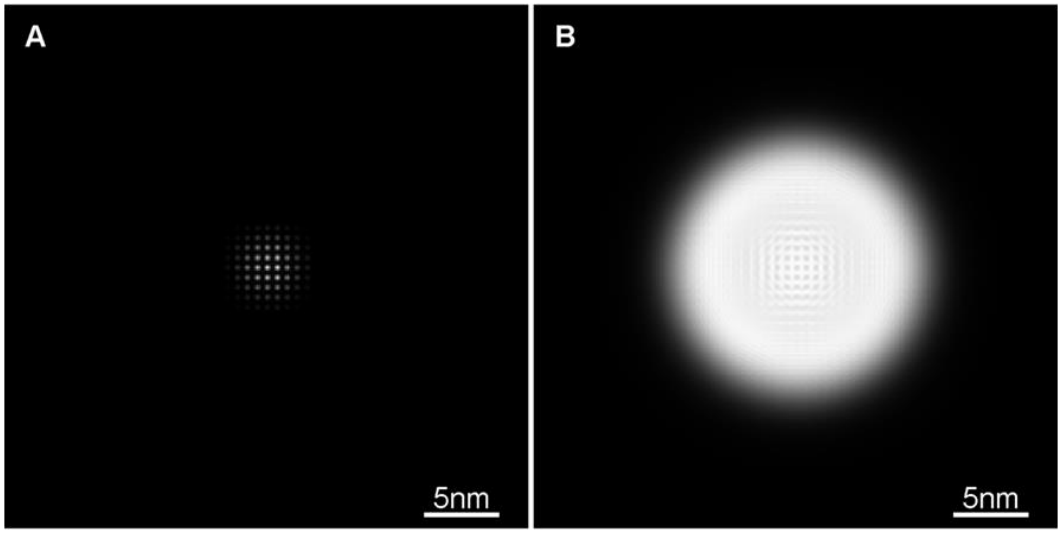

Figure 6.39: Reconstructed distribution of flux as outputted from the PC-PIE algorithm for the 9x9 dataset. a) The distribution of intensity in the source plane, showing the 81 separate points of emission. b) The illumination as seen by the specimen over the exposure time, each source mode has been propagated to the specimen plane and integrated in intensity.

The reconstructed source is a close match to the modelled source (see Figure 6.28c) and demonstrates the algorithm's ability not only to alleviate the effects of partial coherence but also to generate an image of the extended source that caused it. This is a result which could prove itself very useful in the characterisation of electron microscopes (or indeed any microscope on which ptychography is performed) and should be the subject of future work.

For completeness, a PC-PIE reconstruction is now executed with 15x15 source modes (matching that of the simulation). The reconstructed probe and object functions from that reconstruction are shown in Figure 6.40. There is little (if any) improvement over that of the 9x9 reconstruction (Figure 6.37). The distribution of coherent diffraction patterns and probe modes are shown in Figure 6.41. The distribution of intensity appears approximately correct although there is a shift towards the top right corner. This shift can also be seen in the source plane (see Figure 6.42a) although there is little effect to be seen on the incoherent probe as imaged at the specimen plane (Figure 6.42b).

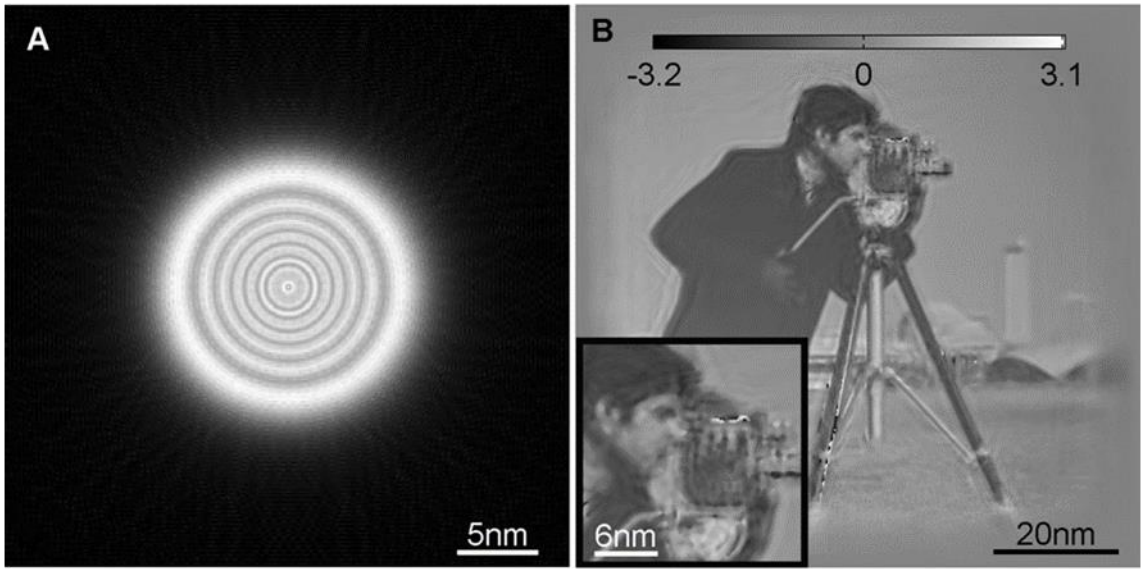

Figure 6.40: Reconstruction outputs from PC-PIE with 225 source elements. a) Modulus of the illumination function, b) Phase of the object with magnified inlay.

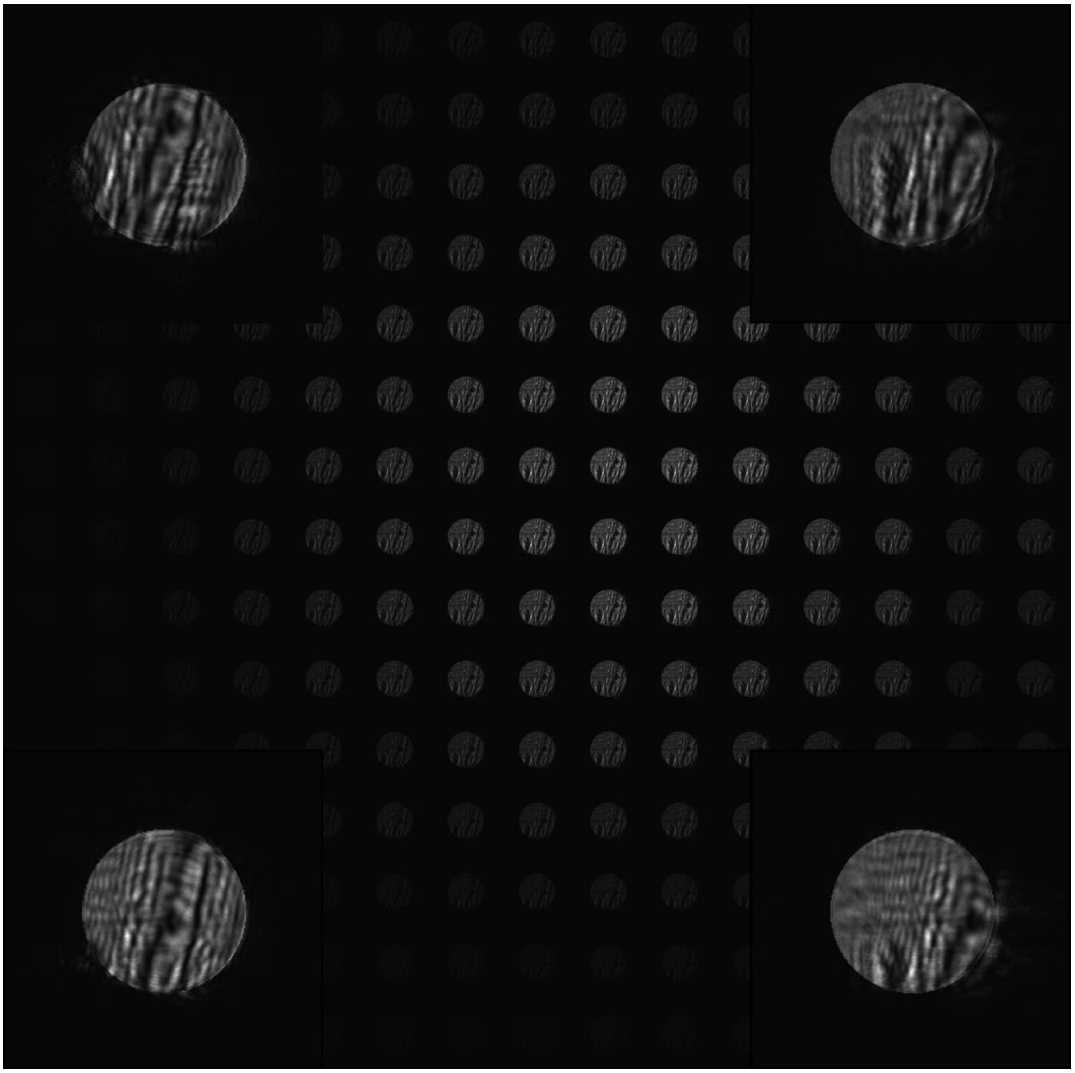

Figure 6.41: Four-dimensional distribution of electrons in reciprocal-space. The four magnified inlays show rescaled versions of the diffraction modes from the corresponding four corners of the source distribution.

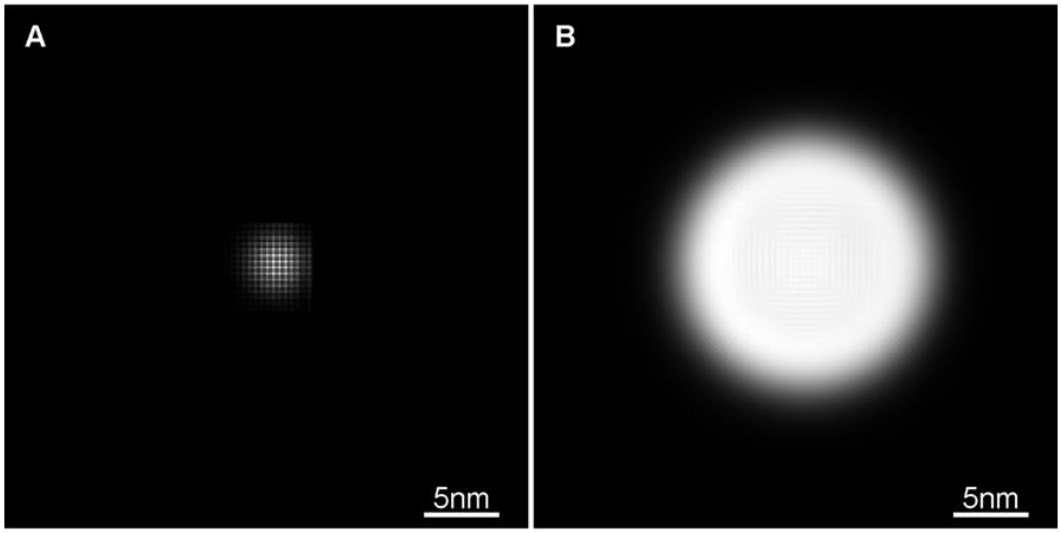

Figure 6.42: Reconstructed distribution of flux as outputted from the PC-PIE algorithm for the15x15 dataset. a) The distribution of intensity in the source plane, showing the 225 separate points of emission. b) The illumination as seen by the specimen over the exposure time, each source mode has been propagated to the specimen plane and integrated in intensity.

In order to ensure that the PC-PIE algorithm behaves well and produces the same quality reconstruction as ePIE when the dataset is coherent, the ideal source dataset is also processed through PC-PIE. The starting estimate for the source is a uniform array of 3x3 pixels and the resultant reconstruction is shown in Figure 6.43.

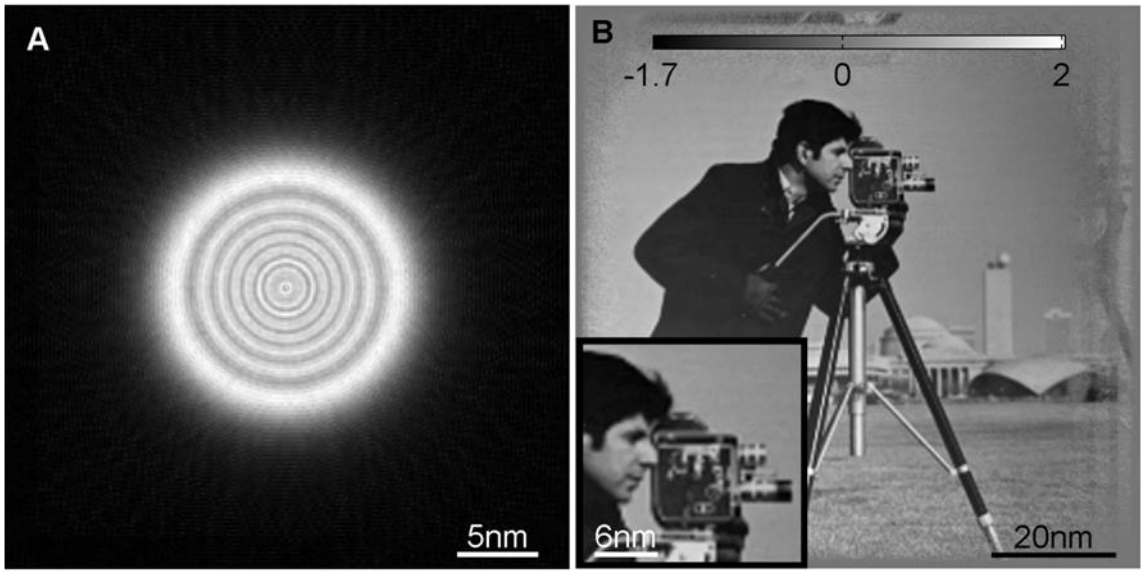

Figure 6.43: Reconstruction outputs from PC-PIE, with a source of 3x3 elements, of the ideal source dataset. a) Modulus of the illumination function. b) Phase of the object with magnified inlay.

The reconstruction very clean and is equally as convincing in reciprocal-space, as can be seen in Figure 6.44, where the simulated and reconstructed diffraction patterns are almost identical.

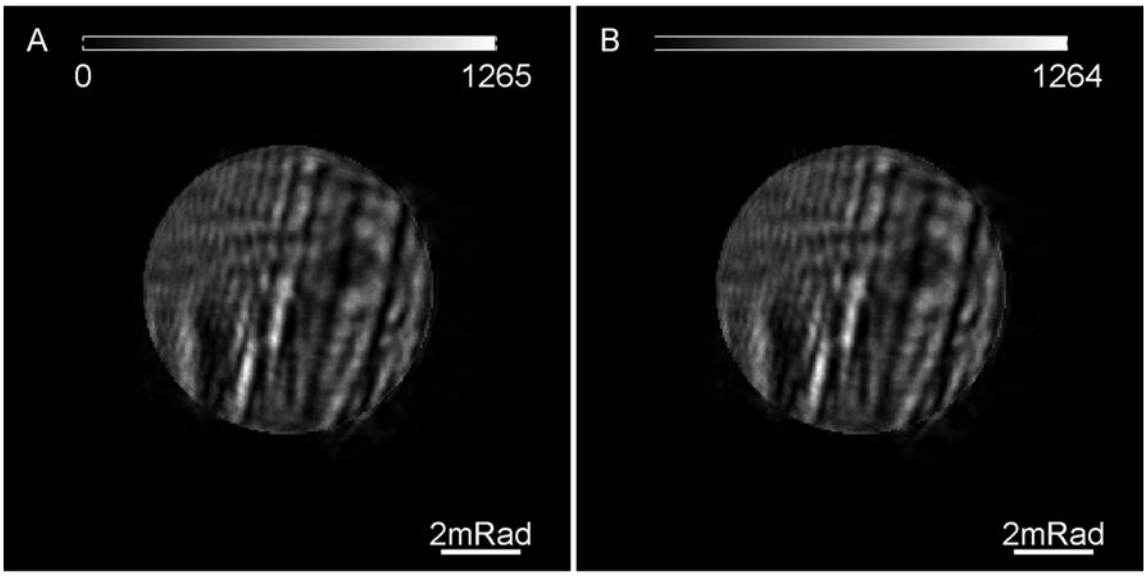

Figure 6.44: Typical diffraction pattern from incoherent dataset. a) Simulated dataset. b) Corresponding sum of reconstructed modes from PCPIE.

In line with the above reconstructions, the four-dimensional distribution of electrons is displayed, see Figure 6.45. As is expected, there only exists a single mode that contains any intensity, which relates to the single point of emission in the source plane. The reconstruction is insensitive to absolute source coordinates and so in this case a source element from the corner of the array has been selected, an ambiguity that tends to vary with specimen structure and is seeded in the initial iterations of a reconstruction. As is clear from the real-space reconstructions though, the quality of the reconstruction is unaffected.

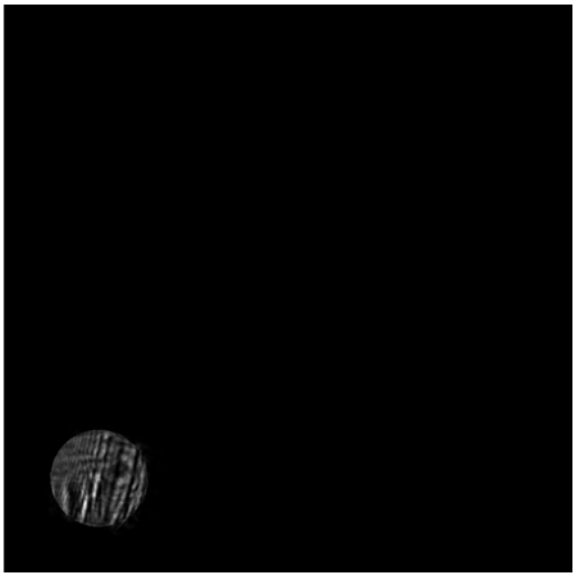

Figure 6.45: Four-dimensional distribution of electrons, with the spatial dimensions represented in reciprocal-space. Only one mode remains populated after the reconstruction process as the source was ideal.

6.5 Summary

The first part of this chapter has shown some of the pre-processing methods that may be employed in order to extract some useful information from sub optimal datasets. Although a reconstruction was made possible by this procedure, the pre-processing of the data alone was insufficient and a peak was present in the probe function that was clearly not real. Using an unconstrained second mode (through the MS-PIE algorithm) the false peak was removed, although some false periodic structure in the probe remained. Attaching the existing detector extrapolation method to the MS-PIE algorithm, the method of 'super resolution' in electron regime was demonstrated for the first time.

In so doing a false constraint was removed from the reconstruction and the probe function was reconstructed more cleanly.

Then, by developing a new detector response correction algorithm, this chapter demonstrated the ability to achieve truly atomic resolution phase images, improving on the point resolution of the microscope in conventional imaging mode, within the relatively simple configuration of an SEM. Through modelled simulations and the development of another new reconstruction algorithm, it has been demonstrated that the effects of spatial coherence may be unlocked by the ptychographic imaging method. Not only does this alleviate the negative effects of low levels of coherence but, by allowing many sources of flux through the system at once, while relating them to a single reconstruction of the response from the optics and the specimen, the coherence of the source is effectively increased. The algorithm produces a reconstruction that appears to have been recorded with a coherent source with all of the flux offered by the physical, extended, source

7 Conclusions

In this thesis ptychography has been investigated in a variety of ways and in a variety of experimental situations. Firstly, the ptychographic imaging framework was described in terms of a sampling mechanism that contains a sampling pitch in both real and reciprocal-space. It was shown that the four-dimensional dataset produced from the ptychographic scan is governed by a four-dimensional sampling condition in which the constraints on beam localisation and coherence from conventional CDI are interchangeable with the scan parameters of that beam relative to the specimen. The demonstration of a ptychographic reconstruction with no reciprocal-space convolution overturns the central tenet of ptychography as it is currently understood and described in the literature (Rodenburg, 2008). Indeed the very name ptychography originates from the 'ptych' or convolution (folding) in reciprocal-space.

As ptychography relies on splitting the full field of view into several subsets it is important to understand how the technique behaves as the number of subsets are increased for a fixed final field of view. Preserving the total flux through the field of view as the sampling pitch of the scan is reduced causes a reduction in the counting statistics within each measured diffraction pattern. It was shown that given the correct adjustments to the widely employed ePIE algorithm, the level dose fractionation within a ptychographic dataset is not critical and that it may even be advantageous to partition the radiation across as many separate diffraction patterns as possible.

The development of the UK's first ptychography setup in the x-ray synchrotron regime has been described. Experimental issues were overcome in order to produce the first images to emerge from the I13 coherence branch at the Diamond Light Source. The data used to produce those images was then modified so that the principles of the sampling requirements within ptychography could be demonstrated on real data and in a regime where reducing the requisite specimen to detector distance has positive consequences. Binning the pixels from groups of 3x3 into 1 placed the dataset well below the requisite sampling conditions as they were then understood. The development of a new reconstruction algorithm, which uses the real-space overlap in order to decompose the large pixels into a set of smaller constituent pixels, showed that the new sampling condition does indeed hold in practice. As this data was not recorded with a demonstration of the up-sampling algorithm in mind, a model dataset was created which demonstrated a successful reconstruction when the whole detector only contains 4 pixels – a remarkable result given that the whole field of diffractive imaging is based around the requirements of fine sampling in reciprocal-space.

The process of decomposing large pixels, which integrate an underlying complex wave-field in intensity through an incoherent process, into many internal pixels of complex value may be seen as a form of source deconvolution. The next step was to understand if, and how, the same principles could be extended to a partially coherent source, both temporally and spatially. In order to introduce a mixture of terms from within all elements of the experiment into the measurements

made at the detector plane, a source comprised of three wavelengths source was used. Employing the conventional ptychographic scan procedure, otherwise ordinary datasets of both a test projector slide and a stained biological specimen were recorded. As the response of both the beam forming optics and the specimen changed as function of photon energy, the resultant diffraction patterns contain the incoherent addition of the diffraction patterns generated from three totally independent microscopes. Alterations to the up-sampling algorithm were made in real-space so that the elements of each separate microscope could be processed in parallel and updated against a mutual incoherent set of diffraction patterns. The results were very clean and subsequent analysis with a resolution test target showed that there was negligible degradation to the quality of any of the three modes when compared to recording and reconstructing each wavelength separately (where each microscope is set to a different wavelength).

Progress in electron ptychography has lagged quite severely behind that in the visible and x-ray regimes. One of the main issues faced when attempting to perform electron ptychography is the stability of certain elements within the microscope. Conventional imaging and ptychography have very contrasting experimental requirements: ptychography does not require a high quality probe, whereas in conventional electron microscopy this is a limiting factor. Conversely, conventional electron microscopy does not require a highly stable and precise specimen stage: for ptychography this is a limiting factor. Although position errors can now be corrected with the algorithms described in the background review, the quality and stability of the source, lenses (which would ideally be removed), and detectors remain a big problem.

Source coherence and lens instabilities have a similar effect on the dataset as multiple wavelength illumination (temporal coherence). When dealing with an extended source though there are likely to be rather more than three contributing modes, or source elements. Using assumptions that the response of the optics and of the specimen to different source elements is identical (they do not change as a function of source shift) it was possible to construct a more refined algorithm for

processing data with partial spatial coherence. Simulated data demonstrated the deconvolution of a source distribution that contained 225 different source elements in order to produce a single reconstruction of the probe and object as though all of the flux had come from a perfectly coherent source.

The issue of detector imperfections was also tackled. Ptychography relies heavily on the intensity measurements made in reciprocal-space and the reconstruction quality is heavily sensitive to any flaws and imperfections in the response profile of the pixels. Exploiting the wide range of values that each pixel is subject to throughout a ptychographic scan, a new algorithm was developed that solved for the offsets and gains that had systematically corrupted the data. Simulations were used to investigate the integrity of the algorithm. A single pixel was tracked throughout a reconstruction which showed that the estimated response profile of the detector converged very well towards that of the actual response. Applying the method to some existing SEM data (Humphry et al., 2012) it was shown that a high quality, large field of view, phase image of atomic resolution could be produced from a ptychographic dataset within an electron microscope.

The results described throughout this thesis have implications in visible light, x-ray, and electron imaging regimes. Future work will involve applying the multiple wavelength methods to x-ray spectromicroscopy, where chemical analysis of specimens will be explored, particularly when combined with three-dimensional methods such as ptycho-tomography and 3PIE. Building on the initial results from the electron microscope, further work will be carried out to isolate all of the instabilities that affect ptychography as well as exploring the possibility of instrument characterisation. The future development of ptychographic methods is full of promise and it seems that many new scientific discoveries may be on the horizon.

8 References

Abbe, E. 1873. Beiträge zur Theorie des Mikroskops und der mikroskopischen Wahrnehmung. *Archiv für mikroskopische Anatomie,* 9**,** 413-418.

Atkinson, K. M., Sweeney, F. & Rodenburg, J. M. 2010. Solving for the phase of STEM probes in real space. *Journal of Physics: Conference Series,* 241**,** 012064.

Beckers, M., Senkbeil, T., Gorniak, T., Reese, M., Giewekemeyer, K., Gleber, S.-C., Salditt, T. & Rosenhahn, A. 2011. Chemical Contrast in Soft X-Ray Ptychography. *Physical Review Letters,* 107.

Bruck, Y. M. & Sodin, L. G. 1979. On the ambiguity of the image reconstruction problem. *Optics Communications,* 30**,** 304-308.

Chapman, H. N. 1996. Phase-retrieval X-ray microscopy by Wigner-distribution deconvolution. *Ultramicroscopy,* 66**,** 153-172.

Chen, B., Dilanian, R. A., Teichmann, S., Abbey, B., Peele, A. G., Williams, G. J., Hannaford, P., Van Dao, L., Quiney, H. M. & Nugent, K. A. 2009. Multiple wavelength diffractive imaging. *Physical Review A,* 79.

Chen, B., Guizar-Sicairos, M., Xiong, G., Shemilt, L., Diaz, A., Nutter, J., Burdet, N., Huo, S., Mancuso, J., Monteith, A., Vergeer, F., Burgess, A. & Robinson, I. 2013. Three-dimensional structure analysis and percolation properties of a barrier marine coating. *Sci Rep,* 3**,** 1177.

Chushkin, Y. & Zontone, F. 2013. Upsampling speckle patterns for coherent X-ray diffraction imaging. *Journal of Applied Crystallography,* 46**,** 319-323.

Claus, D., Maiden, A. M., Zhang, F., Sweeney, F. G. R., Humphry, M. J., Schluesener, H. & Rodenburg, J. M. 2012. Quantitative phase contrast optimised cancerous cell differentiation via ptychography. *Optics Express,* 20**,** 9911-9918.

Claus, D., Robinson, D. J., Chetwynd, D. G., Shuo, Y., Pike, W. T., De J Toriz Garcia, J. J. & Rodenburg, J. M. 2013. Dual wavelength optical metrology using ptychography. *Journal of Optics,* 15**,** 035702.

Cowley, J. M. 1969. Image Contrast in a Transmission Scanning Electron Microscope. *Applied Physics Letters,* 15**,** 58.

Cowley, J. M. & Moodie, A. F. 1957. The scattering of electrons by atoms and crystals. I. A new theoretical approach. *Acta Crystallographica,* 10**,** 609-619.

Cowley, J. M. & Moodie, A. F. 1959a. The scattering of electrons by atoms and crystals. II. The effects of finite source size. *Acta Crystallographica,* 12**,** 353-359.

Cowley, J. M. & Moodie, A. F. 1959b. The scattering of electrons by atoms and crystals. III. Single-crystal diffraction patterns. *Acta Crystallographica,* 12**,** 360-367.

Cxro. *The Center for X-ray Optics* [Online]. Available: http://henke.lbl.gov/optical_constants/.

D'alfonso, A. J., Morgan, A. J., Yan, A. W. C., Wang, P., Sawada, H., Kirkland, A. I. & Allen, L. J. 2014. Deterministic electron ptychography at atomic resolution. *Physical Review B,* 89.

Dierolf, M., Menzel, A., Thibault, P., Schneider, P., Kewish, C. M., Wepf, R., Bunk, O. & Pfeiffer, F. 2010. Ptychographic X-ray computed tomography at the nanoscale. *Nature,* 467**,** 436-9.

Edo, T. B., Zhang, F. & Rodenburg, J. M. Resolution improvement in coherent diffractive imaging (ptychography). 2010. 77291H-77291H-7.

Faulkner, H. & Rodenburg, J. 2004. Movable Aperture Lensless Transmission Microscopy: A Novel Phase Retrieval Algorithm. *Physical Review Letters,* 93.

Fienup, J. R. 1978. Reconstruction of an object from the modulus of its Fourier transform. *Optics Letters,* 3**,** 27.

Fienup, J. R. 1982. Phase retrieval algorithms: a comparison. *Appl Opt,* 21**,** 2758-69.

Fienup, J. R. 1987. Reconstruction of a complex-valued object from the modulus of its Fourier transform using a support constraint. *Journal of the Optical Society of America A,* 4**,** 118.

Friedman, S. L. & Rodenburg, J. M. 1992. Optical demonstration of a new principle of far-field microscopy. *Journal of Physics D: Applied Physics,* 25**,** 147.

Gerchberg, R. W. & Saxton, W. O. 1972. PRACTICAL ALGORITHM FOR DETERMINATION OF PHASE FROM IMAGE AND DIFFRACTION PLANE PICTURES. *Optik,* 35**,** 237-&.

Giewekemeyer, K., Thibault, P., Kalbfleisch, S., Beerlink, A., Kewish, C. M., Dierolf, M., Pfeiffer, F. & Salditt, T. 2010. Quantitative biological imaging by ptychographic x-ray diffraction microscopy. *Proc Natl Acad Sci U S A,* 107**,** 529-34.

Godard, P., Allain, M. & Chamard, V. 2011. Imaging of highly inhomogeneous strain field in nanocrystals using x-ray Bragg ptychography: A numerical study. *Physical Review B,* 84.

Godard, P., Allain, M., Chamard, V. & Rodenburg, J. 2012. Noise models for low counting rate coherent diffraction imaging. *Opt Express,* 20**,** 25914-34.

Godden, T. M., Suman, R., Humphry, M. J., Rodenburg, J. M. & Maiden, A. M. 2014. Ptychographic microscope for three-dimensional imaging. *Opt Express,* 22**,** 12513-23.

Goodman, J. W. 2005. *Introduction to Fourier Optics*, Roberts & Company Publishers.

Guizar-Sicairos, M. & Fienup, J. R. 2008a. Phase retrieval with Fourier-weighted projections. *Journal of the Optical Society of America A,* 25**,** 701.

Guizar-Sicairos, M. & Fienup, J. R. 2008b. Phase retrieval with transverse translation diversity: a nonlinear optimization approach. *Optics Express,* 16**,** 7264.

Guizar-Sicairos, M., Holler, M., Diaz, A., Vila-Comamala, J., Bunk, O. & Menzel, A. 2012. Role of the illumination spatial-frequency spectrum for ptychography. *Physical Review B,* 86.

Haider, M., Uhlemann, S., Schwan, E., Rose, H., Kabius, B. & Urban, K. 1998. Electron microscopy image enhanced. *Nature,* 392**,** 768-769.

Haigh, S. J., Sawada, H. & Kirkland, A. I. 2009. Atomic Structure Imaging Beyond Conventional Resolution Limits in the Transmission Electron Microscope. *Physical Review Letters,* 103**,** 126101.

Hawkes, P. W. 2001. The long road to spherical aberration correction. *Biology of the Cell,* 93**,** 432-439.

Hecht, E. 2002. *Optics*, Addison Wesley.

Hegerl, R. & Hoppe, W. 1970. DYNAMIC THEORY OF CRYSTALLINE STRUCTURE ANALYSIS BY ELECTRON DIFFRACTION IN INHOMOGENEOUS PRIMARY WAVE FIELD. *Berichte Der Bunsen-Gesellschaft Fur Physikalische Chemie,* 74**,** 1148-&.

Holler, M., Diaz, A., Guizar-Sicairos, M., Karvinen, P., Farm, E., Harkonen, E., Ritala, M., Menzel, A., Raabe, J. & Bunk, O. 2014. X-ray ptychographic computed tomography at 16 nm isotropic 3D resolution. *Sci Rep,* 4**,** 3857.

Holt, M. V., Hruszkewycz, S. O., Murray, C. E., Holt, J. R., Paskiewicz, D. M. & Fuoss, P. H. 2014. Strain Imaging of Nanoscale Semiconductor Heterostructures with X-Ray Bragg Projection Ptychography. *Physical Review Letters,* 112.

Hoppe, W. 1969a. Beugung im inhomogenen Primarstrahlwellenfeld. I. Prinzip einer Phasenmessung von Elektronenbeungungsinterferenzen. *Acta Crystallographica Section A,* 25**,** 495-501.

Hoppe, W. 1969b. Beugung im inhomogenen Primarstrahlwellenfeld. III. Amplituden- und Phasenbestimmung bei unperiodischen Objekten. *Acta Crystallographica Section A,* 25**,** 508-514.

Hoppe, W. & Strube, G. 1969. Beugung in inhomogenen Primarstrahlenwellenfeld. II. Lichtoptische Analogieversuche zur Phasenmessung von Gitterinterferenzen. *Acta Crystallographica Section A,* 25**,** 502-507.

Hornberger, B., De Jonge, M. D., Feser, M., Holl, P., Holzner, C., Jacobsen, C., Legnini, D., Paterson, D., Rehak, P., Struder, L. & Vogt, S. 2008. Differential phase contrast with a segmented detector in a scanning X-ray microprobe. *J Synchrotron Radiat,* 15**,** 355-62.

Howie, A. 1978. High resolution electron microscopy of amorphous thin films. *Journal of Non-Crystalline Solids,* 31**,** 41-55.

Hruszkewycz, S. O., Holt, M. V., Murray, C. E., Bruley, J., Holt, J., Tripathi, A., Shpyrko, O. G., Mcnulty, I., Highland, M. J. & Fuoss, P. H. 2012. Quantitative nanoscale imaging of lattice distortions in epitaxial semiconductor heterostructures using nanofocused X-ray Bragg projection ptychography. *Nano Lett,* 12**,** 5148-54.

Huang, X., Yan, H., Harder, R., Hwu, Y., Robinson, I. K. & Chu, Y. S. 2014. Optimization of overlap uniformness for ptychography. *Opt Express,* 22**,** 12634-44.

Hue, F., Rodenburg, J. M., Maiden, A. M. & Midgley, P. A. 2011. Extended ptychography in the transmission electron microscope: possibilities and limitations. *Ultramicroscopy,* 111**,** 1117-23.

Hüe, F., Rodenburg, J. M., Maiden, A. M., Sweeney, F. & Midgley, P. A. 2010. Wave-front phase retrieval in transmission electron microscopy via ptychography. *Physical Review B,* 82.

Humphry, M. J., Kraus, B., Hurst, A. C., Maiden, A. M. & Rodenburg, J. M. 2012. Ptychographic electron microscopy using high-angle dark-field scattering for sub-nanometre resolution imaging. *Nat Commun,* 3**,** 730.

Hurst, A. C., Edo, T. B., Walther, T., Sweeney, F. & Rodenburg, J. M. 2010. Probe position recovery for ptychographical imaging. *Journal of Physics: Conference Series,* 241**,** 012004.

Kirkland, A. I., Saxton, W. O. & Chand, G. 1997. Multiple beam tilt microscopy for super resolved imaging. *Journal of Electron Microscopy,* 46**,** 11-22.

Kirkland, A. I., Saxton, W. O., Chau, K. L., Tsuno, K. & Kawasaki, M. 1995. Super-resolution by aperture synthesis: tilt series reconstruction in CTEM. *Ultramicroscopy,* 57**,** 355-374.

Kirkpatrick, P. & Baez, A. V. 1948. Formation of Optical Images by X-Rays. *Journal of the Optical Society of America,* 38**,** 766-773.

Krivanek, O. L., Dellby, N., Spence, A. J., Camps, R. A. & Brown, L. M. 1997. Aberration correction in the STEM. *In:* RODENBURG, J. M. (ed.) *Electron Microscopy and Analysis 1997.* Bristol: Iop Publishing Ltd.

Liu, C., Walther, T. & Rodenburg, J. M. 2009. Influence of thick crystal effects on ptychographic image reconstruction with moveable illumination. *Ultramicroscopy,* 109**,** 1263-75.

Maiden, A. M., Humphry, M. J. & Rodenburg, J. M. 2012a. Ptychographic transmission microscopy in three dimensions using a multi-slice approach. *Journal of the Optical Society of America A,* 29**,** 1606-1614.

Maiden, A. M., Humphry, M. J., Sarahan, M. C., Kraus, B. & Rodenburg, J. M. 2012b. An annealing algorithm to correct positioning errors in ptychography. *Ultramicroscopy,* 120**,** 64-72.

Maiden, A. M., Humphry, M. J., Zhang, F. & Rodenburg, J. M. 2011. Superresolution imaging via ptychography. *J Opt Soc Am A Opt Image Sci Vis,* 28**,** 604-12.

Maiden, A. M., Morrison, G. R., Kaulich, B., Gianoncelli, A. & Rodenburg, J. M. 2013. Soft X-ray spectromicroscopy using ptychography with randomly phased illumination. *Nat Commun,* 4**,** 1669.

Maiden, A. M. & Rodenburg, J. M. 2009. An improved ptychographical phase retrieval algorithm for diffractive imaging. *Ultramicroscopy,* 109**,** 1256-62.

Maiden, A. M., Rodenburg, J. M. & Humphry, M. J. 2010. Optical ptychography: a practical implementation with useful resolution. *Optics Letters,* 35**,** 2585-2587.

Marchesini, S. 2007. Invited article: a [corrected] unified evaluation of iterative projection algorithms for phase retrieval. *Rev Sci Instrum,* 78**,** 011301.

Marrison, J., Raty, L., Marriott, P. & O'toole, P. 2013. Ptychography--a label free, high-contrast imaging technique for live cells using quantitative phase information. *Sci Rep,* 3**,** 2369.

Mccallum, B. C., Landauer, M. N. & Rodenburg, J. M. 1995. Complex image reconstruction of weak specimens from a three-sector detector in the STEM. *Optik,* 101**,** 53-62.

Mccallum, B. C. & Rodenburg, J. M. 1992. Two-dimensional demonstration of Wigner phase-retrieval microscopy in the STEM configuration. *Ultramicroscopy,* 45**,** 371-380.

Miao, J., Charalambous, P., Kirz, J. & Sayre, D. 1999. Extending the methodology of X-ray crystallography to allow imaging of micrometre-sized non-crystalline specimens. *Nature,* 400**,** 342-344.

Miao, J., Sayre, D. & Chapman, H. N. 1998. Phase retrieval from the magnitude of the Fourier transforms of nonperiodic objects. *Journal of the Optical Society of America A,* 15**,** 1662.

Nellist, P. D., Mccallum, B. C. & Rodenburg, J. M. 1995. Resolution beyond the 'information limit' in transmission electron microscopy. *Nature,* 374**,** 630-632.

Nellist, P. D. & Rodenburg, J. M. 1994. Beyond the conventional information limit: the relevant coherence function. *Ultramicroscopy,* 54**,** 61-74.

Newton, M. C., Leake, S. J., Harder, R. & Robinson, I. K. 2010. Three-dimensional imaging of strain in a single ZnO nanorod. *Nat Mater,* 9**,** 120-4.

Pešić, Z. D., Fanis, A. D., Wagner, U. & Rau, C. 2013. Experimental stations at I13 beamline at Diamond Light Source. *Journal of Physics: Conference Series,* 425**,** 182003.

Plamann, T. & Rodenburg, J. M. 1994. DOUBLE RESOLUTION IMAGING WITH INFINITE DEPTH OF FOCUS IN SINGLE LENS SCANNING MICROSCOPY. *Optik,* 96**,** 31-36.

Ponchut, C., Rigal, J. M., Clément, J., Papillon, E., Homs, A. & Petitdemange, S. 2011. MAXIPIX, a fast readout photon-counting X-ray area detector for synchrotron applications. *Journal of Instrumentation,* 6**,** C01069-C01069.

Putkunz, C. T., D'alfonso, A. J., Morgan, A. J., Weyland, M., Dwyer, C., Bourgeois, L., Etheridge, J., Roberts, A., Scholten, R. E., Nugent, K. A. & Allen, L. J. 2012. Atom-Scale Ptychographic Electron Diffractive Imaging of Boron Nitride Cones. *Physical Review Letters,* 108.

Rau, C., Wagner, U., Peach, A., Robinson, I. K., Singh, B., Wilkin, G., Jones, C., Garrett, R., Gentle, I., Nugent, K. & Wilkins, S. 2010. The Diamond Beamline I13L for Imaging and Coherence. 121-125.

Rau, C., Wagner, U., Pešić, Z. & De Fanis, A. 2011. Coherent imaging at the Diamond beamline I13. *physica status solidi (a),* 208**,** 2522-2525.

Rodenburg, J., Hurst, A., Cullis, A., Dobson, B., Pfeiffer, F., Bunk, O., David, C., Jefimovs, K. & Johnson, I. 2007a. Hard-X-Ray Lensless Imaging of Extended Objects. *Physical Review Letters,* 98.

Rodenburg, J. M. 2008. Ptychography and Related Diffractive Imaging Methods. *Advances in Imaging and Electron Physics.* Elsevier.

Rodenburg, J. M. & Bates, R. H. T. 1992. The Theory of Super-Resolution Electron Microscopy Via Wigner-Distribution Deconvolution. *Philosophical Transactions of the Royal Society of London. Series A: Physical and Engineering Sciences,* 339**,** 521-553.

Rodenburg, J. M. & Faulkner, H. M. L. 2004. A phase retrieval algorithm for shifting illumination. *Applied Physics Letters,* 85**,** 4795.

Rodenburg, J. M., Hurst, A. C. & Cullis, A. G. 2007b. Transmission microscopy without lenses for objects of unlimited size. *Ultramicroscopy,* 107**,** 227-31.

Rodenburg, J. M., Mccallum, B. C. & Nellist, P. D. 1993. Experimental tests on double-resolution coherent imaging via STEM. *Ultramicroscopy,* 48**,** 304-314.

Scherzer, O. 1936. Over some errors of electrons lenses. *Zeitschrift Fur Physik,* 101**,** 593-603.

Scherzer, O. 1949. The Theoretical Resolution Limit of the Electron Microscope. *Journal of Applied Physics,* 20**,** 20-29.

Schropp, A., Boye, P., Feldkamp, J. M., Hoppe, R., Patommel, J., Samberg, D., Stephan, S., Giewekemeyer, K., Wilke, R. N., Salditt, T., Gulden, J., Mancuso, A. P., Vartanyants, I. A., Weckert, E., SchöDer, S., Burghammer, M. & Schroer, C. G. 2010. Hard x-ray nanobeam characterization by coherent diffraction microscopy. *Applied Physics Letters,* 96**,** 091102.

Schropp, A., Hoppe, R., Patommel, J., Samberg, D., Seiboth, F., Stephan, S., Wellenreuther, G., Falkenberg, G. & Schroer, C. G. 2012. Hard x-ray scanning microscopy with coherent radiation: Beyond the resolution of conventional x-ray microscopes. *Applied Physics Letters,* 100**,** 253112.

Shenfield, A. & Rodenburg, J. M. 2011. Evolutionary determination of experimental parameters for ptychographical imaging. *Journal of Applied Physics,* 109**,** 124510.

Snigirev, A., Kohn, V., Snigireva, I. & Lengeler, B. 1996. A compound refractive lens for focusing high-energy X-rays. *Nature,* 384**,** 49-51.

Spence, J. C., Weierstall, U. & Howells, M. 2004. Coherence and sampling requirements for diffractive imaging. *Ultramicroscopy,* 101**,** 149-52.

Stockmar, M., Cloetens, P., Zanette, I., Enders, B., Dierolf, M., Pfeiffer, F. & Thibault, P. 2013. Near-field ptychography: phase retrieval for inline holography using a structured illumination. *Sci Rep,* 3**,** 1927.

Suzuki, A., Furutaku, S., Shimomura, K., Yamauchi, K., Kohmura, Y., Ishikawa, T. & Takahashi, Y. 2014. High-Resolution Multislice X-Ray Ptychography of Extended Thick Objects. *Physical Review Letters,* 112.

Takahashi, Y., Suzuki, A., Furutaku, S., Yamauchi, K., Kohmura, Y. & Ishikawa, T. 2013. Bragg x-ray ptychography of a silicon crystal: Visualization of the dislocation strain field and the production of a vortex beam. *Physical Review B,* 87.

Takahashi, Y., Suzuki, A., Zettsu, N., Kohmura, Y., Yamauchi, K. & Ishikawa, T. 2011. Multiscale element mapping of buried structures by ptychographic x-ray diffraction microscopy using anomalous scattering. *Applied Physics Letters,* 99**,** 131905.

Thibault, P., Dierolf, M., Bunk, O., Menzel, A. & Pfeiffer, F. 2009. Probe retrieval in ptychographic coherent diffractive imaging. *Ultramicroscopy,* 109**,** 338-43.

Thibault, P., Dierolf, M., Menzel, A., Bunk, O., David, C. & Pfeiffer, F. 2008. High-resolution scanning x-ray diffraction microscopy. *Science,* 321**,** 379-82.

Thibault, P. & Menzel, A. 2013. Reconstructing state mixtures from diffraction measurements. *Nature,* 494**,** 68-71.

Whitehead, L. W., Williams, G. J., Quiney, H. M., Vine, D. J., Dilanian, R. A., Flewett, S., Nugent, K. A. & Mcnulty, I. 2009. Diffractive Imaging Using Partially Coherent X Rays. *Physical Review Letters,* 103.

Williams, D. B., Carter, C. Barry 2009. *Transmission Electron Microscopy*, Springer.

Zhang, F., Peterson, I., Vila-Comamala, J., Diaz, A., Berenguer, F., Bean, R., Chen, B., Menzel, A., Robinson, I. K. & Rodenburg, J. M. 2013. Translation position determination in ptychographic coherent diffraction imaging. *Opt Express,* 21**,** 13592-606.

Zheng, G., Horstmeyer, R. & Yang, C. 2013. Wide-field, high-resolution Fourier ptychographic microscopy. *Nature Photonics,* 7**,** 739-745.

Zuo, J. M., Vartanyants, I., Gao, M., Zhang, R. & Nagahara, L. A. 2003. Atomic resolution imaging of a carbon nanotube from diffraction intensities. *Science,* 300**,** 1419-21.